

Stony Brook University



OFFICIAL COPY

The official electronic file of this thesis or dissertation is maintained by the University Libraries on behalf of The Graduate School at Stony Brook University.

© All Rights Reserved by Author.

**Cystoscopic Optical Coherence Tomography and Ultrahigh
Resolution Optical Doppler Tomography for Quantitative
Structural and Functional Imaging**

A Dissertation Presented

by

Hugang Ren

to

The Graduate School

in Partial Fulfillment of the

Requirements

for the Degree of

Doctor of Philosophy

in

Biomedical Engineering

Stony Brook University

August 2012

Stony Brook University

The Graduate School

Hugang Ren

We, the dissertation committee for the above candidate for the
Doctor of Philosophy degree, hereby recommend
acceptance of this dissertation.

Yingtian Pan – Dissertation Advisor
Professor, Department of Biomedical Engineering

Emilia Entcheva - Chairperson of Defense
Associate Professor, Biomedical Engineering Department

Congwu Du - Committee Member
Associate Professor, Department of Biomedical Engineering

Shmuel Einav- Committee Member
Professor, Department of Biomedical Engineering

Jason Kim - Outside Member
Assistant Professor, Department of Urology, Stony Brook University

This dissertation is accepted by the Graduate School

Charles Taber

Interim Dean of the Graduate School

Abstract of the Dissertation

**Cystoscopic Optical Coherence Tomography and Ultrahigh Resolution
Optical Doppler Tomography for Quantitative Structural and
Functional Imaging**

by

Hugang Ren

Doctor of Philosophy

in

Biomedical Engineering

Stony Brook University

2012

This dissertation presents the design, development as well as preclinical and clinical validations of a cystoscopic optical coherence tomography (OCT) system and an ultrahigh resolution optical Doppler tomography (ODT) system for quantitative structural and functional imaging. The core of this dissertation can be divided into three sections.

In the first section of the dissertation, which includes Chapter 3-Chapter 4, we validated the design and development of cystoscopic OCT (COCT) for bladder cancer diagnosis *in vivo*. To break the penetration depth barrier of the light, endoscopic imaging via fiber-optic technique has been developed. In this dissertation, we focused on bladder cancer diagnosis and management. A microelectromechanical systems (MEMS) mirror

based front view COCT system was developed, optimized and validated in the operating room. The touch-and-see feature enables user friendly OCT examinations. Based on 220 cases, MEMS mirror based COCT provided a sensitivity of 92.4% and a specificity of 85.2% for clinical bladder cancer diagnosis. To further enhance early bladder cancer diagnosis in the outpatient, we proposed, designed and developed a hybrid flexible cystoscopic OCT (FCOCT) system. The miniature size (i.e., <2mm) enables smooth integration of the probe into the commercial cystoscopes used in the outpatient examinations. Since the probe is flexible, for those lesions located close to the bladder neck, full access can be achieved by articulating the tip of the cystoscope. Moreover, with a field of view of >8mm, FCOCT allows *in vivo* tumor boundary delineation and guided tumor resection.

In the second section of the dissertation, including Chapter 5-Chapter 7, quantitative image analysis based computer aided diagnosis (CAD) approach was demonstrated. Conventional OCT diagnosis was based on descriptive and qualitative features. To provide quantitative and objective diagnosis, we developed a CAD approach based on *enface* image analysis of the increased urothelial heterogeneity induced by carcinogenesis. To overcome the limitation of small field of view, we designed a comparative study to evaluate the utilities and potential limitations of current optical imaging techniques for early bladder cancer diagnosis. The results of this study demonstrated the potential of narrow band imaging (NBI)-guided cystoscopic OCT to effectively enhance the efficacy and efficiency of current cystoscopic procedure in the diagnosis of bladder cancer. At the same time, we showed that high resolution OCT with

3D image segmentation and analysis enabled delineation of morphological details of the human fetal membrane and early detection of microscopic chronic pseudocysts.

In the last section of the dissertation, from Chapter 8 to Chapter 11, we designed, developed and validated the ultrahigh resolution optical Doppler tomography (μ ODT) system for brain functional imaging. Functional imaging has been achieved with Doppler OCT by probing the blood flow information. To enable microvascular imaging, we developed an ultrahigh resolution ODT system with $\sim 1.8\mu\text{m}$ axial resolution and $<10\mu\text{m/s}$ sensitivity. Moreover, we proposed a frequency binning algorithm to increase the dynamic range ~ 20 times to enable both slow capillary flow and fast branch flow imaging. By taking advantages of the Doppler effect, we demonstrated a label free method to separate veins from arteries at large field of view. The performance of the μ ODT system was validated with an acute cocaine challenge model, and cocaine elicited micro ischemia was observed 45 minutes after cocaine administration, which was exacerbated with repeated administration. To decode the mystery of Doppler effect on capillary flow, we proposed a new method termed particle counting ultrahigh resolution ODT (pc- μ ODT), which enables label free accurate red blood cell (RBC) velocity measurement based on the transient phase information. To investigate the contrast differences between ODT and optical coherence angiography (OCA), we performed both phantom and *in vivo* animal studies and discovered that the high contrast of OCA was partially due to the enhancement from the Brownian motion of the red and white blood cells. With the in depth understanding of the Doppler technique from previous studies, we further improved the performance of the ODT system by employing optimized optical

design, newly developed contrast agent (e.g., intralipid for flow enhancement) and smart scanning protocol. With the enhanced ODT system, the chronic cocaine effect on the cerebral blood flow was investigated based on a rodent model.

Table of Content

| | |
|--|-------------|
| List of Figures | X |
| Acknowledgements | xiii |
| List of Publications | xv |
| Chapter 1 Background and Introduction | 1 |
| 1.1 Principles of Optical Coherence Tomography (OCT) | 2 |
| 1.2 Spectral Domain OCT | 6 |
| 1.3 Endoscopic OCT | 8 |
| 1.4 Doppler OCT | 10 |
| Chapter 2 System Development and Image Reconstruction | 18 |
| 2.1 Design of Spectral Domain OCT Systems | 18 |
| 2.1.1 Light Source..... | 18 |
| 2.1.2 Sample Arm..... | 25 |
| 2.1.3 Reference Arm | 27 |
| 2.1.4 Detection Arm | 27 |
| 2.2 System Specifications | 30 |
| 2.2.1 Axial Resolution | 30 |
| 2.2.2 Lateral Resolution..... | 31 |
| 2.2.3 Imaging Depth | 32 |
| 2.2.4 Frame Rate..... | 34 |
| 2.3 Design of MEMS Mirror Based OCT Endoscope | 34 |
| 2.4 OCT Image Reconstruction..... | 38 |
| 2.4.1 Intensity Image Reconstruction | 38 |
| 2.4.2 Image Segmentation and Computer Aided Diagnosis | 39 |
| 2.4.3 Doppler Flow Image Reconstruction..... | 44 |
| 2.4.4 Vessel Tail Removal..... | 46 |
| 2.4.5 Enhancing Flow Detection Dynamic Range..... | 47 |
| Chapter 3 Cystoscopic OCT for Bladder Cancer Diagnosis <i>in vivo</i> | 49 |
| 3.1 Introduction | 49 |
| 3.2 Materials and Methods..... | 50 |
| 3.2.1 Patient | 50 |
| 3.2.2 COCT..... | 52 |
| 3.2.3 Clinical Examination | 53 |
| 3.2.4 Statistical Analysis..... | 54 |
| 3.3 Results | 54 |
| 3.4 Discussions..... | 60 |
| 3.5 Conclusions | 62 |
| Chapter 4 Flexible Hybrid Cystoscopy/Optical Coherence Tomography for Early Bladder Cancer Diagnosis and Guided Tumor Resection | 64 |
| 4.1 Introduction..... | 64 |

| | |
|--|------------|
| 4.2 Materials & Methods | 65 |
| 4.2.1 Flexible Endoscopic OCT Probe: Optical Design | 65 |
| 4.2.2 Flexible Endoscopic OCT Probe: ZEMAX Simulation..... | 67 |
| 4.2.3 Flexible Endoscopic OCT Probe: Mechanical Design | 71 |
| 4.2.4 Flexible Hybrid Cystoscopy/OCT | 72 |
| 4.2.5 Clinical Protocol | 74 |
| 4.3 Results..... | 74 |
| 4.4 Discussions..... | 77 |
| 4.4 Conclusions..... | 79 |
| Chapter 5 Quantitative 3D OCT to Enhance Diagnosis of Bladder CIS..... | 81 |
| 5.1 Introduction..... | 81 |
| 5.2 Materials and Methods..... | 83 |
| 5.2.1 Transgenic CIS model | 83 |
| 5.2.2 3D OCT Image Acquisition..... | 83 |
| 5.2.3 3D OCT Image Analysis..... | 84 |
| 5.2.4 Statistical Analysis..... | 86 |
| 5.3 Results..... | 86 |
| 5.4 Discussions..... | 92 |
| 5.5 Conclusions..... | 96 |
| Chapter 6 Image Guided 3D OCT for Early Diagnosis of Carcinoma in situ of the Bladder..... | 98 |
| 6.1 Introduction..... | 98 |
| 6.2 Materials and Methods..... | 100 |
| 6.2.1 Transgenic Model | 100 |
| 6.2.2 Image Acquisition..... | 100 |
| 6.2.3 Image Analysis and Diagnosis of CIS | 102 |
| 6.2.4 Statistical Analysis..... | 103 |
| 6.3 Results..... | 104 |
| 6.4 Discussions..... | 110 |
| 6.5 Conclusions..... | 113 |
| Chapter 7 High-Resolution 3D OCT for Imaging Diagnosis of Human Fetal Membrane..... | 115 |
| 7.1 Introduction..... | 115 |
| 7.2 Materials and Methods..... | 117 |
| 7.2.1 Sample Preparation..... | 117 |
| 7.2.2 3D OCT | 118 |
| 7.2.3 Imaging Examination..... | 119 |
| 7.3 Results..... | 121 |
| 7.4 Discussions..... | 128 |
| 7.5 Conclusions..... | 130 |
| Chapter 8 Ultrahigh Resolution Quantitative 3D Optical Doppler Tomography for Brain Functional Imaging..... | 132 |
| 8.1 Introduction..... | 132 |
| 8.2 Methods..... | 133 |
| 8.2.1 Mice | 134 |
| 8.2.2 Surgery..... | 134 |
| 8.2.3 Laser Disruption. | 134 |

| | |
|---|------------|
| 8.2.4 Intravenous Cocaine Induction | 135 |
| 8.2.5 Ultrahigh-resolution Optical Coherence Tomography (μ OCT) | 135 |
| 8.2.7 In vivo Cerebral Blood Flow Imaging | 137 |
| 8.2.8 Image Processing | 138 |
| 8.2.9 Micro Hemorrhagic Stroke | 139 |
| 8.2.10 Separation of Arterioles and Venules | 140 |
| 8.2.11 Minimal detectable flow rate | 142 |
| 8.2.12 Doppler angle correction | 146 |
| 8.2.13 Statistical Analysis..... | 150 |
| 8.3 Results..... | 150 |
| 8.3.1 Microangiography and quantitative capillary CBF imaging..... | 150 |
| 8.3.2 Laser-induced Microvascular Disruption | 152 |
| 8.3.3 Repeated cocaine evokes cerebral microischemia | 155 |
| 8.3.4 Inhomogeneity of spatiotemporal responses of CBF to cocaine | 157 |
| 8.4 Discussions..... | 160 |
| Chapter 9 Quantitative imaging of red blood cell velocity <i>in vivo</i> using optical coherence Doppler tomography..... | 165 |
| 9.1 Introduction..... | 165 |
| 9.2 Methods..... | 166 |
| 9.3 Results..... | 169 |
| 9.4 Discussions & Conclusions..... | 173 |
| Chapter 10 Cerebral Blood Flow Imaged with Ultrahigh-resolution Optical Coherence Angiography and Doppler Tomography | 176 |
| 10.1 Introduction..... | 176 |
| 10.2 Methods..... | 177 |
| 10.3 Results..... | 179 |
| 10.4 Discussions & Conclusions..... | 184 |
| Chapter 11 Enhanced Optical Doppler Tomography System to Investigate the Chronic Cocaine Effects on the Brain..... | 186 |
| 11.1 Introduction..... | 186 |
| 11.2 Materials and Methods..... | 187 |
| 11.2.1 System Setup | 187 |
| 11.2.2 Animal Model..... | 189 |
| 11.2.3 Intralipid as a Contrast Agent..... | 190 |
| 11.2.4 Scanning Protocol..... | 190 |
| 11.3 Results..... | 191 |
| 11.3.1 Imaging Results of Enhanced 3D ODT | 191 |
| 11.3.2 Flow Contrast Enhancement by Intralipid | 193 |
| 11.3.3 Cocaine Self-Administration Rat..... | 195 |
| 11.3.4 Congenital Learned Helplessness (cLH) Rat..... | 196 |
| 11.3.5 Vascular Density of Cocaine Treatment Mice..... | 198 |
| 11.4 Discussions..... | 200 |
| 11.4 Conclusions..... | 202 |
| Chapter 12 Conclusions and Future Work | 204 |
| References | 211 |

List of Figures

| | |
|---|----|
| Fig. 1.1 Principle of coherence and low coherence Michelson interferometer | 3 |
| Fig. 1.2 Principle of time domain OCT | 6 |
| Fig. 1.3 Principle of spectral domain OCT | 7 |
| Fig. 1.4 Schematic diagram showing the principle of Doppler effect | 11 |
| Fig. 2.1 Relationship between spectrum bandwidth and FWHM of auto correlation. | 21 |
| Fig. 2.2 Relationship between spectral shape and auto correlation function | 22 |
| Fig. 2.3 Spectrum of the SLD | 24 |
| Fig. 2.4 Layout of the femtomsecond laser | 24 |
| Fig. 2.5 Spectrum of the Ti:Sapphire laser | 25 |
| Fig. 2.6 Design of a spectral domain OCT system | 28 |
| Fig. 2.7 SEM image of a MEMS mirror | 35 |
| Fig. 2.8 Voltage angle curve of MEMS mirror | 36 |
| Fig. 2.9 Design of OCT endoscope by using MEMS mirror | 37 |
| Fig. 2.10 Packed OCT endoscope with MEMS mirror as the scanner | 38 |
| Fig. 2.11 SDOCT color image reconstruction software | 39 |
| Fig. 2.12 16 bits grayscale OCT image | 39 |
| Fig. 2.13 Mask of the region of interest | 40 |
| Fig. 2.14 Masked result | 40 |
| Fig. 2.15 Normalized image | 40 |
| Fig. 2.16 Filtered image | 41 |
| Fig. 2.17 Segmentation result of decidua vera and epithelium | 41 |
| Fig. 2.18 Segmentation result of chorion and trophoblast layer | 41 |
| Fig. 2.19 Region of interest consists of only subepithelial amnion and epithelium | 42 |
| Fig. 2.20 Final segmentation results | 42 |
| Fig. 2.21 Algorithm for enface image extraction | 43 |
| Fig. 2.22 Image processing algorithm and computer aided diagnosis algorithm | 44 |
| Fig. 2.23 Software for vessel tail removal | 47 |
| Fig. 2.24 Algorithm to enhance the flow dynamic range | 48 |
| Fig. 3.1 MEMS-based COCT for in vivo bladder cancer diagnosis | 52 |
| Fig. 3.2 In vivo surface, cross-sectional COCT and H&E stained histological images of normal human bladder versus a papillary TCC | 55 |
| Fig. 3.3 In vivo surface, COCT and H&E stained histological images of a recurrent TCC post TURBT and a CIS. | 57 |
| Fig. 4.1 Optical design of the flexible cystoscopic OCT probe | 66 |
| Fig. 4.2 ZEMAX model of the designed flexible endoscopic OCT probe | 67 |
| Fig. 4.3 Modulation transfer function (MTF) of the OCT probe without cylinder lens ... | 68 |

| | |
|--|-----|
| Fig. 4.4 Spot diagram of the OCT probe without cylinder lens..... | 69 |
| Fig. 4.5 Modulation transfer function (MTF) of the OCT probe with cylinder lens | 70 |
| Fig. 4.6 Spot diagram of the OCT probe with cylinder lens..... | 71 |
| Fig. 4.7 System setup of the hybrid cystoscopy/OCT | 73 |
| Fig. 4.8 Results of normal, TCC and CIS bladders from the FCOCT platform | 75 |
| Fig. 4.9 Results of transition parts in bladder from FCOCT platform..... | 76 |
| Fig. 4.10 Results of a cured bladder with BCG treatment history | 76 |
| Fig. 4.11 Hough transform based approach to remove the artifact lines in OCT image .. | 79 |
| Fig. 5.1 Results of a normal mouse bladder..... | 87 |
| Fig. 5.2 Results of CIS in a SV40T mouse bladder | 89 |
| Fig. 5.3 Results of ‘advanced’ CIS in SV40T mouse bladder | 91 |
| Fig. 5.4 A comparison between FFT profiles calculated from 2D and 3D OCT..... | 93 |
| Fig. 6.1 Results of a normal mouse bladder..... | 104 |
| Fig. 6.2 Results of an early CIS | 106 |
| Fig. 6.3 Results of a more advanced CIS..... | 107 |
| Fig. 6.4 Results of a minor traumatic bladder..... | 108 |
| Fig. 7.1 A sketch of the 3D OCT setup..... | 118 |
| Fig. 7.2 2D images of a normal human fetal membrane..... | 121 |
| Fig. 7.3 3D image of a normal human FM | 123 |
| Fig. 7.4 2D image of a human FM specimen with MCP | 124 |
| Fig. 7.5 3D OCT image of a human FM with MCP | 125 |
| Fig. 7.6 OCT images of human FM specimens with different-size MCP lesions compared with the corresponding H&E stained histological images..... | 126 |
| Fig. 7.7 3D HFUS image of a human FM with thick MCP | 130 |
| Fig. 8.1 A sketch of ultrahigh-resolution OCT setup for acquiring μ OCA and μ ODT images | 137 |
| Fig. 8.2 Microvascular hemorrhagic stroke on the mouse somatosensory cortex | 140 |
| Fig. 8.3 Illustration of arterial and venous vessel separation..... | 141 |
| Fig. 8.4 Locations to sample background flow noise to characterize μ ODT flow sensitivity | 145 |
| Fig. 8.5 Separation of arterial and venous vessels | 146 |
| Fig. 8.6 3D bidirectional flows before and after angle correction | 148 |
| Fig. 8.7 Selected vessels of interest for angle correction illustrated in the quantitative flow map | 149 |
| Fig. 8.8 Cerebral vasculature and cerebral blood flows (CBF) of the mouse somatosensory cortex..... | 152 |
| Fig. 8.9 Laser induced disruption of a cerebral capillary and a branch vessel on the mouse somatosensory cortex..... | 154 |
| Fig. 8.10 Cocaine evoked microvascular disruptions on the mouse somatosensory cortex | 157 |
| Fig. 8.11 Spatiotemporal evolutions of CBF mouse somatosensory cortex in response to an acute cocaine challenge..... | 159 |
| Fig. 9.1 A sketch to illustrate pc- μ ODT for accurate imaging of capillary flow..... | 167 |
| Fig. 9.2 3D μ ODT of mouse cortical CBF networks in vivo..... | 170 |

| | |
|---|-----|
| Fig. 9.3 Capillary vRBC measured by pc- μ ODT | 173 |
| Fig. 10.1 Comparative results of μ OCA and μ ODT for bi-directional flows..... | 179 |
| Fig. 10.2 Quantitative analyses of the flow-rate changes of directional flow by μ ODT and non-directional flow by μ OCA | 182 |
| Fig. 10.3 Comparative μ OCA and μ ODT images of mouse cortical brain in vivo during baseline after 1st and 2nd laser coagulations | 183 |
| Fig. 11.1 Setup of the enhanced optical Doppler tomography system | 188 |
| Fig. 11.2 Results of CBF imaging from enhanced 3D ODT system | 192 |
| Fig. 11.3 Comparison of contrast enhancement by saline and the same amount of intralipid..... | 194 |
| Fig. 11.4 Quantitative intralipid effect on CBF velocity and statistical analysis | 195 |
| Fig. 11.5 CBF responses to cocaine challenge of control , short access (SA) and long access (LA) rats..... | 196 |
| Fig. 11.6 CBF responses to cocaine challenge | 198 |
| Fig. 11.7 Typical OCA and ODT images of control mouse and chronic cocaine treated mouse | 199 |
| Fig. 11.8 Quantitative evaluation of vascular density difference between control mouse and chronic cocaine treated mouse | 200 |
| Fig. 11.9 Low frequency fluctuation of the CBF in veins and arteries..... | 202 |

Acknowledgements

I would like to express my deep and sincere gratitude to my advisor, Dr. Yingtian Pan. Over the years of my graduate study, he patiently provided the vision, encouragement, guidance, trust and support to make my Ph.D. experience productive and stimulating. He is always enthusiastic and energetic towards scientific research, responsible for his family and lab, which sets an invaluable role model for me and continually encourages me for my future career. It has been a great pleasure to work in his group, and I really appreciate it.

I am also deeply grateful to Dr. Congwu Du, for her insightful guidance on my brain functional studies, for helping me feel like a member of her group, and for dedicating her precious time and efforts advising me on cocaine studies. I would also like to thank the group members. I thank my fellow lab mates Zhijia Yuan and Zhongchi Luo for many fruitful discussions on various topics about OCT and LSCI. I am also indebted to Kicheon Park, for his talent on the animal surgery, which I can always trust and focus my efforts on the OCT part. His close collaboration contributed immensely to my productivity. Many others, not mentioned above, have also helped me in many projects. They have been my reliable source of friendships, good advice and collaboration.

I would also like to thank my collaborators. I thank Dr. Huikai Xie and Kemiao Jia from University of Florida for kindly providing MEMS mirrors. I thank Dr. Wayne

Waltzer, Dr. Rahuldev Bhalla, Dr. Ruth Miles, Dr. Jason Kim and the whole Urology department for their great support to our clinical studies. I thank Dr. Nora Volkow from National Institutes of Health for her tireless efforts on my manuscripts and insightful advice to my projects. I thank Dr. Jingxuan Liu from department of Pathology for reading histology slides. My special thanks go to Dr. Emilia Entcheva for her generous support and help to me over my graduate study.

I am extremely grateful to my committee, Dr. Emilia Entcheva, Dr. Congwu Du, Dr. Jason Kim and Dr. Shmuel Einav, for their support, guidance and valuable suggestions.

I thank all my friends for their help to both my personal and professional life. Thank you for making my life at US so enjoyable.

Lastly, I would like to thank my family for all their love and support. My parents, they raised me from rural China. Life was so hard, but they showed me how strong and brave people can be simply because they love me so much. I owe them everything and wish I could show them just how much I love them. My lovely wife Jing Wen, no matter what happens, she is always the one standing behind me. To support me for my oversea study, she sacrificed a lot. Whether I'm doing well or not, her always positive support and encouragement is the most powerful source of inspiration and energy. Without her support, my Ph.D. experience can never be so productive and my oversea life can never be so happy and enjoyable. I'm also deeply indebted to my brothers, thank you so much for your years' support and help, and I always feel so lucky to have you in my life.

List of Publications

Journal Articles

1. **Ren, H.**, Du, C., Yuan, Z., Park, K., Volkow, N. and Pan, Y.: Cocaine Induced Cortical Microischemia in the Rodent Brain: Clinical Implications. *Nature: Molecular Psychiatry*, in press, (2012)
2. **Ren, H.**, Du, C., Pan, Y.: Cerebral Blood Flow Imaged with Ultrahigh-resolution Optical Coherence Angiography and Doppler Tomography. *Optics Letters*, 37(8):1388-1390, (2012)
3. **Ren, H.**, Du, C., Park, K., Volkow, N. and Pan, Y.: Quantitative imaging of red blood cell velocity *in vivo* using optical coherence Doppler tomography. *Applied Physics Letters*, 100(23): 233702-4, (2012)
4. **Ren, H.**, Park, K., Waltzer, W., Shroyer, K. and Pan, Y.: Early Detection of Carcinoma in situ of the Bladder: A Comparative Study of White Light Cystoscopy, Narrow Band Imaging, 5-ALA Fluorescence Cystoscopy and 3D Optical Coherence Tomography. *Journal of Urology*, 187(3):1063, (2012)
5. **Ren, H.**, Avila, C., Kaplan, C. and Pan, Y.: High-Resolution Imaging Diagnosis of Human Fetal Membrane by 3D Optical Coherence Tomography. *Journal of Biomedical Optics*, 16, 116006, (2011)
6. **Ren, H.**, Yuan, Z., Waltzer, W., Shroyer, K. and Pan, Y.: Enhancing the Detection of Carcinoma in situ of the Urinary Bladder by 3D Optical Coherence Tomography. *Journal of Urology*, 184:1499, (2010)
7. Yuan, Z., Zakhaleva, J., **Ren, H.** et al.: Noninvasive and High-Resolution Optical Monitoring of Healing of Diabetic Dermal Excisional Wounds Implanted with Biodegradable In Situ Gelable Hydrogels. *Tissue Engineering Part C: Methods*, 16: 237, (2010)
8. **Ren, H.**, Waltzer, W., and Pan, Y. et al.: Diagnosis of Bladder Cancer With Microelectromechanical Systems-based Cystoscopic Optical Coherence Tomography. *Urology*, 74:1351, (2009)
9. Yuan, Z., Luo, Z., **Ren, H.** et al.: A Digital Frequency Ramping Method for Enhancing Doppler Flow Imaging in Fourier-Domain Optical Coherence Tomography. *Optics Express*, 17: 3951, (2009)
10. Yuan, Z., Chen, B., **Ren, H.** and Pan, Y.: On the Possibility of Time-lapse Ultrahigh-resolution Optical Coherence Tomography for Bladder Cancer Grading. *Journal of Biomedical Optics*, 14: 050502, (2009)
11. Yuan, Z., **Ren, H.**, Pan, Y. et al.: Optical Coherence Tomography for Bladder Cancer Diagnosis: from Animal Study to Clinical Diagnosis. *Journal of Innovative Optical Health Sciences*, 1: 125, (2008)

Proceedings

1. **Ren, H.**, Park, K., Pan, Y. et al.: Image guided 3D OCT for early diagnosis of carcinoma in situ of the bladder. *SPIE Photonics West*, (2012)

2. **Ren, H.**, Luo, Z., Yuan, Z., Pan, Y. and Du, C.: Multichannel optical brain imaging to separate cerebral vascular, tissue metabolic and neuronal effects of cocaine. *SPIE Photonics West*, (2012)
3. Yuan, Z., Keng, K., Pan, R., **Ren, H.**, Du, C., Kim, J. and Pan, Y.: Characterization of dynamic physiology of the bladder by optical coherence tomography. *SPIE Photonics West*, (2012)
4. **Ren, H.**, Luo, Z., Pan, Y. et al.: Simultaneous Assessing the Intracellular Potassium and Calcium Concentrations Noninvasively in vivo with High Resolution Fluorescence Imaging. *International Conference & Expo on Emerging Technologies for a Smarter World*. (2011)
5. **Ren, H.**, Yuan, Z., Pan, Y. et al.: Enhancing Diagnosis of Bladder Cancer by 2D and 3D Optical Coherence Tomography (OCT). *OSA: Biomedical Optics*, (2010)
6. Yuan, Z., Luo, Z., **Ren, H.**, Pan, Y. and Du, C.: Doppler Optical Coherence Tomography for Flow Imaging with Optimized Digital Frequency Ramping Method. *OSA: Biomedical Optics*, (2010)
7. Yuan, Z., Zakehaleva, J., **Ren, H.** et al.: In vivo Optical Coherence Tomography of Mouse Skin Wound Healing. *OSA: Biomedical Optics*, (2008)

Chapter 1 Background and Introduction

Noninvasive imaging techniques such as computed tomography (CT), magnetic resonant imaging (MRI), positron emission tomography (PET), ultrasound (US), confocal microscopy (CM) and multiphoton microscopy (MPM) have been intensively studied and widely applied to visualize the structure and functions of the living biological samples. Among which, macroscopic imaging modalities including CT, MRI, PET and US provide a typical penetration depth over several centimeters and can be used for whole organ or even whole body imaging. However, their spatial resolutions are usually limited to several hundreds of microns¹. On the other hand, microscopic techniques such as CM and MPM allow micro resolution sub-cellular imaging, their penetration depths are limited to several hundreds of microns². Therefore, there is an imaging gap at tissue level with high resolution at intermediate depth.

Optical coherence tomography (OCT) is an emerging technique enabling 3D noninvasive imaging of living biological tissue at mesoscopic level (e.g., 1~10um resolution, 1~3mm depth). Since the first biomedical demonstration of OCT in the early 1990s³, the recent decades have witnessed a rapid development of various OCT based techniques, such as Fourier domain OCT for high sensitivity real time imaging⁴⁻⁶, endoscopic OCT for cancer diagnosis⁷, polarization sensitive OCT for birefringence detection⁸, angiographic OCT for vasculature visualization⁹ and Doppler OCT for

functional imaging¹⁰⁻¹². The aforementioned technological advances have promoted the wide clinical adoption of OCT in ophthalmology¹³, and further ongoing clinical evaluations in intravascular imaging¹⁴, dental imaging¹⁵, dermatology¹⁶ and cancer diagnosis¹⁷.

Among all these technological advances, here we focus on development of two aspects of OCT technologies: 1) endoscopic OCT, in particular, cystoscopic OCT for quantitative early bladder cancer diagnosis; 2) Doppler OCT for quantitative capillary blood flow imaging, namely, ultrahigh resolution optical Doppler tomography for functional imaging. By combining these two techniques, it's promising to perform quantitative structural and functional imaging simultaneously at real time *in vivo* in the future.

In this chapter, we will first introduce the basic principles of OCT, and then briefly review the historic development and current status of endoscopic OCT and Doppler OCT. In order to solve the clinical problems, we will examine the limitations of current systems and then propose and design specific studies as solutions to address these technical challenges.

1.1 Principles of Optical Coherence Tomography (OCT)

OCT provides coherence-gated information based on light interference, and it originated from Michelson interferometer. As illustrated in Fig. 1.1, light coming from the source is first split into reference and sample arms by a beam splitter. Light

backscattered from the reference arm and sample arm was recombined at the beam splitter and then detected by the photo diode.

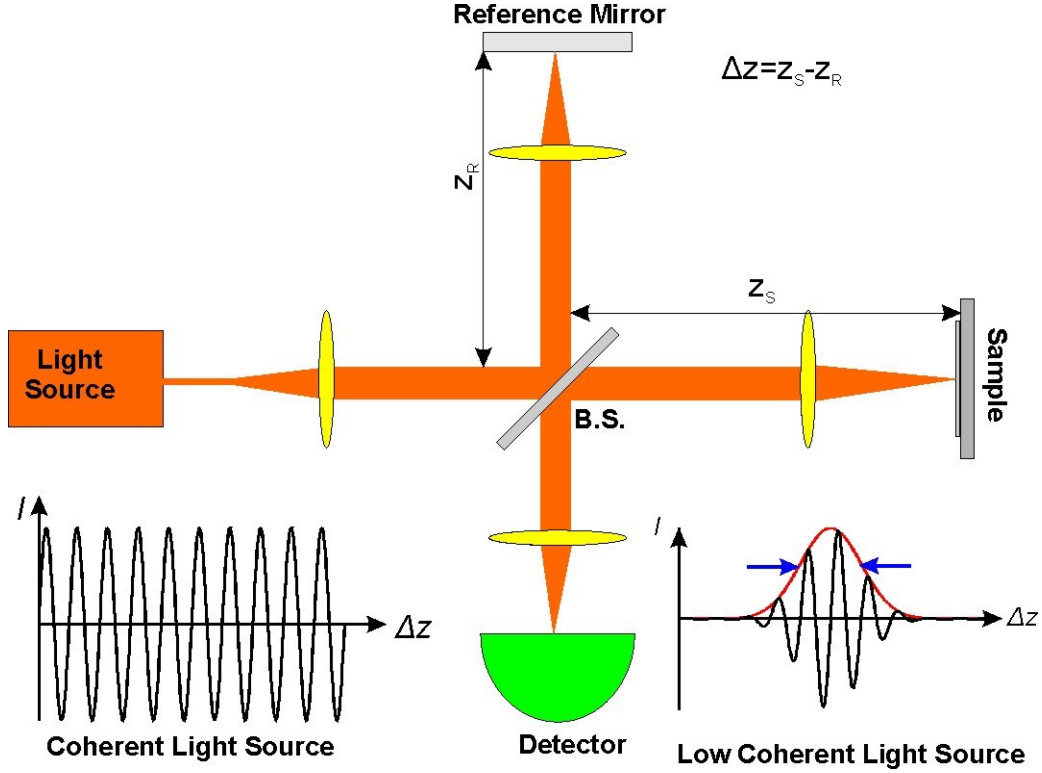


Fig. 1.1 Principle of coherence and low coherence Michelson interferometer. B.S.: beam splitter.

For a monochrome coherent light source, the electric fields of the reference and sample arms can be written as:

$$E_R = A_R \exp[-i(2kz_R - \omega t)] \tag{1.1}$$

$$E_S = A_S \exp[-i(2kz_S - \omega t)] \tag{1.2}$$

The combined electric field becomes:

$$E = E_R + E_S \tag{1.3}$$

Therefore, the light intensity at the photo detector is:

$$I = |E|^2 = I_R + I_S + 2\sqrt{I_R I_S} \cos(i2k\Delta z) \quad (1.4)$$

which indicates that the path length information is encoded by $2\sqrt{I_R I_S} \cos(i2k\Delta z)$. If we translate the reference mirror at a constant velocity v , therefore $\Delta z = v\Delta t$, then a time varying sinusoidal interference fringe can be visualized.

With similar principle, if we employ a low coherence light source, which means the light source has a wide bandwidth rather than a single frequency. Then the electric fields of reference and sample arms can be rewritten as:

$$E_R = A_R(\omega) \exp[-i(2k(\omega)z_R - \omega t)] \quad (1.5)$$

$$E_S = A_S(\omega) \exp[-i(2k(\omega)z_S - \omega t)] \quad (1.6)$$

The combined electric field now becomes:

$$E = E_R + E_S = A_R(\omega) \exp[-i(2k(\omega)z_R - \omega t)] + A_S(\omega) \exp[-i(2k(\omega)z_S - \omega t)] \quad (1.7)$$

And the light intensity at the photo detector changes to:

$$I = |E|^2 = |E_R + E_S|^2 = I_R + I_S + \int_{-\infty}^{+\infty} 2A_S(\omega)A_R(\omega)^* \cos(2k(\omega)\Delta z) \frac{d\omega}{2\pi} \quad (1.8)$$

If we apply Taylor expansion on the wave number k at ω_0 , then

$$k(\omega) = k(\omega_0) + k'(\omega_0)(\omega - \omega_0) + \frac{k''(\omega_0)(\omega - \omega_0)^2}{2!} + \frac{k^{(3)}(\omega_0)(\omega - \omega_0)^3}{3!} + \dots \quad (1.9)$$

If we assume a non-dispersive medium, thus the light source spectrum can be expressed as:

$$S(\omega - \omega_0) = A_S(\omega)A_R(\omega)^* \quad (1.10)$$

$$\text{and } k(\omega) = k(\omega_0) + k'(\omega_0)(\omega - \omega_0) \quad (1.11)$$

So, the detected intensity

$$I \propto \text{real} \left\{ \int_{-\infty}^{+\infty} 2S(\omega - \omega_0) \exp \{-i2[k(\omega_0) + k'(\omega_0)(\omega - \omega_0)]\Delta z\} \frac{d\omega}{2\pi} \right\} \quad (1.12)$$

Considering a Gaussian shape spectrum source, the spectrum can be expressed as

$$S(\omega - \omega_0) = \left(\frac{2\pi}{\sigma_\omega^2} \right)^{\frac{1}{2}} \exp \left[-\frac{(\omega - \omega_0)^2}{2\sigma_\omega^2} \right] \quad (1.13)$$

The interferogram will be:

$$I \propto \text{real} \left\{ \exp[-i2k(\omega_0)\Delta z] \int_{-\infty}^{+\infty} 2 \left(\frac{2\pi}{\sigma_\omega^2} \right)^{\frac{1}{2}} \exp \left[-\frac{(\omega - \omega_0)^2}{2\sigma_\omega^2} \right] \exp \{-i2[k'(\omega_0)(\omega - \omega_0)]\Delta z\} \frac{d(\omega - \omega_0)}{2\pi} \right\} \quad (1.14)$$

And can be simplified as:

$$I \propto \left\{ \exp[-i2k(\omega_0)\Delta z] \exp \left[-k'(\omega_0)^2 2\Delta z^2 \sigma_\omega^2 \right] \right\} \quad (1.15)$$

So, the low coherence interferogram represents the multiplication of two fringes, one is the modulation frequency, the other one is the envelope, while the envelope provides the coherence gate.

For sample under examination, we can consider it consists of lots of micro reflectors at different depths, as shown in Fig. 1.2. By detecting the time-of-flight of these echo pulses, the low coherence Michelson interferometer can be extended as optical coherence tomography (OCT).

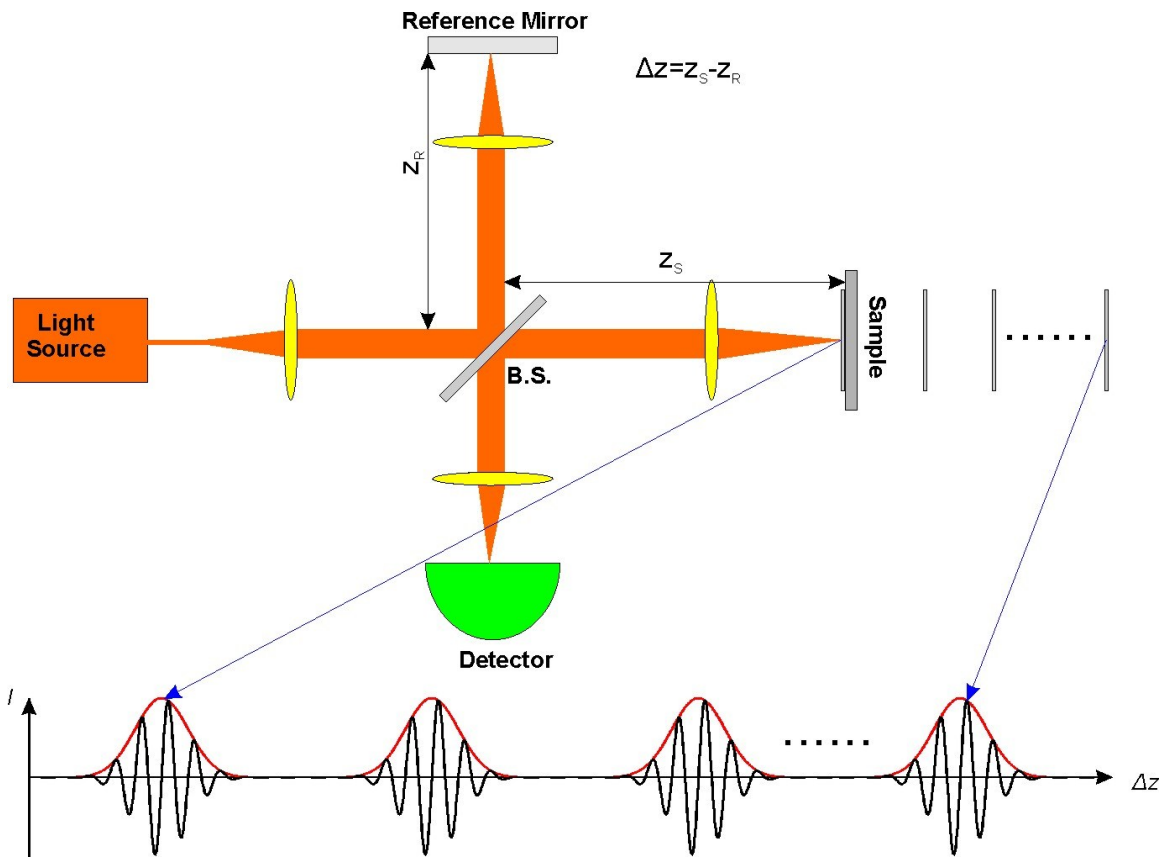


Fig. 1. 2 Principle of time domain OCT

1.2 Spectral Domain OCT

If we examine the detected signal in a different perspective, we can acquire the echo pulses coming from the micro reflectors at different depths simultaneously rather than sequentially. Therefore, for the light source at a specific wavelength, we can rewrite the interferogram and simplified it as following:

$$I(k) \propto \int_{-\infty}^{+\infty} S(k)a(z) \cos(2kn\Delta z) dz \quad (1.16)$$

For a time domain signal $a(\omega)\cos(\omega t)$, given a specific frequency ω , if we perform Fourier transform along time t , we will obtain the amplitude $a(\omega)$ of the frequency component ω in the frequency domain. Therefore, we can consider t and ω are a Fourier transform pair. If the signal contains multiple frequency components, the amplitudes of all frequency components will be recovered by a single Fourier transform.

For the interferogram mentioned above, at a specific depth Δz , if we perform Fourier transform along k , we will retrieve the scattering coefficient $a(\Delta z)$ at the specific depth Δz . So, k and Δz are a Fourier transform pair. The reflectance for reflectors at different depths can also be revealed by a single Fourier transform, which is shown in Fig. 1.3.

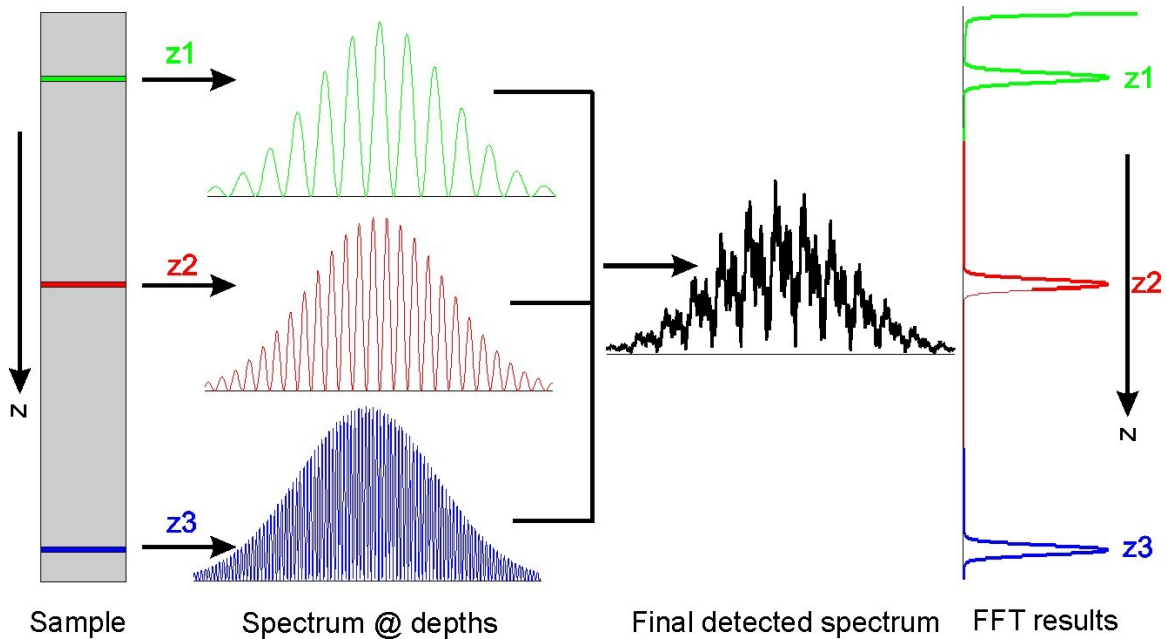


Fig. 1. 3 Principle of spectral domain OCT.

Since spectral domain OCT can measure the back scattering coefficients at different depths at one time, the imaging speed was dramatically increased. Also, because of sensor array detection rather than one single diode detection, the sensitivity of SDOCT is superior to that in the time domain (e.g., >20dB improvement)⁴⁻⁶.

1.3 Endoscopic OCT

By virtue of fiber-optic technique, bulky bench-top OCT system can be converted to portable device for clinical applications. However, for *in vivo* imaging, a miniaturized probe which can directly examine the biological tissue is still required. Endoscopic OCT by integrating OCT sample arm into the working channel of commercial endoscopes can faithfully produce high quality images of living tissue *in vivo* on site.

The challenge of designing OCT endoscopes lies in the compromise between smaller probe size and larger imaging FOV. For most of the commercial endoscopes, the working channel is limited to about 2~5mm or even smaller. However, for OCT B mode imaging, in order to shorten the total examination time and minimize sampling error, a larger FOV which can cover the boundary between normal and abnormal tissue would be highly desired.

Over the past decades, various OCT probes have been developed and validated by *in vivo* studies. Based on the scan mode, they can be divided into two categories: side view and front view.

Most of the OCT probes reported belong to side view mode¹⁸. In this mode, broad band light coming from the light source is first coupled by a single mode fiber, and then relayed and focused by a GRIN lens. Before the beam arrives at its focal spot, a rod mirror or prism is placed at the distal end of the probe to direct the light 90 degree, so that the beam can be focused just outside of the imaging catheter. Then based on different applications, two scanning modes can be achieved. For intravascular as well other tubular cavity imaging, 2D image is acquired by rotating the probe either in the proximal end through a fiber rotary joint, or at the distal end by a miniaturized motor. Rotation at the proximal end can largely reduce the probe sizes as small as limited by the GRIN lens; however, when the probe is very long, torque transmission can complicate the system. Rotation at the distal end eliminates any possible mechanic movements of the probe. However, the probe size is generally large and limited by the size of the micro motor. For other flat surface imaging, linear translation mode can also be applied to the probe by translating angular movement of the galvanometer shaft into linear motion¹⁹. Since images acquired by side view probe are actually 2D, so a back and forth translation is usually required to enable 3D imaging.

The other imaging mode is front view imaging. Unlike side view probe, light coming out from the light source is directly focused in front of the probe. And scan is usually achieved by mechanism inside of the probe. One typical setup is the PZT cantilever based forward scanning²⁰. In this probe, the PZT cantilever will translate the fiber and GRIN lens to move at a specific pattern, the focal spot will move accordingly. Another similar design is to vibrate the cantilever close to its mechanic resonant

frequency in a spiral scanning pattern²¹. Front view probe provides the touch-and-see ability and allows convenient examination. However, the probe size is generally larger, and FOV is smaller. To design a smaller probe with a larger FOV is quite challenging.

1.4 Doppler OCT

Doppler OCT is an OCT based functional imaging modality that can be used to minimum invasively measure the depth resolved blood flow velocity at high resolution and high sensitivity. The basic principle of Doppler OCT is the Doppler effect of light. The frequency of the back reflected light will be shifted if it hits a moving object. If the target is moving towards the beam, the frequency will be shifted towards shorter wave length, namely, blue shift. If the target is moving far away from the beam, the frequency will be red shifted. By calculating the frequency shift and angle at every voxel, 3D quantitative blood flow velocity map can be acquired.

Fig. 1.4 is a simplified diagram showing the basic principle of Doppler OCT. The frequency of the incident beam is f , the velocity of the red blood cells is v , the angle between the blood flow and the incident beam is θ , and then the Doppler shift is $\Delta f = \frac{2v \cos \theta}{c} f$. Based on the measured Doppler shift Δf , We can calculate the red

blood cell velocity as²²:

$$v = \frac{\Delta f c}{2f \cos \theta} = \frac{\Delta f \lambda}{2 \cos \theta} \quad (1.17)$$

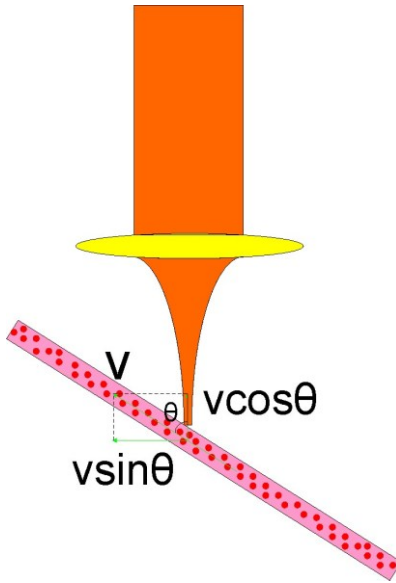


Fig. 1. 4 Schematic diagram showing the principle of Doppler effect.

Based on the analysis above, a straightforward approach to measure the blood flow velocity is to detect the Doppler frequency shift directly. As we explained before, based on the time domain detection technique, the slow OCT envelope signal is carried by a fast varying modulation signal which is directly related to the central frequency of the light source. If a frequency shift happens, the modulation frequency will change accordingly. By taking a short time Fourier transform (STFT)¹¹ along each A line in the depth direction, windowed frequency distribution could be extracted. The difference between the STFT result and the static modulation frequency is the real frequency shift. There are several intrinsic problems with this method. STFT is usually computation intensive, and will slow down the imaging speed¹⁰. Another important issue is that the detection sensitivity is inversely proportional to the imaging frame rate as well as spatial resolution. Since higher velocity sensitivity means better spectral resolution, and thus

larger STFT window. The larger the window, the worse the spatial resolution and the longer imaging time it requires for a single A-line. For *in vivo* functional imaging, this method based Doppler OCT shows severe limitations.

Another method to measure the flow velocity is to detect the local phase change induced by the frequency shift²³. The phase information of each A-line can be extracted through Fourier transform of the interferogram. By subtraction the phase terms between each A-line, the phase change can be readily calculated. This method tackled part of the problems from the STFT method, however, due to phase calculations of every two lines, this method requires higher spatial resolution and dense sampling to achieve high sensitivity.

Another approach is called resonant Doppler flow imaging²⁴. In this method, the reference arm is tuned to a specific velocity range. For flows with the same velocity as the reference arm, the system shows the best sensitivity. By tuning the reference arm, a large dynamic range blood flow can be measured. This method requires a moving reference which will complicate the hardware of the current SDOCT system.

Recently, several approaches by separating moving particles from static tissue either through hardware modification or software processing achieve very high sensitivity. One is called joint time and spectral domain method²⁵, this method performs two FFTs along wave number and lateral direction respectively. Another method is based on a modified Hilbert transform method to remove the static tissue caused noise term in the frequency domain by using a heavy-side function²⁶. Another high sensitive method is the digital frequency ramping method⁷ developed by our lab. By inserting a ramping

frequency into the phase term through post image processing, a Hilbert transform is applied to detect the phase flip caused by the blood flow. Therefore, quantitative flow imaging is achieved.

Besides these quantitative Doppler flow imaging methods, recently, there is a great interest on Doppler OCT based angiographic imaging to visualize the micro vasculature. One method is based on the Hilbert transform on the lateral direction or high pass filtering in the frequency domain^{9,27}, moving part is separated from the static tissue. Another method is to calculate the standard deviation²⁸ of several images scanned at the same location, the speckle contrast is used to visualize vasculature.

These aforementioned Doppler OCT methods provide additional functional features to the traditional structural OCT system, however, one obvious limitation up till now is that they cannot provide quantitative blood flow information down to microcirculation and capillary level, which is critical for many biomedical research and clinical applications.

Despite the rapid development of OCT technology, in particular, endoscopic OCT and Doppler OCT, the current systems and methods still show several limitations. Most of the endoscopes were developed for tubular structure imaging, however, for large cavity flat surface imaging, in our case, for bladder cancer imaging, no available endoscopes could provide large front FOV which is convenient for physicians to operate. Moreover, most of the current OCT based diagnostic methods rely on descriptive features to interpret the images, and is subjective and labor intensive. With 3D imaging modality developed, even large data sets will be generating in the future, therefore, a quantitative

independent computer aided OCT diagnosis is desired in clinical. Also, with the cross sectional depth resolved high resolution *in vivo* imaging capability; it's promising to extend OCT technique into other clinical fields and also for other critical clinical applications. For functional OCT imaging, current systems can never provide quantitative blood flow velocity down to capillary level, which is critical for various functional studies. It is desired to develop the functionality of Doppler OCT for capillary flow imaging.

In order to tackle these problems, in this dissertation, we proposed and developed several approaches to improve endoscopic OCT and Doppler OCT for quantitative structural and functional imaging.

1: Designed and developed a high performance OCT system for the proposed studies; designed and packed large FOV OCT endoscopes and integrated them into commercial cystoscopes for clinical *in vivo* studies; designed the algorithms to extract the quantitative features of OCT images for computer aided diagnosis of early bladder cancer, developed high performance phase detection techniques for ultra-high resolution capillary flow imaging.

2: Bladder cancer is the 5th most common type cancer in the US. However, it's curable if diagnosed early. Preclinical studies have demonstrated that OCT is effective in diagnosis of bladder cancer. Human cancer is more complicated than animal model. We designed high performance MEMS mirror based and flexible COCT probes, and validated their performances in the hospital operating room to enhance the current clinical diagnosis of bladder cancer.

3: 2D OCT based cancer diagnosis mainly relies on descriptive features and the diagnosis is qualitative. For large data sets acquired on huge patient population, especially for complicate cases (e.g., bladder carcinoma in situ (CIS)), 2D OCT shows its limitations as subjective, labor intensive and slow diagnosis. In this dissertation, we designed a computer aided diagnostic method based on quantitative image analysis of enface image extracted from 3D OCT to enhance the diagnosis of early stage bladder CIS based on a transgenic SV40T rodent model.

4: For cancer diagnosis of any specific organ, a complete examination of the whole organ is usually desired so as not to miss any hidden malignant lesions. With high spatial resolution at intermediate depth, OCT is a mesoscopic imaging modality at tissue level. Even with large FOV 3D imaging probes developed, whole organ OCT examination is still time consuming unless guided by other imaging modalities to locate the suspicious lesions first. For bladder cancer diagnosis, narrow band imaging (NBI) and fluorescence cystoscopy (FC) have been proved to be highly sensitive. For this purpose, we conducted a comparative study of white light cystoscopy, NBI, FC and 3D OCT to evaluate the efficacy and potential drawbacks of each modality to examine the hypothesis of NBI guided 3D OCT to enhance bladder CIS diagnosis.

5: Subsurface cysts cause a lot of complicated disorders to various organs (e.g., bladder pain syndrome/interstitial cystitis) and behave as a significant syndrome for some diseases (e.g., microscopic chorionic pseudocysts of human fetal membrane for preeclampsia). Pathological evaluation faces challenge because it cannot differentiate cysts from sample preparation induced artifacts. High resolution 3D OCT can faithfully

delineate the detailed morphological structure of living tissue *in vivo* on site based on high performance probes. Based on this, we applied high resolution 3D OCT on human fetal membranes to evaluate the feasibility of OCT imaging diagnosis of human fetal membrane diseases.

6: Functional imaging based on Doppler OCT have been demonstrated in various studies. However, quantitative blood flow measurement of microcirculation at capillary level still remains an unsolved problem. The major challenge of capillary flow imaging is to obtain both high spatial resolution to resolve the capillary vessels and high sensitivity to detect the slow blood flow. We developed an ultrahigh resolution optical Doppler tomography system and designed a high sensitivity phase detection algorithm to enable quantitative microcirculation imaging. With this technique, we performed multiple functional studies to validate the performance of the system and invented a particle counting method to accurately measure single red blood cell velocity *in vivo*.

7: Recent technological advances in OCT-based flow imaging techniques have evolved to two different approaches, i.e., optical coherence angiography (OCA) and Doppler tomography (ODT) for vasculatural visualization and quantitative imaging of CBF *in vivo*. However, it is known that the vascular turnouts provided by speckle contrast OCA surpass those detected by ODT, especially for capillary beds. In this dissertation, we presented experimental results on both flow phantom and *in vivo* animal (mouse brain following laser-induced microischemia) studies to elucidate the mechanistic differences between these two methods for CBF detections. With this better

understanding of Doppler effect, we optimized our ODT system and provided preliminary results of the chronic cocaine effect on the rodent CBF.

Chapter 2 System Development and Image Reconstruction

In this chapter, we will first design a spectral domain OCT system, and then evaluate the system performance and calculate the detailed specifications. Based on this system, we will then develop a MEMS mirror based OCT endoscope. For the software part, we will discuss the method we used to reconstruct the OCT image, the algorithms to perform the quantitative computer aided diagnosis, and more importantly, the software package we developed for the highly sensitive blood flow detection.

2.1 Design of Spectral Domain OCT Systems

A typical spectral domain OCT system consists of four major parts: light source, sample, reference and detection arms.

2.1.1 Light Source

Since OCT is an interferometric technique, the light sources available for OCT detection are limited based on the following criteria:

- 1) The light source must be spatially coherent;
- 2) The light source must be partially temporally coherent. In other words, the bandwidth of the spectrum should be as wide as possible.

With these general criteria, there are other specific critical parameters that need to be considered carefully when choose a light source. These parameters include central wavelength, spectral bandwidth, power as well as spectral shape. We will first analyze the importance of each parameter mathematically, and then based on the analyses, choose the proper light source and evaluate its performance.

The attenuation of incident light inside the biological tissue mainly comes from absorption and scattering. The major elements that contribute to the absorption are water and blood. Water absorption is low when the wavelength is lower than 2 μ m, at which the absorption is dominated by hemoglobin in the blood. The tissue scattering is almost a monotonic decrease function with increasing wavelength. So, all the factors combined together yield an optical therapeutic window for biological tissue, which lies in between 600nm to 1500nm.

As previously mentioned, the bandwidth of the light source is critical to make sure of low coherence property. Assume we have a Gaussian shape light source; the spectrum can be expressed as:

$$S(\lambda - \lambda_0) = e^{-\left(\frac{2\pi}{\lambda} - \frac{2\pi}{\lambda_0}\right)^2 / 4a} \quad (2.1)$$

Thus, its Fourier transform, the auto-correlation function has the expression:

$$E(x,0) = \sqrt{a/\pi} e^{-ax^2} e^{-k_0x} \quad (2.2)$$

So, the FWHM of the spectrum is actually the band width of the spectrum, which is:

$$\frac{\left(\frac{2\pi}{\lambda} - \frac{2\pi}{\lambda_0}\right)^2}{4a} = \ln 2 \quad (2.3)$$

$$\text{thus, } a = \frac{\left(\frac{2\pi \cdot \frac{1}{2} \Delta\lambda}{\bar{\lambda}^2}\right)^2}{\ln 2} \quad (2.4)$$

Also, for the auto-correlation function, the FWHM is actually the coherence length, which is:

$$a\left(\frac{1}{2}l_c\right)^2 = \ln 2 \quad (2.5)$$

$$\text{Therefore } a = \frac{\ln 2}{\left(\frac{1}{2}l_c\right)^2} \quad (2.6)$$

$$\text{So, } a = \frac{\left(\frac{2\pi \cdot \frac{1}{2} \Delta\lambda}{\bar{\lambda}^2}\right)^2}{\ln 2} = \frac{\ln 2}{\left(\frac{1}{2}l_c\right)^2} \quad (2.7)$$

$$\text{So, } l_c^2 = \frac{4 \ln 2 \ln 2}{2\pi \cdot \frac{1}{2} \Delta\lambda \left(\frac{1}{\bar{\lambda}^2}\right)^2} = \frac{4 \ln 2 \ln 2}{\left(\frac{\pi \Delta\lambda}{\bar{\lambda}^2}\right)^2} \quad (2.8)$$

$$\text{Thus, } l_c = \sqrt{\frac{4 \ln 2 \ln 2}{\left(\frac{\pi \Delta\lambda}{\bar{\lambda}^2}\right)^2}} = \frac{2 \ln 2}{\frac{\pi \Delta\lambda}{\bar{\lambda}^2}} = \frac{2 \ln 2}{\pi} \left(\frac{\bar{\lambda}^2}{\Delta\lambda}\right) \quad (2.9)$$

Based the analysis above we can confirm that the wider the bandwidth, the better the system axial resolution. Fig. 2.1 shows the computer simulation results of the relationship between the band width of the light source and the system axial resolution.

Another critical parameter is the power of the light source. As long as the irradiance is below the ANSI safety level, generally, the higher the power on the sample, the better the system sensitivity and SNR. Especially for endoscopic OCT system, due to miniature size, the light coupling efficiency is often low, thus high power light source is even desired.

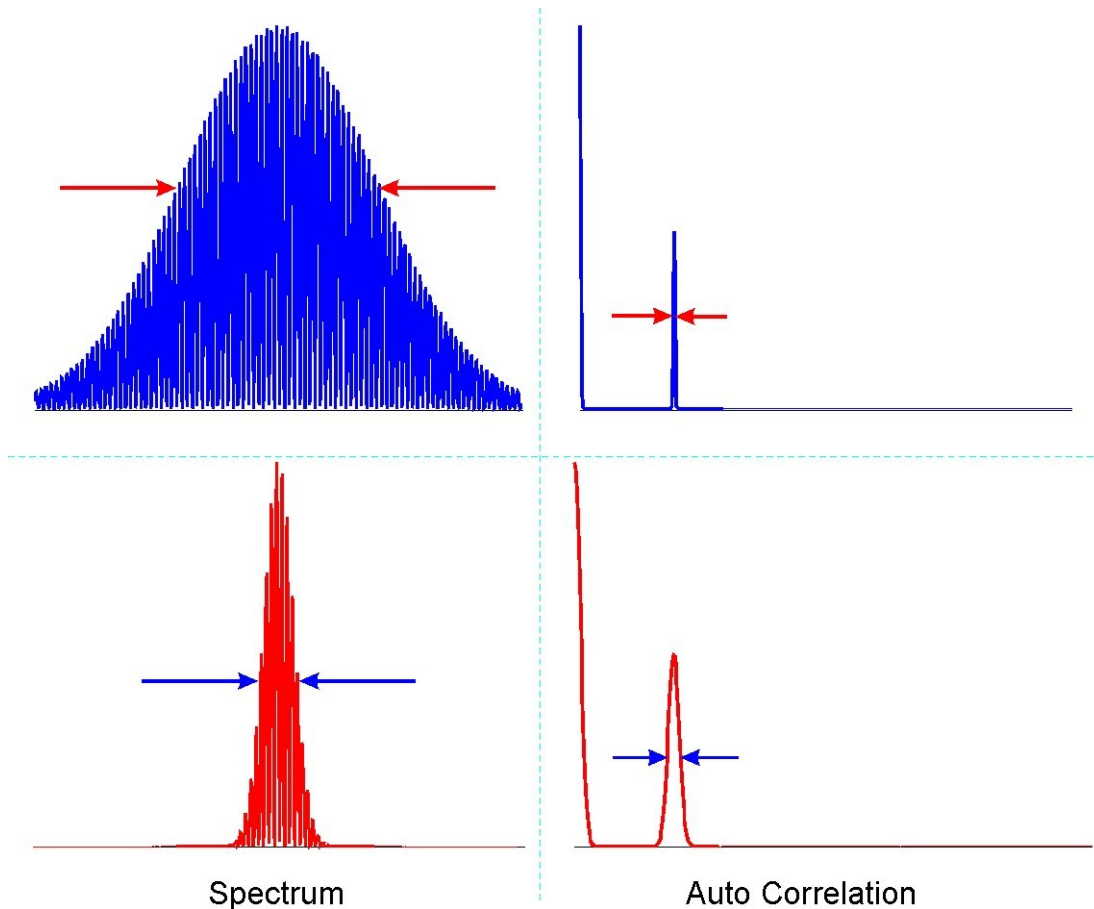


Fig. 2.1 Relationship between spectrum bandwidth and FWHM of auto correlation function.

The last parameter to consider is the spectral shape. Previous analysis was based on Gaussian shape spectrum. In reality, the spectral might not be perfect Gaussian shape. The system axial resolution, or the point spread function (PSF) is actually the Fourier transform of the source spectrum. If the source spectrum is very sharp (e.g., Rect function), then the PSF will have severe side peaks close to its main peak, which could downgrade the system resolution and contrast, as shown in Fig. 2.2. In practice, a smooth spectrum which closely mimics Gaussian shape would be the ideal choice.

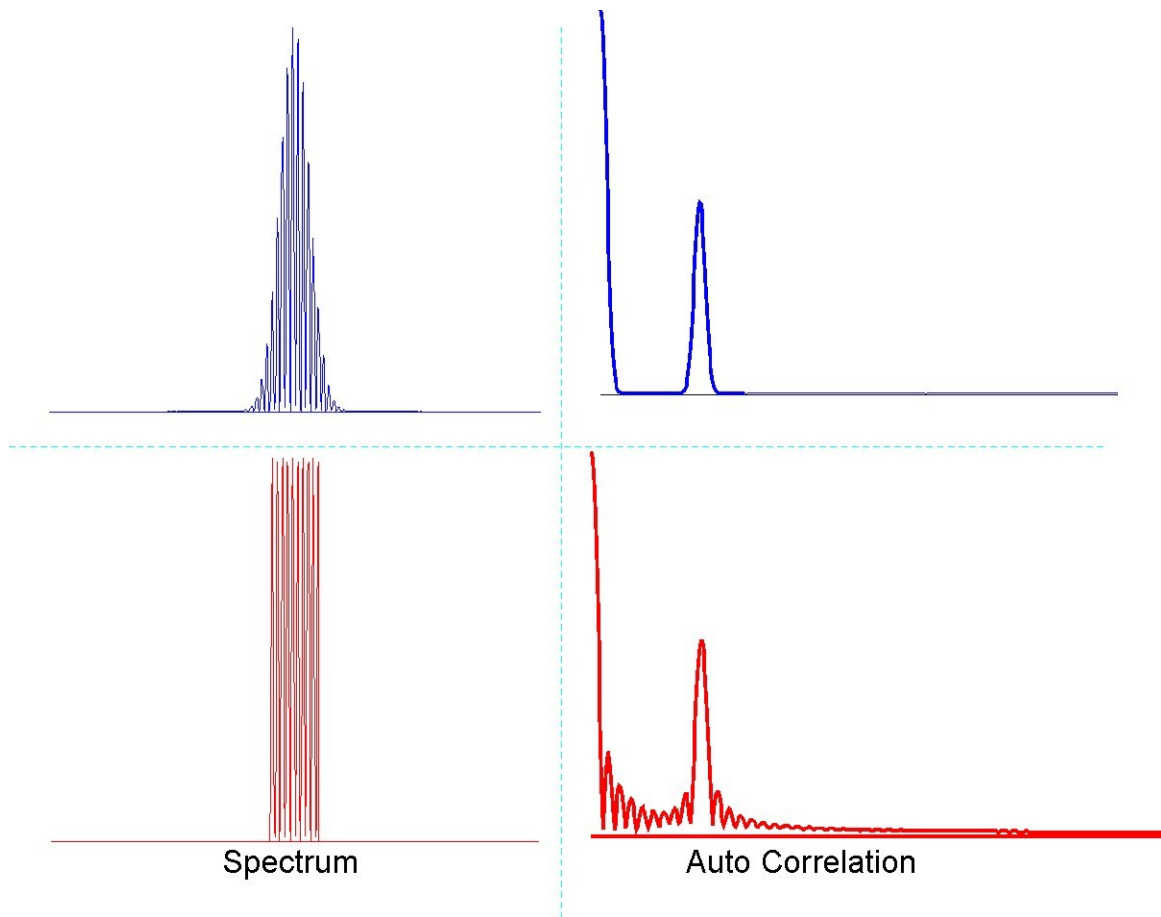


Fig. 2.2 Relationship between spectral shape and auto correlation function

Based on the analysis above, there are two types of light sources available on the market suitable for OCT, superluminescent diode (SLD) and mode-locked solid state laser. We choose the following light sources for our clinical high resolution OCT station and ultrahigh resolution benchtop ODT system.

For clinical high resolution OCT system, the major concerns are compactness, high power as well as stability. Based on this, we choose the following superluminescent diode as the light source:

Table 2.1 Specifications of the superluminescent diode from Inphenix

| | Unit | Min. | Typ. | Max. |
|-----------------------------|------------------|------|------|------|
| Center Wavelength | nm | 1280 | 1291 | 1340 |
| Output power | mW | - | - | 22 |
| Forward Current | mA | - | - | 550 |
| Forward Voltage | V | - | - | 2.5 |
| Ripple | dB | - | - | 0.5 |
| Operation temperature range | C | -20 | - | 65 |
| Storage temperature range | C | -40 | - | 85 |
| Package Type | 14 PIN Butterfly | | | |
| Fiber Type | 900um SMF | | | |
| Connector Type | FC/APC | | | |
| TEC required | Yes | | | |

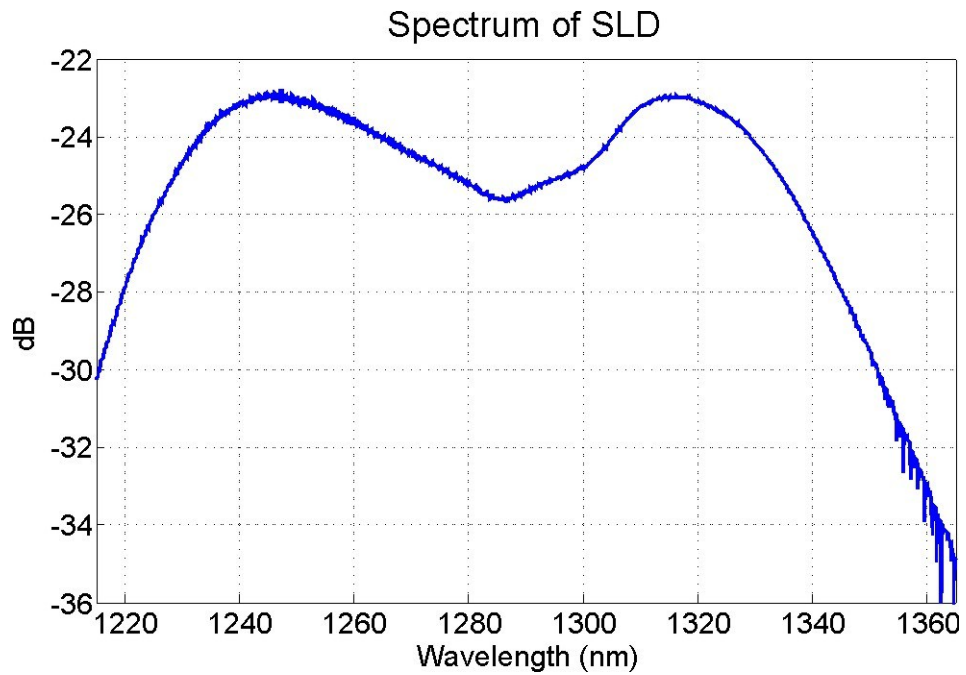


Fig. 2.3 Spectrum of the SLD

For benchtop ultrahigh resolution ODT system, we choose the high power wide band mode locked Ti-Sapphire solid state laser as the light source.

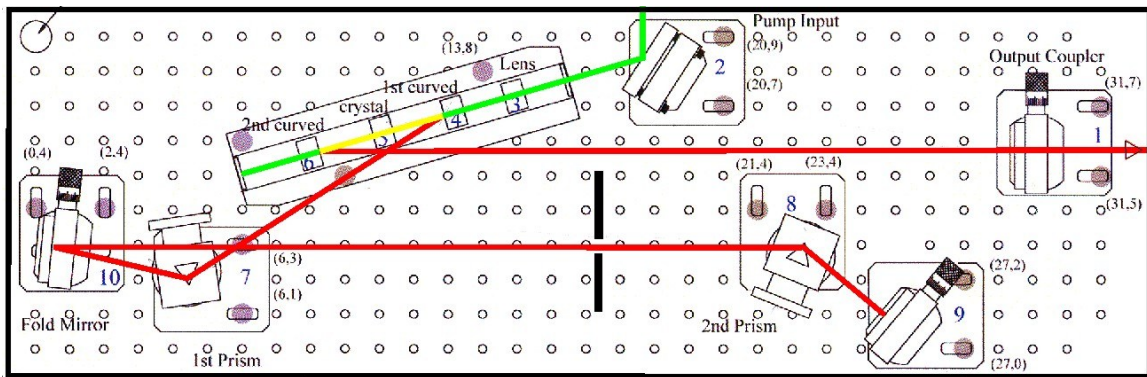


Fig. 2.4. Layout of the femtosecond laser (modified from KM Lab Ti: Sapphire laser manual).

The laser parameter is summarized as following:

Table 2.2 Specifications of the superluminescent diode from Inphenix

| | Unit | Min. | Typ. | Max. |
|-------------------|------|------|------|------|
| Center Wavelength | nm | | 800 | |
| Band Width | nm | 120 | 128 | 140 |
| Pulse width | fs | | 8 | |
| Repetition rate | MHz | 15 | 90 | 100 |
| Output power | mW | - | - | 450 |
| Pump power | W | - | - | 4.4 |
| Pump current | A | - | - | 19.6 |

And the spectrum is as below:

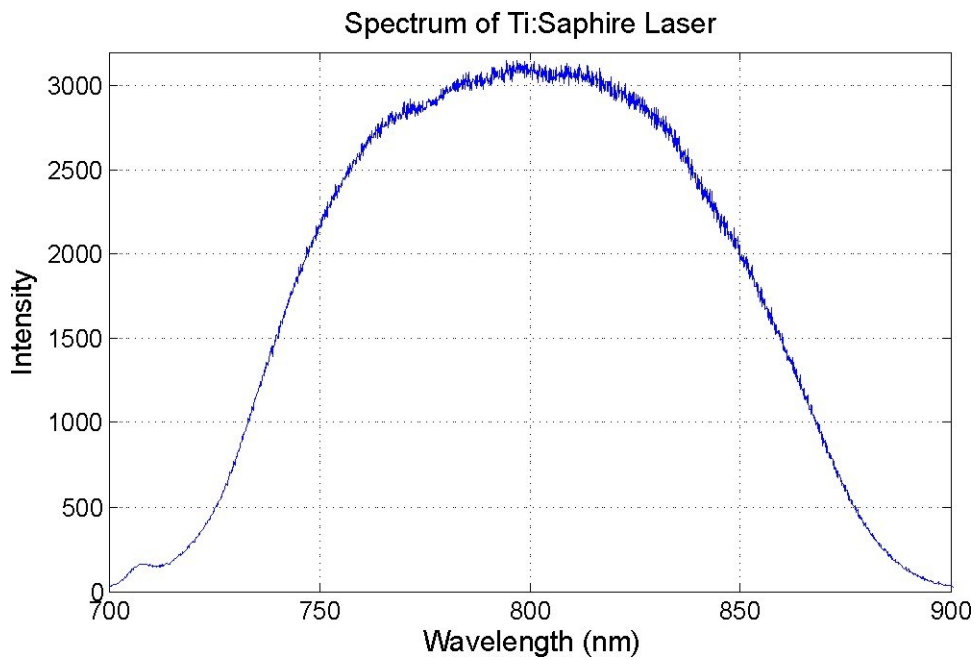


Fig. 2.5. Spectrum of the Ti:Sapphire laser.

2.1.2 Sample Arm

A typical sample arm consists of collimating lens, scanner and objective lens. We will first discuss how to choose each component and then introduce the detailed alignment of the whole sample arm.

A proper scanner needs to be determined first. Generally the sizes of the collimating lens and focusing lens are much larger than the effective scanner size, thus the scanner will determine the largest beam size we can have in the whole sample arm, and eventually the lateral resolution of the whole OCT system. Other than the scanner size, the maximum scanning speed, highest scanning resolution, mechanic stability, jittering as well as driving mode are all critical. For our application, we choose the VM Plus linear Scanner from General Scanning Inc. with a mirror aperture of 8mm and ± 20 degree optical scanning range at $53\mu\text{A}/\text{degree}$ sensitivity.

After the scanner is chosen, we then choose the collimating lens. The light coming from the source is connected to the sample arm through a single mode optical fiber. The NA of the SMF is generally around 0.11. An $f=25\text{mm}$ achromatic lens was chosen as the collimating lens to achieve a $D=5.5\text{mm}$ beam size on the scanner.

The major concern to choose an objective lens is the focal length. The focal length combined with the beam size would determine the system effective NA and then the lateral resolution and depth of field. Also, focal length will largely determine the objective working distance, which is also a critical parameter, especially for in vivo imaging. Two objective lenses were chosen for different applications. An $f=40$ objective lens was chosen for high resolution OCT system to achieve a lateral resolution of $\sim 12\mu\text{m}$.

An $f=16$ objective lens was chosen for ultrahigh resolution ODT system to achieve a lateral resolution of $\sim 3\mu\text{m}$.

In order to align the sample arm, first, light coming out from the collimating lens must illuminate the center of the scanning mirror to eliminate any scanning induced frequency shift, which is critical for Doppler imaging. Next, the scanner has to be placed at the back focal plane of the objective lens to enable telecentric scanning so that the scanning on the sample is linear.

2.1.3 Reference Arm

The alignment of the reference arm is much easier than that in the sample arm. The only thing that needs more attention is to choose exactly the same optics (e.g., same collimating lens, same focusing lens) as those in the sample arm so that material induced dispersion in both arms can be matched. Moreover, in order to optimize the camera SNR, a diaphragm is usually applied to adjust the reference intensity.

2.1.4 Detection Arm

The major part of the detection arm is a high speed spectrometer. The design of the spectrometer will largely determine the performance of the whole system. The basic principle of the spectrometer is based on the grating equation:

$$d^{-1}(\sin \theta_i + \sin \theta_r) = m\lambda$$

where d is the pitch number of the grating, θ_i is the angle of the incident light, θ_r is the angle of the refractive light, m is the diffraction order, and λ is the wavelength of the light. We first design the spectrometer based on our 1320 SLD source.

For grating, the higher the pitch number, the larger the diffraction angle. However, according to equation,

$$d = \frac{(\sin \theta_i + \sin \theta_r)}{m\lambda} \leq \frac{2}{m\lambda} \leq \frac{2}{1.3 \times 10^{-6} \cdot m} \leq \frac{2}{1.3 \times 10^{-6}} = 1538 / mm \quad (2.10)$$

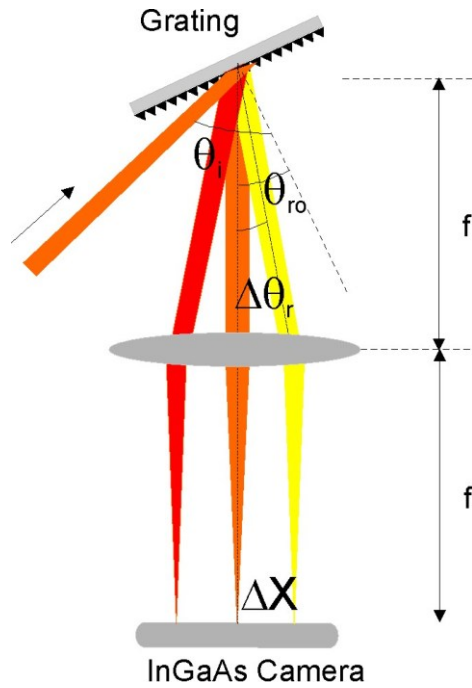


Fig. 2.6 Design of a spectral domain OCT system.

With the gratings available on the market, we pick up the holographic grating with 1200/mm pitch number.

In order to achieve higher diffraction efficiency, the grating should be configured at Littrow condition, which means the refracted light should come back the same way as

the incident light. However, for our system design, in order to align the optical components, we can only approach Littrow condition as close as possible. In our cage system setup, we adopt $\Delta\theta = \theta_i - \theta_{r0} = 12.5^\circ$.

Based on previous analyses, we adopt $m=1$. Then we can calculate the grating layout based on the 1320 central wavelength as following:

$$d^{-1}(\sin\theta_i + \sin\theta_r) = m\lambda \quad (2.11)$$

$$2d^{-1}[\sin(\frac{\theta_i + \theta_{r0}}{2}) \cos(\frac{\theta_i - \theta_{r0}}{2})] = \lambda_0 \quad (2.12)$$

$$\frac{\theta_i + \theta_{r0}}{2} = \frac{\lambda_0 d}{2 \cos(\frac{\theta_i - \theta_{r0}}{2})} = \frac{1.315 \times 1.2}{2 \cos(6.25)} = 52.82 \quad (2.13)$$

$$\text{Therefore, } \theta_i = 59^\circ, \theta_{r0} = 46.6^\circ \quad (2.14)$$

The spectrum ranges from 1260nm to 1370nm, thus,

$$\Delta\theta_r = (\theta_{1370nm} - \theta_{1260nm}) / 2 = 5.5^\circ \quad (2.15)$$

The camera we used has a sensor size of $X=25\text{mm}$ and pixel size of $x=25\mu\text{m}$. In order to fully take use of the camera, we want the dispersed spectrum to fully cover the camera sensor, thus we need choose a proper lens.

$$f \tan(\Delta\theta_r) = \frac{X}{2} \quad (2.16)$$

$$\text{so, } f = \frac{X}{2 \tan(\Delta\theta_r)} = 154\text{mm} \quad (2.17)$$

Since the pixel size is $x=25\mu\text{m}$, in order to fully use the camera resolution, the focal spot size should be smaller than the pixel size, in which case the resolution is limited by camera rather than optics. Based on Raleigh criteria, the focal spot size

$$\phi_f = \frac{1.22\lambda}{2NA} = 0.61 \frac{\lambda 2f}{\Phi} = 25\mu\text{m} \quad (2.18)$$

So, the beam size on the grating should be larger than

$$\Phi = \frac{0.61 \times 2\lambda f}{25} = 1.22 \frac{1.32 \times 154}{25} = 9.92\text{mm} \quad (2.19)$$

To sum up, for the detection arm, we need to couple the SMF with an $f=50\text{mm}$ collimating lens to achieve a $\Phi = 10\text{mm}$ spot on the grating. The grating needs to be tilted 46.6° relative to the axis of the camera. The incident beam should be arranged with an angle of 59° . A focal length of 154mm achromatic lens should be used as the focusing lens to enable full detection of the effective spectrum.

2.2 System Specifications

Based on the design above, we calculate the system specifications to evaluate its performance.

2.2.1 Axial Resolution

In biological tissue, based on the previous analysis, the axial resolution is calculated based on following equation:

$$l_c = \frac{2 \ln 2}{\pi n} \left(\frac{\bar{\lambda}^2}{\Delta \lambda} \right) \quad (2.20)$$

where n is the refractive index of biological tissue (~ 1.3), $\bar{\lambda}$ is the central wavelength of the light source and $\Delta \lambda$ is the FWHM of the spectrum.

For the high resolution clinical OCT system, the axial resolution in tissue is

$$l_c = \frac{2 \ln 2}{\pi n} \left(\frac{\bar{\lambda}^2}{\Delta \lambda} \right) = \frac{0.44}{1.3} \left(\frac{1.32^2}{90 \times 10^{-3}} \right) = 6.6 \mu m \quad (2.21)$$

For the ultrahigh resolution ODT system, the axial resolution in tissue is

$$l_c = \frac{2 \ln 2}{\pi n} \left(\frac{\bar{\lambda}^2}{\Delta \lambda} \right) = \frac{0.44}{1.3} \left(\frac{0.8^2}{120 \times 10^{-3}} \right) = 1.8 \mu m \quad (2.22)$$

2.2.2 Lateral Resolution

The lateral resolution of the system is determined by the sample arm optics. The focal spot size is ultimately limited by diffraction. Under Raleigh condition, the lateral resolution is calculated as:

$$\Lambda = \frac{4f\lambda}{\pi\phi} \quad (2.23)$$

The sample beam size is 5.5mm, for high resolution clinical OCT system,

$$\Lambda = \frac{4f\lambda}{\pi\phi} = \frac{4 \times 40 \times 1.32}{5.5\pi} = 12.22 \mu m \quad (2.24)$$

For ultrahigh resolution ODT system, the lateral resolution is:

$$\Lambda = \frac{4f\lambda}{\pi\phi} = \frac{4 \times 16 \times 0.8}{5.5\pi} = 2.96 \mu m \quad (2.25)$$

2.2.3 Imaging Depth

As we introduced previously, for spectral domain OCT system, the depth z and wave number k are a Fourier transform pair. In other words, the maximum resolvable depth will be determined by the sampling rate in k domain (or in λ domain). We derive the imaging depth equation from the original interference fringes.

The fringes of SDOCT are:

$$I(k) = S(k) \left(1 + 2 \int_0^{\infty} a(z) \cos(2knz) + \int_0^{\infty} \int_0^{\infty} a(z) a(z') e^{-i2kn(z-z')} dz dz' \right) \quad (2.26)$$

Thus the angular frequency of the fringes is $\omega_k = 2nz$

$$\text{So, the period based on } k \text{ is } T_k = \frac{2\pi}{\omega_k} = \frac{2\pi}{2nz} = \frac{\pi}{nz} \quad (2.27)$$

Therefore, the highest frequency, which corresponds to the lowest period based on k is

$$T_{k-\min} = \frac{\pi}{nz_{\max}} \quad (2.28)$$

In order to recover the highest frequency in the fringes, according to Nyquist Sampling theory, one has to have at least two sampling points in the one shortest period:

$$\text{So, the } \delta_k \leq \frac{1}{2} T_{k-\min} = \frac{\pi}{2nz_{\max}} \quad (2.29)$$

Because spectrometer is always in wavelength domain,

$$\text{As we all know, } k = \frac{2\pi}{\lambda}, \text{ thus } dk = d\left(\frac{2\pi}{\lambda}\right), \text{ which means } 1 \cdot dk = \frac{-2\pi \cdot d\lambda}{\lambda^2} \quad (2.30)$$

We can write it as $\delta_k = \frac{-2\pi \cdot \delta_\lambda}{\lambda^2}$ or $|\delta_k| = \frac{2\pi \cdot \delta_\lambda}{\lambda^2}$ (2.31)

Because $\delta_k \leq \frac{1}{2} T_{k-\min} = \frac{\pi}{2nz_{\max}}$ (2.32)

so $|\delta_k| = \frac{2\pi\delta_\lambda}{\lambda^2} \leq \frac{\pi}{2nz_{\max}}$ (2.33)

so $\delta_\lambda \leq \frac{\pi\lambda^2}{4n\pi z_{\max}}$ (2.34)

Thus $z_{\max} \leq \frac{\lambda^2}{4n\delta_\lambda}$, so the maximum depth of SDOCT is $z_{\max} = \frac{\lambda^2}{4n\delta_\lambda}$, which is determined by the spectrometer's spectral resolution.

The spectral resolution can be calculated as following.

Since $d^{-1}(\sin\theta_i + \sin\theta_r) = m\lambda$, if we take the differential of both sides, then

$$d^{-1} \cos\theta_r \Delta\theta_r = \Delta\lambda \quad (2.35)$$

Based on the lens projection, the minimum resolvable angle $\Delta\theta_r$ will just project to the pixel size of the camera $x=25\mu\text{m}$

so, $f\Delta\theta_r = x$ therefore $\Delta\lambda = d^{-1} \cos\theta_r \Delta\theta_r = \frac{xd^{-1} \cos\theta_r}{f} = 0.102\text{nm}$ (2.36)

The spectral resolution of the ultrahigh resolution system is also about 0.1nm.

Then the imaging depth for clinical high resolution OCT system is

$$z_{\max} = \frac{\lambda^2}{4n\delta_\lambda} = \frac{(1.32 \times 10^{-6})^2}{4 \times 1.35 \times 0.102 \times 10^{-9}} = 3.16\text{mm} \quad (2.37)$$

For the ultrahigh resolution ODT system, the imaging depth is:

$$z_{\max} = \frac{\lambda^2}{4n\delta_\lambda} = \frac{(0.8 \times 10^{-6})^2}{4 \times 1.35 \times 0.1 \times 10^{-9}} = 1.19 \text{mm} \quad (2.38)$$

2.2.4 Frame Rate

The highest frame rate of the system is limited by the camera as well as the computer hard disk. For clinical high resolution OCT system, the camera scanning speed is 47K lines per second. If each image consists of 500 A lines, the frame rate is 94fps. The highest scanning speed of the camera used in the ultrahigh resolution ODT system is 27K lines per second. For same images, the frame rate is 54fps. In order to enable large data transfer with fast speed, we configure all the computer hard disk as Raid 0 array to enable ~300MB/s data transfer rate.

2.3 Design of MEMS Mirror Based OCT Endoscope

MEMS mirror is a highly compact scanning device, which is the ideal choice for endoscopic scanning. Since MEMS mirror was introduced into endoscopic OCT by our group, we have made substantial improvements to optimize the performance of OCT endoscope.

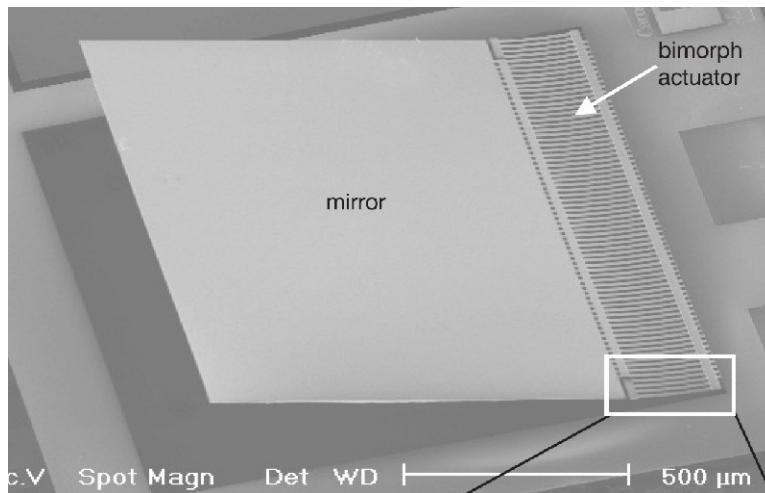
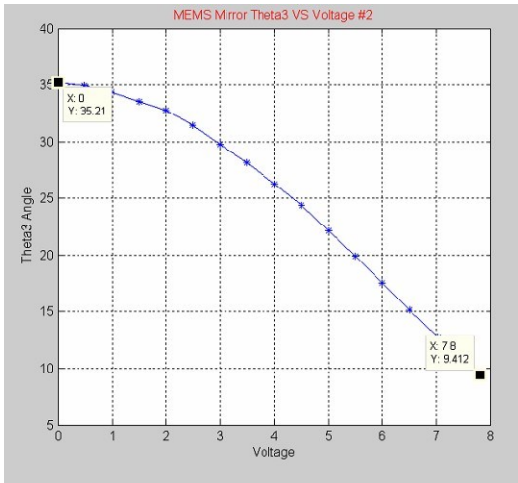
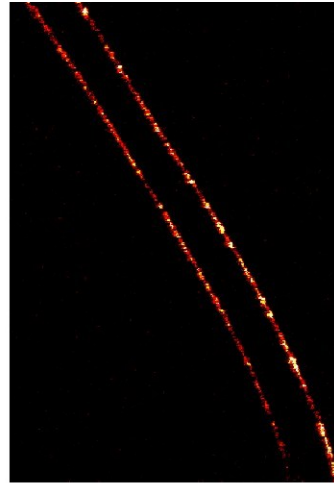


Fig. 2.7 SEM image of a MEMS mirror ²⁹

The MEMS mirror we used is designed by our collaborator Dr. Xie's lab from University of Florida. Fig. 2.7 shows the fine structure of the MEMS mirror²⁹ under scanning electron microscope (SEM). The mirror was fabricated based on CMOS technology. The hinges on the mirror opens the mirror with an initial angle. When the voltage is added onto the mirror, the thermal actuator will adjust the angle based on the expansion caused by temperature differences between the underlying layers. Fig. 2.8 a) shows a typical voltage-angle curve of the MEMS mirror. We do see that at the beginning of the scan, there is a nonlinear range, however, in the middle part; the scanning is still about linear. Generally we can apply voltage from 2V-7V. Fig. 2.8 b) shows a typical OCT image of a tilted cover glass as the MEMS mirror scans from the bottom to the top. It shows similar performance if we use the full scanning range. The good thing is that OCT image can quickly visualize the dynamic responses, which is more valuable for endoscopic application.



a)



b)

Fig. 2.8 a) Voltage angle curve of MEMS mirror; b) OCT image of Voltage angle curve

By integrating MEMS mirror into the commercial cystoscopes, we can readily develop our cystoscopic OCT probe. Fig. 2.9 a) shows the layout of the MEMS mirror on a plastic ferrule. The effective mirror size is 1mm×1mm. Fig. 2.9 b) shows the design of our MEMS mirror based OCT endoscope.

Light coming out from the fiber was coupled through a FC/APC adaptor into the single mode fiber. At the end of the fiber, a quarter pitch gradient refractive index lens was applied to form a collimated beam. The collimated beam was then reflected by a high reflection mirror onto the center of the MEMS mirror. During the scan, the beam was first scanned by the MEMS mirror laterally then focused by a laser achromate onto the outer surface of the endoscope where the tissue is going to be examined. The FOV is 4.8mm and the frame rate can go to ~10fps.

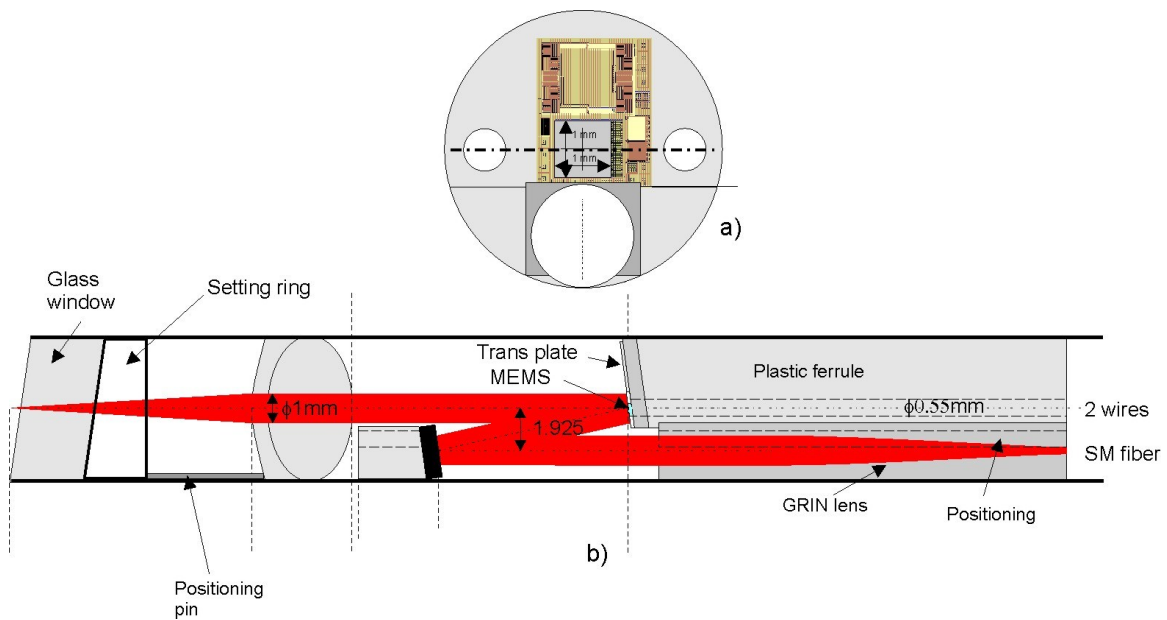


Fig. 2.9 a) Ferrule for MEMS mirror; b) design of OCT endoscope by using MEMS mirror

Fig. 2.10 shows the image of the final packed endoscope. The electric wire is used to control the MEMS mirror scan, while the jacket fiber with a FC/APC adapter is used to couple light into the endoscope. The whole endoscope is sealed by medical glue and is completely water proof and sterilization resistant.

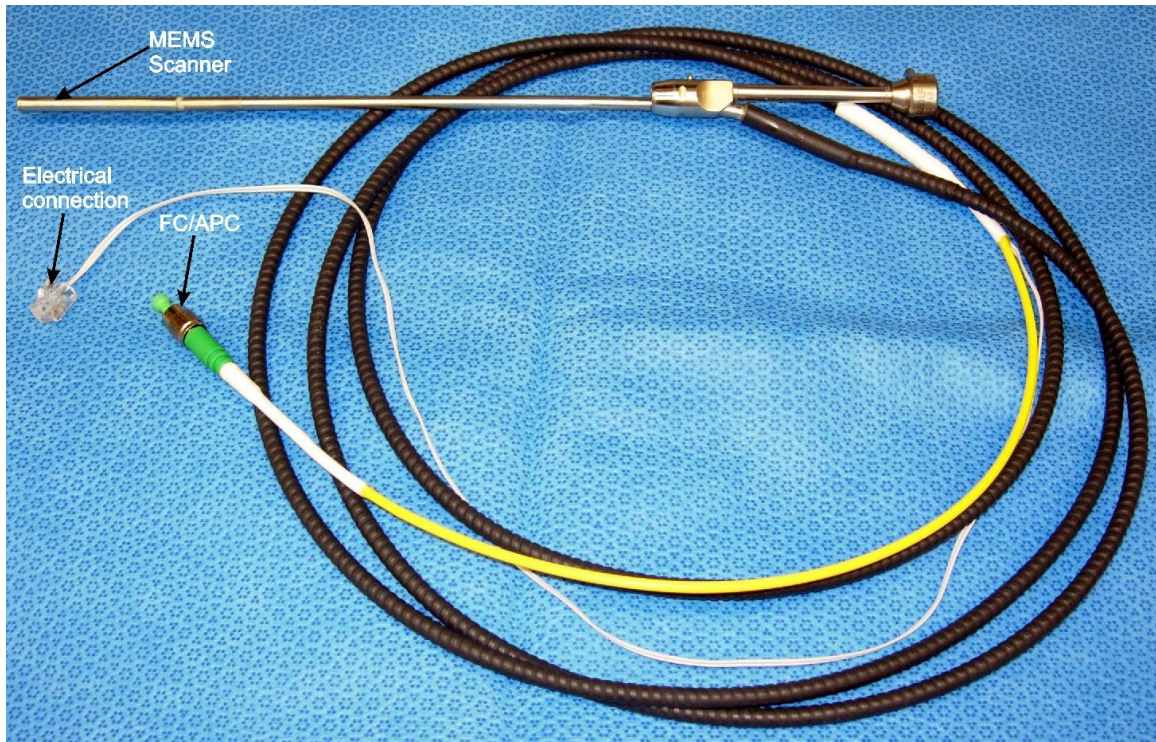


Fig. 2.10 Packed OCT endoscope with MEMS mirror as the scanner

2.4 OCT Image Reconstruction

In this section, we will first discuss the general procedures for OCT image reconstruction. Then focus on image segmentation and 3D OCT based computer aided diagnosis. Last, we will introduce the algorithms for Doppler flow image processing.

2.4.1 Intensity Image Reconstruction

A typical spectral domain OCT image reconstruction algorithm involves following procedures: spectrum reshape--reference removal--calibration--fast Fourier

transform-image adjustment. We programmed in MATALB GUI mode to enable all these procedures, and illustrated as below:

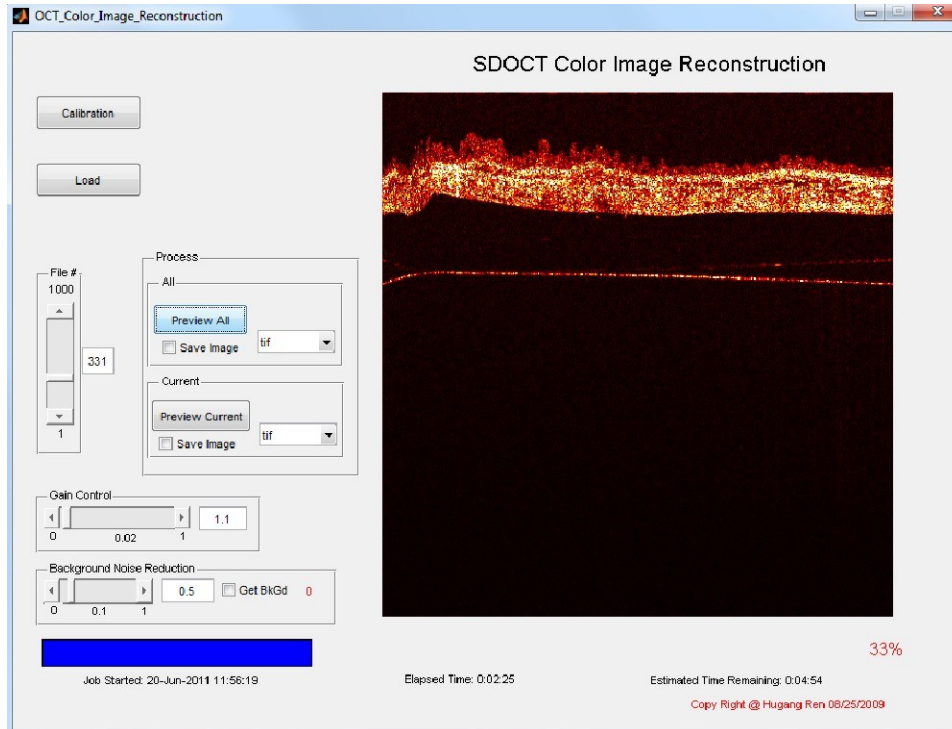


Fig. 2.11 SDOCT color image reconstruction software

2.4.2 Image Segmentation and Computer Aided Diagnosis

The following image processing algorithm was applied to segment both 2D and 3D OCT images¹⁷:

- 1) OCT images were first converted to 16 bits grayscale mode:

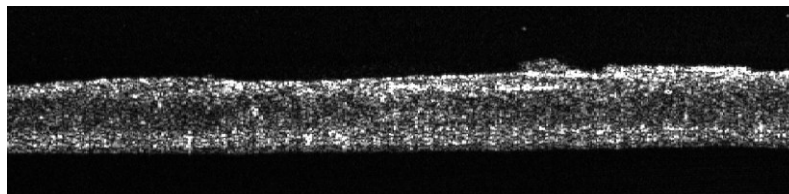


Fig. 2.12 16 bits grayscale OCT image

2) An adaptive mask was generated by converting the grayscale image into BW mode based on a threshold value calculated to minimize the intraclass variance of the black and white pixels (e.g., for some images, 0.15 was set as threshold):



Fig. 2.13 Mask of the region of interest

3) The region of interest was obtained by multiply the mask with the original grayscale image:

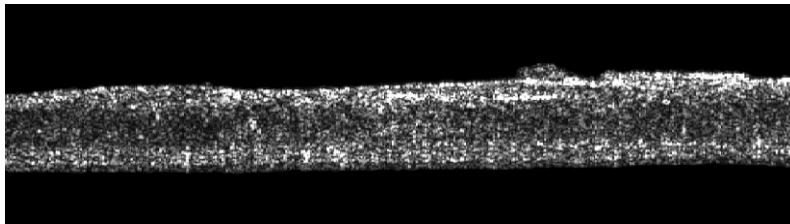


Fig. 2.14 Masked result

4) The masked image was then normalized:

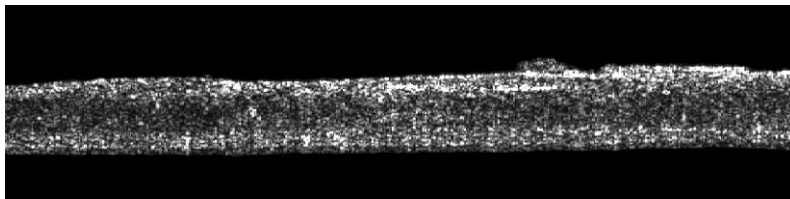


Fig. 2.15 Normalized image

5) A 2D medium filter with a radius of 5 pixels was then employed to minimize the speckle noise:

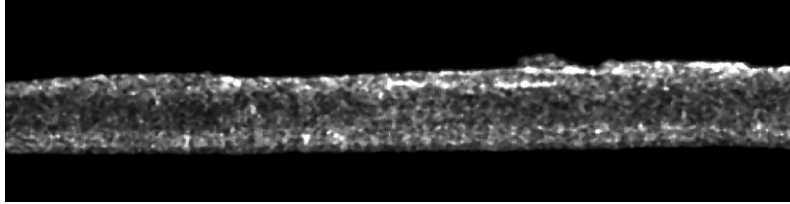


Fig. 2.16 Filtered image

6) For each A-line, the intensity gradient along depth direction is calculated based on first order differentiation. Based on the gradient image, the upper surface of decidua vera (DV) and bottom surface of epithelium (E) were easily segmented with a gradient threshold of 5000:

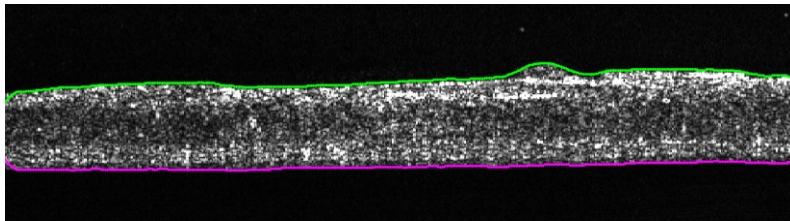


Fig. 2.17 Segmentation result of upper surface of decidua vera and bottom surface of epithelium

8) With these 2 edges segmented, all the other pixels outside of this region were set as zero. Since the chorion and trophoblast (CT) layer is a low scattering layer in the middle, it was then segmented based on an adaptive threshold. (e.g., for some images ~ 20000):

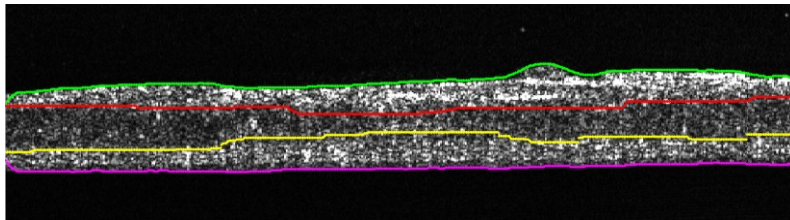


Fig. 2.18 Segmentation result of chorion and trophoblast layer

9) The last step was to segment the edge between subepithelial amnion (A) and E. Since the edge between CT and A as well as the bottom surface of E are both known now, the ROI image was further constrained to A and E layers only:

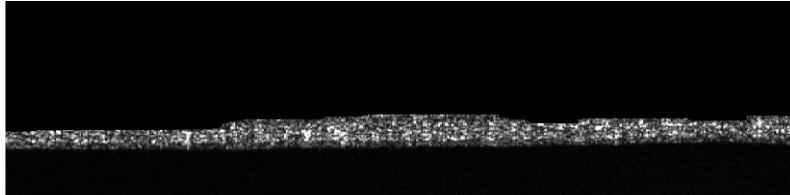


Fig. 2.19 Region of interest consists of only subepithelial amnion and epithelium

As layer E is low scattering, whereas layer A is high scattering, the contrast between them is distinct. An intensity value derived based on Otsu's method was employed as the threshold to segment these two layers (e.g., for some images ~18000):

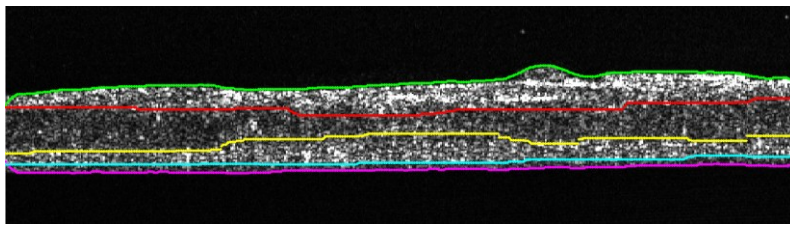


Fig. 2.20 Final segmentation results.* The threshold value for each segmentation was generated by Otsu's method based on the image data (The value can be derived by the MATLAB image processing kits).

For computer aided diagnosis, we developed our algorithm as below:

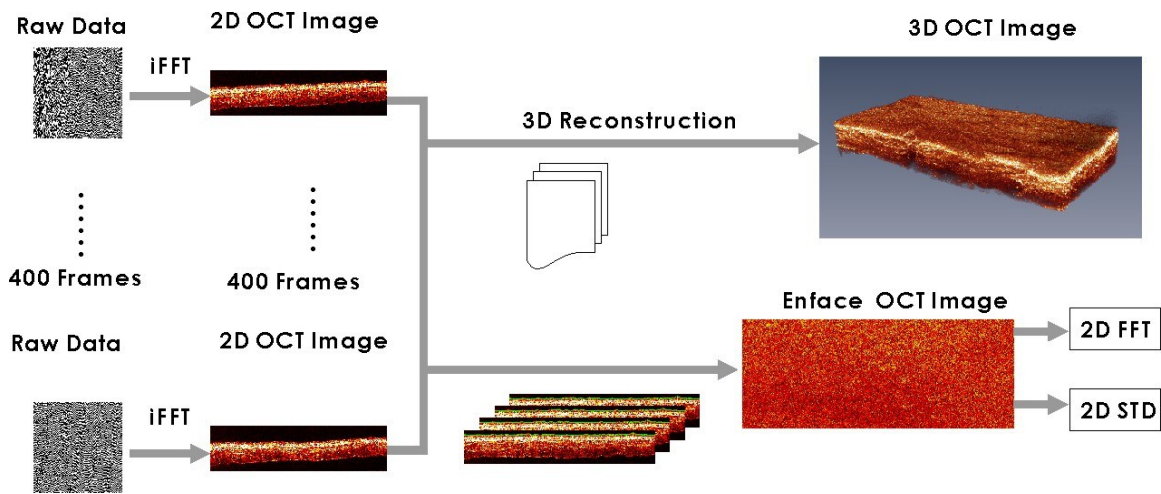


Fig. 2.21 Algorithm for enface image extraction

We first reconstruct all the 3D images, and then extract the enface image as shown in Fig. 2.21. Based on the extracted enface image, quantitative image analysis was performed for computer aided diagnosis. The image processing algorithm is shown in Fig. 2.22¹⁷. 1) An adaptive image segmentation algorithm based on mathematical morphological operation was applied to remove the specular reflection and background ghost image coming from the specimen interfaces. 2) 3D image registration was performed to eliminate artifacts caused by bladder stretching. The A-line at the center of the sample was assigned as the reference, then all the other A-lines were aligned accordingly based on the cross correlation results between the A-lines and the reference. 3) The bladder urothelium was segmented in 3D, then averaged only in the axial direction over 5 pixels at 5 μ m below the surface to extract the enface OCT image. 4) To minimize computation, a region of interest (ROI) of 1mm \times 1mm was randomly selected by the program automatically. 5) Two-dimensional fast Fourier transform (FFT) was performed on each ROI. 6) The 2D FFT result in Cartesian domain was converted into polar

domain. 7) 2D FFT profile was determined in polar domain by averaging across all different angles and normalized based on the summation of all frequency components. 8) Target function was built based on both 2D FFT results and 2D STD results. 9) To provide absolute quantitative diagnoses, the result of the target function was calculated as the unique feature for each specimen, and the diagnosis criteria was illustrate in Fig. 2.22

b)

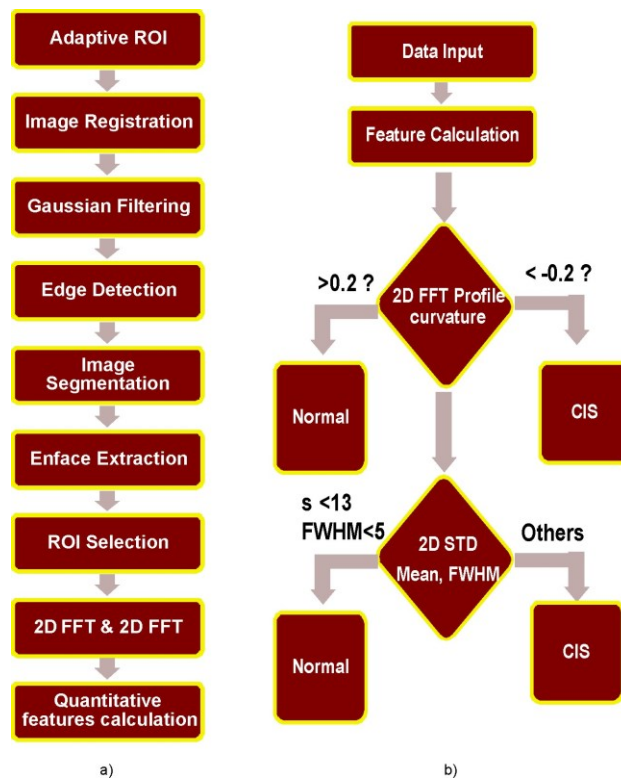


Fig. 2.22 a) Image processing algorithm; b) computer aided diagnosis algorithm.

2.4.3 Doppler Flow Image Reconstruction

For quantitative μ ODT image reconstruction, an image processing algorithm - termed phase subtraction method (PSM) - was developed to enhance the sensitivity of

quantitative Doppler flow detection. The detected spectral interferogram of a A-line at a transverse position x can be derived as,

$$I(k, x) = S(k) \sum_{\Delta z} 2\sqrt{I_r I_s(\Delta z, x)} \cos[2kn\Delta z + \varphi(\Delta z, x)] = \sum_{\Delta z} A(\Delta z, x) \cos[2kn\Delta z + \varphi(\Delta z, x)] \quad (2.39)$$

where $k=2\pi/\lambda$ is the wave number of light, Δz is the path length difference between the reference and sample arms, n is the refractive index of mouse cortex under imaging, and $\varphi(\Delta z, x)$ is the instant phase term at position $(\Delta z, x)$. $A(\Delta z, x)=2S(k)[I_r \cdot I_s(\Delta z, x)]^{1/2}$ is the envelop of spectral interferogram and I_r, I_s are the light intensities in the reference and sample arms, and $S(k)$ is the cross-correlation spectrum. As the total interferogram $I(k, x)$ is a linear summation of the interferogram from different depths of Δz , we only discuss the signal coming from a specific depth for simplicity, i.e., assuming Δz is a constant to analyze the phase change along the transverse direction. Considering it a dark noise free system, we can divide the phase term $\varphi(\Delta z, x)$ to two parts,

$$\varphi(x) = \varphi_0 + \varphi_d(x) \quad (2.40)$$

where φ_0 is the initial phase, $\varphi_d(x)$ is the phase shift induced by Doppler flow. During each cross-sectional imaging (B-scan), the transverse laser scan is at a uniform speed v and the time interval for acquiring individual A-line is Δt (i.e., $\Delta x=v\Delta t$ is the pitch density or step size), then the transverse position x of the i -th A-scan is $x_i=x_0+i\Delta x$. Doppler OCT extracts the flow speed v_d by calculating the immediate phase change between the two adjacent A-lines,

$$v_{d,x_i} = \frac{\Delta\varphi(x_i)}{2nk\Delta t \cos\theta} = \frac{\varphi_d(x_{i+1}) - \varphi_d(x_i)}{2knc\cos\theta\Delta t} \quad (2.41)$$

2.4.4 Vessel Tail Removal

Because of forward scattering of the red blood cells, vessels in the Doppler flow images tend to have long tails, which would downgrade the reconstructed 3D flow map. In order to remove the vessel tails automatically for large data set, a dynamic adaptive vessel tail removal algorithm was developed to completely automatically detect the vessel tails and then remove them.

The algorithm is based on a modified region growth algorithm. First, region of interest was masked based on threshold. Then the flow map was binarized. Starting from the top of the tissue surface, whenever the vessel is detected, the vessel region starts to grow with a shrinking factor until the pixel value decreases to zero. Then the updated flow map was updated as the final flow map for 3D reconstruction. The result is shown as following:

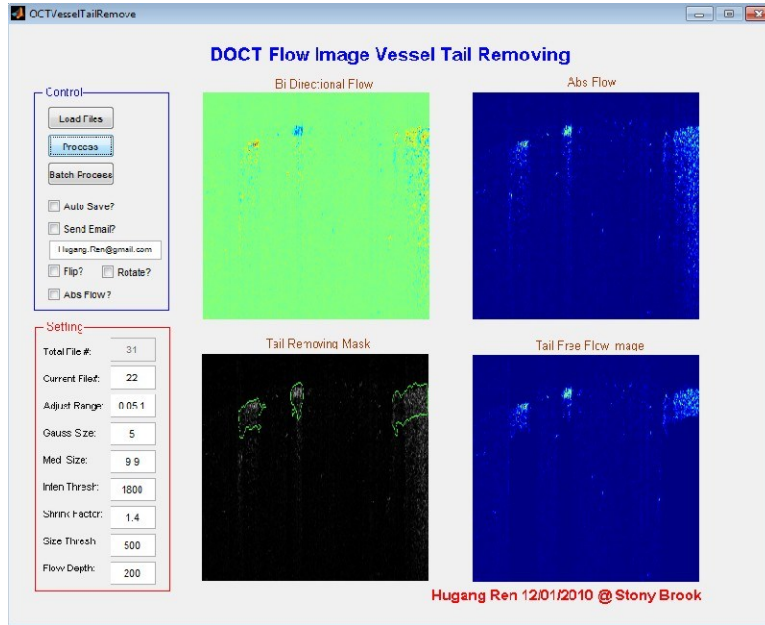


Fig. 2.23 Software for vessel tail removal.

2.4.5 Enhancing Flow Detection Dynamic Range

Additionally, the algorithm to improve the flow detection dynamic range can be derived from Eq. 2.41 to increase the dynamic range for Doppler flow detection. Assume that $P_f(\Delta z, x)$ is the original phase image acquired at f A-lines frame rate (e.g., $f=10\text{kHz}$) and $P_{f/2}(\Delta z, x)$ is the down binning phase image at $f/2$ frame rate (e.g., $f/2=5\text{kHz}$), $P_{f/2}(\Delta z, x)=2P_f(\Delta z, x)$ because the phase shift $\Delta\varphi_0$ is proportional to the sampling time ($\Delta\varphi_0 \propto T_x$ or $\Delta\varphi_0 \propto 1/f$). Each frame, e.g., 20k A-lines at 20kHz, down binned 10k A-lines at 10kHz, ..., 1kHz, are combined using the algorithm (Fig. 2.24) to provide 1000 final Doppler image lines for later 3D image rendering.

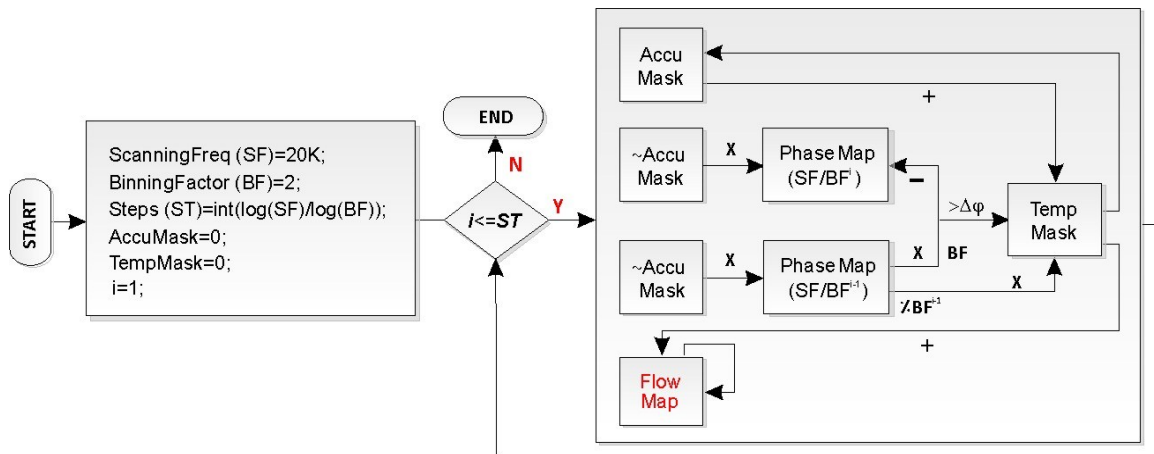


Fig. 2.24 Algorithm to enhance the flow dynamic range.

In summary, a high resolution spectral domain OCT system was developed and its parameters were derived and evaluated. Also, the corresponding image processing software kit was also designed to enable high fidelity OCT image reconstruction.

Chapter 3 Cystoscopic OCT for Bladder Cancer

Diagnosis *in vivo*

3.1 Introduction

Carcinoma or cancer that originates in the urothelium is the 5th most common type of cancer with estimated 68,810 new cases and 14,100 deaths in the US in 2008³⁰. Most transitional cell carcinomas (TCC) are curable if diagnosed and treated early. However, early diagnosis of TCC, in particular, carcinoma in situ (CIS) remains a clinical challenge³¹. For example, urine cytology, FISH and BTA are unable to provide sufficient sensitivity (~50%) for low-grade TCC³²⁻³⁴; Radiologic imaging by way of IVP, CT, MRI fail to detect early-stage bladder cancer due to limited resolution³¹. Cystoscopy is currently the gold standard that has proven highly effective for the diagnosis of papillary TCC; however, as an *en face* imaging modality, it often cannot differentiate non-papillary TCC especially CIS which may have a normal appearance from benign inflammatory lesions and relies on random biopsy, resulting in a low diagnostic sensitivity and specificity^{32, 35}. Therefore, a more effective imaging technique that can see below the bladder surface at a high resolution is highly desirable to enhance the current cystoscopic

procedures to diagnose and locate flat malignant lesions (e.g., non-papillary TCC, CIS), guide TURBT, and detect recurrent tumor following transurethral resection.

Optical coherence tomography (OCT) is a new imaging technique that enables cross-sectional imaging of biological tissue at a resolution 10 times higher than clinical ultrasound. In addition to successful clinical adoption in ophthalmology, OCT can be integrated with conventional endoscopy to permit high-resolution *in vivo* imaging of intraluminal tracts (e.g., bladder). Recent preclinical animal and human studies demonstrate the potential of OCT for detecting bladder cancer³⁶⁻⁴⁰. We developed a microelectromechanicalsystem (MEMS) mirror based spectral-domain OCT cystoscopy (COCT) to improve the image resolution, detection sensitivity, imaging rate and field of view (FOV), all of which are critical to *in vivo* bladder cancer diagnosis⁴¹. In this Chapter, we present a pilot study based on intraoperative cystoscopy for patients suspected of bladder tumors. The diagnoses of COCT were compared with other clinical data such as white-light cystoscopy, histology and voided cytology, so that the utility and potential limitations of MEMS-based COCT for bladder cancer diagnosis may be examined.

3.2 Materials and Methods

3.2.1 Patient

COCT was performed in the first 56 consecutive subjects, including 46 (82.1%) male and 10 (17.9%) female patients (median 70 in the 25-75% range), suspected of bladder cancer and scheduled to undergo intraoperative cystoscopy. These patient cohorts comprised 24 (35.5%) for possible bladder biopsy (e.g., due to positive cytology, hematuria, or suspicious outpatient cystoscopy) and 32 (47.1%) for possible TURBT among which 12 (17.6%) patients underwent repeated surveillance cystoscopy due to suspected recurrence post intravesicle therapy with mitomycin or BCG, totaling 68 cases. All of the studies were performed after approval by the Stony Brook University Institutional Review Board and patients' informed consents. Healthy control subjects were not recruited for this study.

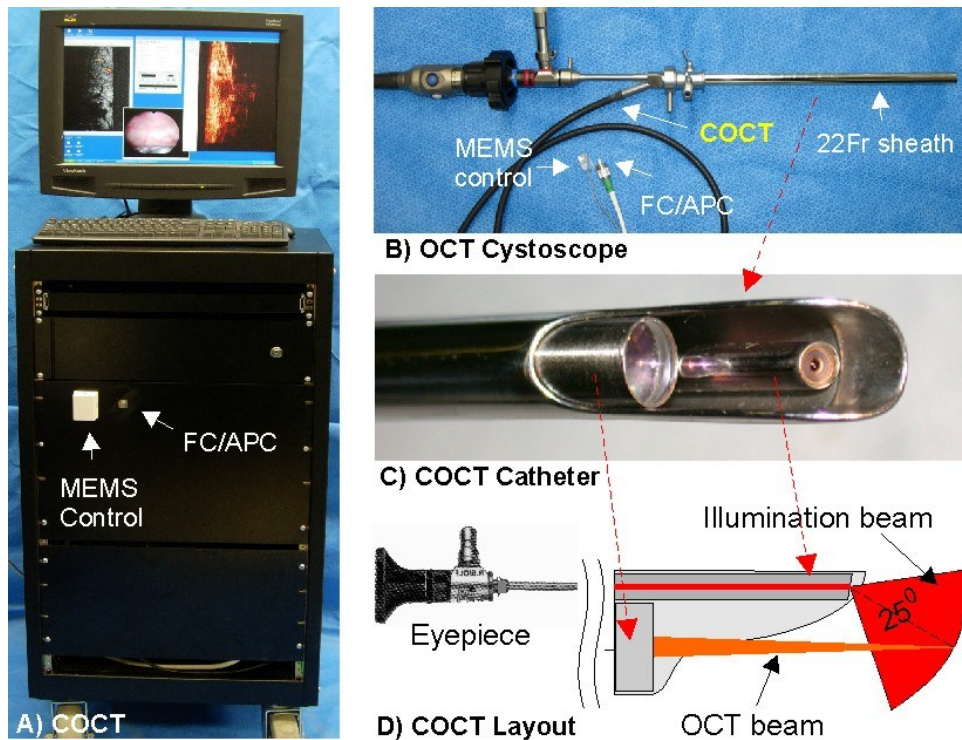


Fig. 3.1 MEMS-based COCT for *in vivo* bladder cancer diagnosis. A) SDOCT station; B) OCT cystoscope; C, D) COCT catheter that allows white-light or fluorescence image guidance. FC/APC: angle polished fiber connector. Transverse laser scanning (up to 4.8mm) within COCT catheter was facilitated by a CMOS MEMS mirror (1.1×1.3mm²).

3.2.2 COCT

Our techniques for MEMS-based spectral-domain cystoscopic OCT have been reported previously⁷. Fig. 3.1 illustrates the image station and OCT cystoscope used in this study. A broadband near infrared (NIR) laser at wavelength $\lambda=1320\text{nm}$ with a spectral bandwidth of $\Delta\lambda=90\text{nm}$ was used to illuminate the fiberoptic spectral-domain OCT system (SDOCT) and a green laser (532nm) was coupled for endoscopic visual guidance. Unlike previous time-domain OCT techniques, SDOCT circumvented the need for mechanical axial scan by virtue of spectral interferometry⁴², thus significantly increasing imaging rate and dynamic range⁴¹, crucial to *in vivo* COCT diagnosis. The sample arm of the OCT system was connected to an OCT catheter integrated via the instrument channel into a 22Fr cystoscope which focused the incident NIR light onto the bladder lumen and collected backscattering from different depths within bladder wall to recombine with the reference light to obtain a depth profile (A-scan) using a 1D spectral camera. Steering of light laterally with a MEMS mirror in OCT catheter following each A-scan facilitated 2D and 3D COCT imaging. Recent technological advances in high-performance MEMS mirror and SDOCT led to improved imaging rate (8fps), dynamic range (>110dB) and resolution ($\sim 10\mu\text{m}$), and a larger FOV ($2.1\times 4.8\text{mm}^2$ in the vertical and lateral directions). The dual-imaging capability permitting white-light or fluorescence

guided COCT greatly improves the diagnostic efficacy³⁷.

3.2.3 Clinical Examination

With the patient under general anesthesia, COCT diagnosis was performed prior to possible biopsy or TURBT treatment. Suspicious lesions, including base and transitional area to the adjacent normal mucosa were examined first, followed by sequential COCT scans of nonspecific or normal-appearing areas (i.e., bladder mapping). COCT diagnosis was given instantaneously using the following criteria: 1) a lesion with diminishing underlying morphology and increased urothelial heterogeneity (e.g., over 3-fold thickened urothelium with varied local backscattering such as fibrovascular cores) was considered to be positive, 2) an area with clearly delineated and uniform urothelium (including inflammatory lesions in the underlying layers) was considered to be negative, and 3) a lesion with ultrahigh surface reflection and missing underlying morphology (e.g., necrosis or scar from prior TURBT) was considered to be negative. The duration of COCT diagnosis was less than 10 minutes per case. Routine cystoscopic evaluation was performed (by urologists only) regardless of COCT diagnosis (by urologists / OCT researchers). Subsequent pathological findings in these lesions, from either random biopsy or TURBT were identified while blind to prior clinical data (e.g., COCT, cystoscopy, cytology), and staged and graded by an independent pathologist. The histological image was then compared with the corresponding COCT cross-section whose surface image (cystoscopy) was cropped from the synchronized video clip.

3.2.4 Statistical Analysis

The sensitivities and specificities of voided cytology, cystoscopy and COCT for detection of bladder cancer were computed with the final biopsied histological diagnosis serving as the gold standard. Their values were compared using chi-squares test or Fisher's exact test, with $p < 0.05$ considered statistically significant.

3.3 Results

For all 68 intraoperative cases, no complications were observed. Among 36 cancer cases confirmed by histology, 34 were detected by COCT, 27 by cystoscopy, and only 17 were identified by cytology; whereas for all 32 histologically confirmed benign cases, 26 were detected by COCT, 20 by cystoscopy, and 24 identified by cytology. The detailed cancer diagnostic statuses calculated on per patient/case bases are indicated in Tab.3.1 (a). The positive and negative predictive values (PPV, NPV) were calculated accordingly as 85% and 93% for COCT, 64% and 65% for cystoscopy, and 85% and 63% for cytology.

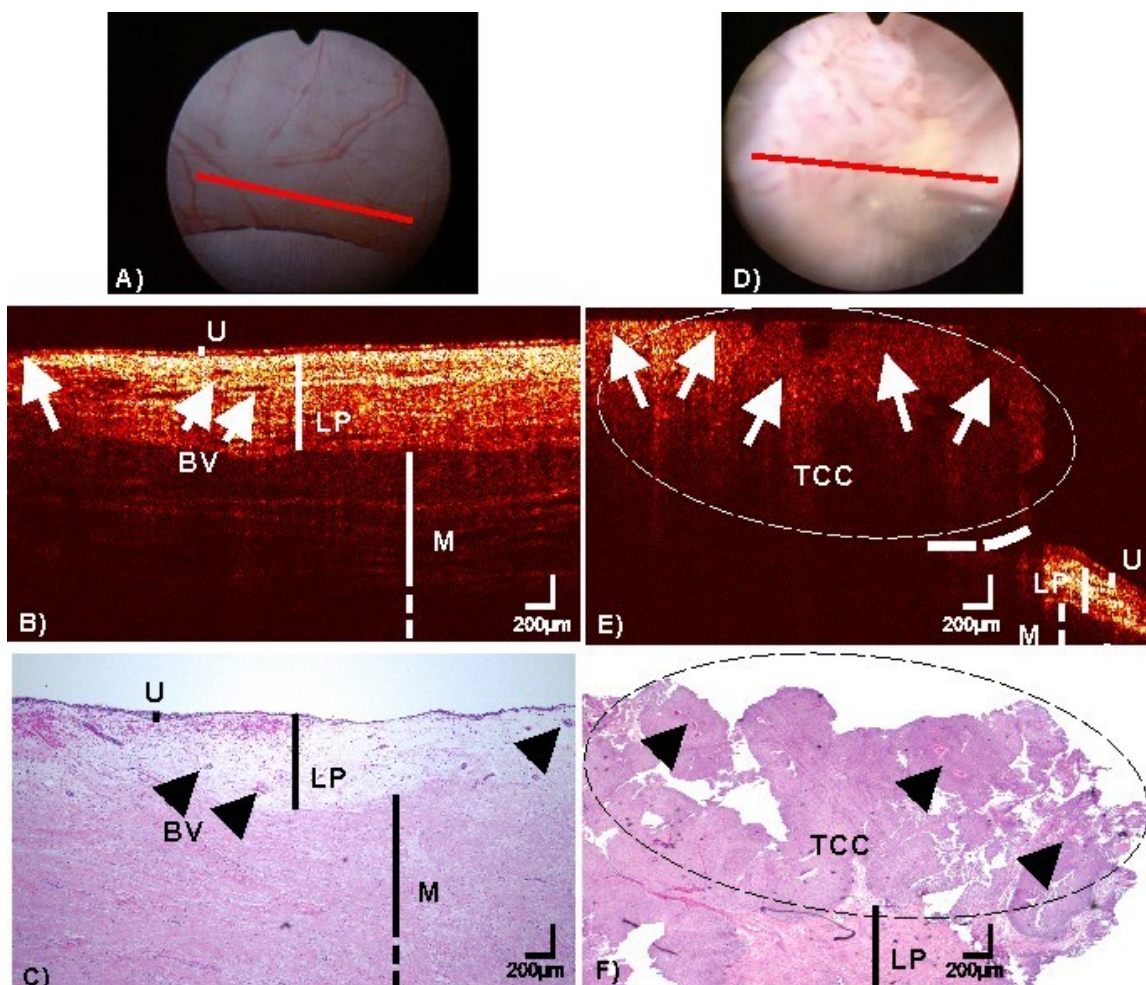


Fig. 3.2 In vivo surface, cross-sectional COCT and H&E stained histological images of normal human bladder versus a papillary TCC (pT1LG). Image sizes: $\sim\phi 20\text{mm}$ (A/D) and 4.6mm laterally by 2.1mm axially (B/E, C/F). The morphological details of normal bladder (B), e.g., urothelium (U), lamina propria (LP) and upper muscularis (M) were clearly delineated by OCT based on their backscattering differences; whereas those (e.g., LP, M) underneath papillary TCC (E) diminished. Solid arrows: subsurface blood vessels; dashed arrows: papillary features; dashed circle: TCC (low backscattering), identified by COCT based on increased urothelial heterogeneity; dashed line: boundary with adjacent normal bladder. Diagnoses of the normal bladder: COCT, cystoscopy and histology were all benign, voided cytology was positive. Diagnoses of papillary lesion: COCT, cystoscopy and histology were positive, cytology was benign.

COCT identification of normal bladder was based on high-resolution delineation of bladder morphology. As shown in Fig. 3.2(B), urothelium (U) appears as a thin,

uniform and low-scattering superficial layer, lamina propria (LP) – composed of mostly collagenous fibers – as highly scattering and heterogeneous, and upper muscularis (M) as largely bifurcated collagen bundles, correlating well with histology (C). The urothelial thickness measured by COCT ($89 \pm 8.3\mu\text{m}$) closely matched that of histology ($82.1 \pm 9.7\mu\text{m}$) and the inter-patient variation was found insignificant ($p>0.82, n=25$) if the bladder was distended properly, thus providing an important landmark for OCT diagnosis. For instance, the majority of inflammatory lesions might exhibit decreased LP scattering as a result of cystitis, edema or vasodilatation, but their urothelium remained thin, uniform and could thus be identified. Among the 6 false-positive lesions by COCT, 5 were lesions with reactive giant cell components and scar tissue or metaplasia, and 1 was necrosis mixed with fat tissue, all of which exhibited architectural similarity to TCC.

COCT identification of TCC was based on enhanced urothelial heterogeneity and/or urothelial thickening attributed to random excessive growth of urothelial neoplasm. Fig. 3.2(E) shows the result of a typical papillary TCC (pT1LG). Compared to normal bladder in Fig. 3.2(B), the architectural boundaries between U, LP and M were disrupted in the bladder tumor. The large FOV of MEMS COCT permitted clear identification between TCC and the surrounding normal bladder, thus potentially allowing precise guidance for TURBT. In contrast to previous preclinical study⁴¹, 76% of human TCC exhibited no significant increase in backscattering but rather enhanced urothelial heterogeneity as indicated by the arrows. It is noteworthy that the stratified architectures (LP, M) underneath the TCC diminished, thus potentially compromising the staging ability of COCT for large papillary TCC to pT1 or lower stage. For instance,

COCT could stage this TCC as greater than T1 but was uncertain to differentiate it as T1 or T2. Among all 25 papillary TCC cases, COCT detected 24 (96%) but missed 1 close to bladder neck; while cystoscopy detected all 25 (100%).

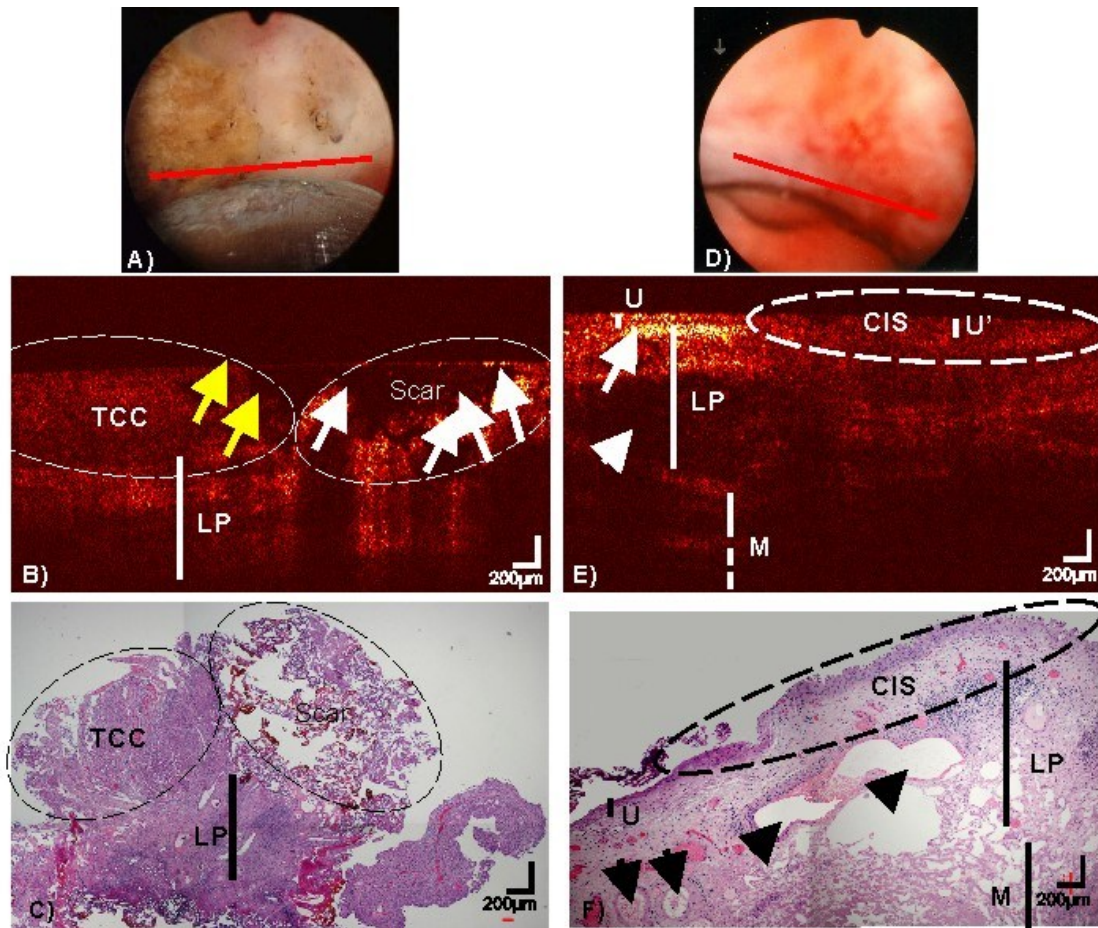


Fig. 3.3 In vivo surface, COCT and H&E stained histological images of a recurrent TCC post TURBT (A-C) and a CIS (D-F). Yellow and white arrows (B): papillary features and scar or necrotic lesions. COCT differentiation of TCC (left circle) vs. scar (right circle) was based on low-scattering and papillary features in TCC vs. ultrahigh superficial scattering with abruptly diminished underlying architecture in scar or necrotic lesion, which was nonspecific under surface image (a). Arrows (E, F): blood vessels; The morphology (e.g., LP, M) under CIS (U*) diminished. CIS (dashed circle), which was slightly reddish and nonspecific under surface image (D), was low backscattering and identified by COCT based on increased urothelial heterogeneity and less distinguishable U'-LP interface. Diagnoses of TCC/scar: COCT and histology were positive; cystoscopy and voided cytology were benign. Diagnoses of CIS: COCT and histology were positive; cystoscopy and voided cytology were benign.

Detection of recurrent tumor remains an unsolved clinical challenge for surveillance cystoscopy because bladder architecture was drastically altered by previous TURBT. Fig. 3.3(B) demonstrated the great potential of COCT to differentiate recurrent TCC from scar or necrosis because the latter exhibited excessive surface reflection with no underlying morphology. Among 4 of the 12 surveillance cases with recurrent cancers, COCT detected all 4 cases while cystoscopy missed 2. On the other hand, 5 of 6 false positive diagnoses of COCT were associated with previous resections, and 9 of 15 cases were for cystoscopy. In addition, Fig. 3.3(E) exemplifies the result of a CIS which remains a critical problem for clinical diagnosis due to its non-specific appearance under cystoscopy Fig. 3.3(D). The lesion under COCT showed no obvious urothelial thickening; instead, the backscattering decreased slightly in the urothelium (U*) but diminished drastically in the underlying LP likely due to coexisting inflammatory response so that the boundary between U'-LP was hardly distinguishable, which was later confirmed by histology Fig. 3.3(F). COCT detected 8 out of 9 histologically confirmed CIS lesions; in comparison, cystoscopy only detected 2.

A total of 110 lesions were biopsied for histological analysis following COCT and cystoscopy diagnoses and entered as gold standard for statistical calculation. The diagnostic status calculated on a per lesion basis was summarized in Tab. 3.1(b), which demonstrated the utility of MEMS COCT to significantly enhance the sensitivity ($p<0.018$) of cystoscopy for superficial, low-grade tumors (pTa-1LG) and CIS (Tis), and of cytology for pTa-1LG tumors ($p<0.001$).

Table 3.1 Diagnostic sensitivities and specificities:
a) calculated on a per case basis

| Methods Tumors | | OCT | | Cyst | | Cyto | | p-values | | |
|------------------------------|-----------|-------|------|-------|------|-------|------|------------|------------|-------------|
| | | n/N | % | n/N | % | n/N | % | OCT : Cyst | OCT : Cyto | Cyst : Cyto |
| CIS (pTis) | | 2/3 | 66.7 | 0/3 | 0 | 3/3 | 100 | 0.400 | 1.000 | 0.100 |
| pTa-pT1 | LG | 12/12 | 100 | 8/12 | 66.7 | 0/10 | 0 | 0.093 | 0.0001 | 0.002 |
| | HG | 6/6 | 100 | 6/6 | 100 | 1/3 | 33.3 | 1.000 | 0.083 | 0.226 |
| Superficial (<pT2) | | 20/21 | 95 | 14/21 | 66.7 | 4/16 | 25 | 0.044 | 0.0001 | 0.012 |
| ≥pT2 | | 14/15 | 93.3 | 13/15 | 86.6 | 11/13 | 84.6 | 1.000 | 0.583 | 1.000 |
| Sensitivity | | 34/36 | 94.4 | 27/36 | 75 | 17/29 | 58.6 | 0.022 | 0.005 | 0.160 |
| Specificity | | 26/32 | 81.3 | 17/32 | 53.2 | 24/27 | 88.9 | 0.017 | 0.488 | 0.003 |

b) calculated on a per lesion basis

| Methods Tumors | | OCT | | Cyst | | Cyto | | p-values | | |
|------------------------------|-----------|-------|------|-------|------|-------|------|------------|------------|-------------|
| | | n/N | % | n/N | % | n/N | % | OCT : Cyst | OCT : Cyto | Cyst : Cyto |
| CIS (pTis) | | 8/9 | 88.9 | 2/9 | 22.2 | 8/8 | 100 | 0.015 | 1.000 | 0.002 |
| pTa-pT1 | LG | 17/17 | 100 | 11/17 | 64.7 | 0/14 | 0 | 0.018 | 0.0001 | 0.0001 |
| | HG | 9/9 | 100 | 8/9 | 88.9 | 4/6 | 66.7 | 1.000 | 0.143 | 0.525 |
| Superficial (<pT2) | | 34/35 | 97 | 21/35 | 60 | 12/28 | 42.9 | 0.002 | 0.0001 | 0.040 |
| ≥pT2 | | 17/18 | 94.4 | 16/18 | 88.9 | 14/16 | 87.5 | 1.000 | 0.591 | 1.000 |
| Sensitivity | | 51/53 | 96.2 | 37/53 | 69.8 | 26/44 | 59.1 | 0.0003 | 0.0001 | 0.271 |
| Specificity | | 51/57 | 89.5 | 42/57 | 73.7 | 45/48 | 93.8 | 0.030 | 0.436 | 0.007 |

* Cyst: cystoscopy, Cyto: cytology; N: total number, LG: low grade, Superficial: all pTis and pTa-pT1 tumors.

Cytology data for 12 cases were unavailable.

3.4 Discussions

Early diagnosis transitional cell carcinoma remains a clinical challenge³¹. Cytology is highly sensitive in high-grade bladder tumor (e.g., HG or CIS)³⁴, yet it relies on other imaging techniques to locate the cancerous lesions. White-light cystoscopy is currently gold standard for bladder cancer diagnosis and has proven highly effective for large papillary tumors as exemplified in Tab. 3.1. However, cystoscopy as an *en face* imaging modality can miss small sessile low-grade TCC and CIS which may appear normal or nonspecific, and relies on random biopsy for a conclusive diagnosis³¹. On the other hand, disrupted (altered) bladder surface by previous TURBT may result in difficulty differentiating recurrent tumors from scar, necrotic tissue or other inflammatory reactions. Interestingly, both the merits and limitations of cystoscopy and cytology were well reflected in this study (Tab. 3.1).

In contrast to *en face* imaging, COCT enables cross-sectional imaging over 2mm of depths to delineate bladder epithelium, lamina propria and upper muscularis at a resolution ($\sim 10\mu\text{m}$) close to histopathology⁴⁰, offering great potential to overcome the limitations of conventional cystoscopy and provide more specific diagnosis of early bladder cancer. Previous preclinical and clinical studies demonstrated the feasibility of OCT for bladder cancer diagnosis^{38, 39}. Here, we present a pilot study to further examine the utility and potential limitations for future clinical diagnosis, in particular, with the advantages resulting from technological advances in SDOCT and MEMS laser scanning

catheter for enhanced image sensitivity, speed and increased FOV⁴¹. The large FOV of MEMS COCT enabled imaging of the transitional area of the lesion with adjacent normal bladder, critical to enhancing the diagnosis of bladder tumor and imaging guidance of TURBT. The technical modification for our COCT merely involved coupling the OCT catheter via the instrument channel of a conventional 22Fr rigid cystoscope⁴³. Moreover, simultaneous surface image guidance and the touch-on-focus capability drastically enhanced the diagnostic efficacy to allow COCT exam of the entire bladder including bladder mapping in less than 10 minutes. For the 68 consecutive cases performed intraoperatively, no adverse events were observed. The COCT system was custom made in our lab for under \$20k, which should be affordable for future clinical adoption.

The preliminary clinical results presented in Tab. 3.1 implied that conventional cystoscopy was sufficient for the diagnosis of large papillary tumors (e.g., pT2, pTa-1HG) counting for the majority (21/36(60%)) of the cancer cases. The major improvement of COCT was for the diagnosis of superficial pTa-1LG tumors (12/12 vs. 8/12, $p < 0.01$) and CIS (8/9 vs. 2/9 lesion based, $p = 0.015$). However, it is noteworthy that only 3 pure CIS cases were encountered ($p = 0.4$), so more CIS enrollment is needed to evaluate the statistical significance between COCT and cystoscopy on a per case basis (all other 6 CIS cases coexisted with TCC). COCT diagnosis was based on identification of decreased urothelial backscattering with enhanced heterogeneity and diminished U-LP interface^{38, 41} (Fig. 3.3E), possibly as a result of enlarged nuclei of CIS cells that favor forward scattering. More quantitative study is needed to compare the difference between CIS and flat dysplasia. An ultimate solution will likely demand subcellular imaging differentiation

for which our recent invention based on time-lapse ultrahigh-resolution OCT has shown great promise⁴⁴.

The rigid COCT missed 1 tumor in retro area close to bladder neck, but this problem can now be tackled by our new flexible COCT catheter. It was interesting to observe the ability of COCT to detect all 6 recurrent TCCs from scar or necrotic lesions induced by previous resections which cystoscopy missed (e.g., 2 pT2 tumors), thereby eliminating unnecessary multiple biopsies and reducing false negative rates of recurrent tumors. Nevertheless, due to disruption of stratified bladder architectures (U, LP, M), 5 out of all 6 false-positive rates of COCT were for surveillance cases. In addition, it is crucial to point out that due to increased urothelial heterogeneity, visualization of the underlying structures (e.g., LP, M) was hampered resulting in limited local staging for large papillary TCC (e.g., pT1 or higher). However, our recent preclinical study⁴⁵ suggested that OCT combining with high-frequency ultrasound (HFUS) could complement each other and thus enhance both bladder cancer diagnosis and extend tumor staging to pT2 or higher.

3.5 Conclusions

In conclusion, results of intraoperative MEMS-based COCT on the first 56 patients revealed a significant improvement on the sensitivity (94% vs. 75%) and specificity (81% vs. 53%) over cystoscopy in the diagnosis of bladder cancer ($p < 0.05$). The major impact was on small superficial low-grade tumors and carcinoma in situ as

well as the detection of recurrent tumors found in surveillance cystoscopy, rendering it a promising adjuvant ‘optical biopsy’ for early detection of non-papillary bladder cancers and image guided therapies. However, considering that intraoperative patients were biased by either more advanced tumors or more complicated cases, the result must be further examined in a more randomized study such as in office diagnosis which is being evaluated by incorporating our newly developed high-performance flexible COCT technology.

Chapter 4 Flexible Hybrid Cystoscopy/Optical Coherence Tomography for Early Bladder Cancer Diagnosis and Guided Tumor Resection

4.1 Introduction

Effective treatment of bladder cancer following early diagnosis plays an important role in the clinical bladder cancer management. Currently, transurethral resection of bladder tumor (TURBT) remains the standard procedure for bladder cancer treatment⁴⁶. As a surgical procedure, complete resection is critical in order to minimize the reoccurrence rate. Therefore, tumor boundary determination during TURBT is crucial. At present, TURBT is performed under the guidance of white light cystoscopy. However, as an en-face imaging modality, white light cystoscopy shows its limitations in flat tumor detection, in particular, carcinoma in situ (CIS).⁴⁷ Thus, there is a clinical demand for more accurate surgical guidance of TURBT.

Optical coherence tomography (OCT) is an enabling technique which can image the subsurface structure at 1~10 μ m resolution noninvasively *in vivo*. Based on more than 200 clinical cases in our previous studies, MEMS mirror based rigid cystoscopic OCT was demonstrated to be able to faithfully provide high quality images to enable early

diagnosis of bladder cancer with both high sensitivity and high specificity.⁷ However, encountered during the clinical studies, the mechanical property of the MEMS mirror endoscope restricted it from even wider applications. For instance, in some clinical cases, the bladder tumors are located close to the bladder neck, making it impossible for the rigid MEMS endoscope to access, and therefore were missed during the diagnoses. Moreover, in order to enable even earlier stage bladder cancer detection, outpatient screening is preferred. However, the large size of the current MEMS endoscope allows it to be used only in the operating room environment. In this Chapter, we first describe the optical and mechanical design of a flexible miniature OCT probe, and then briefly introduce the system setup of the hybrid cystoscopy/OCT. In order to validate the system performance, both preclinical and clinical studies were performed *in vitro* and *in vivo*. In the end, we will discuss the image optimization procedures through post image processing.

4.2 Materials & Methods

4.2.1 Flexible Endoscopic OCT Probe: Optical Design

The development of the flexible endoscopic OCT probe involves both optical and mechanical design. Fig. 4.1 illustrates the optical design of the flexible cystoscopic OCT probe.

A single mode SMF-28 bare fiber was employed to couple the laser light into the OCT probe. Inside the probe, an 8 degree angle cut glass spacer and an AR coated GRIN lens were aligned to form a long working distance ($\sim 1.8\text{mm}$) fiber focuser. This 8 degree design was adopted to minimize the back reflection from the spacer-lens interfaces. On the other end of the fiber focuser, a right angle micro prism was attached onto the end-face of the GRIN lens to enable side-view. Light exiting the fiber end-face passes through the glass spacer, focused by the GRIN lens, and then deflected 90 degree by the micro prism through total internal reflection. The working distance calculated from the prism surface is $0.7\sim 0.8\text{mm}$, which enables laser beam to be focused $\sim 100\mu\text{m}$ below the tissue surface.

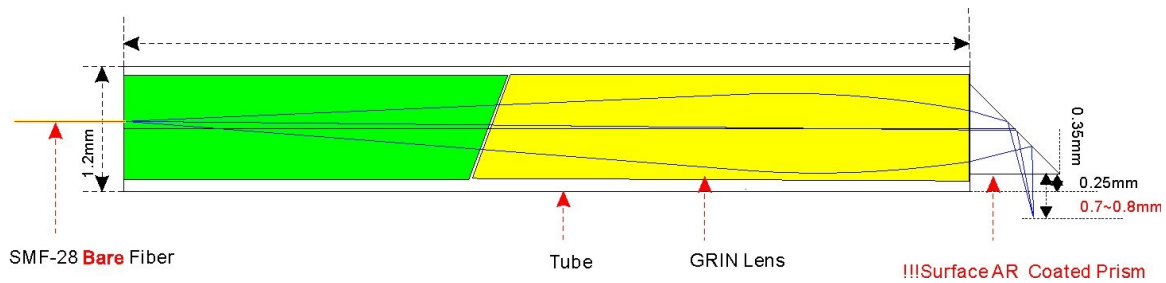


Fig. 4.1 Optical design of the flexible cystoscopic OCT probe.

In order to protect the probe, and to guarantee clinical safety, a translucent plastic (FEP) tube will be added outside of the OCT probe. Because of the 90 degree deflection, the OCT beam will always be perpendicular to the plastic tube, and will therefore induce strong back reflection and severe auto-correlation artifacts. To solve this problem, an off-center design was proposed. In this design, the bare fiber was intentionally shifted off-center to achieve a 49 degree illumination angle between the laser beam and the normal plane of the prism hypotenuse surface. Upon back reflection from the inner surface of the

plastic tube, laser beam will be shifted 4 degree and focused onto the lower part of the GRIN lens, and will not be able to couple back into the single mode fiber. However, it has to be noted that this design works only for highly scattering samples (e.g., biological tissue). For samples with specular reflectance, the imaging efficiency is substantially reduced.

4.2.2 Flexible Endoscopic OCT Probe: ZEMAX Simulation

Due to the refractive index differences, the translucent FEP tube on the optical pathway also functions as a low power cylinder lens. Based on the theoretical analysis, this cylinder lens will not only extend the focal length of the fiber focuser, but also distort the wave front and induce aberrations. To quantitatively analyze the cylinder lens effects, a ZEMAX simulation was performed.

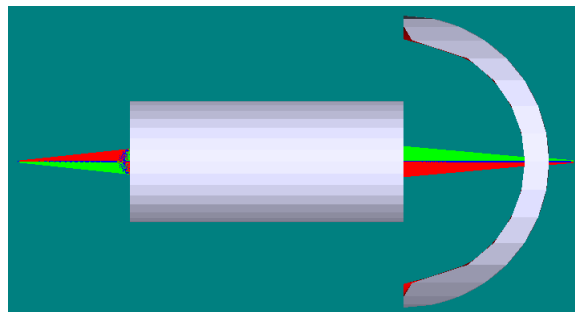


Fig. 4.2 ZEMAX model of the designed flexible endoscopic OCT probe.

Fig. 4.2 shows the 3D shaded ZEMAX model of the designed flexible endoscopic OCT probe. In this model, the single mode fiber was attached onto the surface of a 1.42mm long BK7 glass spacer, and then a 1mm GRIN lens from GRINTECH was

employed as the focus unit. Beam exiting the GRIN lens was deflected by a 0.7mm micro prism and focused 0.7mm outside of the prism surface. The corresponding modulation transfer function (MTF) and spot diagram are illustrated as below in Fig. 4.3 and Fig. 4.4.

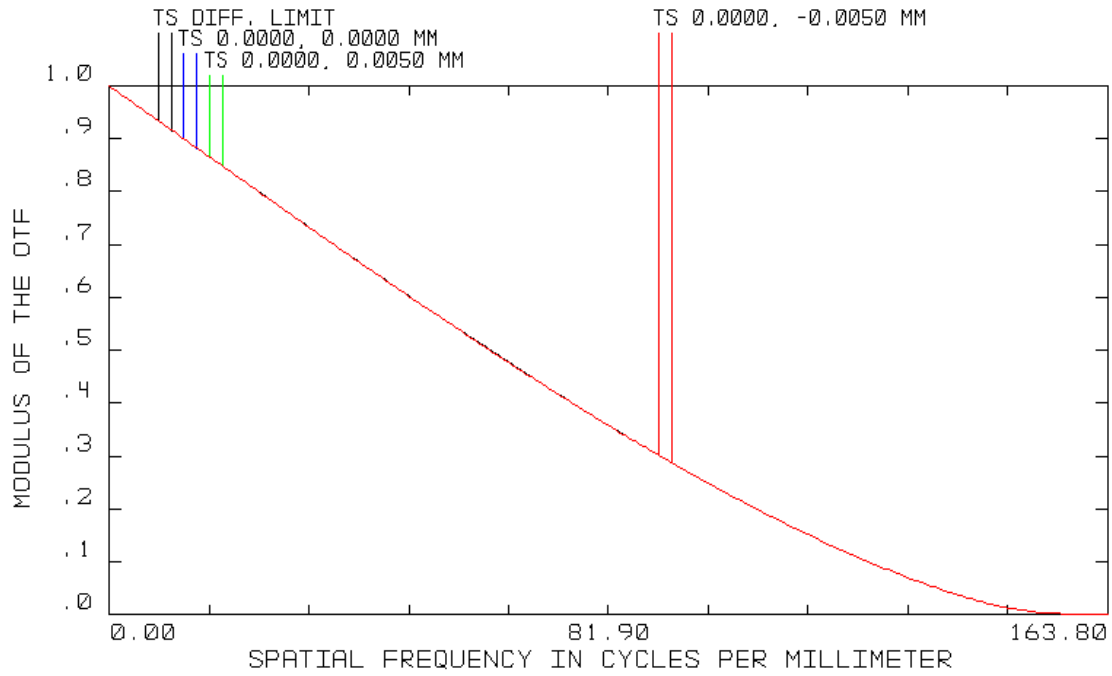


Fig. 4.3 Modulation transfer function (MTF) of the OCT probe without cylinder lens.

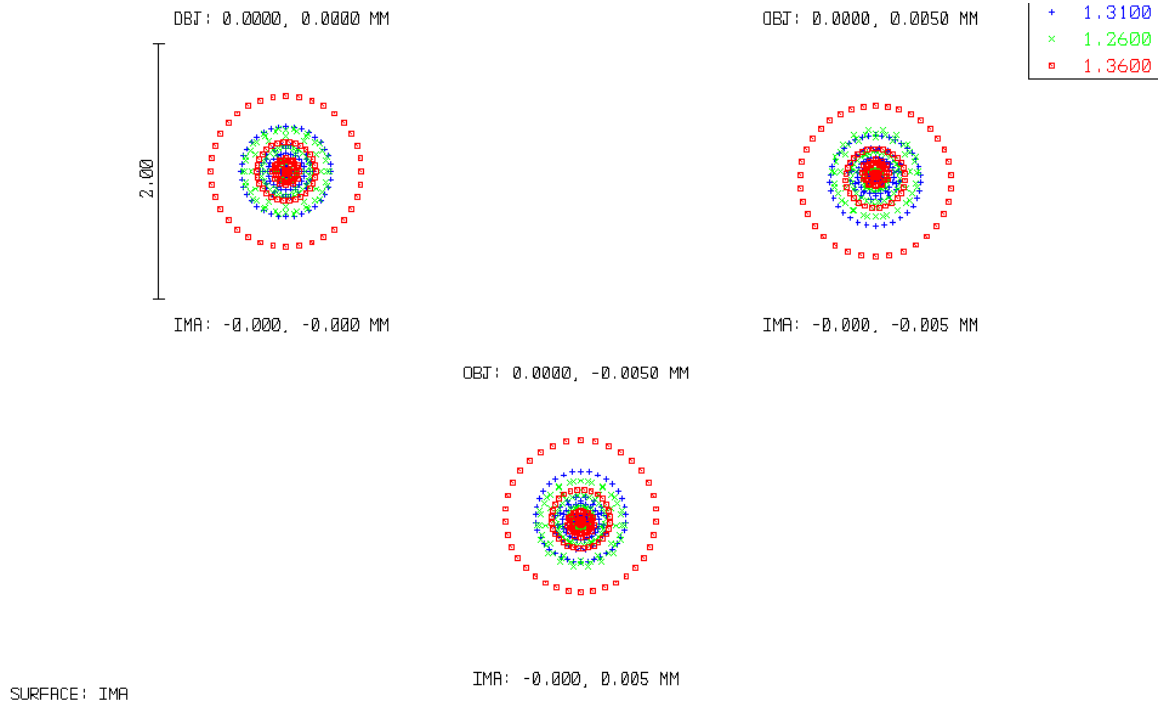


Fig. 4.4 Spot diagram of the OCT probe without cylinder lens

Then the cylinder lens, with a thickness of 0.2mm which corresponds to the wall thickness of the tube, was added into the system. Without changing the alignment, the working distance was extended 90 μ m longer, and the updated MTF and spot diagram are shown in Fig. 4.5 and Fig. 4.6 respectively.

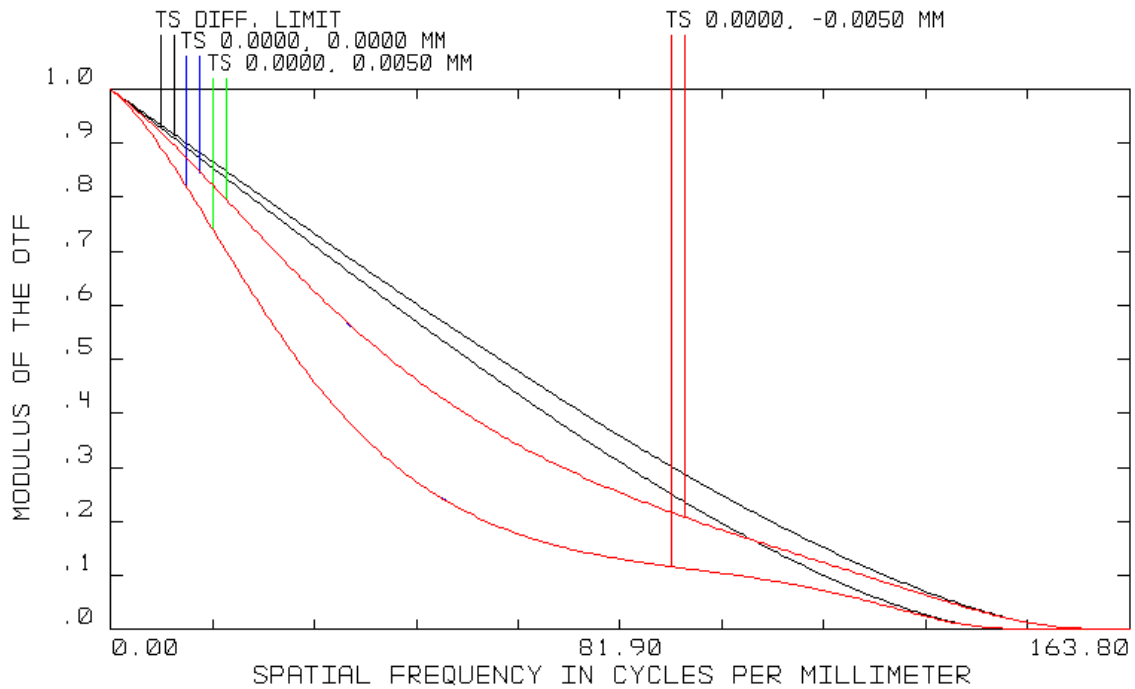


Fig. 4.5 Modulation transfer function (MTF) of the OCT probe with cylinder lens.

A comparison of Fig. 4.5 with Fig. 4.3 shows that: 1) because of the cylinder lens effect, even at diffraction limit, the MTF at the tangential plane is poorer than that at sagittal plane. 2) With aberrations induced by the cylinder lens, the system MTF dropped. A comparison of Fig. 4.6 with Fig. 4.4 shows that the spot size increased substantially. However, with the analysis results in mind, we can adjust the alignment parameters to compensate the cylinder lens effect. By properly adjusting the length of the glass spacer, the FEP tube induced cylinder lens effect can be minimized.

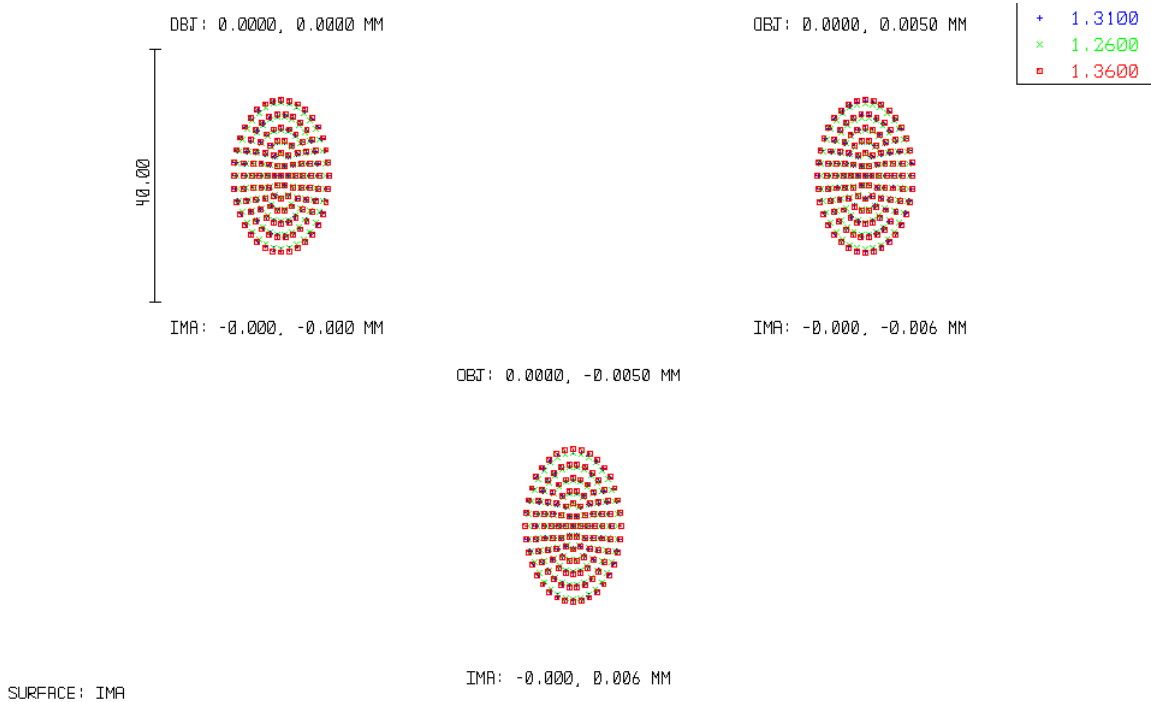


Fig. 4.6 Spot diagram of the OCT probe with cylinder lens

4.2.3 Flexible Endoscopic OCT Probe: Mechanical Design

For side-view OCT imaging, two scanning protocols can be considered. One is the rotational scan, which is the perfect choice for tubular structure imaging (e.g., vessel, colon). The other one is the translational scan, which enables large field of view imaging for flat tissue. Since human bladder surface can be considered quasi-flat within a certain area, here we adopt the translational scan as our scanning protocol.

To enable translational OCT scan, a four-layer mechanical structure was designed. The inner most layer is the single mode bare fiber. A torque transmission flexible metal coil was coated onto the single mode fiber to enable torque transmission from the motor scanner to the OCT probe and functions as the second layer. Then a piece

of flexible hollow core metal sheath was inserted into the plastic FEP tube to provide mechanical support. During the imaging, the fourth layer (FEP tube) was inserted into the working channel of the commercial cystoscope, while the first and second layers were fixed onto a linear high speed translation stage (PILine M663.465, Physik Instrumentet, USA) and scanned inside of the third layer. This mechanical design enables fast sterilization, quick replacement and easy assembling. The final flexible OCT probe is shown in Fig. 4.7.

4.2.4 Flexible Hybrid Cystoscopy/OCT

The flexible hybrid cystoscopy/OCT platform was developed by integrating a flexible endoscopic spectral domain OCT system into a commercial flexible cystoscope. As shown in Fig. 4.7 a), the SDOCT engine was upgraded from our MEMS OCT system reported previously. A broadband light source at 1310nm central wavelength with ~90nm bandwidth was employed to illuminate the fiberoptic Michelson interferometer. A 50/50 fiber coupler was applied to split the light into sample and reference arms. In the reference arm, the laser beam was first collimated, focused by an achromatic lens onto a high reflection mirror, and then reflected back to the fiber coupler. In the sample arm, the light was guided into the flexible OCT probe, and focused ~100 μ m below the tissue surface. The back scattered light was then collected by the OCT probe and interfered with the reference beam inside the fiber coupler. The interference fringes were then detected

by a high speed broadband spectrometer located in the detection arm. The axial and lateral resolutions of the system are $8\mu\text{m}$ and $12\mu\text{m}$ respectively.

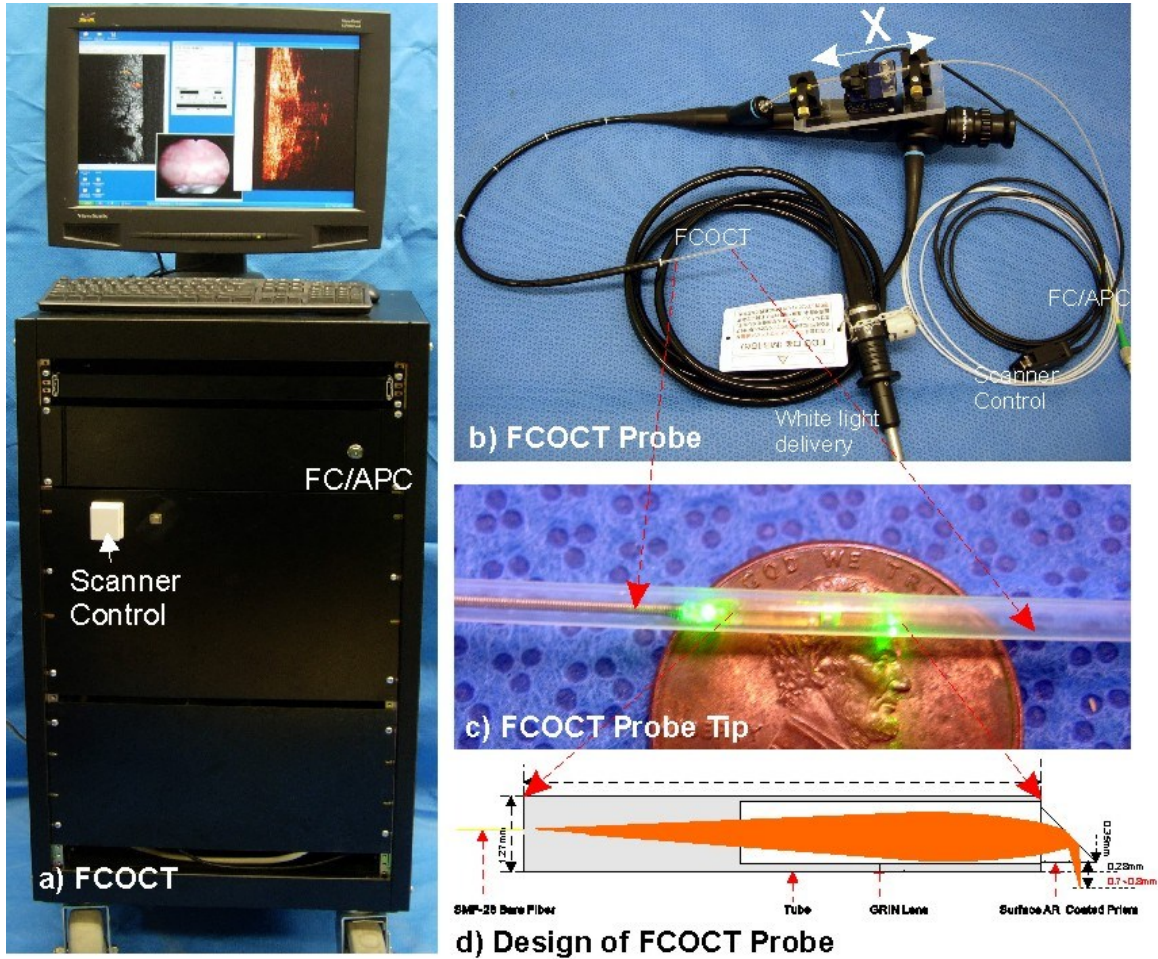


Fig. 4.7 System setup of the hybrid cystoscopy/OCT a), and the design of the FC/OCT probe b,c,d).

Fig. 4.7 b), c) and d) show the design of the flexible OCT probe. An Olympus CYF-4 flexible cystoscope was chosen as the target, which provides a large field of view (i.e., 120°) with intermediate working channel size (i.e., 2.4mm). As shown in Fig. 4.7 c), the outside diameter of the OCT probe is 2mm, and the imaging field of view can be $>15\text{mm}$.

4.2.5 Clinical Protocol

Seven subjects were examined *in vivo* prior to the biopsy or potential TURBT procedures in the operating room. All of the studies were performed after approval by the Stony Brook University Institutional Review Board and patients' informed consents. Healthy control subjects were not recruited for this study.

4.3 Results

Fig. 4.8 shows the image results of normal, TCC and CIS bladder samples obtained by the flexible cystoscopic OCT (FCOCT). Surface images were captured through the white light cystoscopy channel. Panel a) shows the image of a normal human bladder. Cross sectional OCT scan was performed at the location marked by the white dashed line in panel a), and the acquired OCT structural image is shown in panel b). Because of the high resolution, FCOCT clearly delineated the bladder layers based on their back scattering differences. Urothelium (U) appears as a thin layer on the top with low-scattering, lamina propria (LP) as highly scattering and nonuniform layer in the middle, and muscularis (M) as bifurcated collagen bundles at the bottom. Panel c) shows the surface image of a TCC sample, and panel d) is the corresponding OCT image. Compared with the normal sample in panel b), backscattering from TCC tissue appears lower and more heterogeneous. Panel e, f) represent the results from a CIS sample. The

surface image in panel e) shows little reddish symptom, which is nonspecific and can be misinterpreted as hemorrhage. However, OCT image in panel f) clearly differentiates it from normal bladder sample in panel b). Due to the heterogeneous growth and distribution of the cancer cells, structure information is diminished in the CIS sample, and the backscattering is decreased.

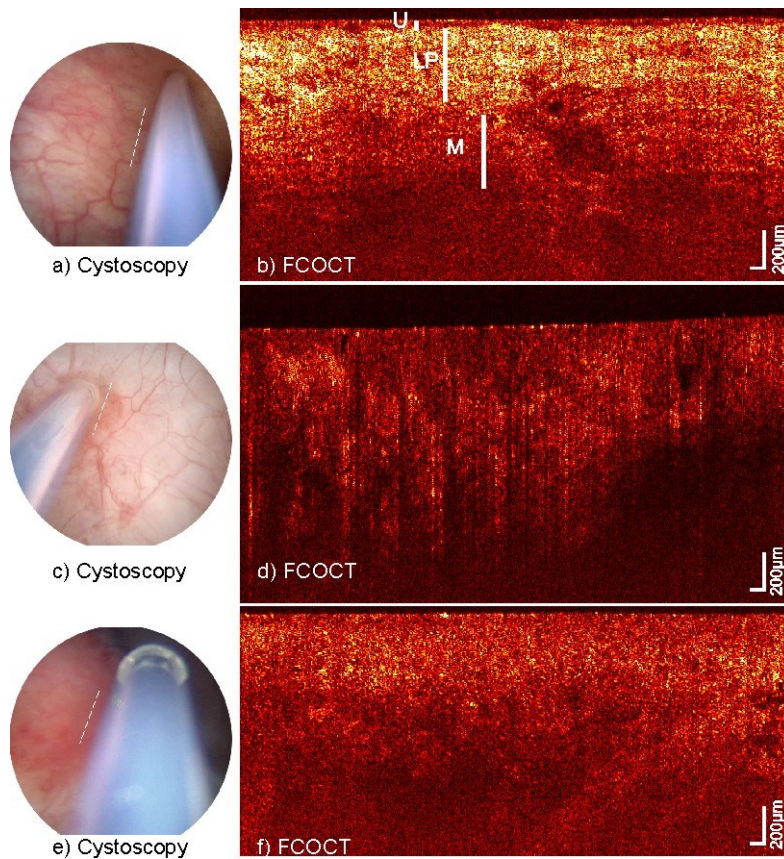


Fig. 4.8 Results of normal, TCC and CIS bladders from the FCOCT platform.

A distinctive advantage of FCOCT is the large field of view, which is critical for tumor boundary detection during TURBT. Fig. 4.9 shows the boundary delineation capability of FCOCT for CIS and TCC samples. Fig. 4.9 a) shows the surface image of a small CIS lesion. The location where OCT scan was performed was marked by the white

dashed line. Fig. 4.9 b) illustrates the boundaries between normal bladder and CIS lesion detected by FCOCT. As a flat lesion, CIS remains a clinical challenge. With the cross sectional imaging feature, FCOCT differentiated CIS from normal bladder by detecting the loss of subsurface layer structure. Fig. 4.9 c) shows the surface image of a papillary TCC lesion. The corresponding OCT result in Fig. 4.9 d) delineated the boundary based on the scattering differences, and correlated well with the surface image.

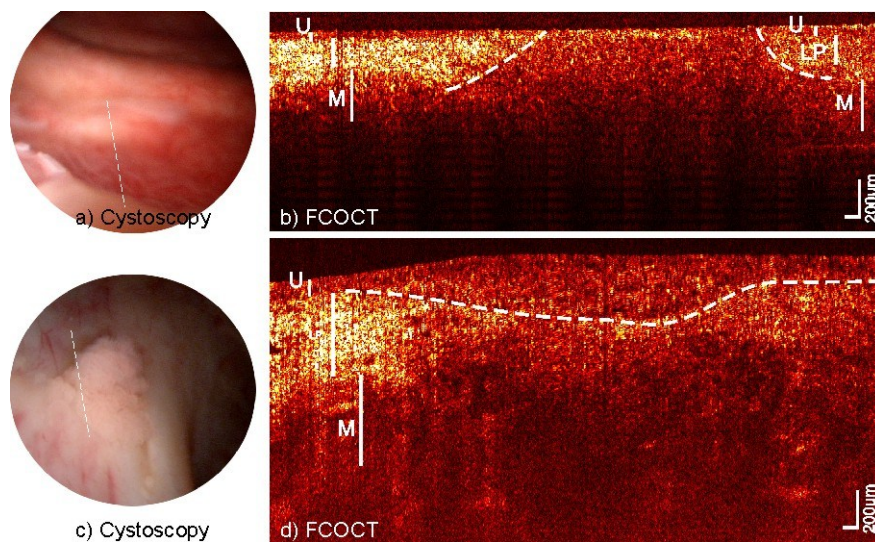


Fig. 4.9 Results of transition parts in bladder from FCOCT platform.

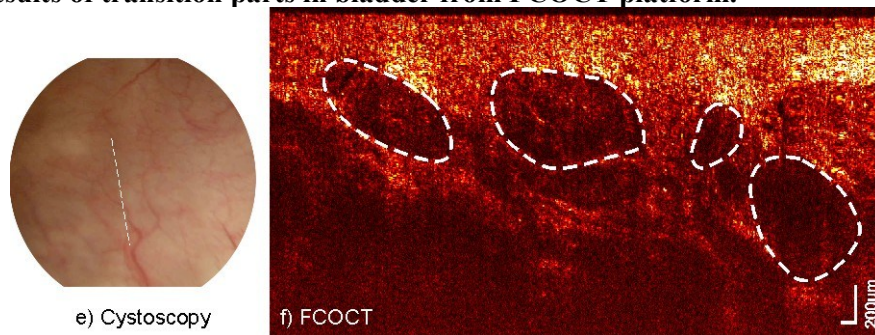


Fig. 4.10 Results of a cured bladder with Bacillus Calmette-Guérin (BCG) treatment history.

Bacillus Calmette-Guérin (BCG) instillation is a standard clinical procedure for superficial bladder cancer treatment. A typical symptom after BCG treatment is the existence of granulomatous cystitis in the muscularis layer. Fig 4.10 shows the results of a cured bladder with BCG treatment history. The dark circular shape inside the muscularis layer represents the BCG induced granulomatous cystitis. With this unique feature detected, we can predict that the subject had a history of superficial bladder cancer.

4.4 Discussions

Early diagnosis is crucial for bladder cancer management. Outpatient screening provides excellent time window for potential early detection. Flexible cystoscopic OCT overcomes the mechanical limitations of the MEMS OCT, and is therefore more suitable for outpatient diagnosis. Moreover, since the probe is flexible, even for tumors located close to the bladder neck, which were not accessible by MEMS OCT, can now be readily detected by the FCOCT. Last, FCOCT is far more robust to mechanical vibrations, sterilizations and chemical erosions compared with the MEMS OCT.

Complete tumor resection plays equal important role as accurate diagnosis for bladder cancer management. Clear tumor boundary delineation on site during TURBT is critical to enable complete resection. The large field of view of FCOCT provides the potential to image both the normal and tumor parts simultaneously in one image. Due to

the backscattering heterogeneity associated with the tumor tissue, the tumor boundary can then be accurately determined.

The construction of the FCOCT probe involves a four-layer structure design. The corresponding multiple interfaces on the optical pathway induce artifact lines on the final reconstructed image. These artifact lines can be removed manually through post image processing. However, it is time consuming and labor intensive. More importantly, for future 3D imaging, huge data sets will be generated continuously. It will be difficult if not impossible to remove these artifact lines manually. Here, we propose a new method to accurately remove the artifact lines automatically through a computer vision approach-Hough transform.

The basic principle of Hough transform is that a straight line in the spatial domain will be transformed as a bright spot in the Hough domain.⁴⁸ By detecting the peak points in the Hough domain, the locations of the straight lines in the spatial domain can then be identified. As shown in Fig. 4.11 a), the upper panel shows two lines intersect with each other in the spatial domain, while the corresponding image in the Hough domain only shows two shining points. However, the location information of the points in the Hough domain fully encodes the location information of the lines in the Hough domain. Fig. 4.11 b) shows a typical cross sectional OCT image from our FCOCT system. A deep penetration depth of about 1.2mm was achieved on the human bladder *in vivo*. More importantly, the three-layer bladder structure was clearly visualized. However, the artifact line in the middle of the OCT image obscures part of the useful structure information, and is constantly changing at different system configurations. The Hough

transform based line artifact removal algorithm was applied on Fig. 4.11 b), and the processed image is shown in Fig. 4.11 c). Compared with Fig. 4.11 b), the line artifact was removed completely without affecting the original OCT image quality. It is noteworthy that since this is an automatic approach performed in MATLAB, it can perform very fast and objectively, which is an ideal choice for future 3D FCOCT imaging.

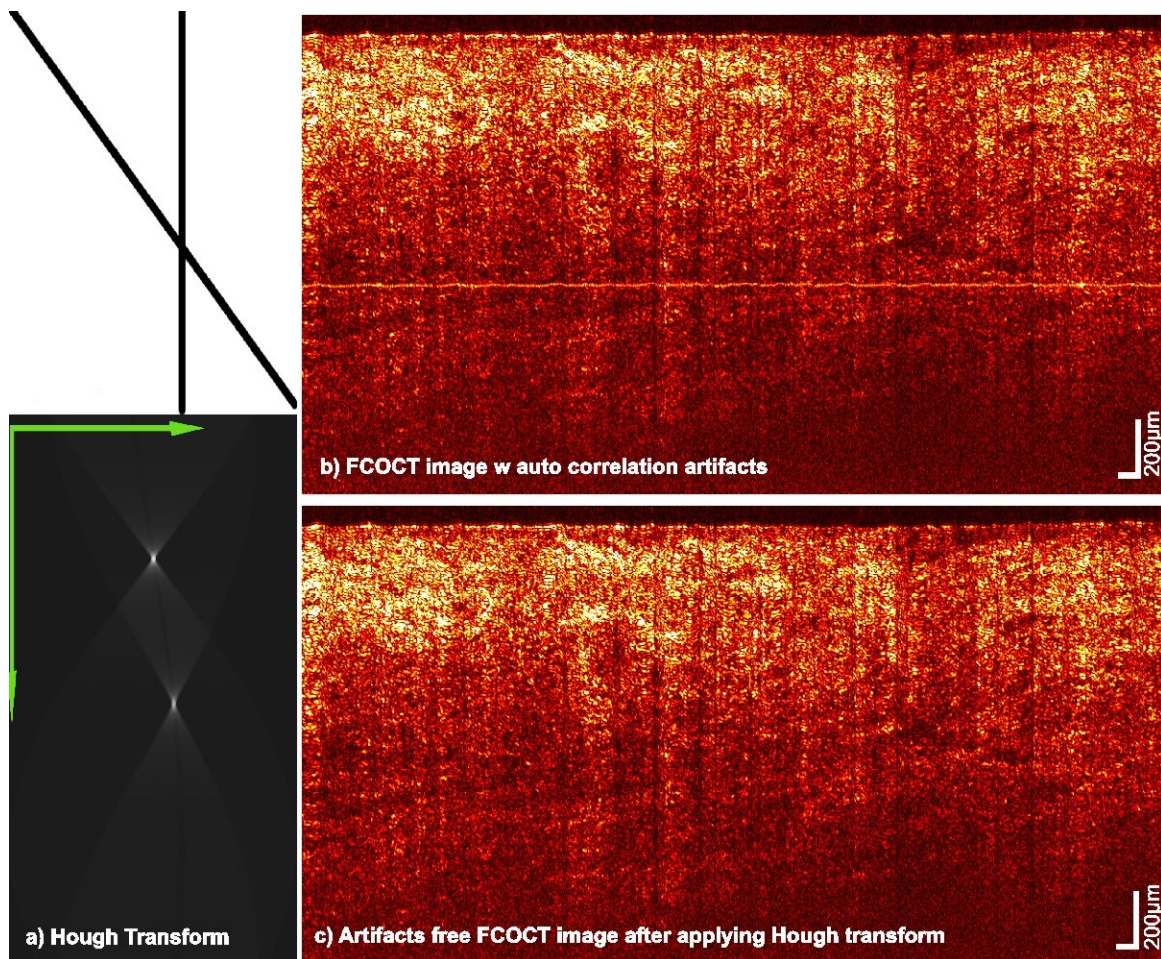


Fig. 4.11 Hough transform based approach to remove the artifact lines in OCT image

4.4 Conclusions

In this chapter, we report on a newly developed flexible cystoscopic OCT system for early bladder cancer diagnosis and guided tumor resection. The flexible and miniature design overcomes the limitations of our previous MEMS OCT probe, enabling full access to the bladder surface including bladder neck and has the great potential for future outpatient applications. With the unique feature of large field of view, tumor boundaries can be delineated on site in real time, enabling accurate and complete resection of bladder tumor to minimize reoccurrence rate. A new computer vision based Hough transform approach was also proposed to eliminate the artifacts induced by the flexible probe.

Chapter 5 Quantitative 3D OCT to Enhance Diagnosis of Bladder CIS

5.1 Introduction

Non-muscle invasive transitional cell carcinoma (TCC) accounts for over 70% of the newly diagnosed bladder cancer cases⁴⁹, among which carcinoma in situ (CIS) is a flat, high-grade, and noninvasive intraurothelial cancer and has a high risk of aggressive cancer progression. However, early diagnosis of CIS, crucial to the therapeutic treatment, remains a clinical challenge³¹. Although urinary cytology⁵⁰, fluorescence in situ hybridization (FISH)⁵¹, and bladder tumor antigen tests (BTA)³² are highly sensitive to high-grade TCC (e.g., CIS), they are unable to locate these lesions to effectively guide transurethral resection and therapy. Cystoscopy via *en-face* imaging of bladder lumen under white-light illumination is the clinical standard for bladder cancer diagnosis. However, owing to its unspecific appearance, cystoscopy often fails to identify CIS and relies on random biopsy for a conclusive diagnosis, which may miss 30%~60% of CIS lesions.⁴⁷

Recent clinical studies shed some light on the potential of new imaging techniques such as fluorescence cystoscopy and narrow-band imaging for improving the

detection of non-muscle invasive TCC (NMI TCC).^{37, 52-54} Optical coherence tomography (OCT) is an emerging imaging technique that enables noninvasive cross-sectional imaging of urinary bladder (e.g., urothelium, lamina propria, and muscularis) at a high resolution (e.g., 1~10µm) over ~2mm of depth. Preclinical and clinical studies^{7, 36, 38, 41} demonstrate the potential of cystoscopic OCT to significantly enhance white-light cystoscopy in the diagnosis of NMI TCC (e.g., CIS). In addition, our recent advances in time-lapse ultrahigh-resolution OCT^{44, 55} permit subcellular imaging differentiation of normal and cancerous urothelia, which is promising for future ‘optical biopsy’ of CIS. While 2D OCT enables delineation of bladder morphology and detection of bladder tumors, the diagnosis is based on qualitative identification and thus likely subject to change depending on the location of OCT scan and physician’s interpretation of the image feature. Recently, there has been increasing interest in quantitative OCT image analysis with computer-aided detection to eliminate diagnostic subjectivity and thus to allow for more affirmative identification and further enhanced diagnosis of complicated TCC, especially CIS. Computation-intensive numerical approaches such as center-symmetric auto-correlation and texture analysis have been applied to 2D OCT, e.g., of skin, esophagus, and bladder to improve the detection⁵⁶⁻⁵⁸. In this Chapter, we present a new quantitative method to enhance the diagnosis of CIS based on 3D OCT to evaluate the increased urothelial heterogeneity induced by carcinogenesis. Experimental validation is conducted using a transgenic bladder CIS model, allowing us to examine the efficacy of this 3D OCT technique to enhance white-light imaging (resembling cystoscopy) and 2D OCT for CIS diagnosis.

5.2 Materials and Methods

5.2.1 Transgenic CIS model

A rodent bladder cancer model (SV40T) was employed in this study. SV40T transgenic mice by expressing simian virus 40T antigen in their urothelium (driven by uroplakin II promoter) routinely develop CIS at ~8-20 weeks of age and then high-grade papillary carcinoma in their bladder according to recent studies.⁵⁹ A close colony of inbred transgenic mice (N=40) from a primary SV40T transgenic strain kindly provided by Dr. Wu's lab were used in the experiment and their genotyping for SV40T was verified by PCR on DNA from tail biopsy. In addition, 10 CFW mice were included in the control group. All animal procedures were performed in compliance with the animal care regulations approved by the Stony Brook University Animal Care and Use Committee.

5.2.2 3D OCT Image Acquisition

At 8-20 weeks of age (mean age: 14wks) when CIS was present in SV40T mice, 2D enface white-light and 3D OCT images were acquired from SV40T and CFW mice (blinded). The mice were euthanized using anesthetic overdose and the intact bladder was removed by a midline laparotomy incision, opened from the urethra to the dome and

mounted uniformly on a custom $\phi 12\text{mm}$ ring holder placed in a modified Ringer's buffer solution (37°C , $\text{pH}7.4$) to undergo *ex vivo* imaging evaluations. Enface image (resembling cystoscopy) of each bladder specimen was taken by a white-light cystoscope over a field of view (FOV) of $\phi 11\text{mm}$ using a high-sensitivity digital video camera previously used in our clinical studies.⁷ Instantaneous 3D OCT image was obtained using our spectral-domain OCT system (SDOCT) which was able to acquire 400 2D OCT images. The 3D OCT prototype was upgraded from our 2D SDOCT system reported previously⁷, in which a broadband source at $\lambda=1310\text{nm}$ central wavelength with a 90nm spectral bandwidth (i.e., coherence length $L_c\approx 8.4\mu\text{m}$) was employed to illuminate a fiberoptic Michelson interferometer and a green laser at $\lambda=532\text{nm}$ was coupled to guide image acquisition. The sample arm was connected to a handheld probe in which light exiting the optical fiber was collimated, steered by high-speed 2D servo mirrors, and then focused onto the bladder surface with a $\text{NA}/0.1$ achromate. The retroreflected light beams from both sample and reference arms were recombined in the detection arm, spectrally diffracted, focused by a lens system to be detected by a high-speed linear InGaAs array Camlink interfaced with a PC at 47kHz per A-scan. The spatial resolution was $\sim 10\mu\text{m}$, the system dynamic range was $>110\text{dB}$, and a large 3D image volume ($\text{FOV}=5\times 2\times 4\text{mm}^3$) could be acquired within $\sim 4\text{s}$.

5.2.3 3D OCT Image Analysis

As previously outlined, each A-scan was retrieved by inverse fast Fourier transform (FFT) from the acquired spectral interferogram so that 2D and 3D OCT images were reconstructed in a way similar to ultrasound B-mode and 3D images. OCT diagnosis of CIS was based on evaluating the enhancement in urothelial heterogeneity induced by carcinogenesis; therefore, minimizing speckle noise was crucial which was difficult for a thin normal urothelium or CIS lesion. This was because with limited urothelial thickness, more lateral averaging was needed which tended to diminish the architectural heterogeneity induced by CIS. Image processing methods were applied, including 3D segmentation of urothelium and cubic low-pass filtering to reduce speckle noise and enhance edge contrast. Image registration was applied to compensate topographic changes of the segmented urothelium and to allow for reconstruction of a speckle-minimized enface urothelial image (i.e., C-mode OCT_{xy} , averaged 8 pixels in depth direction). To enable computer-aided detection, two types of texture features, i.e., 2D power spectral graph/profile (2D FFT) and 2D standard deviation map (2D STD) were extracted to quantify architectural heterogeneity and thus to detect CIS more accurately and objectively. To minimize computation, an area of interest (ROI) over 200×400 pixels was randomly selected for 2D FFT analysis and 4th-order polynomial fitting was applied to calculate the spectral power profile $\psi(f_{x,y})$ whose 2nd-order derivative $\psi''(f)$ was used as the target function to represent the architectural heterogeneity (i.e., spectral components induced by structural variations at a higher frequency against the base power spectrum). In addition, 5×5 binning was applied to OCT_{xy} to calculate 2D STD map and its mean ($\bar{\sigma}$) and histogram (σ_{FWHM}) so that both global and local heterogeneous

properties can be represented for CIS detection. The threshold values ($\psi''(f \approx 0.1) < -0.2$, $\bar{\sigma} > 13$) for final quantitative diagnoses were preselected from the first 10 specimens (5 SV40T mice, 5 controls).

5.2.4 Statistical Analysis

The sensitivities and specificities for both 2D and 3D OCT diagnoses were computed from the frequency tables with the corresponding H&E stained histological evaluation serving as the gold standard. Their values for 3D OCT were compared with the 2D counterparts using chi-squares test or Fisher's exact test, with $p < 0.05$ considered statistically significant.

5.3 Results

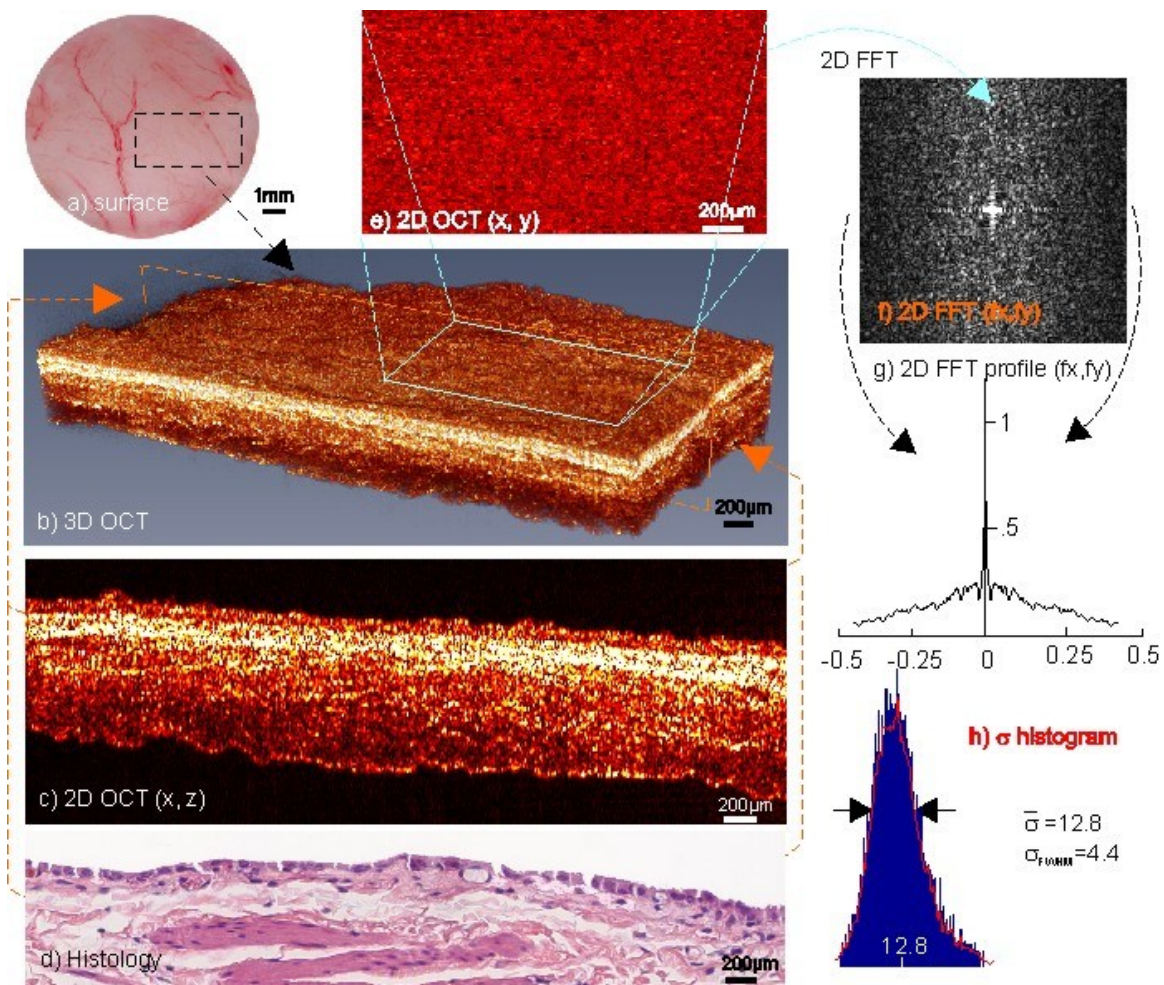


Fig. 5.1 Results of a normal mouse bladder. a) surface image; b) 3D OCT of the region landmarked with a dashed rectangle in a); c, d) 2D OCT and the corresponding histology of the cross-section highlighted in b); e) 2D enface OCT_{xy} of the blue box indicated in 3D OCT b); f) 2D FFT of OCT_{xy} in e); g) 2D FFT profile of f); h) STD map or histogram of OCT_{xy} under 5×5-pixel binning and the calculated mean of standard deviation and variation for normal bladder were $\bar{\sigma} = 12.8$ and $\sigma_{FWHM} = 4.4$, respectively

Owing to its high spatial resolution (e.g., $\sim 10\mu\text{m}$) and intermediate imaging depth (e.g., up to 2mm), OCT enables delineation of the morphological details of bladder, e.g., urothelium (U) as a low-scattering thin layer, lamina propria (LP) as a high-scattering underlying layer, and muscularis (M) as a thick layer with large bifurcated collagen fiber bundles. OCT diagnosis of normal bladder (including benign inflammatory lesions) was

based on high-resolution delineation of thin and uniform urothelium. Fig. 5.1 exemplifies the results of a normal mouse bladder. Surface image (a) which resembled white-light cystoscopy showed a typical normal-appearing bladder surface in which a dashed rectangle landmarked the region of 3D OCT (b). Cross-sectional OCT image (c) clearly identified 3 bladder layers (i.e., U, LP and M) based on their backscattering differences and correlated well with the corresponding histology (d). Importantly, enface OCT_{xy} image (e) processed from 3D OCT (b) over a randomly selected ROI (blue square) showed the architectural uniformity and smoothness within the urothelium after speckle reduction. Quantitative analyses with 2D FFT graph (f) and FFT profile (g) exhibited a power spectral distribution predominantly in the low spectral range (e.g., $f_{x,y} < 0.1$), indicative of urothelial homogeneity. Collaterally, the low mean standard deviation ($\bar{\sigma} = 12.8$) and variation ($\sigma_{FWHM} = 4.4$) in STD histogram (h) correlated well with the low local structural variations in normal urothelium. Statistical analysis revealed that the characteristic features presented in Fig. 5.1 were fairly consistent among all normal bladder samples (e.g., with less than 10% variation).

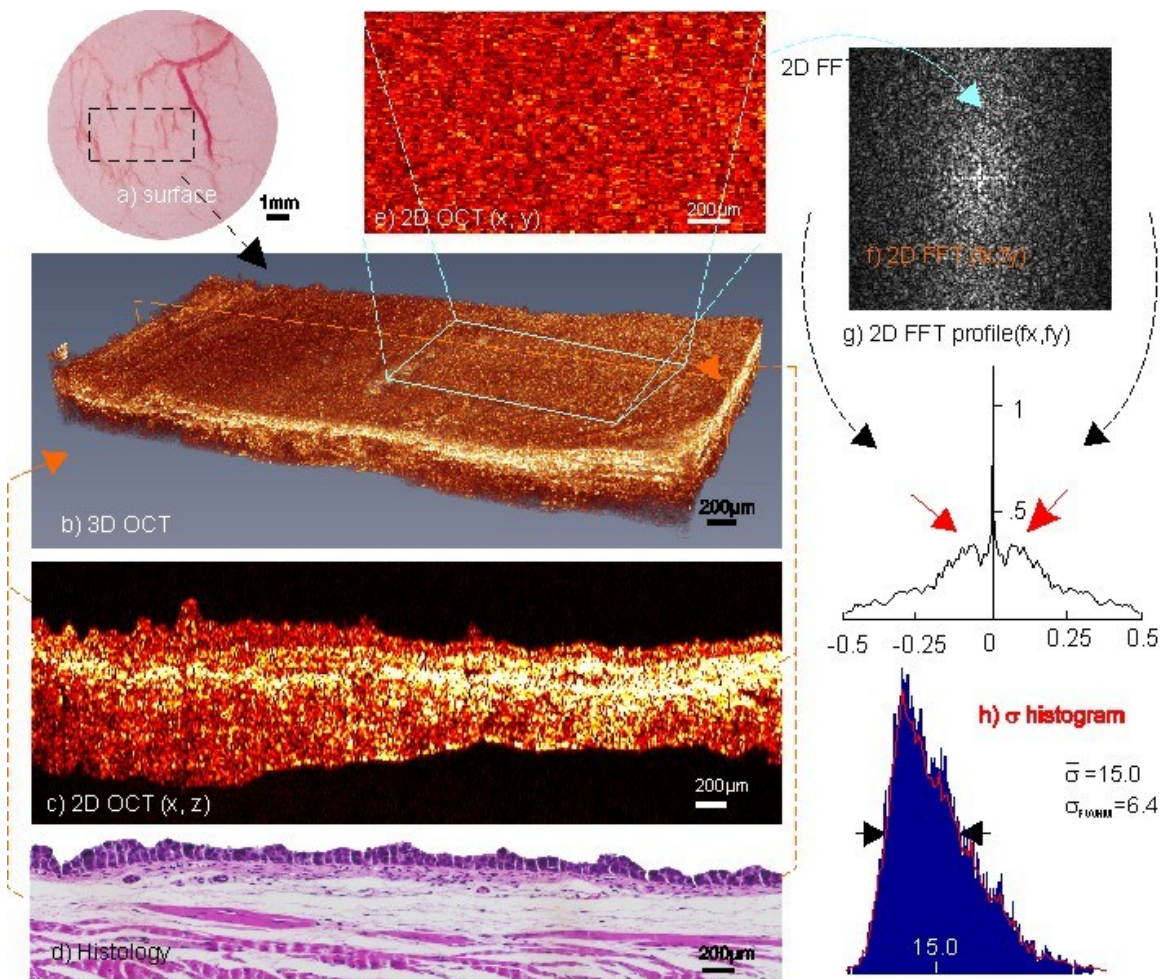


Fig. 5.2 Results of CIS in a SV40T mouse bladder. a) surface image; b) 3D OCT of the region landmarked with a dashed rectangle in a); c, d) 2D OCT and the corresponding histology of the cross-section highlighted in b); e) 2D enface OCT_{xy} of the blue box indicated in 3D OCT b); f) 2D FFT of OCT_{xy} in e); g) 2D FFT profile of f); h) STD map under 5×5-pixel binning and the calculated mean of standard deviation and variation of this early CIS bladder were increased to $\bar{\sigma} = 15$ and $\sigma_{FWHM} = 6.4$, respectively.

OCT identification of CIS was based on enhanced heterogeneity in terms of urothelial backscattering resulted from random growth involved in carcinogenesis (e.g., enlarged nuclei in CIS cells) as exemplified in Fig. 5.2. Surface image (a) showed no specific difference to normal bladder in Fig. 5.1(a), thus precluding differentiation of CIS. Moreover, the gross morphology (e.g., U, LP, M) shown in 3D OCT (b) and 2D

OCT (c) is almost identical to that of a normal bladder except minor urothelial thickening on the left side, which could be missed as artifacts induced by bladder stretching or urothelial hyperplasia. However, subtle architectural changes induced by CIS were well presented by enhanced urothelial heterogeneity, e.g., dark shadows in enface OCT_{xy} (e). Further FFT analyses indicated that the power spectrum (f) was broadened resulted from increased heterogeneity; in addition to the base spectral distribution centered at around $f_{x,y}=0$, a sidelobe was readily identified at $f_{x,y}\approx 0.1$ in the FFT profile (g) likely due to the shaded textures in enface OCT_{xy} (e). For computer-aided detection of CIS, quantitative analysis showed that $\psi''(f\approx 0.1)$ decreased to -0.5 from ~ 2 for normal bladder in Fig. 5.1(h), where $\psi''(f\approx 0.1)\leq -0.2$ was used as thresholding in our quantitative diagnosis to represent the sidelobe (i.e., heterogeneity) induced by CIS. Meanwhile, the standard deviation increased 20% to $\bar{\sigma}=15$ and its variation increased 46% to $\sigma_{\text{FWHM}}=6.4$ due to increased urothelial heterogeneity.

Fig. 5.3 shows the results of a more ‘advanced’ CIS case. Similar to Fig. 5.2, surface image (a) was unable to detect CIS and 2D OCT showed no specific difference of bladder morphology except minor thickening over the entire urothelium. Yet, enface OCT_{xy} (e) was able to clearly identify structural heterogeneity with more dark shadows than in Fig. 5.2(e). Quantitative analyses revealed a stronger sidelobe around $f\approx 0.1$ in 2D FFT graph (h) and a significant decrease of $\psi''(f\approx 0.1)$ to -3.5, indicating increased high-frequency components corresponding to increased texture features. Accordingly, the STD histogram (h) was broadened with $\bar{\sigma}$ increased 70% to 21.7 and σ_{FWHM} increased 109% to 9.2, showing significantly enhanced urothelial heterogeneity induced by CIS.

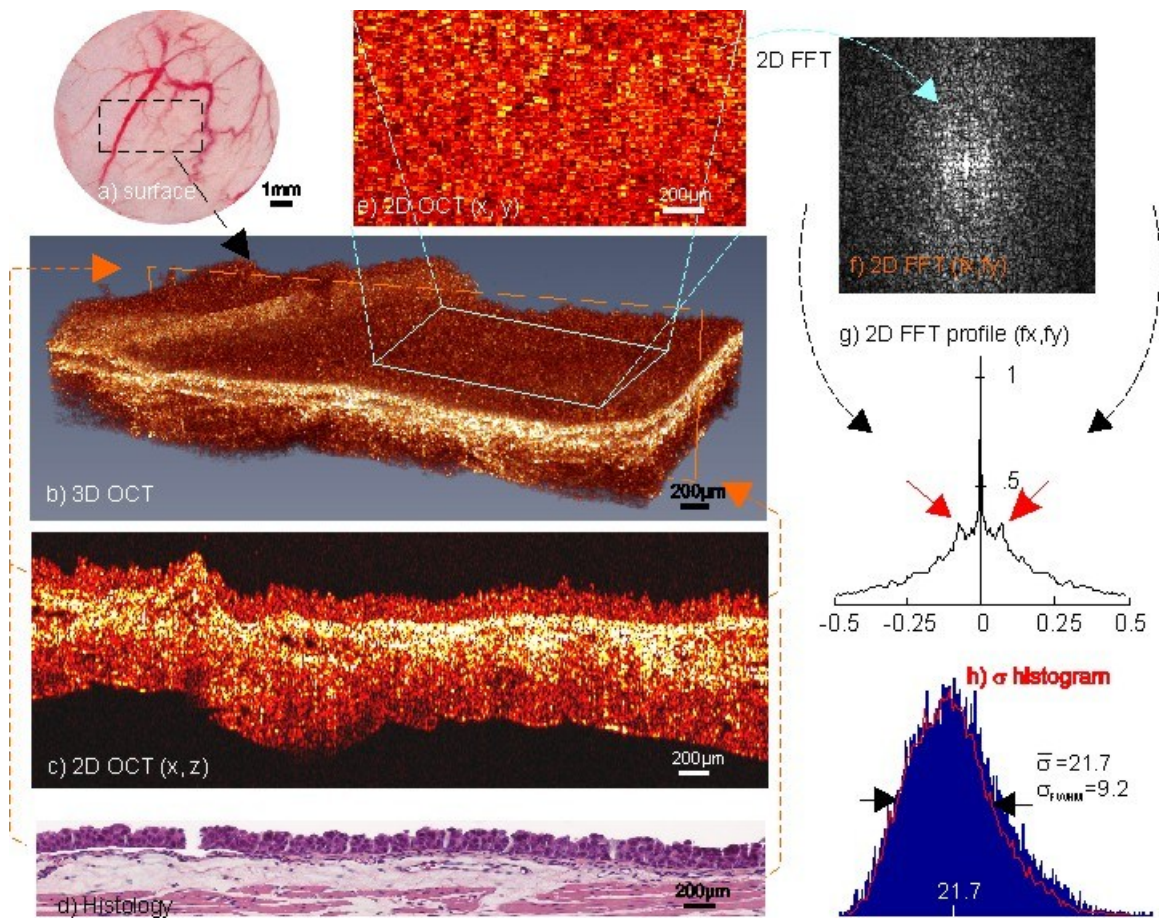


Fig. 5.3 Results of ‘advanced’ CIS in SV40T mouse bladder. a) surface image; b) 3D OCT of the region landmarked with a dashed rectangle in a); c, d) 2D OCT and the corresponding histology of the cross-section highlighted in b); e) 2D enface OCT_{xy} of the blue box indicated in 3D OCT b); f) 2D FFT of OCT_{xy} in e); g) 2D FFT profile of f); h) STD map under 5×5-pixel binning and the calculated mean of standard deviation and variation of this ‘advanced’ CIS bladder were increased to $\bar{\sigma} = 21.7$ and $\sigma_{FWHM} = 9.2$, respectively.

A total of 50 mice (i.e., 40 SV40T mixed with 10 CWF) were enrolled in the study; however, 14 SV40T mice were excluded for exhibiting exophytic papillary bladder tumors. Among 23 pure CIS samples later confirmed by histology, 22 were detected by 3D OCT, 13 were detected by 2D OCT, and none was differentiable with surface imaging; whereas for all 13 histologically confirmed normal or benign samples (3 were SV40T mice), 12 were detected by 3D OCT and 8 by 2D OCT. The detailed diagnostic

status calculated on a per sample basis was summarized in Tab. 5.1, which indicated that surface imaging failed to detect CIS in SV40T mice and 2D OCT was unable to provide effective diagnosis. In contrast, 3D OCT was able to significantly enhance the diagnostic sensitivity and specificity of CIS to 95.7% and 92.3%, respectively ($p \leq 0.031$).

Table 5.1 Diagnostic sensitivities, specificities, PPV and NPV

| Methods \ Results | 3D OCT | | 2D OCT | | Cyst | | p-values | | |
|---------------------------------|--------|------|--------|------|-------|------|----------|----------|----------|
| | n/N | % | n/N | % | n/N | % | 3D: 2D | 3D: Cyst | 2D: Cyst |
| CIS (pTis) / Sensitivity | 22/23 | 95.7 | 13/23 | 56.5 | 12/23 | 52.2 | 0.001 | <0.001 | 0.767 |
| Benign / Specificity | 12/13 | 92.3 | 8/13 | 61.5 | 7/13 | 53.8 | 0.031 | 0.027 | 0.691 |
| PPV | 22/23 | 95.7 | 13/18 | 72.2 | 12/18 | 66.7 | 0.018 | 0.014 | 0.717 |
| NPV | 12/13 | 92.3 | 8/18 | 44.4 | 7/18 | 38.9 | 0.003 | 0.003 | 0.735 |

* Cyst: cystoscopy resembled by surface imaging, N: total number, PPV, positive predictive value, NPV, negative predictive value.

5.4 Discussions

Noninvasive early diagnosis of CIS remains a clinical challenge.³¹ While white light cystoscopy (following urine cytology) is the current clinical standard for the diagnosis of NMI TCC, it often fails to detect CIS because of its flat and nonspecific appearance and relies on random biopsy which may miss ~60% of CIS lesions.⁴⁷ Recent advances in endoscopic subsurface imaging techniques (e.g., 2D cross-sectional OCT) may permit high-resolution imaging identification of architectural features underneath the bladder surface and have shown promising outcomes based on preliminary clinical

validation studies of our group and of others^{7, 36, 38, 41} Yet, OCT diagnosis of epithelial cancers, e.g., TCC conducted so far has been primarily based on imaging identification of bladder layers and abnormal architectural variations in the urothelium (e.g., urothelial thickening, increases in urothelial backscattering and/or heterogeneity), which relies on examiner's interpretation of OCT image features and the diagnostic results can be subjective. Therefore, quantitative OCT image analysis and differentiation with computer-aided detection is highly desirable for enabling objective and more accurate diagnosis of highly complicated bladder cancer cases, particularly for CIS.

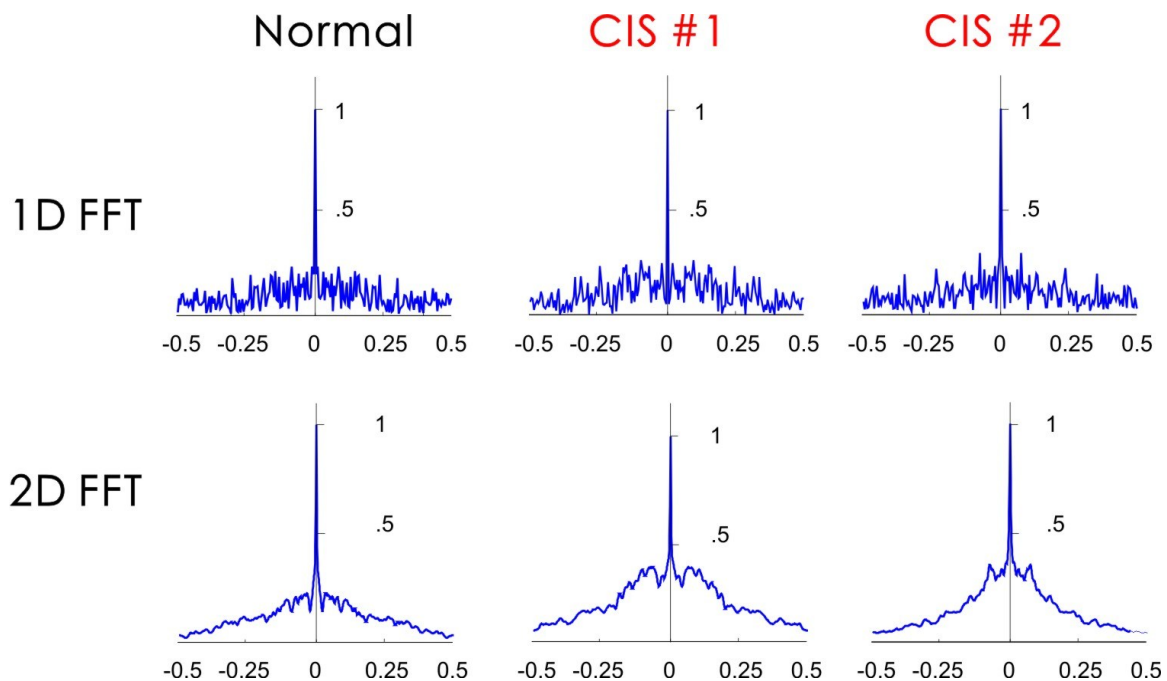


Fig. 5.4 A comparison between FFT profiles calculated from 2D and 3D OCT. a, c) FFT profiles of normal bladder and of CIS computed from 2D OCT, in which severe speckle noise buried the spectral components of the texture changes induced by CIS; b, d) FFT profiles of the normal bladder and of CIS computed from 3D OCT, in which random speckle noise was effectively minimized so that the spectral components of the texture changes induced by CIS was readily differentiated to enable quantitative diagnosis with computer-aided detection.

A major clinical challenge encountered in our pilot study on cystoscopic OCT diagnosis of TCCs lies in the fact that unlike animal cancer models, almost 75% of NMI TCC cases exhibited no obvious increase in urothelial backscattering⁴¹; therefore, one of the primary diagnostic criteria for NMI TCC diagnosis was based on detection of increased urothelial heterogeneity induced by carcinogenesis. However, the inherent speckle noise in OCT image may compromise OCT diagnosis because of difficulties in separating speckle noise or patterns from architectural texture features; therefore, effective speckle reduction is crucial to improving OCT image identification and cancer diagnosis, and quantitative image analysis with computer-aided detection can potentially further enhance the diagnosis of TCC and improve diagnostic subjectivity to allow for physician's independent diagnosis. In fact, there has been increasing interest in quantitative OCT analysis with computer-aided detection to enable more reliable identification and enhanced diagnosis of skin, esophageal, and bladder tumors. Numerical approaches, including center-symmetric autocorrelation and texture analysis have been applied to OCT images to analyze the morphological changes resulted from cancer growth.⁵⁶⁻⁵⁸ However, these methods were based on image processing of 2D OCT which might vary dramatically from cross section to cross section and be difficult for effective speckle reduction. This could be particularly challenging in quantitative diagnosis of CIS which is confined in thin urothelium within 10~20 pixels (e.g., equivalently 30-60 μ m) in a 2D OCT image in Fig. 5.1(c)-Fig. 5.3(c), because speckle reduction required interpixel averaging across adjacent pixels in the lateral and vertical directions. As a result, 2D OCT quantitative analysis (e.g., 1D FFT) often suffers from random speckle noise and

poor repeatability from sample to sample even within one sample at different locations. To overcome these technical problems, we propose more advanced image segmentation and quantitative image analysis algorithms (e.g., ‘speckle free’ enface OCT, 2D FFT, $\psi''(f)$, and STD map) based on 3D OCT image dataset and the results presented Fig. 5.1- Fig. 5.3 clearly demonstrate the potential to significantly enhance the diagnosis of CIS. For instance, Fig. 5.4 compares the FFT profiles (ψ) of a normal bladder (upper panels) and a CIS bladder (lower panels) computed from 2D OCT (left) and 3D OCT (right), respectively. The results show that spectral fluctuation in panels (a, c) induced by severe speckle noise in 2D OCT images buried the texture changes induced by CIS, rendering it very difficult to differentiate each other. Whereas 3D OCT which permitted effective speckle reduction and elimination of random variation of textures owing to cross correlation between adjacent OCT cross sections, was able to effectively minimize the random speckle noise background to provide distinct spectral profile differences and sufficient SNR for quantitative diagnosis with $\psi''(f)$, as shown in panels (b, d).

Noteworthy, increase in urothelial heterogeneity is a unique feature of TCC including CIS; however, the subtle texture difference can be easily washed out by over averaging for speckle reduction or overlooked by only analyzing global features. Therefore, it is important to take into account of both local and global heterogeneities. In this respect, both 2D FFT and σ_{FWHM} provided the quantitative global features parameters; whereas $\bar{\sigma}$ based on 5×5-pixel binning and $\psi''(f)$ tended to reflect local or regional texture features. Such combinative assessment could be more important for the quantitative diagnosis of focal CIS lesions in which CIS only partially occupies the field

of view. Another important factor for future *in vivo* clinical adoption is to optimize the algorithm and computation efficiency so as to be suited for on-site immediate diagnosis. In this study, image acquisition was ~4s and quantitative analysis was ~4s for each sample, but this can be further reduced to ~5s or less which should be suitable for instantaneous on-site clinical diagnosis.

Lastly, it is noteworthy that the type and severity of the CIS cases presented in this study were so minor compared with those encountered in previous clinical studies that surface imaging (white-light cystoscopy) completely failed and even 2D OCT barely detected. Although the quantitative algorithm was more effective and robust in papillary TCCs, they were not presented because 2D OCT was able to provide sufficient diagnosis.

5.5 Conclusions

We reported a new method to enable quantitative diagnosis of CIS of the bladder with computer-aided detection based on 3D OCT. To examine the efficacy of the methodology, a CIS model with SV40T transgenic mice was imaged *ex vivo* tri-modally using surface imaging (mimicking cystoscopy), 2D OCT and 3D OCT and validated by the corresponding histology. Results of our comparative study demonstrated that 3D OCT with computer-aided detection was able to identify subtle morphological changes (i.e., urothelial heterogeneity) induced by CIS that surface imaging completely failed and 2D could barely detect. This new technique promises to be an effective diagnostic of bladder CIS with an estimated 95.7% sensitivity and 92.3% specificity. More importantly, such

quantitative method with computer-aided detection may permit physician's on-site independent diagnosis which will be very helpful to improve diagnostic objectivity. The results justify the development of 3D OCT cystoscopy for clinical study to enhance the diagnosis of early TCC, particularly CIS. It is noteworthy that unlike SV40T model, human CIS lesions are likely focal, so selecting the proper ROI for quantitative diagnosis is important. In this respect, more effective fluorescence image guidance^{53, 54} can be beneficial to enhance the efficacy to locate the ROI for 3D OCT diagnosis of CIS *in vivo*.

Chapter 6 Image Guided 3D OCT for Early Diagnosis of Carcinoma in situ of the Bladder

6.1 Introduction

Carcinoma in situ (CIS) of the bladder is a type of flat, high-grade, non-muscle invasive (NMI) urothelial cell carcinoma (TCC). However, unlike other NMI TCCs, CIS is highly malignant and has a great tendency of aggressive progression if left untreated;⁶⁰ therefore, early detection is crucial to the effective treatment of CIS. Early diagnosis of CIS remains a clinical challenge.⁶¹ Current methods include urinary cytology and white light cystoscopy (WLC) following random biopsy.⁶² While urinary cytology is highly sensitive to high-grade TCC (e.g., CIS), it is unable to locate the lesions to effectively guide transurethral treatment such as resections. WLC is the current clinical standard for TCC diagnosis. However, as most CIS lesions are flat and unspecific, WLC often misses CIS and relies on random biopsy for a conclusive diagnosis (e.g., 30%~60%)⁴⁷; therefore, new diagnostic approaches are highly desirable for improving early clinical detection of CIS.

Recent advances in optical imaging techniques⁵², including narrow band imaging (NBI)⁶³, fluorescence cystoscopy (FC)^{37, 54, 63} and optical coherence tomography (OCT)⁷,

^{36, 38, 41} have demonstrated the potential to markedly improve the diagnosis of NMI TCC. NBI is a simple modification of WLC to enhance visualization of subsurface vasculature under narrow-band illumination at strong hemoglobin absorption wavelengths (e.g., ~415nm or/and ~540nm). Based on detection of increased vascular density and pattern changes associated with tumor development, NBI has been reported to enhance the diagnosis of TCC in clinical studies. FC has been shown in the clinical studies to enhance the diagnosis of NMI TCC by detecting the fluorescence emission of photosensitizers (e.g., 5-ALA or HAL) which tend to accumulate preferably in neoplastic tissues. However, this technique requires systemic or intravesical administration of photosensitizers. Similar to NBI, the diagnostic specificity is relatively low, which leads to high false-positive rates (e.g., bladder inflammation, infection, cystitis). OCT is a novel imaging modality that enables noninvasive, 3D imaging of biological tissues at a high spatial resolution (e.g., 1~10um) over ~2mm of depths. Preclinical and clinical studies^{7, 36, 38, 41} have demonstrated the efficacy of cystoscopic OCT to significantly enhance WLC in the diagnosis of NMI TCC (e.g., CIS). Moreover, the newly developed time-lapse ultrahigh resolution OCT^{44, 55} allows subcellular imaging of urothelium for grading of TCC, which shows the promise for future 'optical biopsy' *in vivo*. Additionally, to enable physician's independent diagnosis and minimize diagnostic subjectivity to allow for more affirmative identification of CIS based on characterization of increased urothelial heterogeneity resulting from carcinogenesis, our recent preclinical study showed significantly improved sensitivity and specificity of CAD based 3D OCT in detection of CIS compared with 2D OCT.¹⁷

In this Chapter, we present a newly designed comparative study on a transgenic animal bladder CIS model to systemically evaluate the efficiency and potential limitations of WLC, NBI, FC and 3D OCT (with a new CAD algorithm) for early CIS detection. This study also allows us to examine the potential of combining the advantages of these techniques for more efficacious and efficient diagnosis of TCC (e.g., CIS) in future clinical application *in vivo*.

6.2 Materials and Methods

6.2.1 Transgenic Model

A detailed description of the transgenic CIS rodent model was reported previously.^{17, 59} By expressing simian virus 40T antigen in the urothelium, CIS routinely develops in the bladder of SV40T transgenic mice during 8-20 weeks and then high-grade papillary tumors start to emerge. Twenty nine SV40T mice were used in the experiment and their genotyping was verified by polymerase chain reaction based on tail biopsy. Additional 18 Balb/c mice (blinded) were included as the control group. All animal procedures were approved by the Stony Brook University Animal Care and Use Committee.

6.2.2 Image Acquisition

During weeks 8-22, 3 mice were studied weekly. The mice were anesthetized with inhalational 2% isoflurane mixed with pure oxygen and then freshly prepared 5-ALA solution (100mg/ml in 0.9% saline, pH \approx 5.5) was instilled intravesically into the mouse bladder through a PE10 catheter tube at 0.2ml/100g body weight. The bladder was left occluded for \sim 2 hrs, then the mice were released to the cage to void for additional 2hrs for inducing peak PpIX production (i.e., 5-ALA fluorescence emission). The mice were euthanized using isoflurane. The intact bladder was harvested by a midline laparotomy incision, opened from the urethra to the dome and mounted uniformly on a custom ϕ 12mm ring holder placed in a modified PBS solution (37⁰C, pH7.4) to undergo various imaging procedures.

WLC, NBI and FC images of mouse bladders were acquired by a modified Nikon zoom microscope using a 1X APO ultraviolet objective to provide a field of view (FOV) of ϕ 11mm and a 12-bit high-sensitivity CCD camera (Retiga Exi, QImaging) interfaced with a liquid crystal tunable filter module for 8bit RGB (WLC, NBI) and 12bit monochromatic (FC) imaging. Illumination from a 100W Xe lamp was delivered through a liquid fibercord for WLC, and by inserting a narrow bandpass filter (λ =415nm, $\Delta\lambda\approx$ 15nm) to pass blue light for NBI. For FC imaging, blue light (λ_{ex} : 380-420nm) was used for fluorescence excitation to yield red PpIX fluorescence emission (λ_{em} : 620-700nm). Instantaneous 3D OCT dataset was obtained using our spectral-domain OCT engine previously reported⁷, in which a broadband source (λ =1310nm, $\Delta\lambda\approx$ 90nm; coherence length $L_c\approx$ 8.4 μ m) illuminated a fiberoptic Michelson interferometer and a green laser (λ =532nm) provided visual guidance for image registration. The sample arm

was connected to a portable OCT probe in which light exiting the optical fiber was collimated to $\phi 5\text{mm}$, steered by fast 2D servo mirrors, and then focused onto the bladder surface by an NIR objective (4X/0.1NA). The backreflected light from both sample and reference arms was recombined in the detection arm, spectrally dispersed, then focused by a lens system to be detected by a high-speed linear InGaAs array Camlink interfaced with a PC (Raid 0 configured) at 47kHz per A-scan. The spatial resolution of OCT was $\sim 10\mu\text{m}$, the system dynamic range was over 110dB, and a large 3D image volume (FOV: $5\times 5\times 2\text{mm}^3$) were acquired within $\sim 5\text{s}$. This can be further reduced to $\sim 1\text{s}$ for a smaller FOV ($5\times 1\times 2\text{mm}^3$) to minimize motion artifacts for in vivo endoscopic diagnosis.

6.2.3 Image Analysis and Diagnosis of CIS

Diagnoses of CIS were based on visual identifications of bladder surface lesions by WLI, increased tumor vasculature by NBI, and enhanced 5ALA fluorescence by FC. Quantitative diagnosis of CIS by 3D OCT was based on computer-aided detection (CAD) of enhanced urothelial heterogeneity, whose algorithms were previously reported¹⁷. Several new features were implemented to effectively improve diagnostic accuracy and reduce computation time, which included: 1) adaptive image segmentation based on mathematical morphological operation to remove artifacts resulting from bladder interfaces (e.g., specular reflection and ‘ghost’ image), 2) 3D image registration to eliminate artifacts induced by rugged bladder surface, and more importantly 3) a new target function $\psi_I(\Delta f)$ based on normalized 2D FFT polar profile $\psi(f)$ to improve the

robustness of the CAD algorithm for CIS diagnosis. Instead of previous 2nd-order derivative $\psi''(f)$, $\psi_I(\Delta f)$ by integrating $\psi(f)$ over a frequency range of $\Delta f = 0.02-0.15\text{Hz}$ (e.g., spatial variations over 30-250 μm) was used to represent the architectural heterogeneity of the urothelium, which minimized the influences of the sample DC difference ($f < 0.02\text{Hz}$) and high frequency speckle noise ($f > 0.15\text{Hz}$). Data analysis reveals that the chosen frequency of interest (Δf) represents both microscopic and macroscopic heterogeneities of the urothelium; in other words, higher $\psi_I(f)$ referred to more urothelial heterogeneity. The threshold value ($P_{\Delta f/T} > 0.45$) for quantitative 3D OCT diagnosis of CIS was derived by optimizing the receiver operating characteristic (ROC) curve based on the $\psi_I(\Delta f)$ values from preselected 10 specimens (5 SV40T mice, 5 controls) of previous experiment.

6.2.4 Statistical Analysis

The sensitivities and specificities for WLC, NBI, FC and 3D OCT diagnoses were computed from the frequency tables with the corresponding H&E stained histological evaluation serving as the gold standard. Their values were compared between each other by using chi-squares test or Fisher's exact test, with $p < 0.05$ considered statistically significant.

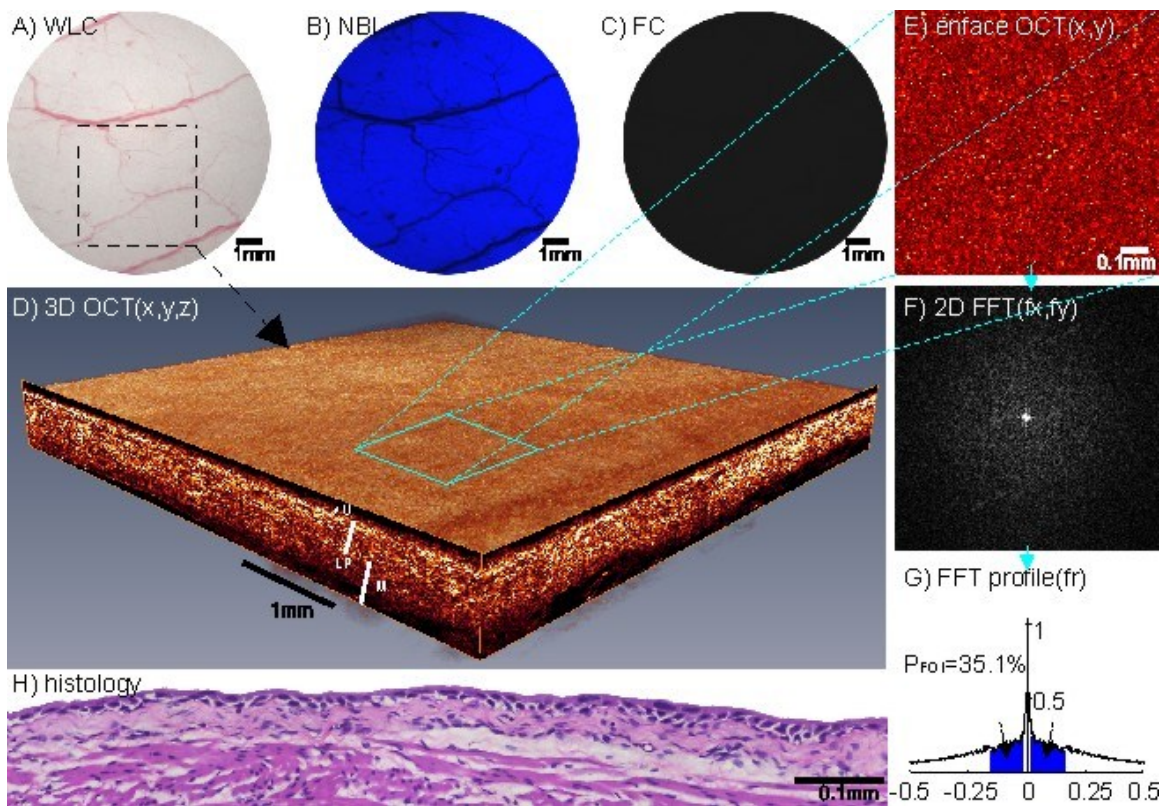


Fig. 6.1 Results of a normal mouse bladder. A) WLC image, B) NBI image, C) FC image, D) 3D OCT of the region landmarked with a dashed rectangle in A), E) 2D enface OCT_{xy} of the blue box indicated in D), F) 2D FFT of OCT_{xy} in E), G) normalized polar frequency profile $\psi_f(\Delta f)$ of F), H) the corresponding histology. CAD diagnosis: “-” for CIS ($P_{\Delta f} = 35.1\% < P_{\Delta f} = 45\%$). U: urothelium; LP: lamina propria; M: muscularis.

6.3 Results

Fig. 6.1 shows the results of a normal mouse bladder. Both WLC (6.1A) and NBI (6.1B) diagnosed it as a typical normal bladder whose surface was flat and smooth with normal vasculature; FC (6.1C) diagnosed it as normal based on undetectable fluorescence even under extended exposure (e.g., 1s). 3D OCT (6.1D) clearly delineated the morphological details of the bladder based on their backscattering differences, e.g.,

urothelium (U) as a low scattering thin layer (~30um) on top, lamina propria (LP) as a thicker, high-scattering underlying layer, and muscularis (M) as a thick layer with bifurcated collagen bundles, all of which correlated with the corresponding histology (6.1H). 3D OCT for CIS diagnosis was based on quantitative CAD of enhanced urothelial heterogeneity. The enface image (6.E) derived from 3D OCT (6.1D) over a selected ROI showed a uniform backscattering distribution of the urothelium; its 2D FFT (6.1F) and polar frequency profile $\psi_f(\Delta f)$ (6.1G) indicated a low-percentage power distribution within Δf (e.g., shaded area) with $P_{\Delta f}=35.1\%$, which was significantly lower than the pre-determined threshold value $P_{\Delta f/T}=45\%$ for CIS and was therefore diagnosed as normal or benign for CIS. This specimen was later confirmed to be normal by histology (6.1H).

Fig. 6.2 shows the results of an ‘early’ CIS. Compared with Fig.6.1, WLC (6.2A) failed to detect any specific difference and missed CIS; however, NBI (6.2B) revealed increased vasculature (e.g., increased sizes of main vessels and dense, irregular distribution of branch vessels) and thus diagnosed it as CIS. Although slightly brighter than Fig. 6.1(C), FC (6.2C) did not show obvious fluorescence increase and missed CIS. 3D OCT (6.2D) only showed minor urothelial thickening (~50um) without obvious increase in urothelial backscattering, which could not be differentiated from urothelial hyperplasia³⁹ (benign for CIS) or artifacts induced by sample preparation. On the other hand, the enface image (6.2E) showed increased urothelial heterogeneity as identified by the dark shadows, and quantitative analysis showed clear spreading of 2D FFT (6.2F) and increased power distribution $\psi_f(\Delta f)$ within Δf (6.2G) compared to normal bladder in Fig. 6.1. The increased urothelial heterogeneity led to $P_{\Delta f}=48.5\%$ over $P_{\Delta f/T}= 45\%$ and was

thus diagnosed as CIS, which was later confirmed by histology (6.2H). Of note, it was found that WLI, FC and 2D OCT failed to identify almost all of the CIS cases at this early stage.

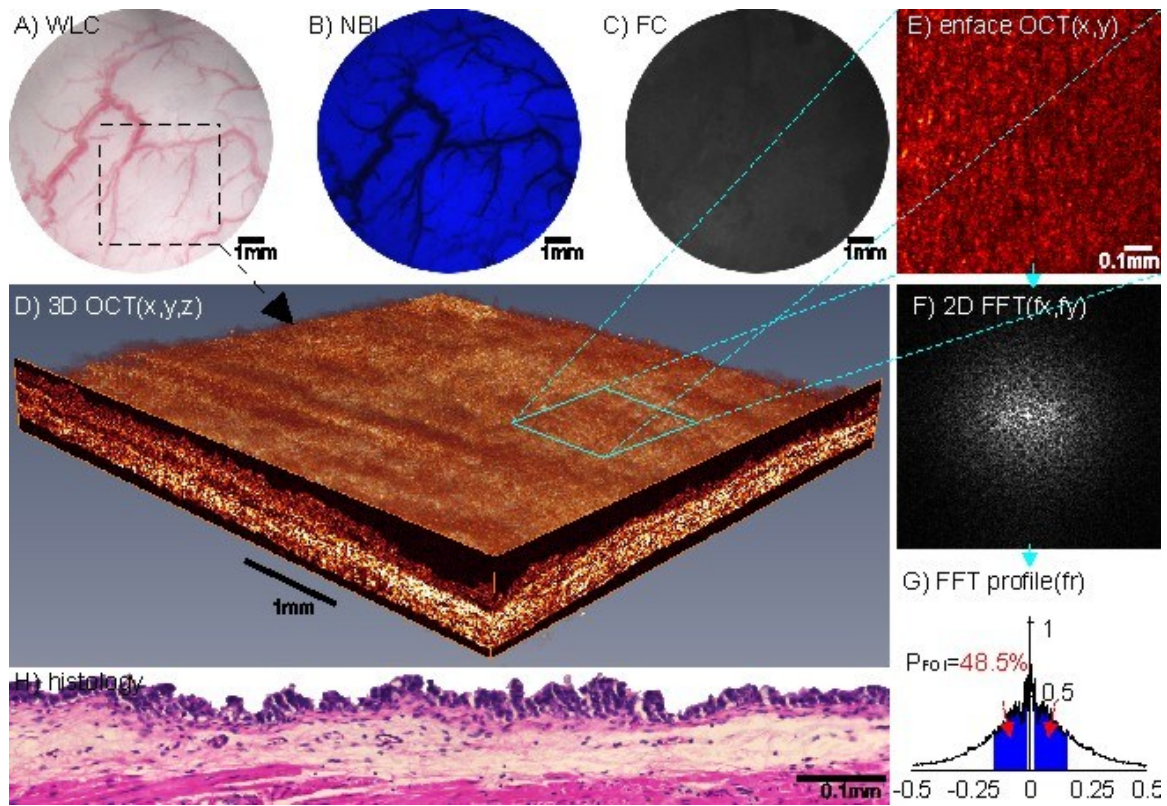


Fig. 6.2 Results of an early CIS. A) WLC image, B) NBI image, C) FC image, D) 3D OCT of the region landmarked with a dashed rectangle in A), E) 2D enface OCT_{xy} of the blue box indicated in D), F) 2D FFT of OCT_{xy} in E), G) normalized polar frequency profile $\psi_1(\Delta f)$ of F), H) the corresponding histology. CAD diagnosis: “+” for CIS ($P_{\Delta f}=48.5\% > P_{\Delta f/T}=45\%$).

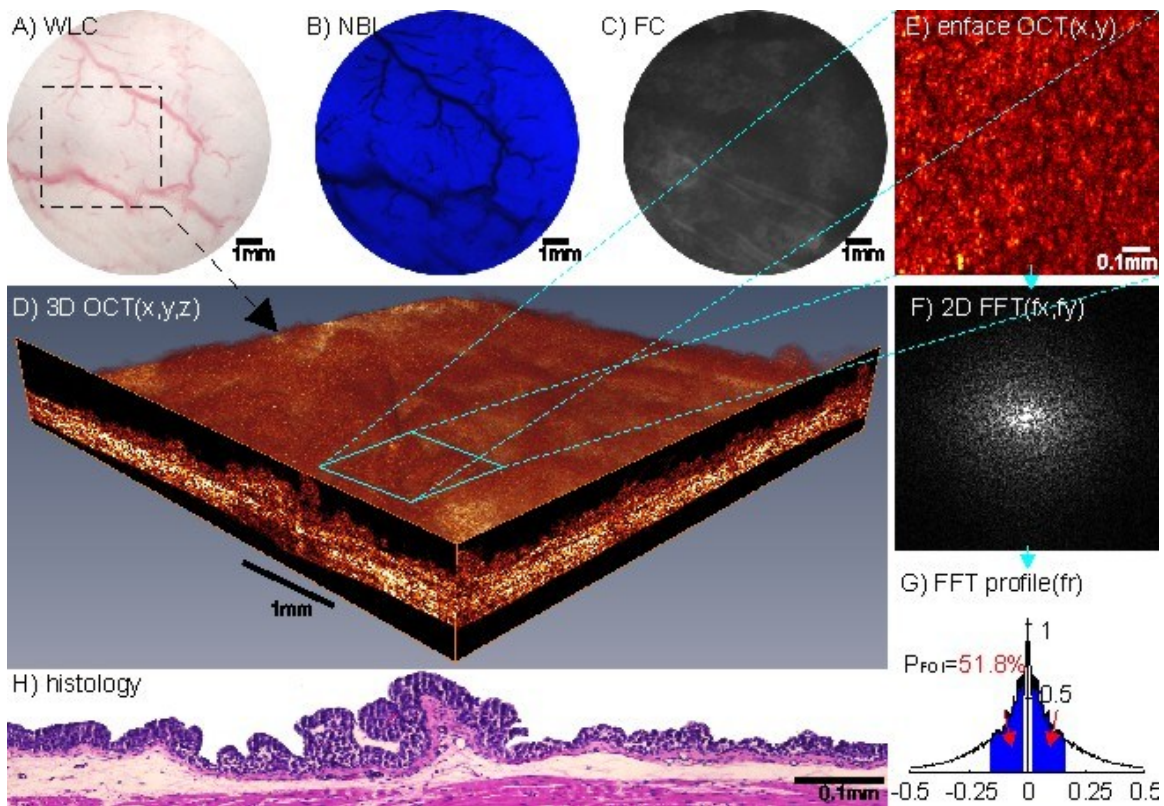


Fig. 6.3 Results of a more advanced CIS. A) WLC image, B) NBI image, C) FC image, D) 3D OCT of the region landmarked with a dashed rectangle in A), E) 2D enface OCT_{xy} of the blue box indicated in D), F) 2D FFT of OCT_{xy} in E), G) normalized polar frequency profile $\psi_f(\Delta f)$ of F), H) the corresponding histology. CAD diagnosis: “+” for CIS ($P_{\Delta f}=51.8\% > P_{\Delta f/T}=45\%$).

Fig. 6.3 shows the results of a more advanced CIS specimen with increased mucosal thickness and early signs of the development of papillary architecture. Again, WLC (6.3A) did not provide any specific diagnosis and missed the lesion; NBI (6.3B) showed a similar pattern of increased vasculature to Fig. 6.2(B) and diagnosed it as CIS. Interestingly, FC (6.3C) was able to detect some areas on the bladder with increased fluorescence over the dark background and diagnosed it as CIS. 3D OCT (6.3D) revealed slightly more urothelial thickening ($\sim 100\mu m$) and rugged surface; similar to Fig. 6.2, the

identification was unspecific for CIS diagnosis. On the other hand, the enface image (6.3E) showed a higher degree of urothelial heterogeneity. Quantitative analyses of spreading of 2D FFT (6.3F) and more concentrated power distribution $\psi_I(\Delta f)$ than Fig. 6.2(G). The calculated $\psi_I(\Delta f)$ was further increased to $P_{\Delta f}=51.8\% > P_{\Delta f/T}=45\%$ and was thus diagnosed as CIS. Histology (6.3H) later confirmed it a more advanced CIS.

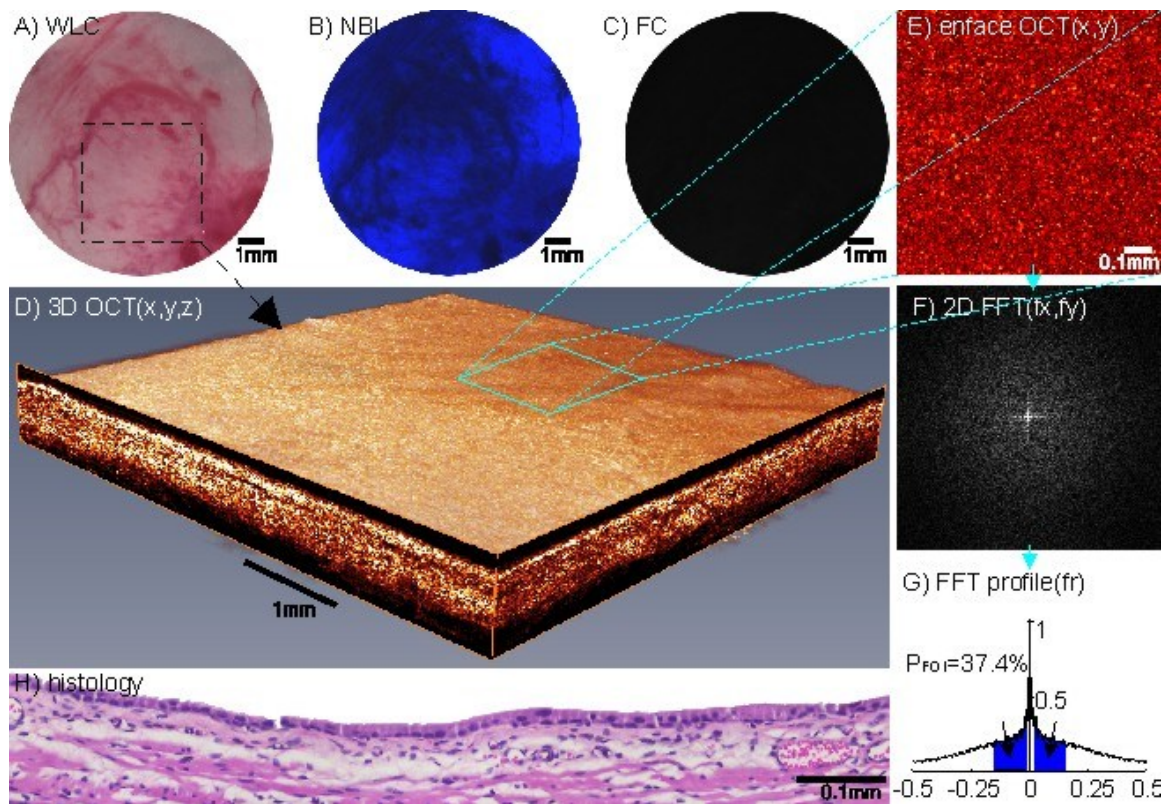


Fig. 6.4 Results of a minor traumatic bladder. A) WLC image, B) NBI image, C) FC image, D) 3D OCT of the region landmarked with a dashed rectangle in A), E) 2D enface OCT_{xy} of the blue box indicated in D), F) 2D FFT of OCT_{xy} in E), G) normalized polar frequency profile $\psi_I(\Delta f)$ of F), H) the corresponding histology. CAD diagnosis: “-” for CIS ($P_{\Delta f}=37.4\% < P_{\Delta f/T}=45\%$), NBI diagnosis: “+” for CIS.

Fig. 6.4 shows the results of a minor traumatic injury to the bladder that was induced by prior catheterization for 5ALA induction, which was later confirmed normal or negative for CIS by histology (6.4H). WLC (6.4A) showed the reddish bladder mucosa and diagnosed it as CIS. NBI (6.4B) showed high-density, diffusive or disorganized vascular patterns and misinterpreted it as CIS. FC (6.4C) showed no detectable fluorescence and diagnosed it as normal or benign for CIS. 3D OCT (6.4D), on the other hand, revealed it as a typical normal-appearing bladder like the one shown in Fig. 6.1. Quantitative CAD analyses of 2D FFT (6.4F) and FFT profile (6.4G) indicated that the urothelial heterogeneity $P_{\Delta f}=37.4\%$ was far below $P_{\Delta fT}=45\%$ and thus diagnosed it as normal or benign for CIS.

Table 6.1 Diagnostic sensitivities, specificities, PPV and NPV

| Methods Results | 3D OCT | | WLC | | NBI | | FC | | p-values | | | | | |
|--------------------|--------|------|-------|------|-------|------|-------|------|----------|-------|-------|---------|-------|-------|
| | n/N | % | n/N | % | n/N | % | n/N | % | O: W | O: N | O:F | W: N | W:F | N:F |
| Sensitivity | 27/29 | 93.1 | 1/29 | 3.4 | 26/29 | 89.7 | 13/29 | 44.8 | 0.001 | 1.000 | 0.001 | 0.001 | 0.001 | 0.001 |
| Specificity | 17/18 | 94.4 | 14/18 | 77.8 | 5/18 | 27.8 | 18/18 | 100 | 0.338 | 0.001 | 1.000 | 0.003 | 0.104 | 0.001 |
| PPV | 27/28 | 96.4 | 1/5 | 20.0 | 26/39 | 66.7 | 13/13 | 100 | 0.001 | 0.003 | 1.000 | 0.065 | 0.002 | 0.023 |
| NPV | 17/19 | 89.5 | 14/42 | 33.3 | 5/8 | 62.5 | 18/34 | 52.9 | 0.001 | 0.136 | 0.007 | 0.232 | 0.085 | 0.709 |

* OCT: optical coherence tomography; WLC: white light cystoscopy; NBI: narrow band imaging; FC: fluorescence cystoscopy; N: total number, PPV, positive predictive value, NPV, negative predictive value.

A total of 47 mice (i.e., 29 SV40T mixed with 18 Balb/c) were enrolled in the study, including 29 with CIS and 18 with normal or benign lesions of the bladder mucosa. Among 29 CIS samples, 27 were detected “+” by 3D OCT, 1 by WLC, 26 by NBI, and 13 by FC. For all 18 histologically confirmed normal or benign samples, 17 were detected “-” by 3D OCT, 14 by WLC, 5 by NBI, and 18 by FC. The detailed statistical analysis calculated on a per sample basis was summarized in Tab. 6.1. The results indicated that both WLC and FC failed to detect early CIS lesions ($SN_{WLC}=3.4\%$, $SN_{FC}=44.8\%$); NBI provided sufficient sensitivity to identify CIS ($SN_{NBI}=89.7\%$), but its diagnostic specificity was poor ($SP_{NBI}=27.8\%$). In contrast, 3D OCT with quantitative CAD significantly enhanced the diagnosis of CIS to $SN_{OCT}=93.1\%$ and $SP_{OCT}=94.4\%$ ($p^*<0.001$).

6.4 Discussions

Noninvasive early detection of CIS remains a clinical challenge. White light cystoscopy (following urine cytology) is the current clinical standard, it may miss 30%~60% of CIS.⁴⁷ Recent advances in optical imaging (e.g., NBI, FC, OCT) have shown great promise for enhancing early diagnosis of NMI TCC.⁵² Since these techniques are based on different principles, their advantages and potential drawbacks are not yet fully investigated. Based on SV40T transgenic CIS rodent model, we conducted a comparative study to probe into each imaging modality to examine their utilities and potential limitations for future clinical applications.

WLC, via direction visualization of bladder surface, has been proven effective for identifying papillary TCC; meanwhile, it may miss CIS and often relies on random biopsy for a conclusive diagnosis. NBI enhances the image of subsurface vasculature by taking advantage of strong hemoglobin absorption to narrow-band blue light, based on the premise that bladder tumor demands more nutrition supply from blood circulation, resulting in enhanced angiogenesis and denser microvascular environment than the surrounding normal bladder. Additionally, because of its random growth, the vascular patterns tend to be more irregular. Therefore, by identifying these features, NBI was able to provide an impressive high sensitivity (SN=89.7%) in the detection of CIS. However, such vascular changes can be induced by other bladder disorders or disruptions such as trauma, inflammatory response, and cystitis. As shown in the results part, Fig. 6.4 exemplifies the limitations of NBI for differentiating CIS from benign lesions of the bladder mucosa that led to a low specificity (SP=27.8%).

FC diagnosis of CIS is based on detection of PpIX fluorescence of porphyrin preferably accumulated in tumor tissue under blue light excitation. Previous clinical studies showed that FC provided a high sensitivity for the diagnosis of bladder cancer (including CIS) but compromised specificity. However, the results in this animal study revealed a low sensitivity vs. a high specificity. This difference was likely associated with the animal model. Although this type of CIS closely mimicked human CIS, the imaging study was conducted at a very early stage of carcinogenesis which was very difficult to detect by current modalities. The low sensitivity of FC was likely resulting

from the thin mouse urothelium compared to rat or human counterpart so that the PpIX emission from such thin urothelium was too weak to detect. It was found that 5ALA fluorescence could be detected in many SV40T specimens over the noise background if overexposed (e.g., 30s), suggesting the reported FC sensitivity could be underestimated with respect to human CIS diagnosis.

OCT is capable of delineating morphological details of bladder (e.g., U, LP and MS) based on their backscattering differences. Our *in vivo* human studies revealed that detection of increased urothelial heterogeneity provided more accurate diagnosis of bladder cancer than the urothelial backscattering (μ_b) change itself. For CIS, our recent animal study showed that the despeckled 2D enface urothelial image derived from 3D OCT provided a close correlation between urothelial μ_b heterogeneity and the subtle pathological variations induced by TCC. The new CAD target function $\psi_f(\Delta f)$ for quantitative image analysis and differentiation overcame the limitations for our previous models (e.g., reducing sample to sample difference, minimizing computation time). Results of this preclinical study based on 47 animals (e.g., SN=93.1%, SP=94.4%) clearly demonstrate the utility of our new method to significantly enhance current methods (WLI, NBI, FC and 2D OCT) in early diagnosis of CIS.

While SV-40T transgenic mouse model provides an excellent controllable animal platform which allows us to examine the utility of these imaging techniques to detect the morphological, vascular and biochemical changes at different phases of carcinogenesis, the CIS lesions are likely to develop in a diffuse fashion (i.e., spreading all over the bladder surface) rather than focally as commonly seen in a clinical setting. In other

words, due to its relatively small field of view (e.g., <5mm laterally), the reported high diagnostic sensitivity of 3D OCT might be affected in clinical practice because deliberate scan across human bladder wall (i.e., bladder mapping) is often not practical due to the extensive time needed unless image-guided OCT is implemented to effectively locate suspicious lesions. Clinical studies have showed the efficacy of FC to enhance the sensitivity for detection of TCC; however, its diagnostic specificity needs further improvement and the procedure involves intravesical induction of fluorescence dye, which might add risk of side effects, discomfort and additional time to the patient, and cost. To the contrary, NBI has also been shown to provide sufficient sensitivity for detection of TCC despite its poor diagnostic specificity. Importantly, this technique detects TCC based on enhanced vasculature in tumors, so it circumvents the need for dye loading and the associated complications. The results of our animal study suggest the promise of NBI-guided endoscopic OCT, which combines the merits of these two modalities, i.e., high sensitivity and large FOV of NBI to efficaciously guide 3D OCT for quantitative, effective and accurate diagnosis of CIS.

6.5 Conclusions

We compared the efficacies and potential limitations of WLC, NBI, FC and 3D OCT for early detection of CIS of the bladder. The bladders of control and SV40T transgenic mice (blinded) were sequentially imaged by these image modalities and their diagnoses were later validated by their histological evaluations. The results indicated that

quantitative 3D OCT with newly improved CAD significantly enhanced the sensitivities of WLC (3.4%) and FC (44.8%) to 93.1% ($p < 0.01$) and the specificity of NBI (27.8%) to 94.4% ($p < 0.01$) for early diagnosis of CIS. The results of this study demonstrate the potential of NBI-guided cystoscopic OCT to effectively enhance the efficacy and efficiency of current cystoscopic procedure in the diagnosis of TCC and CIS, in particular. However, it is noteworthy that more work needs to be done to deal with potential complications for in vivo clinical diagnosis such as motion artifacts in 3D cystoscopic OCT and the limited time for scanning across the large surface area of human bladder, specifically for outpatient diagnosis of CIS where effective image guidance for 3D OCT is crucial.

Chapter 7 High-Resolution 3D OCT for Imaging Diagnosis of Human Fetal Membrane

7.1 Introduction

Preeclampsia is a medical disorder associated with increased blood pressure and proteinuria during pregnancy or postpartum period⁶⁴. It persists as a major cause of maternal and fetal mortality and morbidity in the US and worldwide, affecting 5%~8% of all pregnancies⁶⁵. Preeclampsia may progress to eclampsia which is potentially a fatal medical condition, thus rendering it crucial for clinical management⁶⁶. Current diagnosis of preeclampsia mainly relies on clinical observation of the symptoms and other unspecific tests⁶⁷ (e.g., over 140/90 blood pressure or 300mg protein in urine). However, these methods become effective only when preeclampsia develops to advanced stages. At that moment, the only treatment option is abortion or early delivery, which may lead to various medical complications to both preterm newborn and the pregnant woman. Preeclampsia is a complicated syndrome that may exhibit different symptoms and no definite causative factors are found to be responsible for the disease.⁶⁸ Therefore, studies on specific features that have significant correlations with preeclampsia would be of great interest for providing an earlier, more accurate and objective clinical diagnosis.

A recent study on fetal membranes (FMs) revealed that microscopic chorionic pseudocysts (MCP) arising in the chorion leave of the FMs were found to be strongly associated with preeclampsia ($p \leq 0.001$)^{69, 70}. Although the results were based on an ex vivo FM specimen study and artifacts induced by pathological preparation (e.g., formalin fixation) could potentially be misinterpreted as MCP due to their similar appearances, the interesting finding that correlates MCP with preeclampsia may provide a new perspective in clinical prediction of preeclampsia. In this respect, an endoscopic imaging technique that enables instantaneous, noninvasive or minimally invasive ‘optical biopsy’ would be of high clinical relevance in the diagnosis of pathological conditions of pregnancy such as preeclampsia.

Among several emerging biomedical imaging techniques, optical coherence tomography (OCT) has shown great promise for noninvasive or minimally invasive ‘optical biopsy’ of various subsurface tissue owing to its high resolution (e.g., 1-12 μ m), intermediate imaging depth (e.g., 1-3mm) and high detection sensitivity (e.g., over 100dB dynamic range). Recent technological advances in OCT have enabled real-time 2D and 3D imaging, Doppler OCT for functional subsurface blood flow imaging, ultrahigh-resolution OCT for subcellular imaging, and endoscopic OCT for noninvasive imaging of various internal organs^{7, 55}. Meanwhile, preclinical and clinical studies have demonstrated the utility of OCT in delineating morphological details of biological tissues (e.g., skin, oral cavity, esophagus, colon, bladder, and cervix)^{7, 71, 72} and thus the potential for detecting cancers in these organs. While our recent human study showed the clinical feasibility of our endoscopic OCT to significantly enhance early bladder cancer

diagnosis,⁷ in this Chapter, we present a pilot feasibility study on fresh human fetal membrane specimens from normal controls and from patients with MCP to explore the potential of OCT for early detection of pathological changes, which might serve in the prediction of preeclampsia or other diseases of pregnancy. We compare the image results of OCT and high-frequency ultrasound (HFUS) with the corresponding histological counterparts (clinical standard), so that the utility and potential limitations of OCT for high-resolution delineation of the morphology of human FMs and identification of pathological changes can be examined.

7.2 Materials and Methods

7.2.1 Sample Preparation

3D OCT imaging examination was performed on 60 human FM specimens. These specimens were acquired from 10 different subjects undergoing term cesarean delivery. For each subject, 6 samples were obtained from different sectors of the FMs, e.g., 4 from the posterior and anterior uterine wall and 2 near the cervix. The fresh human specimens were preserved in 0.9% saline, rinsed, stretched uniformly to the thickness closely mimicking the anatomic architecture of FMs *in vivo*, and then mounted on a custom ϕ 20mm ring holder placed in a modified Ringer's buffer solution (37⁰C, pH7.4) to undergo *ex vivo* imaging evaluations. All of the human specimen studies were approved

by the Stony Brook University Institutional Review Board and with patients' prior informed consents.

7.2.2 3D OCT

Fig. 7.1 depicts the schematic of the spectral-domain OCT (SDOCT) used to acquire all of the 3D images of the fetal membrane specimens in this study. The 3D OCT engine was upgraded from a high-speed 2D SDOCT setup previously reported⁷, in which a pigtailed broadband laser at central wavelength of $\lambda=1310\text{nm}$ and with a spectral bandwidth of $\Delta\lambda=90\text{nm}$ (i.e., coherence length $L_c\approx 8.5\mu\text{m}$) was used to illuminate a fiberoptic Michelson interferometer. Green light from a laser diode ($\lambda=532\text{nm}$) was coupled into the fiberoptic system for visual guidance of OCT scans. In the reference arm, a prism pair

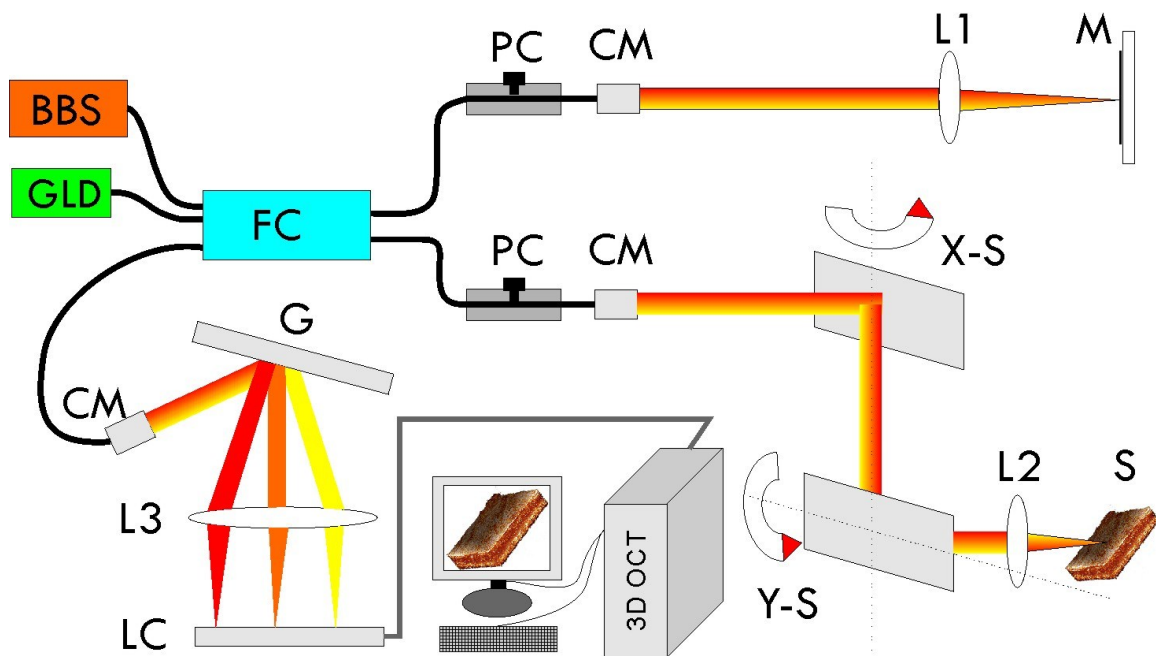


Fig. 7.1 A sketch of the 3D OCT setup. BBS: broadband source; GLD: green diode laser; FC: fiberoptic coupler; PC: polarization controller; CM: collimator; M: mirror; G: grating; LC: linear InGaAs camera; S: specimen (fetal membrane); X-S, Y-S: X, Y axes of the 2D servo scanner; L1-L3: lenses.

(e.g., using adjustable BK7 and fused silica wedge prisms) were used for dispersion compensation and a stationary retroreflective mirror was used to match the pathlength with the sample arm. The sample arm was connected to a handheld stereoscope in which light exiting the monomode fiber was collimated, scanned laterally by 2D servo mirrors (x-y scanners), and then focused by a NIR objective lens (f40mm/NA0.12) onto the surface of the FM specimen under examination. Light from both reference and sample arms was recombined in the detection fiber and connected to a spectrometer in which the spectral interferograph was detected by a line InGaAs camera (1024×1 pixels, up to 47 kHz line rate) and interfaced via Camlink with a workstation for 2D and 3D image acquisition and reconstruction. Recent system development in detection optics and image acquisition and control resulted in enhanced axial and lateral resolutions ($\sim 9\mu\text{m}$), large field of view (FOV: $5\times 5\times 2.5\text{mm}^3$) at high dynamic range ($>110\text{dB}$) and fast frame rate (8-47fps).

7.2.3 Imaging Examination

With the FMs properly stretched and the maternal side facing upwards to mimic in vivo endoscopic imaging diagnosis, a number of 2D OCT pre-scans across the entire specimen were performed first to quickly locate the regions of interest (ROI). For each

ROI, sequential OCT scans were performed within 60s to acquire a 3D OCT image over a cubic volume of $5 \times 5 \times 2.5 \text{mm}^3$ and displayed in pseudo color to enhance visualization. By visual guidance with a green laser, the enface FOV for each 3D OCT image was landmarked to align the subsequent scans for 3D HFUS imaging⁴⁵, which was acquired for some thickened specimens with advanced preeclampsia. 3D HFUS scans were performed using a miniature 40MHz probe with an axial resolution of $\sim 40 \mu\text{m}$ (Vevo 770, Visualsonics Inc., Toronto, Canada). OCT delineates the morphological details (e.g., layers) of human FMs according to their backscattering differences. For simplicity, tissue backscattering was expressed by back reflectance, defined as the measured OCT intensity normalized to that of the top layer (i.e., decidua vera). Quantitative computer segmentation of FMs in both 2D and 3D OCT images was performed based on intensity gradient by adapting the algorithm previously reported¹⁷, and the average thickness (d) and back reflectance (r) of each layer were then analyzed. After the imaging study, the specimens were preserved in 10% formalin fixative together with the ring holders to avoid artifacts such as tissue deformation for H&E stained histological examination. A double blind histologic evaluation was independently performed by a clinical pathologist later to compare with the prior OCT and HFUS identifications and diagnoses.

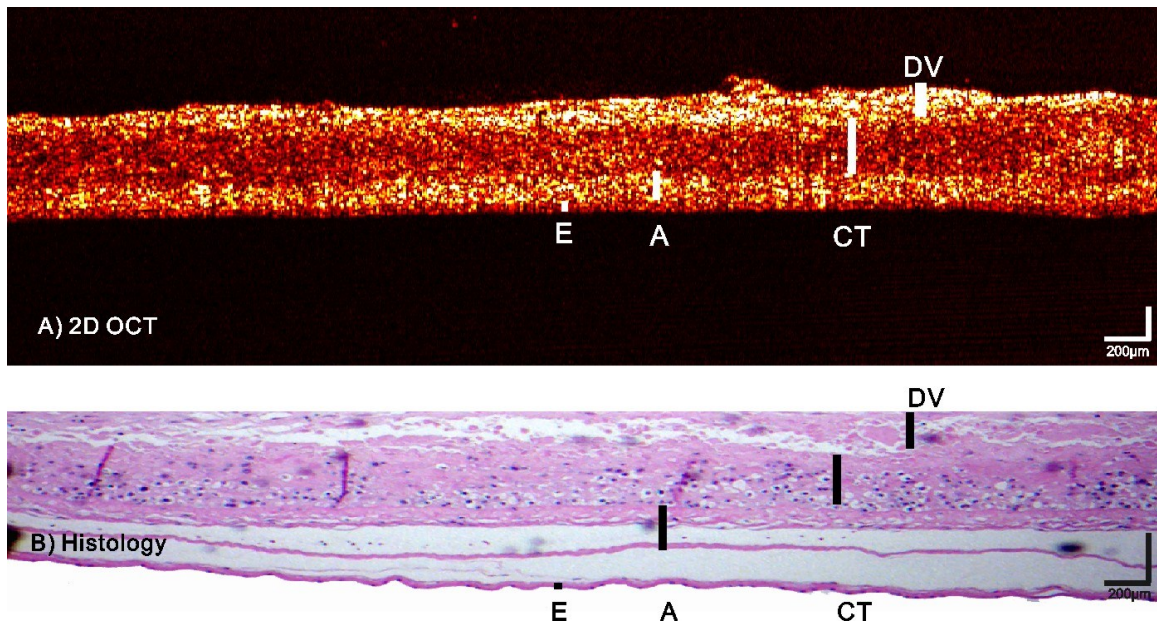


Fig. 7.2 2D images of a normal human fetal membrane. A): cross-sectional OCT image; B): corresponding H&E stained histology. DV: decidua vera ($d_{DV} \approx 70 \mu\text{m}$), CT: chorion and trophoblast ($d_{CT} \approx 187 \mu\text{m}$), A: subepithelial amnion ($d_A \approx 70 \mu\text{m}$), and E: epithelium ($d_E \approx 35 \mu\text{m}$).

7.3 Results

Previous studies have demonstrated the utility of OCT to enable high-resolution delineation of the morphological features of biological tissues (e.g., urinary bladder) based on their backscattering differences that attribute to the structural properties. Fig. 7.2 exemplifies a typical cross-sectional 2D OCT image (A) of a normal FM acquired from the maternal side and the corresponding H&E stained histological evaluation (B). OCT was able to identify the four layers of the FMs according to their backscattering differences. For instance, the outermost layer, decidua vera (DV) was relatively thin ($d_{DV} \approx 92 \pm 38 \mu\text{m}$), heterogenous and high scattering. The underlying chorion and

trophoblast (CT) layer was thick ($d_{CT} \approx 150 \pm 67 \mu\text{m}$) and relatively low scattering ($r_{CT/DV} = 0.51 \pm 0.17$) possibly due to its loose structure and high interstitial fluid content. The subepithelial amnion (A) layer was slightly thinner ($d_A \approx 95 \pm 36 \mu\text{m}$) than the CT layer and was high scattering ($r_{A/DV} = 0.84 \pm 0.45$) resulting from subepithelial connective tissue. The innermost epithelium (E) was very thin ($d_E \approx 29 \pm 8 \mu\text{m}$ or less, with 1~2 cell depths), uniform and low scattering ($r_{E/DV} = 0.44 \pm 0.20$). It must be noted that the thickness of FMs, in particular the thickness of intermediate amnion (A) and chorion (CT) layers might vary with the trimester of pregnancy, the extent of tissue stretching, and the location of OCT scans. Overall, the OCT identifications of the four layers within the FMs correlated well with the counterparts in the corresponding histological image (B) except detachment of amnion in some specimens, which is a common artifact induced by tissue fixation during histological processing.

In addition to 2D OCT presented in Fig. 7.2, 3D OCT image, e.g., by rendering 350 slices of sequential 2D cross-sectional OCT images, may provide improved image fidelity and more affirmative identifications of morphological features. For example, Fig. 7.3 summarizes the results of normal human FMs in which panel (E) shows a pie-cut graph of 3D OCT image and panel (F) illustrates a 2D OCT slice with the four layers of the FMs automatically segmented based on their backscattering differences. Panels (A-D) show the 3D images of the segmented 4 layers sequentially from DV and CT to A and E layers. Compared with 2D OCT in Fig. 7.2, 3D OCT in Fig. 7.3, owing to its improved spatial correlation (along y-axis), provides enhanced image quality, which may enable

more detailed quantitative analysis (e.g., backscattering μ_b and standard deviation σ) to characterize the architectural features of individual layers.

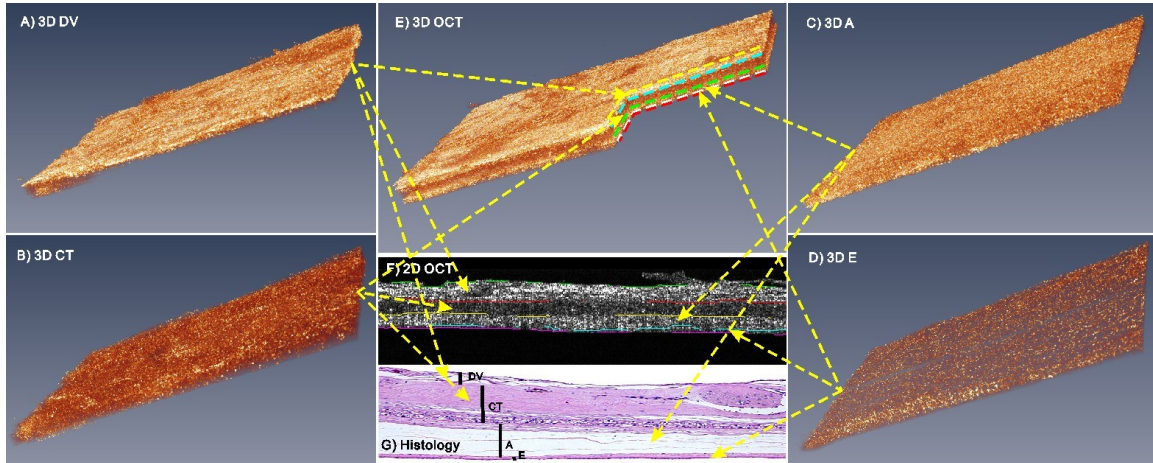


Fig. 7.3 3D image of a normal human FM. A)-D): 3D OCT images of the segmented DV, CT, A, and E layers; E): 3D OCT image of the entire human FMs; F): 2D OCT image to illustrate the automatic segmentation procedure based on the backscattering differences of each layer; G): corresponding H&E histology of OCT image in F).

In this pilot human specimen study, not only normal human FMs but also potential pathological human FM specimens were examined to evaluate the utility of OCT for noninvasive and high-resolution imaging diagnosis of FM diseases (e.g., MCP). Fig. 7.4 shows 2D OCT image (A) of a FM sample with MCP which was characterized by dark holes (low backrefection) with thickness of $d_{MCP} \approx 320\mu\text{m}$ between A and CT layers. The low-scattering characteristics of MCP (dark holes with $r_{MCP/DV} = 0.17 \pm 0.06$) were caused by fluid buildup (i.e., edema) within the lesions. Fig. 6.4(B) represents the corresponding H&E histology which correlated well with the OCT identifications of the 4 layers and the cysts (MCP) within the CT and A layers except that the lesions ($d_{MCP} \approx 400\mu\text{m}$) appeared larger than those ($d_{MCP} \approx 320\mu\text{m}$) in OCT image (A). This

discrepancy was likely resulted from the artifacts induced by tissue fixation and histological processing.

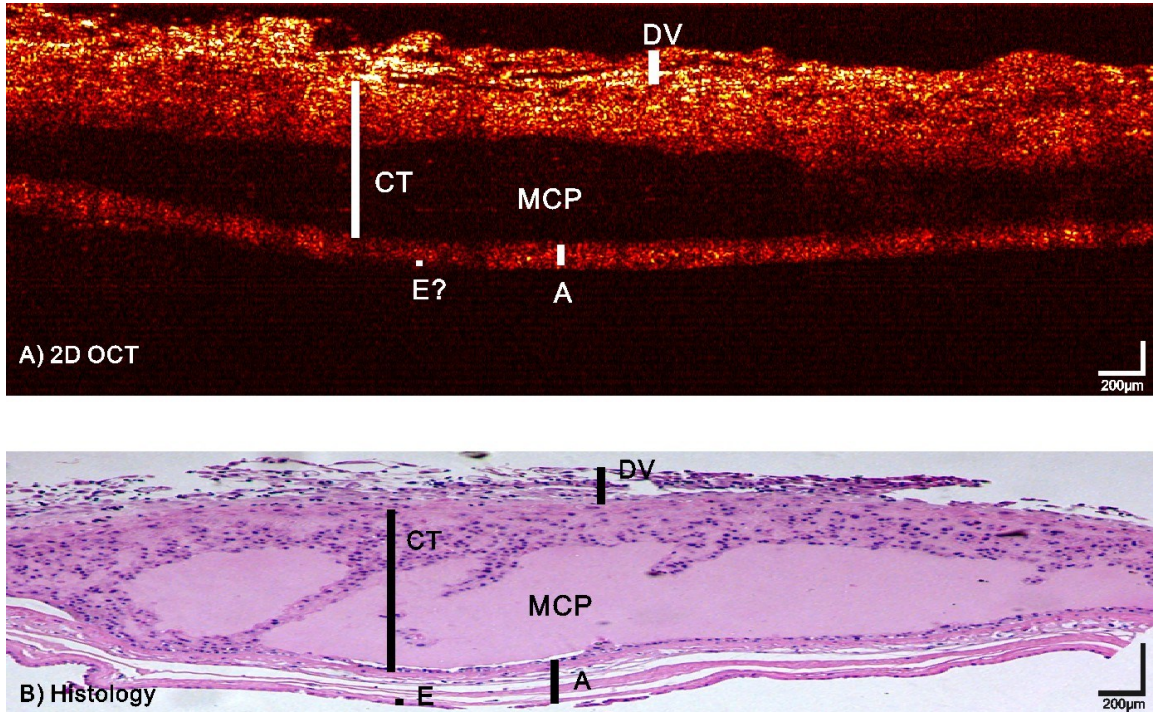


Fig. 7.4 2D image of a human FM specimen with MCP. A): 2D OCT image; B): corresponding H&E histology. The MCP lesions characterized by OCT as dark holes correlated with the cysts in histology. The thickness of MCP lesions in OCT ($d_{MCP} \approx 320 \mu m$) matched the histological counterpart ($d_{MCP} \approx 400 \mu m$).

Similarly, Fig. 7.5 shows the results of 3D OCT of a human FM specimen with ‘early stage’ MCP progression. Despite the fact that the surface image appeared normal, the segmented 3D OCT images revealed early, minor detachment ($d_{MCP} \approx 80 \mu m$, $r_{MCP/DV} = 0.14$) within the CT and A layers, resulting in drastically increased inhomogeneity within the CT layer (panel C). Interestingly, the innermost epithelial layer (panel A) also became less uniform than the normal counterpart in Fig. 7.3(a), which could be associated with the inflammatory reactions of MCP. By detecting the size

progression of MCP lesions, OCT was potentially capable of providing noninvasive evaluation (i.e., ‘staging’) of MCP development and severity, in particular by 3D image segmentation to provide quantitative assessments of cyst depth (e.g., $d_{MCP} \approx 80 \mu\text{m}$ in Fig. 7.5, $d_{MCP} \approx 320 \mu\text{m}$ in Fig. 7.4) and the resultant inhomogeneity which was associated with fluid buildup, vasodilation, local micro hemorrhage, macrophage and mast cell accumulations. It should be noted that although the corresponding histological image in Fig. 7.5(G) correlated favorably with the OCT delineations, the artifacts induced by tissue fixation complicated the identification of MCP (cysts) from distortion (fall off) of CT and A layers, which might compromise the utility of histology for affirmative staging of MCP growth and spreading.

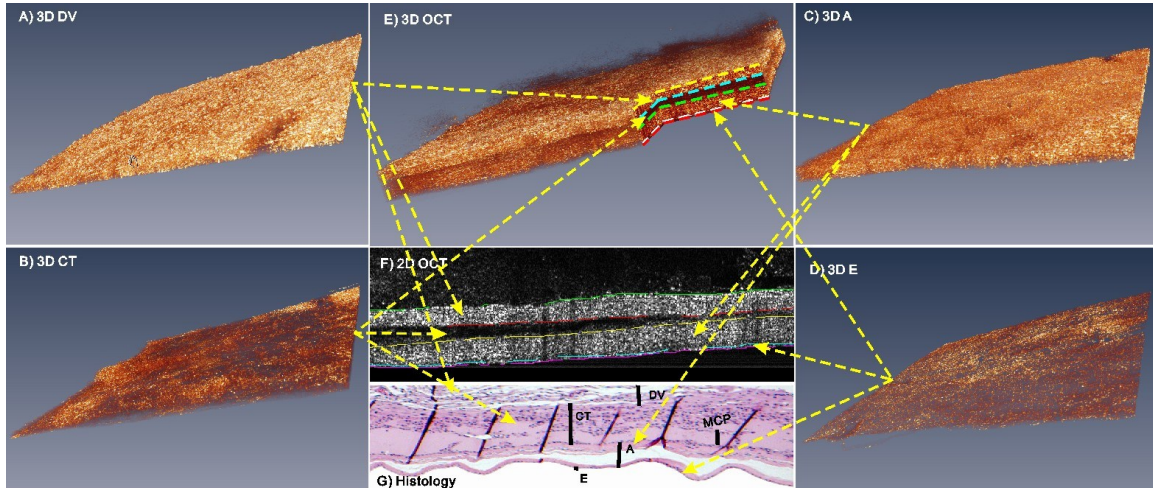


Fig. 7.5 3D OCT image of a human FM with MCP. A)-D): 3D OCT images of the segmented DV, CT, A, and E layers. E): 3D OCT image of the intact human FMs with MCP; F) segmented 2D OCT image to illustrate automatic segmentation based on their backscattering differences; G) corresponding histology of the OCT image in F). The CT and E layers were more heterogeneous than the previous normal specimen in Fig. 6.3.

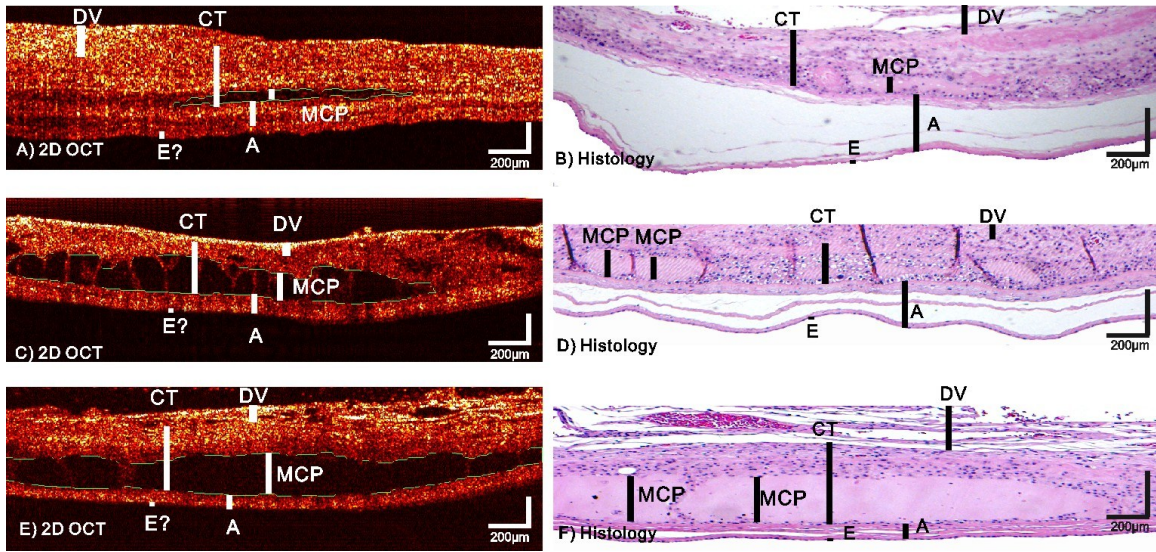


Fig. 7.6 OCT images of human FM specimens with different-size MCP lesions compared with the corresponding H&E stained histological images. A), C), E): 2D OCT images with the MCPs automatically segmented as landmarked by green dashed circles. The thicknesses of MCPs were $d_{\text{MCP}} \approx 60 \mu\text{m}$ (A), $d_{\text{MCP}} \approx 150 \mu\text{m}$ (C) and $d_{\text{MCP}} \approx 265 \mu\text{m}$ (E), respectively. The percentage areas of MCP, i.e., the ratios of the area of MCPs against the entire FM cross-section were 3.7% (A), 25.6% (C), and 28.3% (E). B), D), F): the corresponding histological images. The thicknesses of MCPs were $d_{\text{MCP}} \approx 53 \mu\text{m}$ (B), $d_{\text{MCP}} \approx 141 \mu\text{m}$ (D), and $d_{\text{MCP}} \approx 251 \mu\text{m}$ (F), which correlated with the OCT measurements despite artifacts such as tissue detachment induced by histological process.

Fig. 7.6 compares three human SM specimens to show the capability of OCT to assess the growth of MCP lesions. Although the thickness of MCP (d_{MCP}) may vary with the point of measurement, the increase of MCP lesions could be differentiated by their mean thickness. OCT measurement of $d_{\text{MCP}} \approx 60 \mu\text{m}$, $r_{\text{MCP/DV}} = 0.13$ for the small MCP lesion in panel (A) correlated with the histological evaluation $d_{\text{MCP}} \approx 53 \mu\text{m}$ in panel (B); the two large lesions $d_{\text{MCP}} \approx 150 \mu\text{m}$, $r_{\text{MCP/DV}} = 0.18$ (panel C) and $d_{\text{MCP}} \approx 265 \mu\text{m}$, $r_{\text{MCP/DV}} = 0.19$ (panel E) measured by OCT (C) were correlated favorably with the corresponding histological measures, $d_{\text{MCP}} \approx 141 \mu\text{m}$ in panel (D) and $d_{\text{MCP}} \approx 251 \mu\text{m}$ in panel (F), respectively. Alternatively, the percentage area of MCP lesion, i.e.,

$\Delta S_{MCP}(\%) = S_{MCP}/S_{FM}$ (S_{MCP} and S_{FM} are the cross-sectional areas of the PCM lesions and FMs) can be employed; the results of OCT measures were 3.7%, 25.6% and 28.3% for panels (A, C, E), respectively. In addition, we calculated the statistical result of the average thickness of MCP based on 32 lesions. The result showed that the MCP detectable by OCT varied from $d_{MCP}=24\mu\text{m}$ to $d_{MCP}=615\mu\text{m}$ with a mean thickness of $160\mu\text{m}$ and a median thickness of $120\mu\text{m}$. These results suggest that endoscopic OCT could potentially be deployed to instantaneously diagnose MCPs and quantitatively evaluate (i.e., ‘stage’) their progress as well as the treatment effects. It is noteworthy from the histological images in panels (B, D, F) that distortion and other artifacts (e.g., formalin infiltration) might compromise the evaluation of histological specimens.

The limited imaging depth of OCT (e.g., $\sim 1\text{-}3\text{mm}$) may potentially restrict its utility to the diagnosis and assessment of later-stage severe MCP lesions. For instance, for a few FM specimens (e.g., different locations on the FMs) with a thick DV layer (e.g., $2\text{-}4\text{mm}$) from the maternal side, OCT was unable to fully delineate the layered structures of the FMs, in particular, the innermost epithelium (E). In cases like this, high-frequency ultrasound (HFUS) might compliment OCT to overcome the imaging-depth limitation. To examine the feasibility, additional 3D HFUS scans following OCT imaging were performed using a miniature 40MHz probe. Fig. 7.7 exemplifies a 3D HFUS image of human FMs. The results show that because of lower resolution than OCT, the boundaries between the layers (e.g., DV, CT and A) in HFUS images (panels A, B) were not as well defined than the counterparts in Figs. 7.2-7.5 and were unable to resolve the innermost epithelial layer (e.g., $d_E < 30\ \mu\text{m}$). Nevertheless, the increased imaging depth of HFUS

allowed it to visualize the full-thickness architecture of the thickened FMs. Interestingly, despite drastically reduced image contrast, HFUS was still able to detect the embedded intermediate-size MCP lesion. In contrast, due to markedly thicker ($d_{EV} > 1\text{mm}$) DV layer and drastically increased heterogeneity in this FM specimen, OCT was unable to delineate the underlying layers within the FMs.

7.4 Discussions

Early diagnosis of preeclampsia, crucial to effective therapeutic treatment, remains a clinical challenge due to the multifactorial nature of this disease^{67, 68}. Previous study revealed that MCP originating from the chorion leave (involving mostly CT and A layers) of the FMs was demonstrated to be closely related to preeclampsia ($p \leq 0.001$)⁶⁹, thus early diagnosis and evaluation of the progression of MCP could be of great clinical relevance. Current diagnosis is based on *ex vivo* histopathologic examination of the excised tissue specimens, whose clinical value is restricted by its invasive and destructive natures. Moreover, little has been studied about potential pathological misinterpretation of MCP as a result of artifacts induced by tissue fixation and processing.

In contrast, noninvasive early diagnosis of MCP could potentially benefit the treatment. Current medical imaging techniques such as MRI and ultrasound may provide limited diagnostic values because of their insufficient spatial resolution and other technical imperfections (e.g., potential radiation hazard to fetus). OCT is an emerging optical imaging modality that, if integrated with endoscopy, permits noninvasive cross-

sectional 2D and 3D imaging of biological tissue at high spatial resolutions (e.g., 1-10 μ m) and over intermediate depths (e.g., 1-3mm). Previous preclinical studies validated the capability of OCT for delineating the morphological details of various biological tissues such as oral cavity, bladder, esophagus, and cervix^{7, 71, 72}. More interestingly, recent *in vivo* clinical studies clearly demonstrated the utility of our endoscopic OCT technique in significantly enhancing current clinical approach (i.e., white-light cystoscopy) for noninvasive diagnosis of early bladder cancer. Technically, the areas of fetal membranes prone to preeclamptic changes can potentially be imaged *in vivo* using our newly developed miniature (e.g., ϕ 2mm) flexible OCT catheter during intrauterine examination. We have presented a preliminary study based on human tissue specimens, including both normal control and diseased FMs. Results in Fig. 7.2 and Fig. 7.3 show that OCT was capable of delineating the morphological details of normal human FMs as the four layers (e.g., DV, CT, A and E) based on their backscattering differences (e.g., $r_{CT/DV}=0.51\pm 0.17$; $r_{A/DV}=0.84\pm 0.45$; $r_{E/DV}=0.44\pm 0.20$). Results in Fig 7.4 and Fig 7.5 further demonstrate the utility of OCT to affirmatively detect the MCP lesions (cysts) in the CT layer of human FMs based on their drastically reduced backscattering (e.g., $r_{MCP/DV}=0.17\pm 0.06$). More importantly, by applying post-image processing techniques (e.g., image segmentation and registration, standard deviation analysis) to the original 3D OCT image dataset, OCT morphometric placental analysis could potentially be implemented to provide quantitative, accurate evaluation of MCP progress (i.e., “staging” of MCP), which is essential to potentially monitor the preeclampsia development and to evaluate treatment effects. Our initial study using HFUS suggests that despite its limited

spatial resolution to delineate layered structures in FMs, HFUS could be a complimentary method to detect large MCP lesions in markedly thickened FMs where a deeper penetration is needed. However, in order to further justify the utility and potential limitations of OCT and HFUS in the diagnosis of preeclampsia, further detailed and more quantitative studies should be performed in the future, in particular, in vivo imaging evaluations.

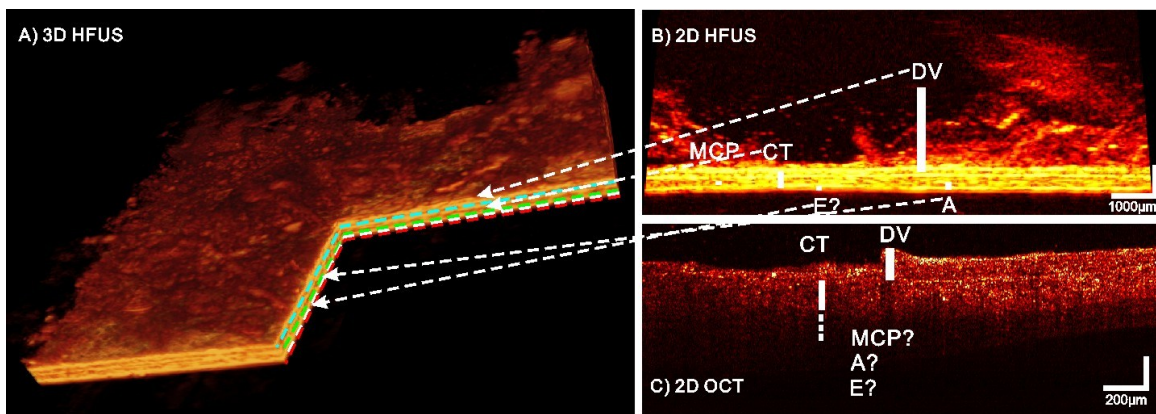


Fig. 7.7 3D HFUS image of a human FM with thick MCP. A): 3D HFUS image; B): a slice of 2D HFUS from image A); C) corresponding 2D OCT image. Despite the lower spatial resolution, HFUS was able to penetrate the entirety of the thicker FMs while the image depth of OCT was limited to layer DV or top CT.

7.5 Conclusions

In summary, we performed an in vitro study on fresh human FM specimens to examine the efficacy and limitations of OCT for future noninvasive or minimally invasive hysteroscopic OCT imaging of fetal membranes. Results presented above show that the high resolution and 3D imaging capability of OCT enabled delineation of morphological details of human FMs (e.g., DV, CT, A and E layers) based on their

backscattering differences, which correlated well with the corresponding histological evaluations. Additionally, OCT was able to identify early MCPs and accurately measure the size of these lesions. It was also noted that quantitative OCT image analysis revealed increased backscattering heterogeneity (e.g., standard deviation) in the CT layer of almost all the MCP specimens and in the E layer of some MCP specimens. Further histomorphometric and immunohistochemical studies are needed to characterize the increases in these layers with the presence of different cell types and their accumulations so that more specific diagnosis of the severity and progress of MCP can be predicted. In addition, more in vivo animal and human studies will be required to fully examine the efficacy, technical feasibility and safety of OCT hysteroscopy as well as HFUS for potential future clinical application to minimally invasive diagnosis of MCP and staging their progress.

Chapter 8 Ultrahigh Resolution Quantitative 3D Optical Doppler Tomography for Brain Functional Imaging

8.1 Introduction

Cocaine's vasoactive effects result in marked disruption in cerebral blood flow (CBF) in cocaine abusers⁷³ and are also likely to contribute to the reported occurrences of hemorrhagic and ischemic strokes in cocaine abusers.⁷⁴⁻⁷⁹ However, effective treatment remains elusive in part due to lack of knowledge regarding the nature and the mechanisms that underlie the cerebrovascular changes resulting from cocaine abuse. Studies on the vasoactive effects of cocaine (and other drugs of abuse) in animal models have been hindered by the technical limitations of current neuroimaging techniques. Conventional techniques (e.g., MRI, CT angiography) fail to provide sufficient spatiotemporal resolutions to measure rapid CBF changes in small vessel compartments¹; while multiphoton microscopy (MPM)⁸⁰⁻⁸² can detect capillary CBF, its small field of view (FOV) restricts its use for assessing cocaine's cerebrovascular network effects, and it may not be suitable for repeated imaging of disease progression² or the dynamics to cocaine responses (e.g., due to complications associated with exogenous fluorescence dye

loading and clearance). Recent advances in optical coherence angiography (OCA)^{2, 9, 83, 84} have markedly improved *in vivo* visualization of the microvascular networks, including 3D microscopy of tumor microenvironments. Yet, methods to enable quantitative capillary CBF imaging remain a technical challenge in Doppler OCT (ODT).

We developed a novel optical imaging technique that allowed us to image 3D capillary cerebrovascular networks quantitatively and at ultrahigh spatial resolution. Specifically, we combined ultrahigh-resolution optical coherence angiography (μ OCA)^{16, 85} to enable visualization of capillary cerebrovascular networks, and a new phase-intensity-mapping (PIM) algorithm to optimize the detection sensitivity of ultrahigh-resolution Doppler flow imaging (μ ODT). Additionally, this technique allowed separation of arterial and venous branches and thus characterization of their differences in response to stimuli (e.g., cocaine). After validating the technique by imaging the microcirculatory responses to laser disruptions in the mouse brain, we apply it to study the cerebral microvascular network changes induced by acute and repeated cocaine administration using clinically relevant doses. Our findings show for the first time, that cocaine-induced neurovascular 'like' microischemia, and that these effects were exacerbated with repeated administration (1 vs. 3 doses). Inasmuch as cocaine abusers repeatedly administer cocaine in binges, this indicates that the vasoactive effects of cocaine will jeopardize oxygen delivery to cerebral tissue making it vulnerable to ischemia and neuronal death.

8.2 Methods

8.2.1 Mice.

CD1 mice (Charles River, 35~40g, 7~8 weeks of age, female) were used to conduct the cerebral flow imaging studies. All mouse experiments were approved by the Institutional Animal Care and Use Committee at Stony Brook University.

8.2.2 Surgery.

Mice were anesthetized with inhalational 2% isoflurane (in 100% O₂) and mounted on a custom stereotaxic frame to minimize motion artifacts. A ~ ϕ 5mm cranial window was created above the right somatosensory motor cortex. The exposed cortical surface was immediately covered with 2% agarose gel and affixed with a 100 μ m-thick glass coverslip using biocompatible cyanoacrylic glue. The physiological state of the mice, including electrocardiography (ECG), mean arterial blood pressure (MABP), respiration rate and body temperature, was continuously monitored (SA Instruments, NY).

8.2.3 Laser Disruption.

A pigtailed green laser (60mW, 532nm) was coupled into the sample arm of the μ OCT system to disrupt an individual vessel on focus (spot size: ~ ϕ 3 μ m) whose

coordinates (x, y, z) were accurately determined by prior 3D μ OCA image. Laser exposure (2min) was used to disrupt a capillary vessel and repeated exposures were used to disrupt a branch vessel.

8.2.4 Intravenous Cocaine Induction.

A mouse tail vein was cannulated with a 30-gauge hypodermic needle connected to PE10 tubing, through which a bolus of cocaine (2.5mg/kg, body weight) was administered (<15sec).

8.2.5 Ultrahigh-resolution Optical Coherence Tomography (μ OCT)

The image platform that combines ultrahigh-resolution optical coherence angiography (μ OCA) and optical Doppler tomography (μ ODT) involves modification of previously described μ OCT instrumentation⁵⁵ depicted in Fig. 8.1. In brief, a mode-locked 8fs Ti: Al₂O₃ laser provides ultra-broadband ($\lambda=800\text{nm}$, $\Delta\lambda_{\text{FWHM}}=128\text{nm}$) illumination (1) to a 2 \times 2 wavelength-flattened fiberoptic Michelson interferometer. The reference arm (2) is connected to a grating-lens-based optical delay unit (RSOD, dashed box) to match the pathlength with the sample arm and to compensate the dispersion mismatch and maximize the cross-correlation spectrum between the sample and the reference arms of the interferometer. Light exiting the fiber endface of the sample arm (3)

is collimated to $\phi 5.5\text{mm}$, scanned transversely (along x-axis) by a precision servo mirror G (VM500, General Scanning), and focused by a microscopic objective L1 on the capillary beds within the mouse somatosensory cortex under examination. The backscattered light from the different depth (z-axis) within the cortical brain is collected by the same optics back to the sample arm and recombined with the reference light in the detection fiber (4) to be detected by a spectral imager (dashed box), in which the light is collimated to $\phi 10\text{mm}$, diffracted by a holographic grating (1200/mm, Spectral Physics) and focused by a custom lens system L2 ($f=85\text{mm}$) onto a linear CCD camera (2048 pixels, Atmel) at a frame rate up to 27kHz. By synchronizing the servo mirror G for sequential x scanning (e.g., 500 pixels), 2D μOCT image (z-x cross section) can be acquired at up to 54fps. The acquired dataset are fast transferred via Camera Link interface to a Raid hard disk array (300MB/s, Raid 0 configured) on the workstation for parallel image processing and display. As each spectrograph comprises spectral interference fringes which are frequency modulated or encoded by the pathlength difference or depth z, sequential inverse fast Fourier transforms (FFT) are implemented to derive the depth-resolved backscattering profiles (i.e., A-scans or A-lines). An axial resolution of $1.8\mu\text{m}$ in brain tissue was reached by maximizing the bandwidth of cross-correlation spectrum (e.g., $\Delta\lambda \geq 154\text{nm}$) via spectral reshaping and fully compensating the dispersion mismatch with a pair of wedge prisms (D) in the sample arm together with RSOD in the reference arm⁵⁵. For the achromatic lens ($f16\text{mm}/\text{NA}0.25$, Melles Griot) used in the study, the focal spot size (i.e., transverse resolution) was $\sim\phi 3\mu\text{m}$.

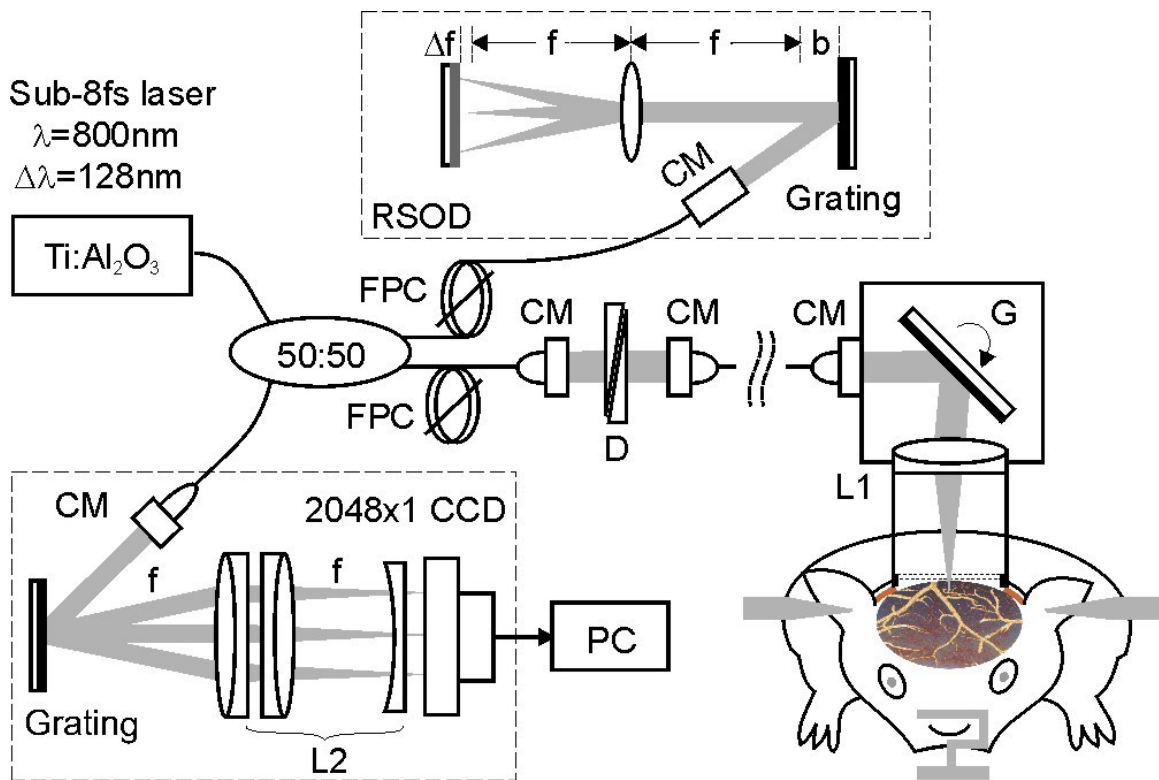


Fig. 8.1 A sketch of ultrahigh-resolution OCT setup for acquiring μ OCA and μ ODT images. A mode-lock sub 8fs Ti:Al₂O₃ laser was used to provide ultra broadband illumination ($\lambda=800\text{nm}$, $\Delta\lambda\approx 128\text{nm}$). CM: fiberoptic collimator; FPC: fiber polarization controller, D: wedge prism pair for fine dispersion adjustment; G: servo scanner, L1: objective lens, L2: lens group; RSOD: optical delay line for dispersion compensation (by adjusting spacing b); Δf and FPC are adjusted to maximizing the bandwidth $\Delta\lambda$ (e.g., $\Delta\lambda\approx 154\text{nm}$) of the cross spectrum. Measured axial resolution (coherence length in brain tissue, $n=1.38$) $L_c\approx 1.8\mu\text{m}$; transverse resolution $\Delta r\approx 3\mu\text{m}$.

8.2.7 In vivo Cerebral Blood Flow Imaging

Unlike μ OCT for structural imaging, specific raster scanning schemes for servo mirror G are developed to optimize vascular detection sensitivity for μ OCA and μ ODT image acquisitions. For 3D μ OCA, the camera is configured at its full speed of 27k A-lines/s to acquire 4 cross-sectional images for each x-z plane with a $2\mu\text{m}$ pitch in x-axis

following sequential scans along y-axis with a 2.4 μ m pitch. A typical 3D image with 2048 \times 500 \times 500 voxels takes \sim 37s, which covers a FOV of 1 \times 1.2 \times 1mm³ in cortical brain. For 3D μ ODT, the camera is configured to operate at 20k A-lines/s and occasionally at 10k A-lines/s for fast flows. However, dense sampling with a 0.05 μ m pitch along x-axis is performed so that each frame (z-x plane) comprises 20k A-lines that are binned down to 10k, 5k and 1k A-lines/s in post-image processing to extract slow capillary flow. For the same FOV of 1 \times 1.2 \times 1mm³, a typical 3D μ ODT image with 20,000 \times 500 \times 2048 voxels may take \sim 8min. To increase the temporal resolution for studying the transient effects of intravenous cocaine challenge, a small FOV of 1 \times 0.12 \times 1mm³ was imaged to raise the acquisition rate to \sim 1min per frame and the procedure was repeated for 36min.

8.2.8 Image Processing

For quantitative μ ODT image reconstruction, a new image processing algorithm - termed phase intensity mapping (PIM) approach - was developed to enhance the sensitivity of quantitative Doppler flow detection, and the algorithm can be simplified as:

$$P(\Delta z, x) = \frac{FFT^{-1}[I'(k, x)|_k]}{FFT^{-1}[I(k, x)|_k]} = \omega_x \quad (8.1)$$

The algorithm for μ OCA image reconstruction is based on speckle contrast image. Assume that $I(\Delta z, x)$ is the reconstructed μ OCT image (amplitude image), i.e.,

$I(\Delta z, x) = FFT^{-1}[I(k, x)/k]$. For the 4 consecutive images $I_j(\Delta z, x)$ where $j=0, \dots, 3$, the 2D angiographic image can be expressed as the relative standard deviation²⁸,

$$A(\Delta z, x) = \frac{1}{\bar{I}(\Delta z, x)} \left[\frac{1}{3} \sum_{j=0}^3 [I_j(\Delta z, x) - \bar{I}(\Delta z, x)]^2 \right]^{1/2} \quad (8.2)$$

where $\bar{I}(\Delta z, x) = \sum_{j=0}^3 I_j(\Delta z, x)/4$ is the mean of the acquired 4 consecutive images.

After each 2D flow image is acquired and reconstructed, the cubic dataset was loaded into image processing platform (Amira) for 3D animation and to display the maximum-intensity-projection (MIP) image for both μ OCA and quantitative μ ODT images of cortical vasculature.

8.2.9 Micro Hemorrhagic Stroke

As was encountered in the Results regarding ischemic strokes, vessel rupture can be readily identified by μ OCA. Fig. 8.2 shows an μ OCA image of a micro hemorrhagic stroke which was evidenced by local blurring due to pronounced blood backscattering. Vessel rupture was created by a microinjection needle under the visual guidance of an injection microscope. Injection induced local brain surface deformation around the injection spot is noticeable.

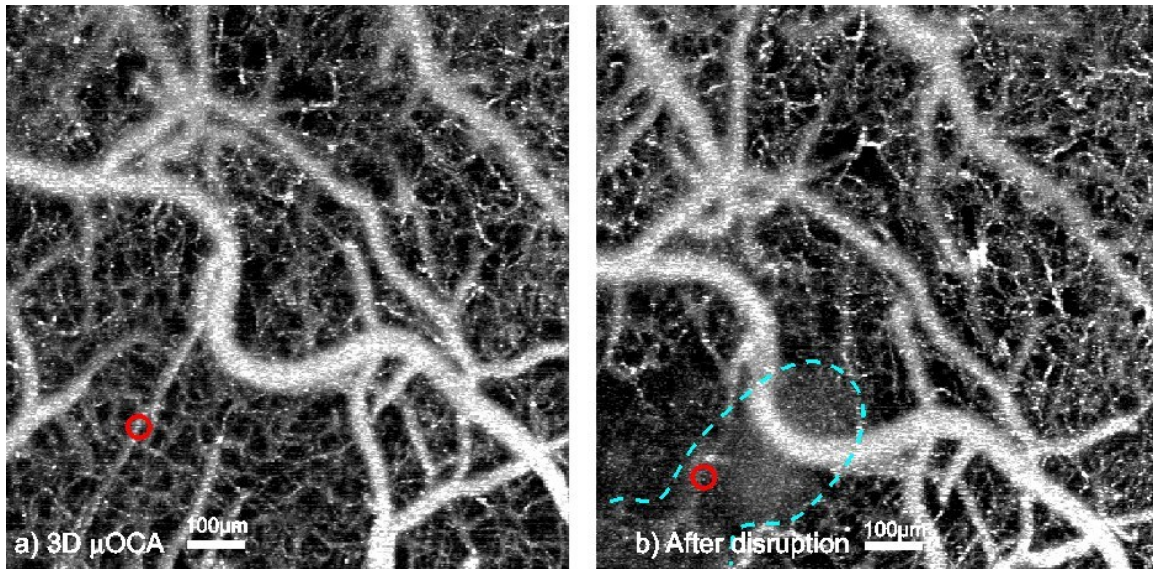


Fig. 8.2 Microvascular hemorrhagic stroke on the mouse somatosensory cortex. a) baseline μ OCA image, b) vascular disruption and hemorrhage by a microinjection needle. Image size: $1 \times 1 \times 1 \text{mm}^3$. Red circle: injection spot; Blue dashed line: region of local blurring induced by bleeding.

8.2.10 Separation of Arterioles and Venules

Separation of veins and arteries is desirable in neuroscience studies to characterize their differences in response to physiological, pharmacological and functional activations. Here, we present a new method to effectively separate these 2 types of vessels by taking advantage of high-fidelity microvascular images provided by 3D μ ODT. Fig.8.3 illustrates the procedure for vessel separation for Fig. 8.9. To enhance the vascular tree connectivity of the branch vessels, we reprocess the 3D μ ODT image at 10kHz so the slow capillary beds are eliminated. In Fig. 8.3 (a), the CBF directionality is preserved with red ('+') and blue ('-') representing downward and upward flows, respectively. Note that this 'apparent flow' map derived from PIM must be corrected with

θ . As most of larger branch vessels are aligned nearly along the cortical surface, i.e., $\theta \approx 90^\circ$, so we substitute $\alpha = 90^\circ - \theta$ for θ , where α is the tilting angle of a vessel with the horizontal plane. These flows flip signs when θ crosses 90° (e.g., $\cos\theta = \sin\alpha$), if the vessel turns from downward ($\alpha > 0$) to upward ($\alpha < 0$). Although image processing for accurate angular correction of 3D ODT remains computation intensive, we can select a few sections of a vascular tree to

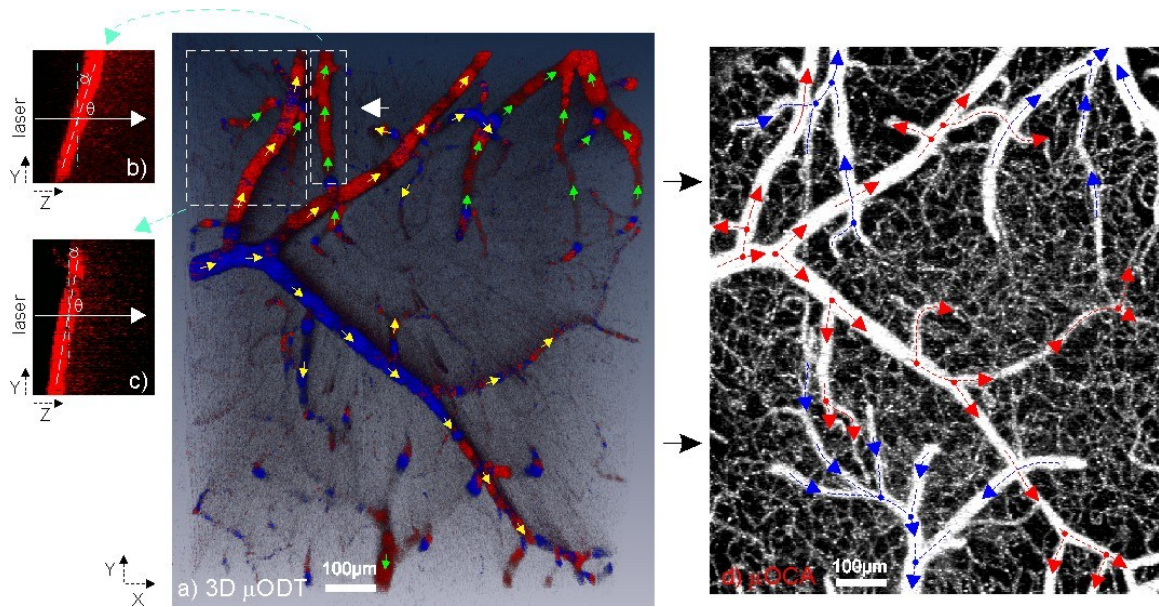


Fig. 8.3 Illustration of arterial and venous vessel separation. a) 3D μ ODT image at 10kHz to show branch vessel connectivity and apparent flow direction (angle uncorrected) with red '+' flow for flowing inwards and blue '-' for flowing outwards. b, c) cross-sectional projection images (Y-Z plane) of two flows from the dashed boxes in a). As their tilting angles $\alpha < 90^\circ$, both flow upwards (towards 'Y+'). Tracing back in a), we can separate flow directions in arterial vessels with yellow arrows (flowing out to smaller branches) and venous vessels with green arrows (flowing into larger branches). d) μ OCA image (Fig. 7.6a) with red arrows to represent arterial flows and blue arrows to venous arrows to avoid confusion.

determine the flow orientation. For instance, 2 apparent red '+' flows in the 2 dashed boxes are selected to trace their orientations. As shown in the 2 side panels, i.e., cross-

sectional images (b, c) in the y-z plane, both vessels point downwards ($\alpha > 0$), so we can confirm that these 2 vessels flow upwards (i.e., towards y+ axis) in 3D μ ODT (a). Then, tracing back the vessels trees of these 2 branches, we can find that the left branch is flowed out from a major vessel, so this vessel tree is arterial (marked by yellow arrows). Whereas the right branch merges into a large branch vessel, so we can determine it is a venous (marked by green arrows). Similarly, all of the branch vessels can be separated as marked by yellow and green arrows which point to their flow directions. To avoid confusion with color map, we add these arrows to the grayscale μ OCA image (d) in which red arrows refer arterial trees and blue arrow refer to venous trees, and red or blue dots indicate the crossings are connected. Additionally, separation of vessel types for Fig.8.11 is shown in Fig. 8.5.

8.2.11 Minimal detectable flow rate

For PSM, the minimum detectable flow velocity v_{min} (i.e., flow sensitivity) is ultimately limited by the system phase instability and can thus be calculated based on the phase noise $\sigma_{\Delta\phi}$, which, for Doppler OCT, can be theoretically derived as^{86, 87},

$$\sigma_{\Delta\phi} = (SNR)^{-1/2} \quad (8.3)$$

where SNR refers to the signal-to-noise ratio of an OCT system (amplitude imaging). Then, the minimal detectable flow can be expressed as^{9, 25, 84, 88, 89},

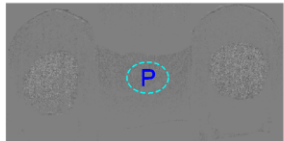
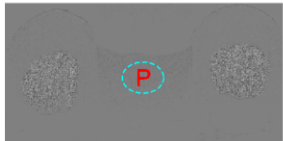
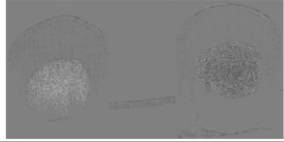
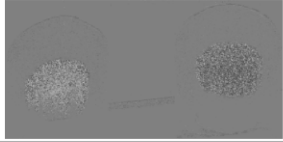
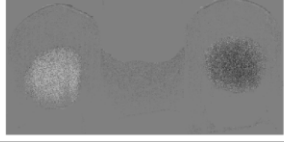
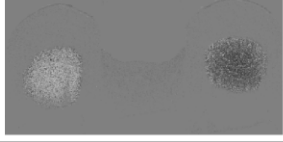
$$v_{\min} = \frac{\sigma_{\Delta\phi}}{2kn\Delta t \cos \theta} = \frac{\lambda\sigma_{\Delta\phi}}{4\pi n\Delta t \cos \theta} \quad (8.4)$$

For the μ ODT system in this study, $\lambda \approx 800\text{nm}$, $\text{SNR} \approx 98\text{dB}$ and $\Delta t = 1\text{ms}$ (i.e., at a low scanning rate $f = 1\text{kHz}$), v_{\min} can be calculated as

$$v_{\min} = \frac{\lambda(\text{SNR})^{-1/2}}{4\pi n\Delta t} \approx 4.8 \mu\text{m} / \text{s} \quad (8.5)$$

To validate the flow sensitivity experimentally, a phantom study was performed in which 2 blood vessels were simulated using 0.5% intralipid in a bidirectional translucent capillary tubing (PE10, $\phi 280\mu\text{m}$) surrounded by solidified scattering matrix using 0.5% intralipid mixed with 1% agarose which mimicked the brain tissue. A high precision syringe pump (CMA400, CMA Microdialysis, Sweden) was connected to the capillary tubing for accurate flow rate control (v_p) and the flow direction with respect to the laser beam was set to $\theta \approx 84^\circ$ to further reduce the apparent Doppler flow. μ ODT images were reconstructed by both traditional PSM and our newly developed PIM for comparison.

Tab.8.1 Experimental comparison of flow sensitivity

| Pump Rate ($\mu\text{L}/\text{min}$) | Theoretical Flow ($\mu\text{m}/\text{s}$) | PSM | Measured Flow ($\mu\text{m}/\text{s}$) | Phase Noise ($\mu\text{m}/\text{s}$) | PIM | Measured Flow ($\mu\text{m}/\text{s}$) | Phase Noise ($\mu\text{m}/\text{s}$) |
|--|---|---|--|--|--|--|--|
| 0.1 | 3.0 |  | 8.5 | 6.6 |  | 6.5 | 4.9 |
| 0.5 | 14.9 |  | 16.4 | 7.0 |  | 15.6 | 5.1 |
| 1.0 | 29.7 |  | 34.6 | 6.4 |  | 33.3 | 5.1 |

* The measured flows were calculated based on the mean values of the randomly distributed bidirectional flows. However, if calculation was based on absolute flow (unidirectional flow, similar to μOCA) measurement, then the measured flow rates were $38\mu\text{m}/\text{s}$ and $36\mu\text{m}/\text{s}$ for PSM and PIM, respectively.

Tab.8.1 compares the μODT images by PSM and PIM under 3 different flow rates. The results indicate the system $\sigma_{\Delta\phi}$ was Brownian-motion limited⁸⁴. At near-zero flow with $v_p=0.1\mu\text{L}/\text{min}$, a theoretical flow rate of $3\mu\text{m}/\text{s}$ was predicted inside the capillary tubes; however, μODT images with both PSM and PIM affirmatively detect the slow flows in the range of $30\sim 40\mu\text{m}/\text{s}$ (based on averaged absolute flow similar to that detected by μOCA) due to Brownian motion above the background phase noise level (sampled within the solidified tissue area P). The measured noise level of PSM ($v_{min}\approx 6.6\mu\text{m}/\text{s}$) is higher than that of PIM ($v_{min}\approx 4.9\mu\text{m}/\text{s}$). Interestingly, based on μODT , the measured directional flow rates are $8.5\mu\text{m}/\text{s}$ by PSM and $6.5\mu\text{m}/\text{s}$ by PIM, which is close to pump rate of $3\mu\text{m}/\text{s}$ but with phase noise included. At the pump rates of $v_p=0.5\mu\text{L}/\text{min}$ and $1\mu\text{L}/\text{min}$ (allowed 15min to stabilize flow), the measured flow rates by

PSM (16.4 $\mu\text{m/s}$, 34.6 $\mu\text{m/s}$) and PIM (15.6 $\mu\text{m/s}$, 33.3 $\mu\text{m/s}$) are in close agreement with their theoretical predictions (14.9 $\mu\text{m/s}$ and 29.7 $\mu\text{m/s}$), except a minor overestimation (1.5~5 $\mu\text{m/s}$) likely induced by uncanceled Brownian motion. Overall, the measured minimal detectable flow rates $v_{min}\approx 6.7\mu\text{m/s}$ for PSM and $v_{min}\approx 5.0\mu\text{m/s}$ for PIM, the latter approaching the theoretical limit of $v_{min}\approx 4.8\mu\text{m/s}$ given by Eq.(8.5).

It is noteworthy that for *in vivo* animal studies, additional phase noise induced by bulky motions (e.g., animal respiration, heart beat and other types of involuntary motions) cannot be ignored and may degrade the system phase detection sensitivity. To take these artifacts into account, the overall phase sensitivity should be measured and evaluated on *in vivo* experimental data. For example, the SNR performance in Fig. 8.4 can be analyzed by measuring the background phase noise levels at 20 spots in no-flow zones (based on μOCA as shown in Fig. 8.4). The measured μODT flow sensitivity (noise flow rate) $v_{min}\approx 9.2\pm 0.2\mu\text{m/s}$ was slightly higher than that of phantom value ($v_{min}\approx 5.0\mu\text{m/s}$), which was likely reflecting the phase noise induced by motion artifacts of *in vivo* imaging.

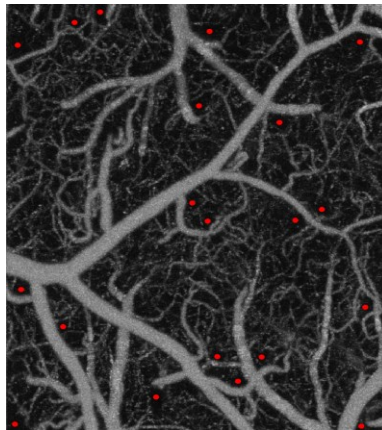


Fig.8.4 Locations to sample background flow noise to characterize μODT flow sensitivity

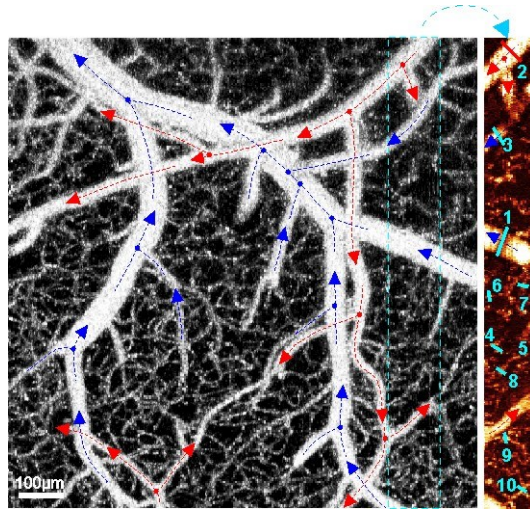


Fig. 8.5 Separation of arterial and venous vessels for Fig. 8.11(a).

8.2.12 Doppler angle correction

Although several algorithms have been reported to enable absolute quantification of Doppler flow velocity^{90, 91}, angle correction to the measured apparent flow image remains a challenge for Doppler OCT, especially when the angle approaches $\theta=90^0$ ($\cos\theta\rightarrow 0$), resulting in severe flow underestimation. Here, we introduce a simple vessel tracking algorithm based on 2D cross correlation to dynamically trace the vessel angle in 3D and convert the measured apparent μ ODT to absolute quantitative μ ODT image accordingly.

For a vessel of interest, a small rectangular area in a 2D cross-sectional μ ODT image ($y=y_0$) encompassing the vessel boundary was cropped and served as the template to correlate with this vessel across different cross sections ($y=y_1, \dots, y_n$). The normalized

2D cross correlation function between the small template and the adjacent cross section can be computed⁹²,

$$\gamma(p, q)|_y = \frac{\sum_{x,z} [v(x-p, z-q) - \bar{v}] \cdot [f(x, z) - \bar{f}_{u,v}]}{\{\sum_{x,z} [v(x-p, z-q) - \bar{v}]^2 \cdot \sum_{x,z} [f(x, z) - \bar{f}_{u,v}]^2\}^{1/2}} \quad (8.6)$$

where $v(x', z')$ is the flow distribution ($x'=x-p$, $z'=z-q$) within the small window projected on the cross section and \bar{v} is its mean flow, $f(x, y)$ is the flow distribution within the template ($y=y_0$) and $\bar{f}_{u,v}$ is the mean of $f(x, y)$, and (p, q) are the linear shifts of the (x, z) coordinates. Using Eq.(8.6), the corresponding coordinates $(p, q)|_y$ under the maximum cross correlation γ are retrieved to generate a 3D vessel coordinate matrix, and the 1D rescaling matrix $\cos\theta_j$ for $y=y_j$ ($j=1, \dots, n$) is calculated accordingly,

$$\cos\theta_j = \frac{\Delta q}{\sqrt{\Delta p^2 + \Delta q^2 + \Delta y^2}} = \frac{q_{j+k} - q_j}{\sqrt{(p_{j+k} - p_n)^2 + (q_{j+k} - q_j)^2 + (y_{j+k} - y_j)^2}} \quad (8.7)$$

where θ_j is the angle between laser beam and the flow direction, $k=2-5$ is the step size between the adjacent cross sections to be adopted as a compromise between angular resolution and phase noise. Applying Eq.(8.7) to the apparent flow image $v(x, z)$, the absolute flow $v^*(x, z)$ with angle correction can be derived as,

$$v^*(x, z, y) = \frac{v(x, z, y)}{\cos\theta_y} \quad (8.8)$$

Here, the correction is only applied to the pixels within the segmented vessel boundary.

To validate the algorithm, a phantom study was performed in which 0.5% intralipid flowing through a pair of bidirectional translucent capillary tubing (PE10,

$\phi 280\mu\text{m}$) was used to mimic 2 blood flows whose flow rate was accurately adjusted to $v_p=1.35\text{mm/s}$ using a high-precision syringe pump. Fig.8.6 shows the measured apparent bidirectional flows (a) and the absolute flows (b) after angle correction using Eqs.(8.6)-(8.8). Depending on the angle, the measured apparent flow is underestimated to $v_A\approx 0.11\text{mm/s}$ around A ($\theta\approx 84^\circ$, $\cos\theta\approx 0.10$) and to $v_B\approx 0.26\text{mm/s}$ around B ($\theta\approx 79^\circ$, $\cos\theta\approx 0.19$). After correction, $v^*_A\approx 1.1\text{mm/s}$ (error $\Delta\approx 18\%$) and $v^*_B\approx 1.38\text{mm/s}$ (error $\Delta\approx 3\%$), which indicates that the algorithm is able to effectively correct the angle effect. As anticipated, however, the correction error rises when the flow direction approaches $\theta\rightarrow 90^\circ$.

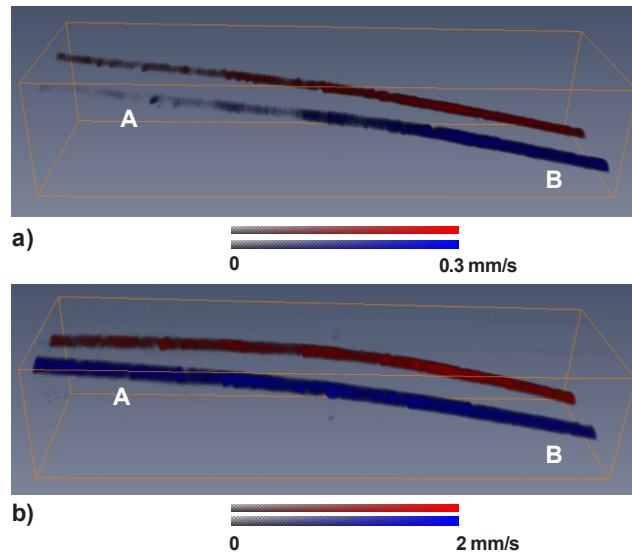


Fig.8.6 3D bidirectional flows before a) and after b) angle correction.

The algorithm can also be applied to the *in vivo* CBF images to correct the angle-induced artifacts. For example, the CBF rates after angle correction of several large (1, 2,

3), intermediate (4, 5) and small (5, 7) vessels in Fig 3 (Fig.S9) are presented in Tab.S2 for comparison.

Table 8.2. Angle correction for *in vivo* study

| Position | Size (μm) | Vein/Artery | Apparent flow (mm/s) | Angle | Angle corrected flow (mm/s) |
|----------|-----------|-------------|----------------------|-------------------|-----------------------------|
| 1 | 40 | A | 0.26 | 87.0 ⁰ | 5.0 |
| 2 | 39 | A | 0.47 | 84.7 ⁰ | 5.2 |
| 3 | 44 | V | 0.25 | 82.6 ⁰ | 1.9 |
| 4 | 28 | A | 0.28 | 87.4 ⁰ | 6.2 |
| 5 | 22 | A | 0.33 | 86.6 ⁰ | 5.5 |
| 6 | 19 | V | 0.18 | 80.6 ⁰ | 1.1 |
| 7 | 8 | C | 0.25 | 62.0 ⁰ | 0.53 |

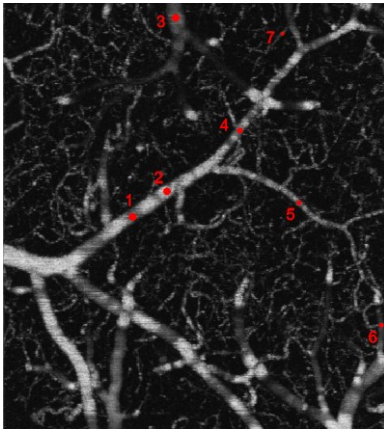


Fig.8.7 Selected vessels of interest for angle correction illustrated in the quantitative flow map

Interestingly, due to angle-induced artifact, the apparent flow rates at spots 1 and 2 differ substantially (e.g., $v_1=0.26\text{mm/s}$, $v_2=0.47\text{mm/s}$) along a same vessel tree without major branches, the corrected results merge (e.g., $v^*_1=5\text{mm/s}$, $v^*_2=5.2\text{mm/s}$), which

indicates the effectiveness of the algorithm. However, it should be noted that like other published angle-correction algorithms, this method may fail in areas of vessel crossings due to the shadowing effects of ODT and for capillary vessels due to limited SNR, which is why we have not been able to correct the entire μ ODT image.

8.2.13 Statistical Analysis.

Data are presented as mean \pm s.e.m. P values to determine significant difference between groups were analyzed by performing either a paired t-test (two tail) or a 1-way ANOVA test (Systat software).

8.3 Results

8.3.1 Microangiography and quantitative capillary CBF imaging

Arterial and capillary vasculatures play a crucial role in maintaining the energy requirements of the functioning brain and can accommodate to increasing tissue demands by modifying the diameters and speeds of flow in the vessel. Although the contrast of both μ OCA and μ ODT originates from the Doppler shifts induced by moving scatterers including red and white blood cells flowing in a blood vessel, they are detected under two distinct regimes. μ OCA uses dynamic laser speckle contrast to offset moving parts

(causing speckle variance) against the surrounding ‘stationary’ brain tissue, whereas μ ODT uses intrinsic Doppler phase shift to render CBF quantification. The upper panels in Fig. 8.8 illustrate how the enhanced spatial resolution of μ OCA (b) enabled us to accurately resolve the vessel-size diversity of the capillary beds on mouse cortical brain, which would have been otherwise overestimated by conventional OCA (a). For instance, the red arrows show that the two capillaries measured by OCA ($\phi 15\mu\text{m}$, $\phi 13\mu\text{m}$) were accurately determined by μ OCA ($\phi 5.4\mu\text{m}$, $\phi 3.5\mu\text{m}$). Fig. 8.8c illustrates the advantage of 3D μ OCA to image capillary cerebrovascular networks at high resolution and across a large FOV ($1\times 1\times 1\text{mm}^3$). The lower panels show the efficacy of our new phase detection technique (PIM vs. PSM) for eliminating the phase noise induced by tissue motion, so that capillary CBF with both small vessel sizes ($<\phi 5\mu\text{m}$) and slow flow speeds ($\leq 10\mu\text{m/s}$) could be readily detected and quantified. A comparison between Fig. 8.8c and Fig. 8.8f illustrates the capability for quantitative μ ODT of cerebral microvascular networks with spatial resolution (for measuring capillary vessels) fairly comparable to that of μ OCA. More importantly, as both images were acquired simultaneously, it allowed us to study vasculatural (μ OCA) and physiological (μ ODT) changes in response to functional and pharmacological interventions.

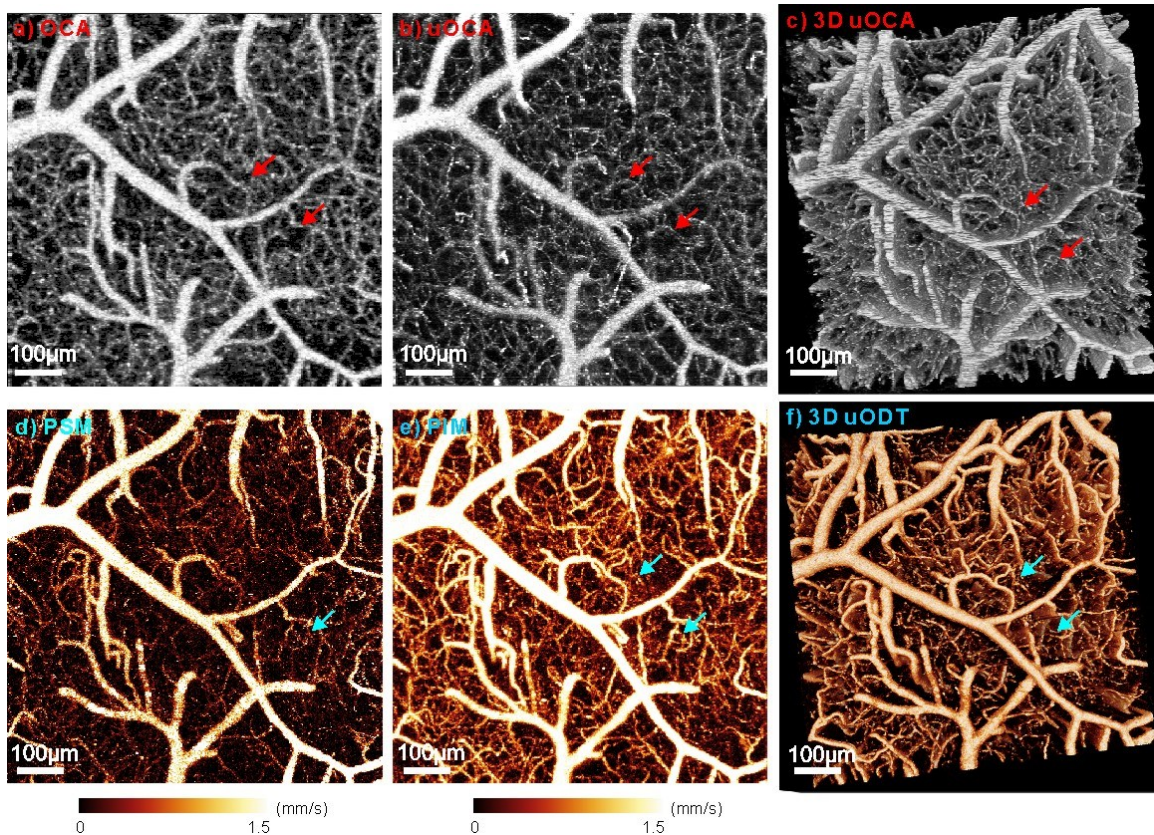


Fig. 8.8 Cerebral vasculature (upper panel) and cerebral blood flows (CBF) (lower panel) of the mouse somatosensory cortex imaged by 3D μ OCA/ μ ODT. a)–b) Maximum intensity projection (MIP) images of vasculature by OCA ($\sim 10\mu\text{m}$) and by μ OCA ($\sim 3\mu\text{m}$). Capillary vessels that appear largely identical ($\sim \phi 15\mu\text{m}$) in OCA are fully restored to their real sizes (e.g., $\phi 3.5\mu\text{m}$) by μ OCA. c) 3D projection of the μ OCA image. d)–e) The corresponding MIP images of quantitative CBF rates by existing PSM algorithm and by the new PIM algorithm. PIM effectively enhanced the flow detection sensitivity to uncover capillary CBFs embedded in the noise background. f) 3D projection of the μ ODT image. Image size (FOV): $1\times 1\times 1\text{mm}^3$; Arrows illustrate two capillary vessels ($\phi 5.4\mu\text{m}$, $\phi 3.5\mu\text{m}$) for comparison.

8.3.2 Laser-induced Microvascular Disruption

To validate the utility of this technique for assessing microvascular networks, we used laser disruption as a reference intervention since it allowed us to assess the

downstream and compensatory responses of cerebral microvascular networks to an insult that is restricted to a single microvessel. Fig.8.9 shows the results of laser disruption of a small $\phi 35.8 \pm 1.2 \mu\text{m}$ arteriole and of a $\phi 9 \mu\text{m}$ capillary. The laser's disruption of the capillary (1) elicited only a small localized change in the μOCA image (Fig.8.9b); in contrast, the μODT image showed not only the disruption of flow in this capillary but also the CBF decrease in the surrounding microenvironment ($\sim \phi 0.13\text{mm}$, inner circle) as well as a massive vasodilatation across almost the entire FOV ($\sim \phi 1\text{mm}$, outer circle). Quantitative analyses in Fig.8.9g-h showed a significant CBF increase ($p < 0.001$) within the outer circle from $0.105 \pm 0.049\text{mm/s}$ (baseline) to $0.211 \pm 0.048\text{mm/s}$ (30min after laser disruption), which corresponds to the average CBF change from 20 capillaries. This is interesting, for it documents that interruption of flow in a single capillary will have a significant effect on CBF of the surrounding cerebral microvascular networks. Similarly, for disruption of the branch arteriole (2), both μOCA and μODT detected laser-induced occlusion of the vessel, but μODT was able to track the quenching effect of local microvascular networks, i.e., the capillaries with an active circulation, over a much large area ($\sim \phi 0.5\text{mm}$, dashed half circle) than that detected by μOCA ($\sim \phi 0.21\text{mm}$, dashed circle). The results show the value of quantitative μODT for monitoring not only local but also downstream CBF responses to a circumscribed insult to a small vessel in cerebrovascular networks, which is necessary for understanding the buffering capacity of microvascular networks to cerebrovascular pathology.

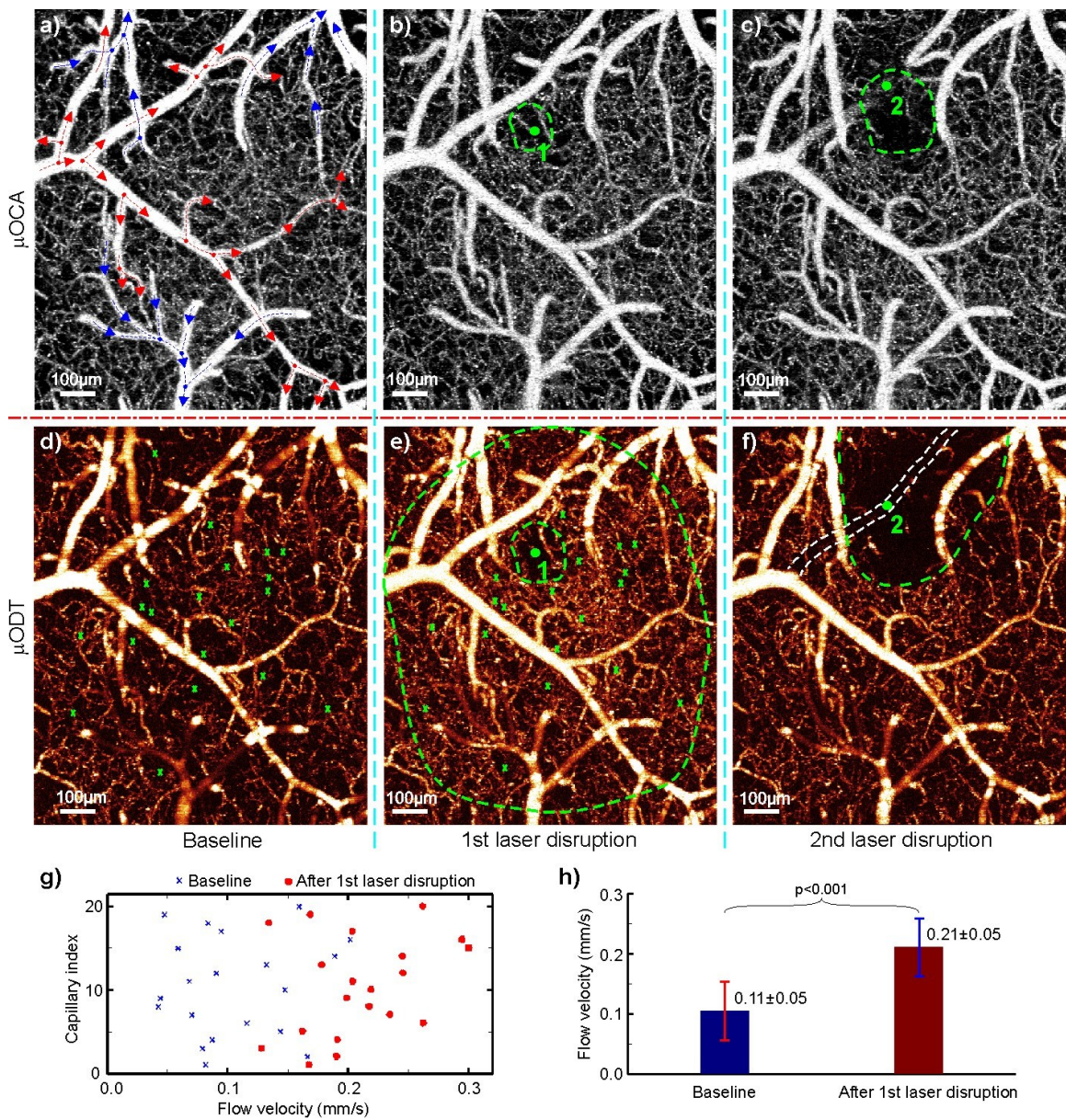


Fig. 8.9 Laser induced disruption of a cerebral capillary and a branch vessel on the mouse somatosensory cortex. Upper panel: MIP images of vascular architecture by μ OCA at baseline in a), after laser disruption of a $\phi 9\mu\text{m}$ capillary vessel 1 in b), and of a $\phi 35.8\mu\text{m}$ arteriolar vessel 2 in c). Red and blue arrows show the flow directions of arteriolar and venial vessels (see Fig. S5 for vessel-type separation), and the dots indicate that vessel junctures. Lower panel: MIP images of the CBF rates by μ ODT at baseline d) and after laser disruptions e) and f), respectively. Angiography showed no difference except reduced vasculature in the immediate areas (dashed green circles in b, c) around the site of laser disruption (green dots); whereas the quantitative CBF image reveals the vastly expanded vasodilatation seen almost over the entire field after laser disruption of a capillary (dashed outer green circle in e) and the quenching of local CBF networks seen over a much larger

area (dashed green circle in e). Quantitative comparisons among 20 capillaries indicate that the CBF rate increased significantly from 0.105 ± 0.049 mm/s at baseline to 0.211 ± 0.048 mm/s at 30min after laser disruption (g and h; $p < 0.001$). Image size: $1 \times 1.2 \times 1 \text{mm}^3$; laser radiation dosages: $\lambda = 532 \text{nm}$, $P = 60 \text{mW}$, $\sim \phi 3 \mu\text{m}$ focal spot, 2min exposure for capillary 1 and 6min exposure for branch arteriole 2.

8.3.3 Repeated cocaine evokes cerebral microischemia

Neuroimaging studies on the hemodynamic effects of cocaine are crucial to elucidating the mechanisms underlying its neurotoxicity including microcirculatory pathology (micro-hemorrhagic stroke) and hemodynamic dysfunction (microischemic stroke). The ultrahigh resolution/sensitivity and large FOV of $\mu\text{OCA}/\mu\text{ODT}$ (Figs.8.8-8.9) show its relevance for these studies. Fig.8.10 shows the results of mouse cortex before and after acute cocaine challenge (2.5mg/kg , *i.v.*) and identifies the occurrence of what appears to be a cocaine-induced microischemia along with the CBF response patterns of the adjacent cerebrovascular networks. The upper panel (a, b) shows the shunt of an arcade ($\sim \phi 23 \mu\text{m}$) interconnecting two side branch arterioles. Cocaine abolished the flow in this vessel which appeared as indiscernible by μODT even though it was fully detectable by μOCA . This suggests that the cocaine-induced ischemic dysfunction probably reflected vasoconstriction of an isolated vessel rather than vessel rupture vessel rupture resulting in hemorrhage would be evidenced by local blurring due to pronounced blood backscattering) or upstream vasoconstriction. Moreover, the fact that there was no CBF drop in the surrounding microvascular networks suggests that the interruption of flow in this arcade was compensated by the microcirculatory networks, even when the shunt was long lasting (remained for $> 40 \text{min}$). More importantly, this result suggests

quantitative CBF imaging (μ ODT) is more sensitive for detecting ischemic events than angiography (μ OCA).

In contrast, the lower panels (c-j) show the progression of vasoconstrictions and local ischemia (mostly shunts of terminal vessels) after repeated acute cocaine injections (3 repeated doses of 2.5mg/kg/each, *i.v.*), although no vasculatural impairment such as vessel rupture was observed. The dashed green, blue and yellow circles outline the deactivated branch vessels elicited by 1-3 cocaine doses, respectively (c-i). A comparison between panels (c, d) shows that terminal arterioles (~77%) were more vulnerable to ischemic shunts than terminal venules (~23%). Noticeable drops of active circulation in the immediate capillary circuits and the spreading of vasoconstrictive clouds (dashed dark circles) with repeated cocaine revealed that the microcirculation was bypassed (local cerebral microvascular network was unable to compensate). Such microischemic events were focal and probably undetectable by current imaging methods, including OCA (e.g., no obvious disruption was detected by μ OCA in panel (d) even after the 3 repeated cocaine injections). Note that the differences between the $\Delta\mu$ ODT responses of different vessels (f, h, j) are likely to reflect the heterogeneity in neurovascular responses to cocaine, e.g., some areas in the bottom show increased (red) flow. This type of approach will enable to systematically evaluate the effects of acute and repeated cocaine administration on vascular architecture and CBF and to help understand the mechanisms underlying cocaine-induced ischemic and hemorrhagic strokes and provide with a tool to monitor potential therapeutic interventions.

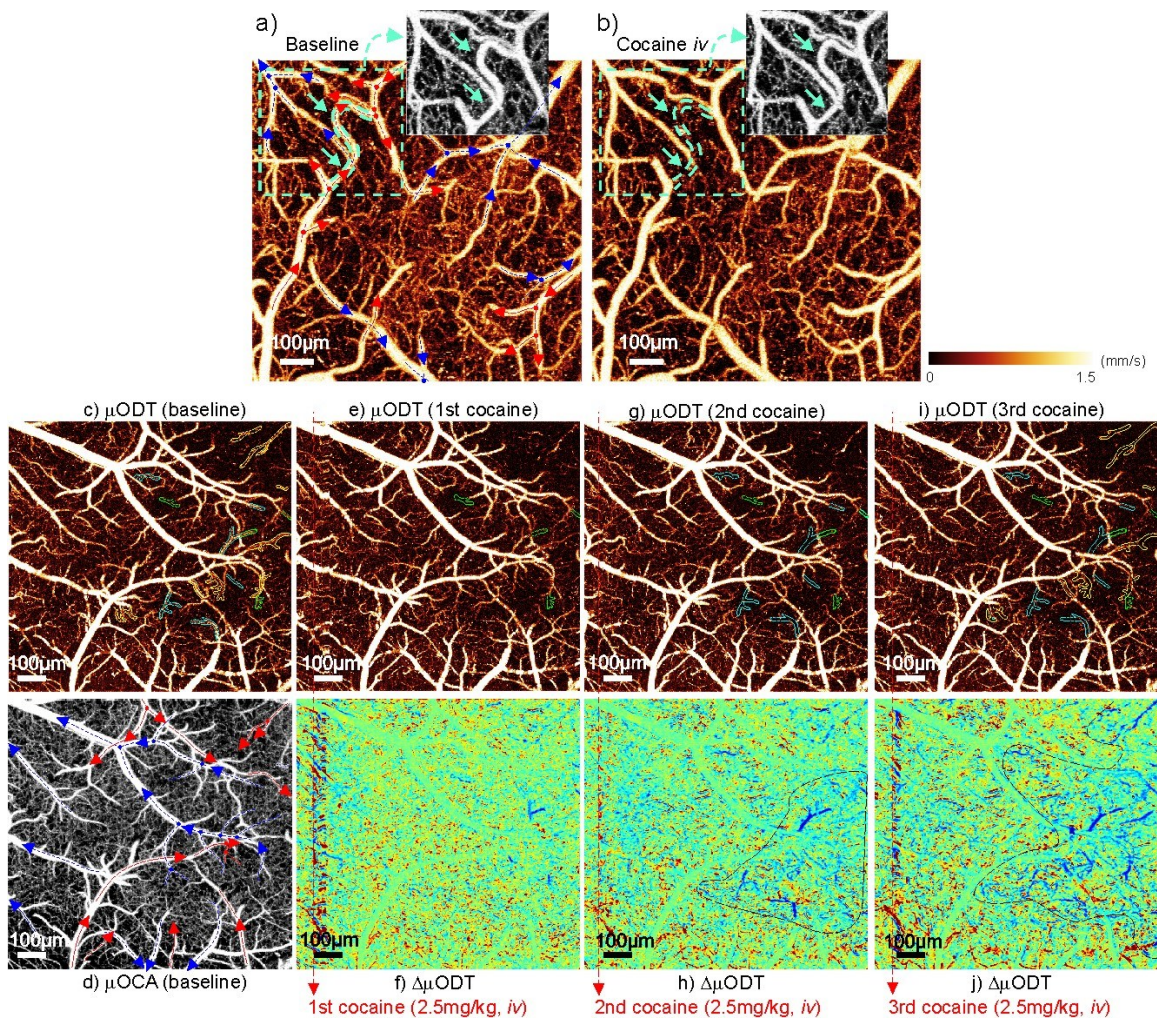


Fig. 8.10 Cocaine evoked microvascular disruptions on the mouse somatosensory cortex. Upper panel is quantitative CBF images (μODT) to show disruption of a $\sim\phi 23\mu\text{m}$ interconnecting branch arteriole (arcade arteriole); low panels show the progression of cocaine-evoked deactivations of branch vessels and the spreading of vasoconstriction (dark dashed areas) with repeated cocaine challenges. a) baseline, b) 30min after acute intravenous cocaine injection; insets: μOCA images to illustrate vascular architecture of the dashed area. Image size: $1\times 1\times 1\text{mm}^3$. c, d) μODT and μOCA at baseline, e-j) μODT and $\Delta\mu\text{ODT}$ (ratio image) after 1-3 acute intravenous cocaine injections (green, blue, and yellow dashed circles: occluded vessels after 1st, 2nd and 3rd cocaine, respectively; dark circles: vasoconstrictive clots). Image size: $2\times 2\times 1\text{mm}^3$. Red and blue arrows show the flow directions of arteriolar and venial vessels, and the dots indicate that vessel junctures.

8.3.4 Inhomogeneity of spatiotemporal responses of CBF to cocaine

As a prolonged time is needed for quantitative detection of capillary CBF, a full-size 3D μ ODT image (e.g., Figs.8.8-8.10) might require over 8min of scanning, which may not be adequate to observe the fast dynamic responses of the cerebrovascular networks during functional or pharmacological activation such as those that occur after an intravenous cocaine challenge. As a compromise, we reduced the image size in the y-axis (anterior-posterior) so that the spatial and the temporal dynamics of cocaine-evoked CBF responses could be visualized. Fig.8.11 illustrates the time-lapse 3D μ ODT images ($1 \times 0.12 \times 1 \text{mm}^3$) following a bolus injection of cocaine (2.5mg/kg, *i.v.*). The upper panels show the quantitative CBF images with extended flow dynamic range. The middle panels plot the time-lapse ratio images defined as $\Delta CBF(t) \equiv [CBF(t) - CBF(t_b)] / CBF(t_b)$ to illustrate the spatiotemporal evolutions of arterioles, venules, and capillaries. The lower panel shows cocaine-evoked dynamic responses of CBF in vein (1), arteriole (2), venule (3) and capillaries (4-6). The transient $\Delta CBF(t)$ of branch vessels (1-3) involved a rapid CBF drop (2~4min) followed by a slow recovery lasting 10-30min, with the arteriole (2) showing more pulsate features. In contrast, the capillary flows exhibited vigorous pulsive changes in response to cocaine challenge and more diverse patterns including transient overshooting.

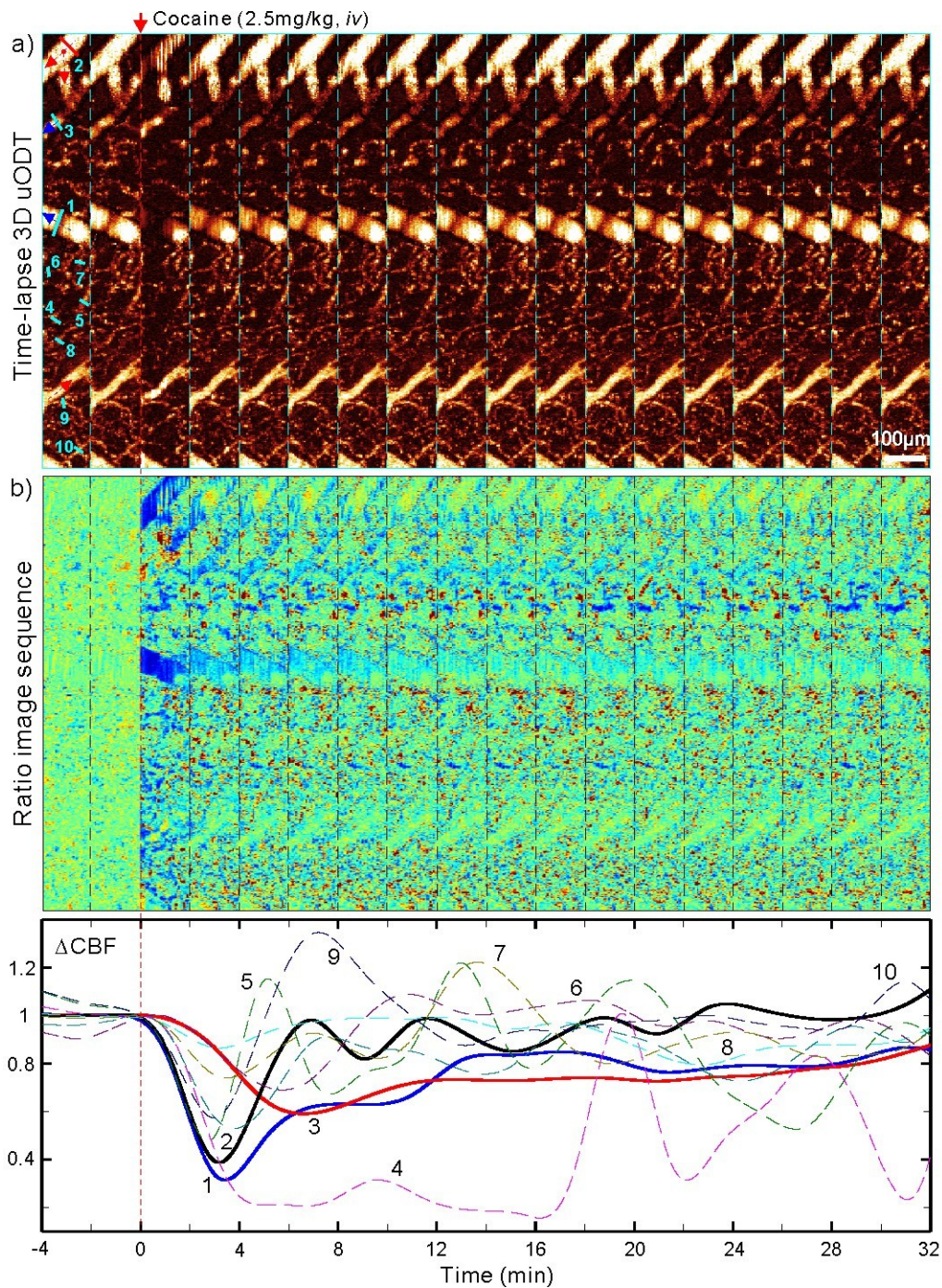


Fig. 8.11 Spatiotemporal evolutions of CBF mouse somatosensory cortex in response to an acute cocaine challenge (2.5mg/kg, *i.v.*). **a)** Time-lapse CBF images ($1 \times 0.12 \times 1 \text{mm}^3/\text{panel}$); **b)** Normalized ratio images (ΔCBF) with time, showing heterogeneous patterns in response to cocaine; **c)** time-lapse ΔCBF curves for 3 branch vessels (solid curves) and 7 capillary vessels (dashed curves) whose positions are marked by light green lines in **a)**. The CBF rates in larger branch vessels (1: vein, 2: arteriole) show a dramatic transient drop ($\sim 60\text{-}70\%$)

within the first 2-3min followed by a slow recovery, similar responses are seen in the smaller vein (3: venule) except the dip is smaller (~40%) and delayed to 6-7min. Noteworthy, the arteriole recovers faster (at ~5min) and exhibits more pulsive patterns than the 2 venules (e.g., at ~12min for 1). In contrast, capillary vessels show dramatically different patterns and more vibrant or pulsive changes with cocaine. Red and blue arrows show the flow directions of arteriolar and venial vessels, and the dots indicate that vessel junctures.

8.4 Discussions

Here we show that cocaine interrupted CBF in some arteriolar branches for over 45min and this effect was exacerbated with repeated cocaine administration. In addition we show that cocaine produced marked decreases in CBF (e.g., ~70%) shortly after acute cocaine administration (2-3min) and that the magnitude and recovery differed between vessels, showing faster recovery in arterioles (~5min) than in venules (~12min) and revealing marked variability and pulsatility in capillaries (recovery varied from 4-20min). These findings provide evidence that acute cocaine elicits cerebral microischemic dysfunction that seems to get exacerbated with repeated cocaine administration. It also uncovers significant heterogeneity in the cerebrovascular responses to cocaine, highlighting the importance of separately assessing vessels of different calibers. Our findings were possible due to the enhanced capabilities of μ OCA/ μ ODT, which demonstrates its value as a novel and more sensitive tool for investigating neurovascular toxicity by drugs or other insults.

Our cocaine findings are relevant since stroke is one of the most serious clinical complications associated with cocaine abuse. Indeed cocaine is a main risk factor for stroke among young abusers.⁹³ Though it was hypothesized that cocaine-induced cerebral

microischemia was involved in some of the clinical complications seen in cocaine abusers, there was no data to support this. Here we show evidence of long-lasting CBF interruptions in cerebral microvessels (>45min) that are exacerbated with repeated cocaine administrations. Specifically, 3 sequential cocaine doses induced greater changes than those induced after a single dose, which is clinically relevant since cocaine when abused is repeatedly administered in binges and rarely used as a single administration.⁹⁴ Thus a sensitized response of cerebral microvessels to repeated cocaine administration could contribute to cocaine's neurotoxic effects. More specifically, the long-lasting interruption in flow observed in some of the vessels, if it is exacerbated with repeated cocaine use could result in microischemic dysfunction and if prolonged could lead to neuronal death and loss of function. We had previously used Doppler OCT to show decreases in CBF after acute cocaine,^{89, 95, 96} but the limited resolution and sensitivity did not allow us to measure the effects of cocaine on capillary beds. In the current study the enhanced capabilities of μ OCA/ μ ODT allowed us to document cocaine-induced microischemic events in capillaries and to show marked differences in the responses to cocaine between arterioles, venules and capillaries in the cerebrovascular networks (Figs.8.10-8.11). Of these the capillaries showed the greatest variability and pulsatility upon intravenous cocaine administration, and the terminal arterioles (~77%) seemed more vulnerable to cocaine-elicited microischemia than terminal venules (~23%).

The mechanisms underlying cocaine vasoactive effects are likely to reflect in part its dopaminergic effects. Indeed there is evidence of dopamine terminals in close contact with arterioles and capillaries in cortical tissue that when stimulated results in

vasoconstriction.⁹⁷ Studies on isolated cerebral arterioles have shown that application of cocaine or its metabolites induced vasoconstriction corroborating a direct effect of cocaine on blood vessels as opposed to indirect effects secondary to neuronal actions⁹⁸. Moreover, vasoconstriction from cocaine was prevented by haloperidol, which suggests the involvement of dopamine (D2) receptors in cocaine induced vasoconstriction⁹⁸. There is also evidence of dopamine transporter expression (target of cocaine's effects) in cerebral blood vessels in the brain⁹⁹. However, it is also possible that the local anesthetic effects of cocaine may contribute to its vasoactive actions¹⁰⁰.

Our findings also demonstrate the enhanced capabilities of our μ OCA/ μ ODT tool for simultaneously rendering angiographic (μ OCA) and quantitative CBF (μ ODT) images of 3D cerebrovascular networks with capillary details comparable to those by MPM. Specifically, we incorporate ultrahigh-resolution OCT for improving spatial resolution ($\sim 3\mu\text{m}$) and PIM (based on FFT analysis in lateral direction^{9, 84, 89}) for optimizing phase detection sensitivity ($\leq 10\mu\text{m/s}$, Tab.8.1), and show that the new μ OCA/ μ ODT platform offers several unique capabilities that are highly relevant to brain functional studies, yet lacking in current imaging modalities (e.g., MPM, OCA). This technique, based on intrinsic Doppler effect (i.e., tracker free), enables time-lapse imaging of the dynamic responses to brain functional activation (Fig.8.11) and disease progression². It extends the image depth of MPM ($\sim 300\mu\text{m}$) to $700\mu\text{m}\sim 1\text{mm}$ and the vastly increased FOV (e.g., $2\times 2\times 1\text{mm}^3$) is crucial for mapping cerebral microvascular network effects. Noteworthy, μ ODT is uniquely capable of CBF quantization in both capillaries and branch vessels (Figs.8.9-8.11), which provides more sensitive

physiological changes (e.g., microischemia) in the local microvascular networks than μ OCA (Figs.8.9-8.10). Additionally, it allowed us to separate venous and arterial vasculatures and thus to study their respective physiological responses to various functional and pharmacological interventions (Figs.8.9-8.11).

A limitation in our study was that the mice had to be anesthetized (as is the case for most rodent imaging studies), which raises concerns of potential interactions between cocaine and the anesthetic agent. However, we specifically chose isoflurane since in a prior study addressing the influence of anesthetic drugs on cocaine's effects we showed that the findings from the isoflurane-anesthetized rodents agreed with those reported in human subjects¹⁰¹ and more recently with those reported in awake macaques.¹⁰² Moreover, isoflurane did not uncouple cocaine's effects on CBF from those in oxygen metabolism, which suggests that at the doses used to anesthetize the mice, isoflurane did not disrupt the autoregulation of CBF. Also to control for potential confounds secondary to cocaine-induced peripheral vascular effects¹⁰² we monitored the mean arterial blood pressure (MABP) throughout the experiments. Although MABP decreased in response to cocaine this effect was modest (MABP>70mmHg) and short lasting (<5min), suggesting that neither the immediate (Fig.8.11) nor the long-lasting (Fig.8.10f, h, i) decreases in CBF following cocaine administration were due to cocaine's peripheral effects. In addition, the measured apparent CBF comprises artifacts (e.g., underestimation) due to Doppler angle effect, especially when the angle $\theta \rightarrow 90^0$. The error can be accurately corrected; however, angle correction of the entire CBF network is challenging because of high correction errors for flows with $\theta \rightarrow 90^0$ and limited sensitivity for capillary beds. It

should also be noted that due to limited temporal resolution of 3D μ ODT (e.g., 1min), the imaged CBF change in response to cocaine (e.g., Fig.8.11) was confounded with the inherent CBF fluctuation over time (e.g., basal $\Delta CBF(t: t < 0)$ variations in Fig.8.11). Although this change in larger vessel (e.g., $> \phi 50\mu\text{m}$) was negligible ($\sim 8\%$) compared to the changes induced by cocaine (e.g., 50%), the influence was more obvious in smaller vessels and capillaries.

In summary, we provide evidence that cocaine induced cerebral microischemic changes that in some vessels were long lasting ($> 45\text{min}$) and were exacerbated with repeated administration. This could underlie some of the neurologic deficits reported in cocaine abusers ranging from mild and transient facial paralysis, to severe and irreversible tetraplegia.¹⁰³ We also show evidence of the enhanced capabilities of μ OCA/ μ ODT for studying the dynamic responses of cerebral microvessels to drugs and other insults.

Chapter 9 Quantitative imaging of red blood cell velocity *in vivo* using optical coherence Doppler tomography

9.1 Introduction

Cerebrovascular networks play a vital role in regulating brain oxygenation and energy supplies and thus serve as the basis for most functional neuroimaging approaches (e.g., PET, f-MRI).¹⁰⁴ However, studying the physiology of cerebral microvascular hemodynamics requires quantitative imaging tools that can provide both high spatiotemporal resolutions and a large field of view (FOV). For instance, multiphoton microscopy (MPM)¹⁰⁵, which enables imaging of red blood cell (RBC) velocities v_{RBC} in capillaries at up to $\sim 300\mu\text{m}$ of depth is very useful for studying neurovascular physiology *in vivo*; however, the measurements are limited to capillary vessels and require administering fluorescence dyes, thus limiting its use in studies that require repeated imaging as may be needed when monitoring dynamic vascular responses. Recent advances in photoacoustic microscopy¹⁰⁶ and coherence-domain optical techniques (e.g., optical microangiography)^{83, 107, 108} have permitted label-free 3D

visualization of the cerebral networks with unprecedented neurovasculatural details. Although quantitative 3D imaging of cerebral blood flow speeds (CBF) has been reported using optical coherence Doppler tomography (ODT), the flow sensitivity and spatial resolution are insufficient to fully resolve the capillary CBF in brain cortices. In this Chapter, we present a technique, termed "particle-counting ultrahigh-resolution ODT" (pc- μ ODT) that allows accurate imaging of capillary vRBC without the need for fluorescence labeling. In addition, we demonstrate the capability of pc- μ ODT for functional neuroimaging studies on a mouse model of cerebral hypercapnia.

9.2 Methods

pc- μ ODT operates in a similar manner to MPM for imaging RBC velocity (i.e., RBCs passing through a capillary per unit time) in that MPM counts the intensity transient of a fluorescently labeled RBC whereas pc- μ ODT counts the resultant Doppler phase transient of a moving RBC. The ultra-sensitive detection of individual RBC-induced phase transients is made possible by the combination of ultrahigh-resolution OCT (μ OCT) with a phase-intensity-mapping (PIM) algorithm recently developed in our lab to enhance the sensitivity of Doppler flow detection¹⁰⁹. Fig. 9.1 illustrates the principle of pc-ODT, in which a broadband spectral-domain OCT was illuminated by a sub-8fs laser ($\lambda=800\text{nm}$, $\Delta\lambda\approx 128\text{nm}$). A high axial resolution (i.e., coherence length $L_c=2(\ln 2)/\pi \cdot \lambda^2/\Delta\lambda_{cs}$) of $1.8\mu\text{m}$ was achieved in brain by maximizing the bandwidth (e.g., $\Delta\lambda_{cs}\geq 154\text{nm}$) of the cross spectrum ($S_{cs}(\lambda)\equiv[S_s(\lambda)\cdot S_r(\lambda)]^{1/2}$, where $S_s(\lambda)$, $S_r(\lambda)$ are the

sample and reference power spectra) and compensating the dispersion mismatch between sample and reference arms⁵⁵. The collimated light in the sample arm was transversely scanned (x/y-axes) by a high-precision servo mirror and focused with a f16mm/NA0.25 objective (lateral resolution: $\sim\phi 3\mu\text{m}$) onto the capillary beds through a cranial window, enabling the resolution of individual capillaries (e.g., $\phi 3\text{-}7\mu\text{m}$) in the cortex of a mouse brain. The backscattered light from the mouse cortex of different depths (along z-axis) was collected back to the sample arm and recombined with the reference light in the detection fiber to be detected by a spectral imager (a 2048-pixel linear CCD camera, Atmel) synchronized with sequential x/y-scans at 20kHz to acquire 2D/3D μOCT images. The raw image data were stream-lined via camera link to Raid-0 hard disks (300MB/s) of a PC for image processing by FFT analysis to reconstruct and display the Doppler flow (μODT) images.

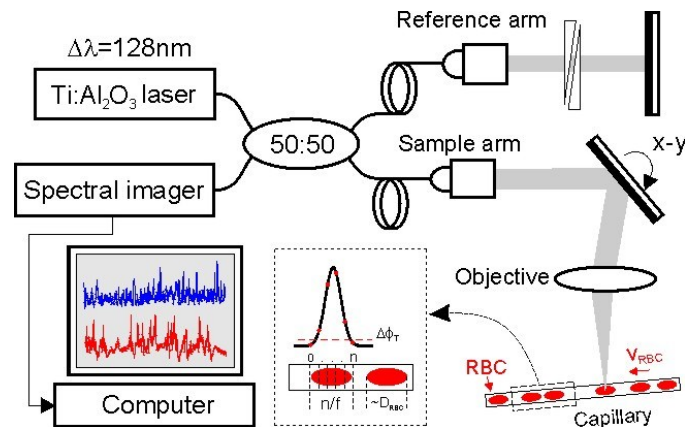


Fig.9.1. A sketch to illustrate pc- μODT for accurate imaging of capillary v_{RBC} , which was based on spectral-domain 3D μOCT . v_{RBC} was measured by counting the number of frames (n) across a RBC, where $f=1.1\text{kHz}$ is the frame rate for pc- μODT .

PIM for high-sensitivity 3D μ ODT reconstruction¹⁰⁹ is based on linearly projecting the flow-induced Doppler frequency shift $v_{x, \Delta z}$ to its intensity in the Fourier domain (in x-axis),

$$P(\Delta z, x) = \frac{2\pi FFT^{-1}[v_{x_i} I_i(k, x) |_k]}{FFT^{-1}[I(k, x) |_k]} = 2\pi v_{x, \Delta z} \quad (9.1)$$

where $P(\Delta z, x)$ is a linear intensity projection to $v_{x, \Delta z}$ and $I(k, x)$ is the detected spectral μ OCT signal. $k=2\pi/\lambda$ is wave number and i refers to the i -th flow $v_{xi, \Delta z}$. As PIM requires high-capacity data acquisition (e.g., a $0.05\mu\text{m}$ -pitch sampling over 1mm or 20k points in x-axis) and intensive computation, 3D μ ODT was reconstructed by post-image processing (e.g., ~ 4 min for a 3D μ ODT of $20\text{k} \times 0.5\text{k} \times 2\text{k}$ voxels). A pre-scan with simple phase-subtraction method (PSM)²³ was applied to permit real-time flow display, so that the parameters for cortical flow imaging such as the focus onto the capillary beds and the field of view of interest could be optimized. With the coordinates (z, x, y) of individual capillaries accurately located by 3D μ ODT, pc- μ ODT is then performed to quantitatively image capillary v_{RBC} . In this study, cross-sectional μ ODT scans perpendicular to a capillary of interest were implemented. Assume that a capillary is of $\sim 7\mu\text{m}$, a minimal of $7.6\mu\text{m}$ lateral scanning range is needed to fully cover the cross section of the capillary. And as a high pitch density such as $\Delta x \approx 0.32\mu\text{m}$ is required by PIM to detect v_{RBC} -induced minute Doppler phase changes, 24 A-lines ($x_{\text{N}} = 7.6/0.32 \approx 24$) per 2D μ ODT were adopted. Meanwhile, as a RBC is of $D_{\text{RBC}} \approx 5\mu\text{m}$ and capillary $v_{\text{RBC}} \approx 1\text{mm/s}$, an μ ODT scanning rate of $f \approx 1\text{kHz}$ (i.e., $\sim 1\text{kfps}$) is needed to ensure $n \approx 5$ time-lapsed μ ODT frames

to be captured during the crossing of a RBC through the capillary in order to provide sufficient temporal resolution for accurate v_{RBC} quantification. Both requirements were fulfilled by running the μ ODT system at its full A-scan rate (27kHz), which provided a frame rate of $f \approx 1.1$ kHz for pc- μ ODT. The image reconstruction of pc- μ ODT was post-processed by PIM, similar to that of μ ODT. An oversampling across the vessel wall provided sufficient points ($x_N=24$) in the lateral direction for PIM to calculate its phase image $\varphi(x, z; t)$, and phase subtraction $\Delta\varphi(x, z; t)$ between 2 adjacent 2D phase images was used to retrieve the instantaneous phase change profile, by which the background phase noise (ϕ_n) caused by the micromotion of the vessel wall was largely removed with a dynamic mask generated based on phase thresholding (e.g., $\Delta\phi_T \geq 1.2\phi_n$). This was because an abrupt phase transient was generated upon the arrival ('+') or the departure ('-') of a RBC across the small imaging section. v_{RBC} could be assessed by

$$v_{RBC} = D_{RBC} \times (f/n) \quad (9.2)$$

where n is the total number of sampling cross-sections over a RBC. As the length (D_{RBC}) and v_{RBC} are in the same direction, Eq.(9.2) can be approximated to a more general situation where the capillary flow has angles with x-/y- axes.

9.3 Results

To demonstrate the capability of pc-ODT for accurate capillary v_{RBC} measurement *in vivo*, we chose a mouse model of cerebral hypercapnia as it has been

extensively validated and widely used as a means to increase CBF.¹¹⁰ Female CD-1 mice (~8wks of age) were used in the experiments during which they were anesthetized with inhalational 2% isoflurane mixed with 100% O₂ and mounted on a custom stereotaxic frame. A ~ϕ5mm cranial window was created on the mouse brain with the dura left intact. The exposed brain surface was then covered with 2% agarose gel under a glass coverslip. Mild hypercapnia was induced by switching the gas from 100% O₂ to a mixture with 5% CO₂. All the animal procedures were approved by the Institutional Animal Care and Use Committee of the Stony Brook University.

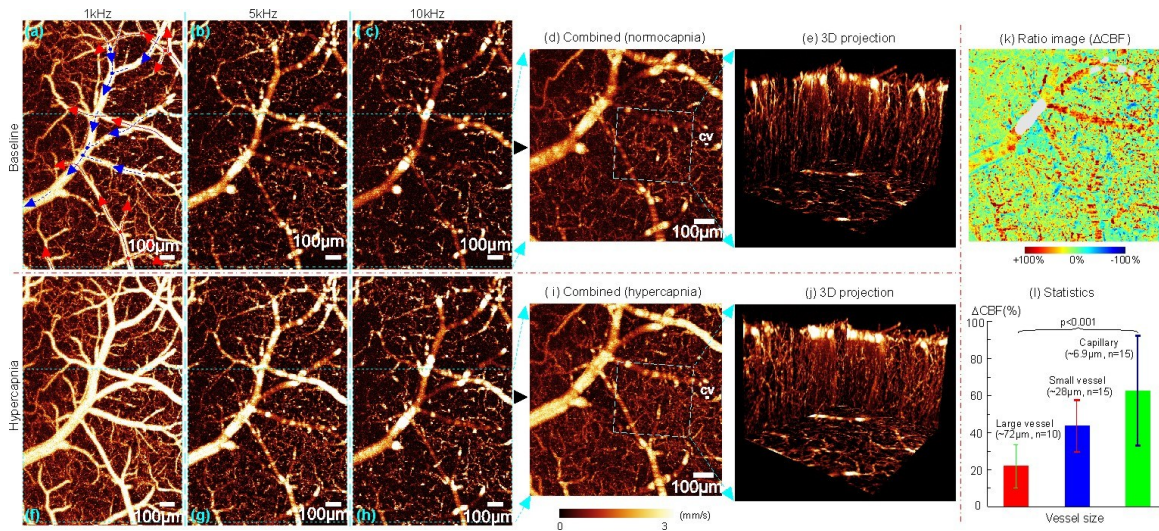


Fig.9.2 3D μ ODT of mouse cortical CBF networks *in vivo*. (d, i): quantitative CBF images with enhanced sensitivity (0-3mm/s) by phase unwrapping. k, l): hypercapnia-elicited CBF changes in vessels of different caliber. Red, blue arrows in (a): arteriolar and venous flows. Image size: $1.6 \times 1 \text{mm}^3$; CV in (d, i): a capillary vessel chosen to perform pc- μ ODT in Fig.9.3.

Fig. 9.2 shows quantitative 3D μ ODT images of cortical CBF networks in normocapnia vs. hypercapnia. As CBFs in large branch vessels and capillaries are vastly different, μ ODT acquired at 10kHz (c, h) was temporally down binning (i.e., to prolong

Δt) to 5kHz (b, g) and 1kHz (a, f) and then recombined (d, i) by phase-unwrapping to extend the dynamic range to 0-3mm/s for enhancing flow detection. Owing to significantly improved flow detection sensitivity of PIM and spatial resolution of μOCT , the 3D projection images (e, j) over a small region ($0.4 \times 0.4 \times 0.6 \text{mm}^3$) show abundant microcirculatory CBF networks, in particular, the high turnout of the capillary CBF. Although the CBF increase elicited by hypercapnia was clearly visualized by comparing the corresponding images (e.g., d vs. i or e vs. j), their ratio image ($k=d/i$) exhibits the heterogeneous CBF responses to hypercapnia in the cerebrovascular networks. The statistical figures by student's t tests in Fig. 9.21 indicate that CBF increased $61 \pm 30\%$ in capillaries vs. $42 \pm 14\%$ in small and $22 \pm 12\%$ in large branch vessels.

Fig. 9.3 shows pc- μODT images across a $\phi 5.6 \mu\text{m}$ capillary (CV) in Fig. 9.2(d, i). The two subsets on top of panel a) show the microangiographic (μOCA) and Doppler phase (μODT) images at time points without and with a RBC flowing through the capillary, indicating that the passage of a RBC elicited a predominant phase transient compared to the phase noise induced by the motion artifacts of the vessel wall and of plasma. Thus, by analyzing time-lapse pc- μODT images, important microcirculatory parameters such as RBC flux (RBC counts/s), and v_{RBC} and hematocrit (i.e., fractural volume of RBCs) can be quantified. For instance, by averaging the pc- μODT images within the masked vessel wall over two 0.48s traces, the erythrocyte flux, mean v_{RBC} and hematocrit in normocapnia (a) were $\sim 19/\text{s}$, $v_{\text{N}} = 0.72 \pm 0.15 \text{mm/s}$ and 8.80% during hypercapnia (b), the flux increased 52.6% to 29/s and the mean v_{RBC} increased 36.1% to

$v_H=0.98\pm0.29\text{mm/s}$ (i.e., $\Delta v_{H/N}=36.1\%$) while the hematocrit remained 9.86%. But it is noteworthy that high v_{RBC} fluctuations were evident in most capillaries; therefore, measurements over a longer period of time (e.g., $>1\text{min}$) should have been made. Interestingly, based on Fig. 9.2(d, i), v_{CBF} in the same capillary (CV) measured directly by μODT (Doppler CBF speed) were $v_N\approx0.27\pm0.03\text{mm/s}$ and $v_H\approx0.37\pm0.05\text{mm/s}$, respectively. Taking into account the angle effect of light incidence (e.g., $\theta=57.6^\circ$, $\cos57.6^\circ\approx0.54$), the values could be corrected to $v_N=0.51\pm0.06\text{mm/s}$ and $v_H=0.69\pm0.09\text{mm/s}$. The results indicate that the capillary CBF rates can be markedly underestimated by errors resulting from both uncorrected angles of Doppler measurement (more severe for horizontally oriented flows) and low hematocrit (e.g., $<50\%$). Nevertheless, the relative change ($\Delta v_{H/N}=36.1\pm5.3\%$) by pc- μODT matched that ($\Delta v_{H/N}=35.3\%$) by μODT .

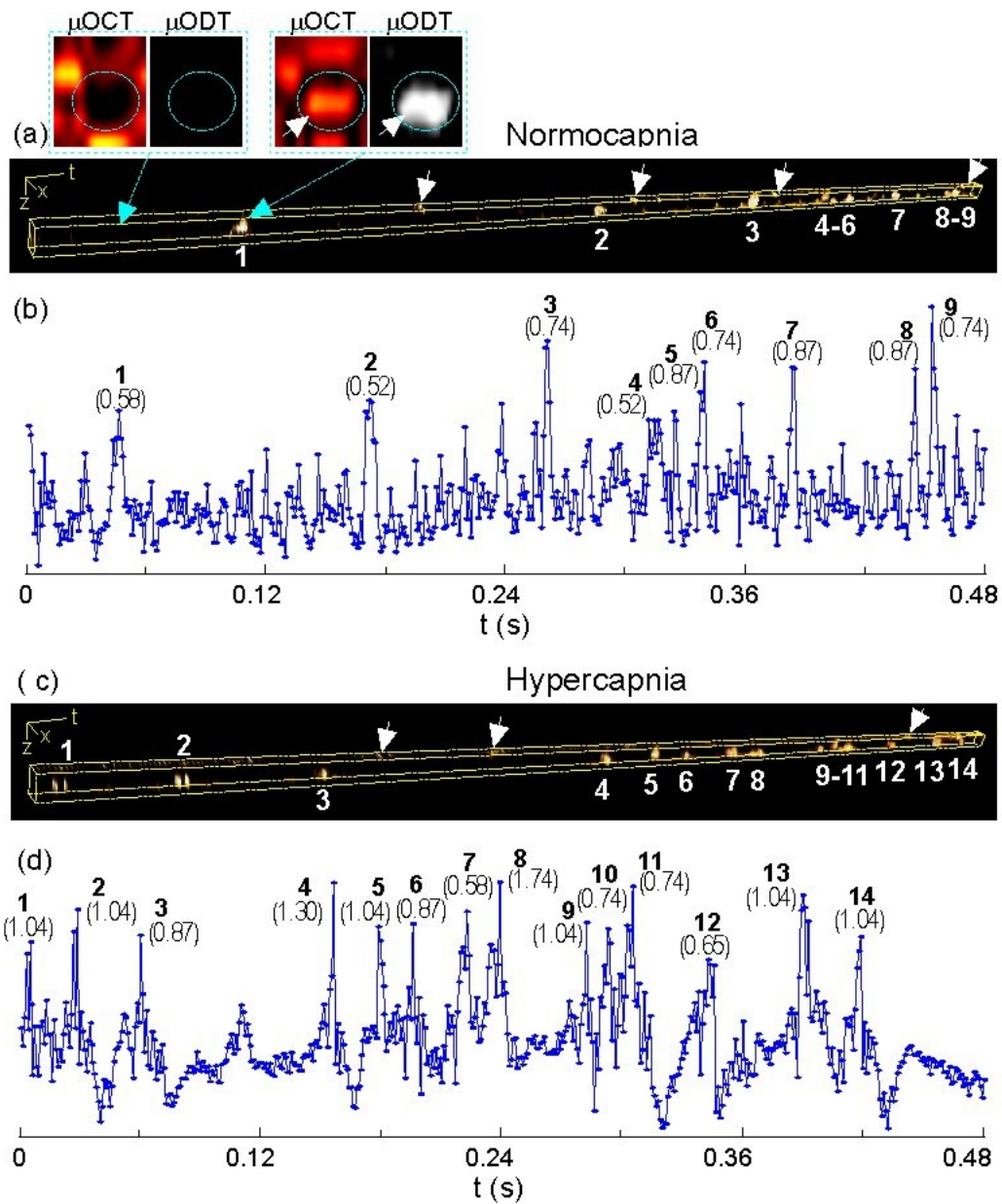


Fig.9.3 Capillary v_{RBC} measured by pc- μ ODT. **a, c):** time-lapse pc- μ ODT images; **b, d):** their RBC traces. Top 2 sublets show the Doppler phase transient with the passage of RBC.

9.4 Discussions & Conclusions

In summary, we present a method pc- μ ODT based on Doppler phase thresholding technique that enables accurate measures of cerebral capillary RBC velocity, and flux and hematocrit with no need of fluorescence labeling (e.g., tracker free). While the Doppler-based μ ODT measures average velocity of all moving scatterers (RBCs) over the camera exposure, pc- μ ODT accurately tracks the velocity of individual RBC (v_{RBC}). For laminar flow (e.g., arterioles or venules in Fig. 9.2), μ ODT provides sufficient accuracy to retrieve their continuous parabolic flow profiles. However, for discrete flow in capillaries, the low hematocrit (e.g., <50%) leads to severe underestimation of v_{RBC} (averaged over time), as confounded by the angle effects. Similar to MPM, pc- μ ODT - although accurate - is unable to quantify large laminar flows. Interestingly, our results in Fig. 9.3 show that, despite underestimation, the hypercapnia-elicited CBF increase ($\Delta v_{H/N}$) measured by μ ODT matched that by pc- μ ODT, suggesting that μ ODT can be suited for quantitative imaging of the CBF changes (ΔCBF) in the cerebrovascular vessels of different calibers (including capillaries). This is crucial for brain functional studies, because μ ODT is a unique neuroimage tool that enables quantitative imaging of changes in CBF networks (both branch vessels and capillaries) at high spatiotemporal resolutions, over a FOV, and without fluorescence dye loading. It is noteworthy that pc- μ ODT may not be able to separate the contributions of RBCs from other moving particles such as white blood cells in the blood stream. In addition, pc- μ ODT at a higher frame rate (e.g., 140kHz by employing new CMOS linescan cameras) and by employing other scanning scheme is being performed to further enhance the temporal resolution for v_{RBC} detection or to

extend the lateral scanning region to allow for simultaneous pc- μ ODT detection of v_{RBC} in multiple capillaries.

Chapter 10 Cerebral Blood Flow Imaged with Ultrahigh-resolution Optical Coherence Angiography and Doppler Tomography

10.1 Introduction

Cerebral blood circulation is essential to preserve the function of a living brain. Visualization and quantification of cerebral blood flow (CBF) can greatly advance our understanding of cerebral microcirculation and hemodynamics. Recent technological advances in OCT-based flow imaging techniques have evolved to two different approaches, i.e., optical coherence angiography (OCA) and Doppler tomography (ODT) for vasculatural visualization and quantitative imaging of CBF in vivo. OCA extracts comprehensive vascular contrast based on image processing methods to separate apparent flows from the background phase noise, including phase-based approach such as optical microangiography (OMAG)¹¹¹ by Hilbert analysis in the lateral direction, Doppler variance method²⁸ by characterizing the broadening of the Doppler spectrum, frame subtraction method⁸³ by high-pass filtering in the slow lateral direction, and speckle variance method¹¹² by analyzing the intensity variance across sequential cross-sections.

Meanwhile, ODT measures the Doppler phase change induced by moving scatterers (e.g., red and white blood cells) to enable quantitative CBF imaging. In addition to phase subtraction method (PSM)²³ which measures the Doppler phase shift between adjacent A-scans, several new algorithms have been reported to enhance flow detection sensitivity, including joint spectral- and time-domain method²⁵ with 2D fast Fourier transform (FFT) analysis, digital frequency ramping method⁷ to circumvent the need of hardware modification for flow quantification, volumetric flow imaging²⁶ by Hilbert analysis to remove background phase noise, and dual-beam approaches^{113, 114} to enable detection of both slow and fast flows. However, it is known that the vascular turnouts provided by speckle contrast OCA surpass those detected by ODT, especially for capillary beds. In this letter, we present experimental results on both flow phantom and in vivo animal (mouse brain following laser-induced microischemia) studies to elucidate the mechanistic differences between these two methods for CBF detections.

10.2 Methods

The imaging platform used in this study -combining 3D ultrahigh-resolution OCA (μ OCA) and ODT (μ ODT)- involved modification of previously reported ultrahigh-resolution spectral-domain OCT (μ OCT) setup⁵⁵, in which a sub-8fs laser was used for ultra-broadband illumination ($\lambda=800\text{nm}$, $\Delta\lambda\approx 128\text{nm}$) to a 2 \times 2 broadband fiberoptic Michelson interferometer. Its reference arm was connected to a grating-lens-based optical delay line (together with a prism pair in the sample arm) to compensate the dispersion

mismatch and maximize the bandwidth (e.g., $\Delta\lambda_{cs} \geq 154\text{nm}$) of the cross-spectrum ($S_{cs}(\lambda) \equiv [S_s(\lambda) \cdot S_r(\lambda)]^{1/2}$) between the sample and reference arms ($S_s(\lambda)$, $S_r(\lambda)$: sample and reference power spectra), so that an axial resolution (i.e., coherence length $L_c = 2(\ln 2)/\pi \cdot \lambda^2/\Delta\lambda_{cs}$) of $1.8\mu\text{m}$ in brain tissue was reached. Light from the sample arm was collimated, scanned transversely by a precision servo-mirror (x-, y-axes), and focused by an f16mm/NA0.25 microscopic objective (e.g., transverse resolution: $\sim \phi 3\mu\text{m}$) on the capillary beds of mouse cortex through a cranial window. The back scattered light from cortical brain at different depths (along z-axis) was collected back to the sample arm and recombined with the reference light to be detected by a spectral imager in which the collimated light ($\phi 10\text{mm}$) was spectrally diffracted ($1200^{-1}/\text{mm}$) and focused ($f=85\text{mm}$) onto a linear CCD camera (2048pixels, Atmel) running at 27kHz. Synchronizing the CCD camera with sequential x-scans (e.g., 500 pixels), 2D μOCT (z-x image) was acquired at $\sim 54\text{fps}$ and streamlined via camera link to the hard disks (300MB/s, Raid 0) of a workstation for parallel 2D/3D image processing and display by inverse FFT. However, unlike μOCT for architectural imaging, specific scanning schemes were implemented to facilitate simultaneous μOCA and μODT for in vivo visualization of microvascular networks and quantitative imaging of capillary CBF. For μOCA imaging, the camera was configured at its highest rate (27kHz) to acquire 4 consecutive $I(z, x)$ images per z-x plane (e.g., $I_j(z, x) = \text{FFT}^{-1}[I(k, x)/k^j]$, $j=0 \rightarrow 3$); thus, μOCA could be expressed as their relative standard deviation ($\sigma_{OCA}(z, x) = \Sigma |I_j(z, x) - I(z, x)| / (4I(z, x))$), where $I(z, x) = \Sigma I_j(z, x) / 4$, $j=0 \rightarrow 3$) based on modified speckle contrast approach¹¹². For

μ ODT imaging, the camera was configured to acquire at 10kHz (down binned to 5, 1 kHz) and the Doppler flow images were reconstructed by our newly developed phase-intensity-mapping algorithm (PIM)¹⁰⁹ for enhancing CBF detection sensitivity.

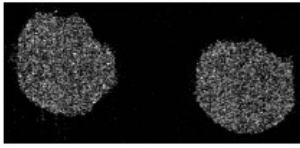
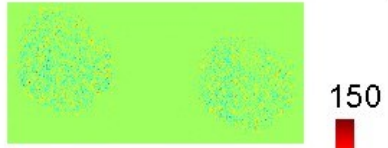
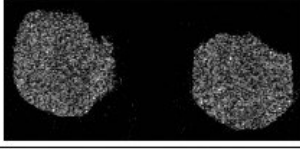
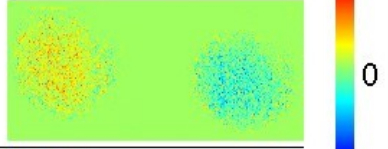
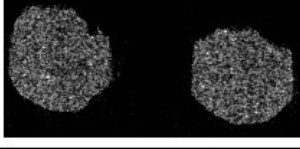
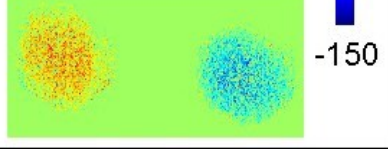
| Pump Rate | Flow Rate | μ OCA | μ ODT ($\mu\text{m/s}$) |
|---------------------|----------------------|--|---|
| 0 $\mu\text{L/min}$ | 0 $\mu\text{m/s}$ |  |  |
| 1 $\mu\text{L/min}$ | 23.6 $\mu\text{m/s}$ |  |  |
| 2 $\mu\text{L/min}$ | 47.2 $\mu\text{m/s}$ |  |  |

Fig. 10. 1 Comparative results of μ OCA and μ ODT for bi-directional flows in a translucent $\phi 280\mu\text{m}$ capillary tube at the pump rate of $v_p=0, 23.6$ and $47.2\mu\text{m/s}$. While the nondirectional flow imaged by μ OCA was offset by Brownian motion and only exhibited minor increase with v_p , the directional flow imaged by μ ODT varied linearly with v_p

10.3 Results

A flow-phantom study was performed to compare the differences between OCA and ODT for flow detection, in which 0.5% intralipid in a translucent capillary tubing ($\phi 280\mu\text{m}$) was driven by a precision syringe pump (CMA400, Microdialysis) for accurate flow rate control. The bidirectional capillary tubes were immersed in a solidified scattering scaffold by mixing 0.5% intralipid with 1% agarose to mimic brain tissue. The micro fluidic chamber was tilted $\theta \approx 85^\circ$ to the OCT beam to reduce apparent Doppler

flow. Fig. 10.1 compares the results of μ OCA and μ ODT at the pump flow rate (v_p) of 0, 23.6, 47.2 $\mu\text{m/s}$. At $v_p=0\mu\text{m/s}$ (with pump stopped and exhaust curtailed), μ ODT showed no directional flow ($v_{ODT}\approx 0$) as expected. In contrast, μ OCA showed that the speckle contrast in the tubes ($\sigma_{OCA}=16\text{k counts}$)-representing their flows- was significantly higher than that of background noise level ($\sigma_b=10\text{k counts}$), resulting from Brownian motion of solidified scaffold (scatterers) and the system noise. These results indicate that unlike μ ODT that detected directional flow (i.e., random Brownian motion was canceled), μ OCA detected random motion within the tubes. This implies that the higher sensitivity of μ OCA for detecting microvasculature was likely contributed from the Brownian motion of scatterers within the blood vessels including capillaries rather than directional flow (CBF). For instance, when the pump rate was increased to $v_p=23.6, 47.2\mu\text{m/s}$ ($\sim 15\text{min}$ was allowed to stabilize flow in each case), the results showed that μ ODT was able to identify directional flows and their flow rate increase; whereas μ OCA based on speckle contrast exhibited minor increase, likely due to the high offset of Brownian motion.

For more quantitative analysis of the differences between these two approaches, we measured the changes of μ OCA and μ ODT with gradual increases of the pump rate v_p from $0\mu\text{m/s}$ to $35\mu\text{m/s}$. At each v_p , the μ ODT image was reconstructed and a small circular area around the tube center was selected as the region of interest (ROI) and its mean flow velocity was calculated to represent its flow rate (v_{ODT}). Fig. 10.2 illustrates the quantitative analysis, in which curve fitting showed a close linear correlation between

μ ODT data v_{ODT} and the pump rate v_p ($R^2=0.98$). On contrary, the non-directional flow index (σ_{OCA}) behaved very differently as shown by the red triangles. For $v_p \leq 12 \mu\text{m/s}$, $\Delta\sigma_{OCA} \approx 5\text{k}$ counts due to predominant Brownian motion and remained unchanged; for $v_p > 12 \mu\text{m/s}$, it increased slightly with v_p . Quantitative analysis in Fig. 10.2 confirms that the high vasculatural detectability of μ OCA was mainly attributed to the Brownian-motion offset ($\Delta\sigma_{OCA} \approx 5\text{k}$ counts). More importantly, μ ODT provided better sensitivity for detecting directional flow and the minimal detectable flow rate ($v_{ODT} \approx 5 \mu\text{m/s}$, with no offset) was substantially lower than that of μ OCA which was under Brownian-motion limit with a large offset of $\Delta\sigma_{OCA} \approx 5\text{k}$ counts in the phantom study.

To further validate these phenomena in vivo, we applied a mouse cerebral microischemia model. In this study, CD-1 mice (8 weeks old) were anesthetized with inhalational 2% isoflurane and then mounted on a custom stereotaxic frame. A $\phi 5\text{mm}$ cranial window was created on the somatosensory motor cortex with the dura left intact. The exposed brain surface was covered by 1% agarose gel and sealed with a glass coverslip. After μ OCA pre-scan to accurately locate the coordinates of individual blood vessels, a pigtailed green laser (532nm, 60mW) was interconnected via the sample arm to disrupt the vessels (2min exposure for capillary CBF and multiple exposures for intermediate CBF). The physiology of mice, including electrocardiography (ECG), respiration rate and body temperature, was continuously monitored.

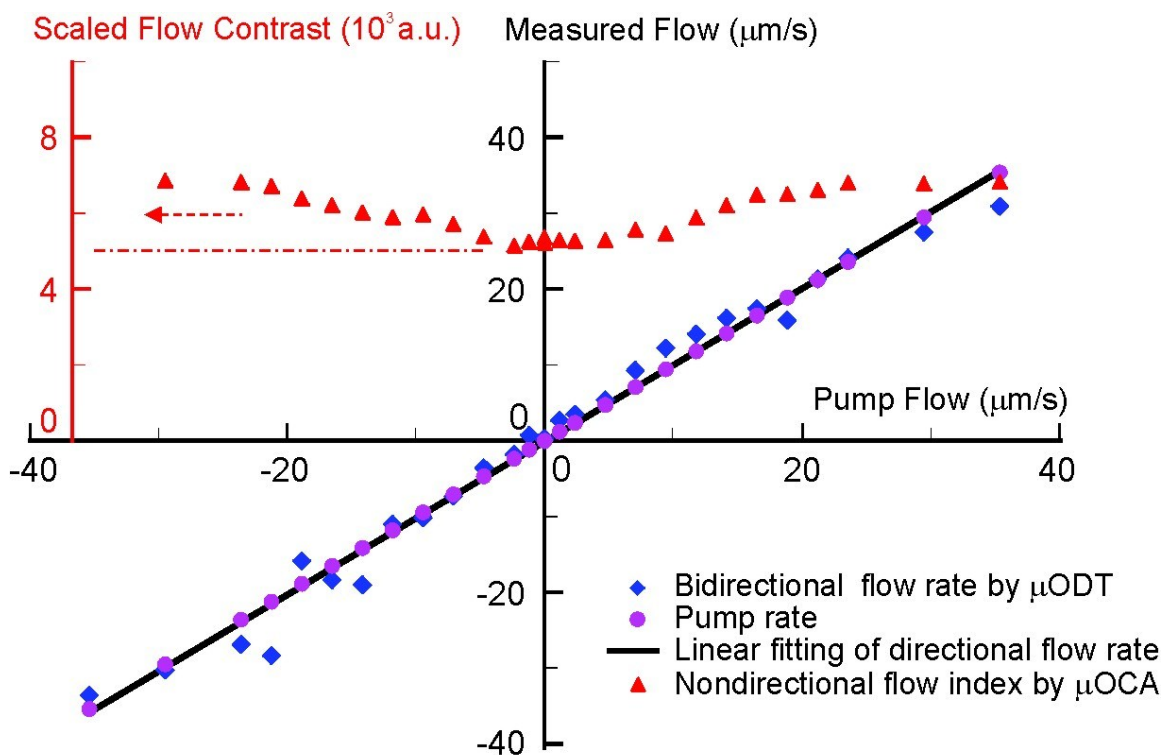


Fig. 10. 2 Quantitative analyses of the flow-rate changes of directional flow by μ ODT and non-directional flow by μ OCA with the pump rate v_p . μ OCA provided high sensitivity for detecting vasculature of minute slow flows due to the enhancement by random Brownian motion ($\Delta\sigma_{OCA}\approx 5k$ counts), μ ODT was able to detect directional flow velocity at an ultrahigh sensitivity of $v_{ODT}\approx 5\mu\text{m/s}$ in flow-tissue phantom.

Fig. 10.3 shows the comparison results of μ ODT (pseudo color) and μ OCA (grayscale) over a field of view of $2\times 2\text{mm}^2$ on mouse cortical brain. Because of ultrahigh resolution ($\sim 1.8\times 3\mu\text{m}^2$) of μ OCT, high vasculatural details including capillary beds (e.g., $\phi 3\text{-}8\mu\text{m}$ capillaries) were readily visualized by μ OCA. Furthermore, the enhanced flow sensitivity by PIM allowed for detection of the quantitative CBF networks, especially minute slow CBFs (e.g., $\leq 10\mu\text{m/s}$) in capillaries, with almost identical vascular densities as those by μ OCA. To compare with the baseline data (panels a, b), upper half (c, d) and

lower half(e, f) panels show laser disruptions of a $\phi 35\mu\text{m}$ (1) and a $\phi 27\mu\text{m}$ (2) branch arterioles whose locations are marked by 2 green dots. As shown in μODT images (d, f), the downstream CBFs including those in the

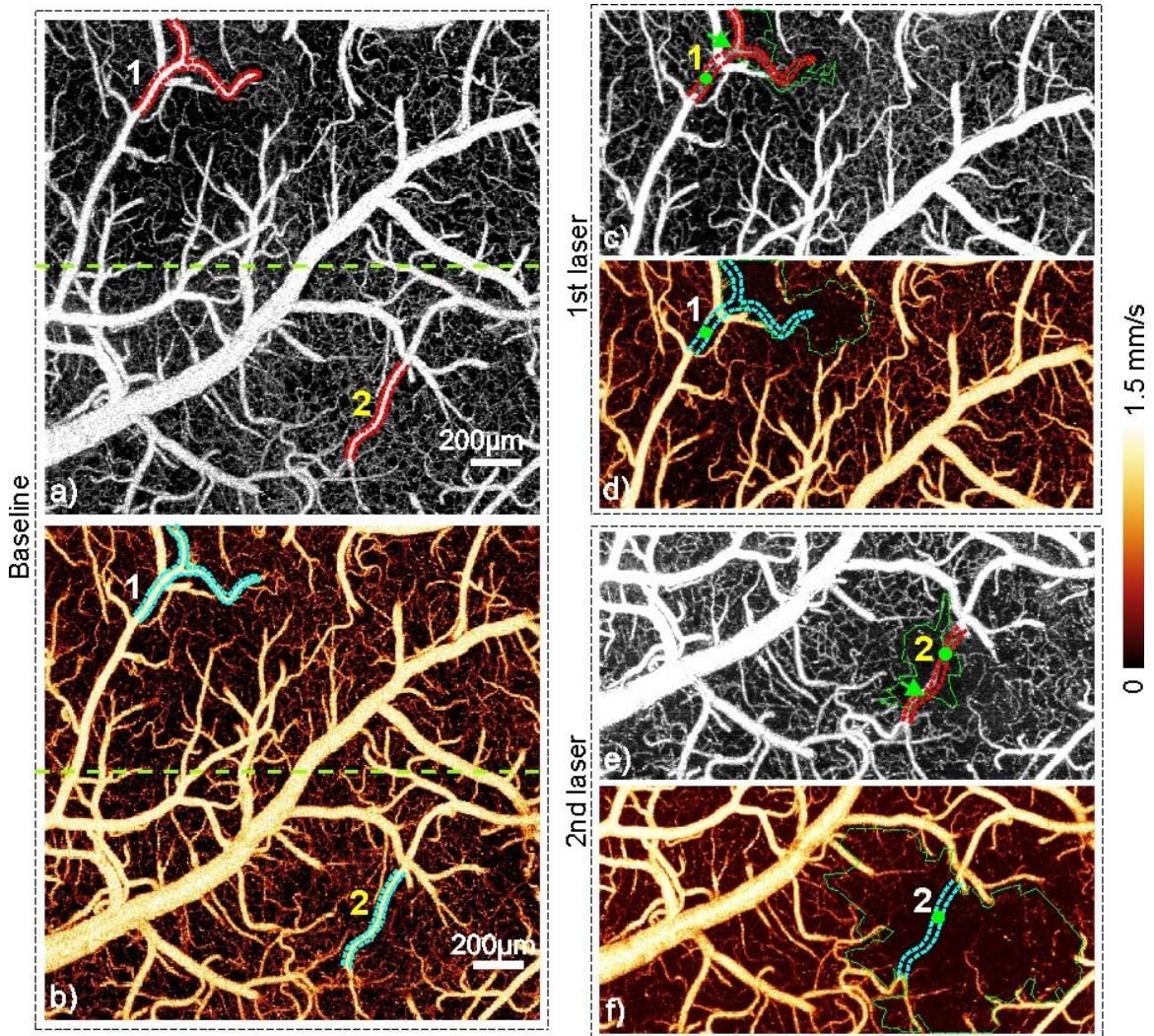


Fig. 10.3 Comparative μOCA (upper panels) and μODT (lower panels) images of mouse cortical brain in vivo during baseline (a, b), after 1st (c, d) and 2nd (e, f) laser coagulations that induced microischemia. The locations of laser disruptions are marked with green dots. The dashed green circles highlight the spreading of CBF showdowns due to laser disruptions of 2 arterioles. Apparently, because of offset by Brownian motion, the areas of vasoconstriction (i.e., CBF shutdown) in μOCA were smaller (underestimated) than those in μODT . Except at the coagulation spots, the disrupted vessels (both up- and down-streams) remain visible (although dimmer) due to Brownian motion.

interconnected capillary beds diminished in 2 dashed green circles (the margins were determined by segmentation of ratio image, i.e., $\Delta=(d-b)/b$ or $(f-b)/b$ using threshold $\Delta \leq -35\%$). In other words, the CBFs in those vessels were deactivated as a result of laser disruptions. On contrary, the vascular shutdown of capillary beds by 2 laser disruptions (e.g., dashed green areas segmented with $\Delta=(c-a)/a$ or $(e-a)/a$ using threshold $\Delta \leq -35\%$) was drastically smaller in μ OCA images. Interestingly, except those in close proximity to the disrupted spots (1, 2) where laser thermal coagulation might either solidify the blood or dramatically increase its viscosity that tranquilized Brownian motion, the speckle contrast signals within the arterioles (at $\sim 100\mu\text{m}$ downstream) remained to be visualized, as highlighted by green arrows (decreased -28% for 1 and -24% for 2 by μ OCA vs. over -95% by μ ODT). This was attributed to the contrast enhancement by the Brownian motion of blood inside the deactivated vessels. Therefore, the results of this in vivo study further validate that, while μ OCA may detect more vasculatures such as capillary beds due to Brownian motion enhancement, μ ODT provides more sensitive CBF quantification (e.g., unidirectional flow) and is thus more suitable for brain functional studies.

10.4 Discussions & Conclusions

In summary, we present new experiments to elucidate the differences between OCA (speckle contrast based) and ODT for imaging cerebral hemodynamic responses to functional brain activation and neurotoxicity. Although both μ OCA and μ ODT

techniques are based on detecting Doppler phase shift of moving backscatterers, our tissue-flow phantom and *in vivo* mouse brain studies suggest that these 2 approaches operate under different regimes of flow-induced motion detections. In the low-flow domain, μ OCA provides high vascular turnouts resulting from the enhancement of Brownian motion of free-moving red and white blood cells within the blood vessels. This renders μ OCA to visualize more vasculatural networks, including deactivated branch vessels as evidenced by the images of no-flow tubes (Fig. 10.1) and laser disrupted arteriolar branches (Fig. 10.3c,e). On contrary, μ ODT detects directional flows and is thus more suitable than μ OCA for studying cerebral hemodynamic responses to brain functional changes. By combing ultrahigh resolution of μ ODT and high phase sensitivity of PIM, we are able to readily detect microvascular CBF with capillary details (e.g., ϕ 3-8 μ m capillaries) and at ultrahigh sensitivity ($\leq 10\mu\text{m/s}$). It is noteworthy that more work is needed to compare the results of flow detectability by other OCA approaches (e.g., phase-based OMAG or DFR-OCT) and the potential differences of Brownian motion offset value between intralipid ($\Delta\sigma_{OCA} \approx 5\text{k}$ counts) and blood (potentially lower, due to less Brownian motion) in capillary tubes of smaller sizes (e.g., ϕ 100, 30, 8 μ m).

Chapter 11 Enhanced Optical Doppler Tomography System to Investigate the Chronic Cocaine Effects on the Brain

11.1 Introduction

Investigations into the mechanisms of drug addiction play a crucial role in understanding the rewarding system of the brain.^{115, 116} Cocaine challenge is an established model¹¹⁷ for drug addiction research and has been extensively studied through conventional imaging methods (e.g., fMRI, PET)¹¹⁸. These approaches provide excellent results based on the whole brain at macroscopic level. However, due to limited resolutions (e.g., ~1mm), responses from different compartments at different calibers cannot be fully resolved. Recently, optical imaging methods, in particular, optical coherence tomography (OCT), shed light on the cocaine study because of its high resolution at large FOV. In Chapter 8, we reported on a new technique developed by our group- ultrahigh resolution optical Doppler tomography (μ ODT) for label free quantitative cerebral blood flow imaging at capillary level¹⁰⁹. With intravenous cocaine challenge, this technique uncovered that CBF responses varied substantially among

different vessels, and cocaine induced microischemia in some arteriolar branches lasted for over 45 minutes and this effect was exacerbated with repeated cocaine administration¹⁰⁹. However, that study focused on understanding the acute cocaine effects. To better understand the clinical cocaine addiction mechanisms, investigation into the vascular responses to chronic cocaine challenge is desired.

Several established rodent models have been developed for chronic cocaine study, including the cocaine self-administration rat model, congenital learned helplessness (cLH) chronic treated rat model, and intraperitoneal cocaine treated mouse model. Meanwhile, technical advances in optical design, contrast agent and scanning protocol development have dramatically improved the performance of our current ODT system. In this Chapter, we study the chronic cocaine effect based on several rodent models by our enhanced ODT system.

11.2 Materials and Methods

11.2.1 System Setup

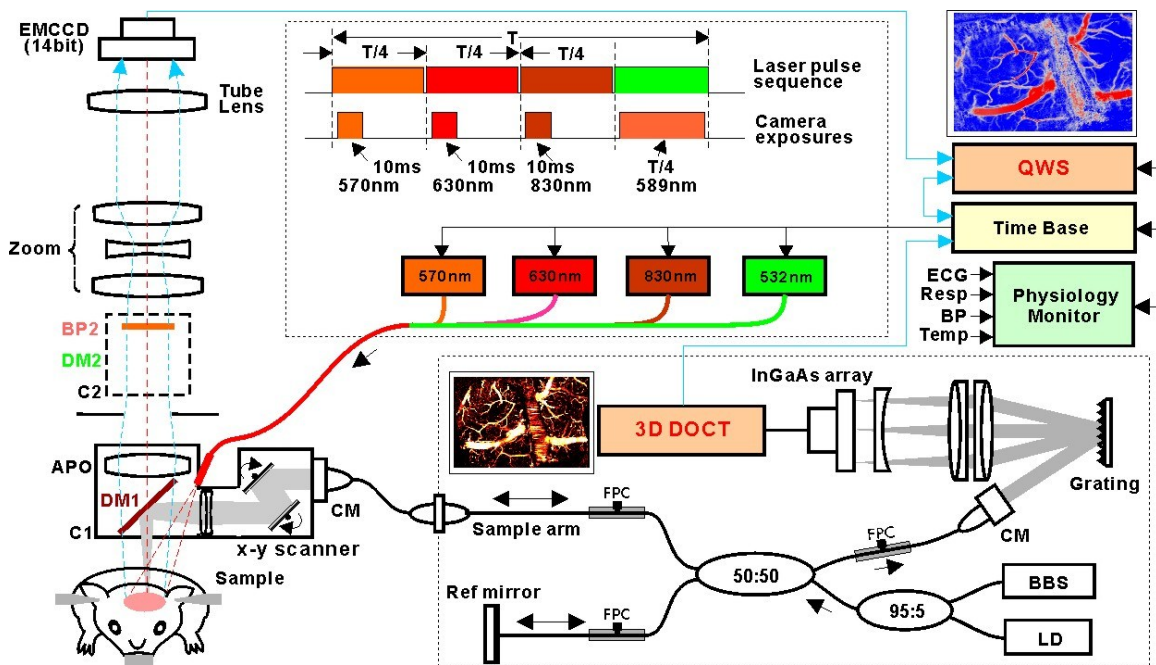


Fig. 11.1 Setup of the enhanced optical Doppler tomography system.

Fig. 11.1 shows the enhanced ODT system. A high speed 3D Doppler OCT system was integrated into the multimodality microscope system through a home designed objective adapter. A broadband pigtailed light source with $\sim 90\text{nm}$ bandwidth at 1300nm central wavelength was employed to provide illumination for the fiberoptic Michelson interferometer. In the reference arm, the beam was collimated to pass through a wedge prism pair and focused onto a high reflective mirror to minimize the dispersion and match the path length with the sample arm. In the sample arm, the beam was collimated to 5mm and transversely scanned by a pair of galvo scanners and deflected by a hot mirror onto the stereoscope optical path, and then focused by an achromate onto the biological tissue under examination. Light back scattered from the reference and sample arms was recombined and detected in the detection arm through a home built high speed

spectrometer, in which light exiting the single mode fiber was collimated to 10mm, linearly dispersed by a holographic grating, and focused by an achromatic lens group onto a high speed InGaAs line scan camera (Sensors Unlimited Inc., NJ, USA). The OCT engine runs at an A-line rate of 47kHz with lateral and axial resolutions of 12 μ m and 8 μ m respectively.

11.2.2 Animal Model

Chronic cocaine treated rats were anesthetized and ventilated with 2% isoflurane mixed with 100% oxygen through the surgical procedures. A $\sim\phi$ 7mm cranial window was created on the frontal cortex. After the dura was carefully removed, the exposed brain was covered with 2% cerebrospinal fluid based agrose gel and then affixed with a 100 μ m-thick glass coverslip using biocompatible glue. A bolus of cocaine (1mg/kg, i.v.) was administered through the femoral vein followed by 0.5cc saline to induce cocaine challenge. During the experiment, the physiology of the animal, including electrocardiography (ECG), mean arterial blood pressure (MABP), respiration rate and body temperature, was continuously monitored (SA Instruments, Stony Brook, NY, USA). Moreover, the blood gases were measured (ABL 700, Radiometer Medical) to make sure the animal remained under normal physiological condition. For chronic treated mice, no ventilation was applied. The cranial window size was also reduced to $\sim\phi$ 5mm, and the dura of the brain was kept intact through the whole experiment. All of

the animal procedures were approved by the Institutional Animal Care and Use Committee of Stony Brook University.

11.2.3 Intralipid as a Contrast Agent

Intralipid is a fat emulsion of soy bean oil, egg phospholipids and glycerin, and was approved by FDA in 1972 for intravenous administration as a source of energy and nutrition. Because of its high similarity in backscattering property compared with biological tissue, intralipid has been widely used as a phantom to mimic tissue for biomedical optical imaging studies. Here, for the first time, we discovered that intralipid can be applied as a contrast agent to substantially improve the performance of capillary blood flow imaging *in vivo*. Compared with other contrast agents, intralipid is safe, low cost and highly efficient. Prior to the ODT data acquisition, 20% intralipid (e.g., 0.15ml) was quickly injected into the blood stream intravenously through a 30 gauge tail vein needle catheter.

11.2.4 Scanning Protocol

To decode the vascular information at different sensitivity levels, several different scanning protocols were applied during the ODT data acquisition. First, the vasculature of the rodent brain was delineated in 3D through angiographic imaging, in which four repeated B-scans were performed at the same lateral location. The minute speckle

contrast change derived from the intensity images represents the moving particles inside the vessels. Then a raster scan was applied across the imaging FOV to achieve 3D imaging of the brain vasculature. The total imaging time for a $5 \times 5 \times 3 \text{mm}^3$ 3D volume is less than 30s. The angiographic scans were performed at the baseline before the cocaine challenge, 2 minutes after cocaine challenge and 30 minutes after cocaine challenge. These volumetric datasets therefore record the dynamic vasculature responses to cocaine challenge at several critical time points. Under time sharing mechanism, quantitative 3D Doppler flow velocity map was also recorded simultaneously. As a quantitative imaging method, ODT imaging provides cerebral blood flow rate responses to the cocaine challenge at a higher sensitivity. In order to record the dynamic cocaine responses at a higher temporal resolution (e.g., $<10\text{s}$), a BM mode scanning was performed through the whole experiment for ~ 45 minutes at 1f/s. During the BM mode scanning, a line of interest was selected to intersect different sizes of arterials and veins. Continuous B mode scans were then performed on this line of interest. The data recorded were all streamlined to the solid state hard drive on the workstation computer via Camera link interface, waiting for further advanced signal processing.

11.3 Results

11.3.1 Imaging Results of Enhanced 3D ODT

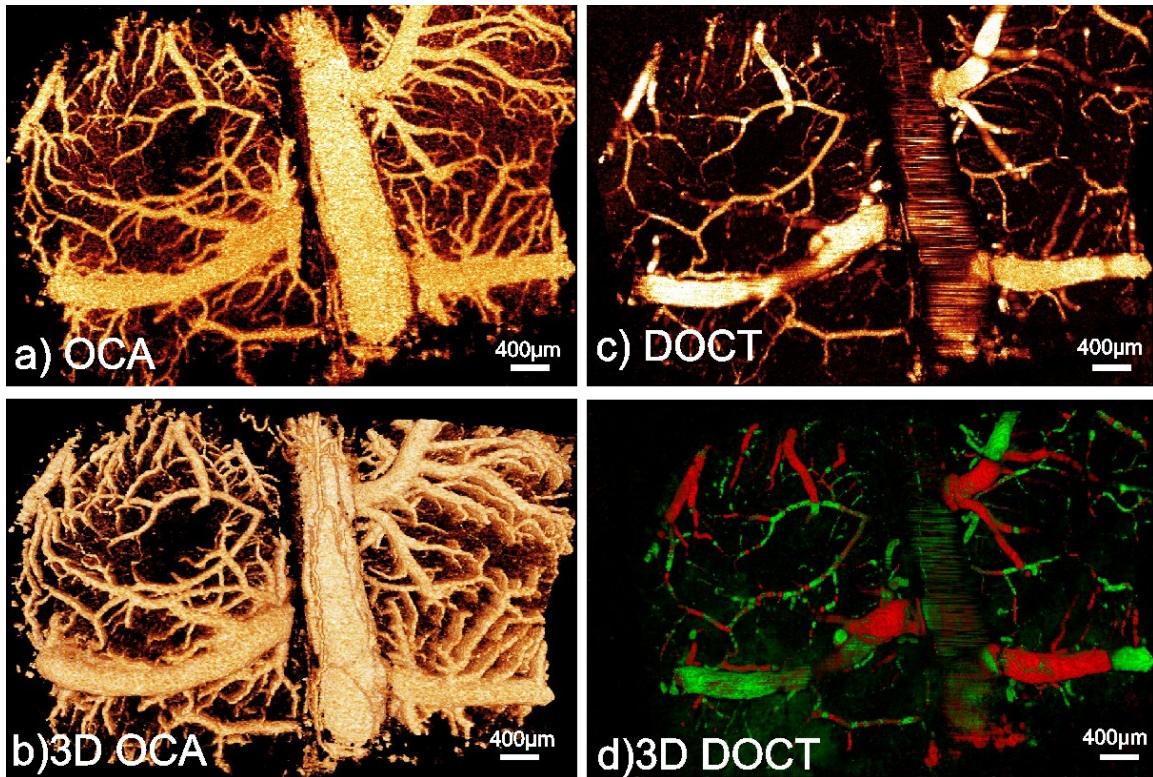


Fig. 11.2 Results of CBF imaging from enhanced 3D ODT system.

Fig. 11.2 shows the CBF imaging results of a chronic cocaine treated rat from our enhanced 3D ODT system. Fig. 11.2 a) shows the MIP angiographic image of the rat brain. Since angiographic imaging is sensitive to motions in any direction, arterioles and venules that are smaller than $30\mu\text{m}$ can still be visualized as continuous vessels. Angiographic image provides excellent vasculature information at high sensitivity. Fig. 11.2 b) shows the 3D angiographic image of the same FOV. As a 3D imaging modality, OCA provides accurate spatial location information of the vessels, which is critical for Doppler angle correction, vein and artery separation as well as 3D visualization. Not only the vasculature information, but also the quantitative blood flow velocities can be retrieved through our enhanced ODT system. Fig. 11.2 c) shows the corresponding ODT

flow velocity map recorded simultaneously. The flow velocity was color coded, in which brighter means faster flow velocity, while dimmer means slower flow velocity. Compared with Fig. 11.2 a), even though the vascular turnouts seem to be lower, Fig. 11.2 c) provides a live “traffic map” of the rodent brain, which can be more critical for functional studies. Since Doppler effect is sensitive to the directions of the moving target (e.g., approaching, blue shift; far away, red shift), therefore, we can reconstruct a 3D Doppler directional map based on the ODT data set. Combining Fig. 11.2 b) and Fig. 11.2 d), as explained in Chapter 8, veins and arteries can be differentiated.

11.3.2 Flow Contrast Enhancement by Intralipid

Fig. 11. 3 shows the comparison of contrast enhancement by saline and the same amount of intralipid. The upper panel shows the angiographic images at baseline, after 0.15ml saline injection and after 0.15ml 20% intralipid injection. After saline injection, the contrast of the flow signal doesn't change. However, after intralipid administration, the whole field, in particular, the capillary bed lighted up, which indicated an increase of the flow contrast.

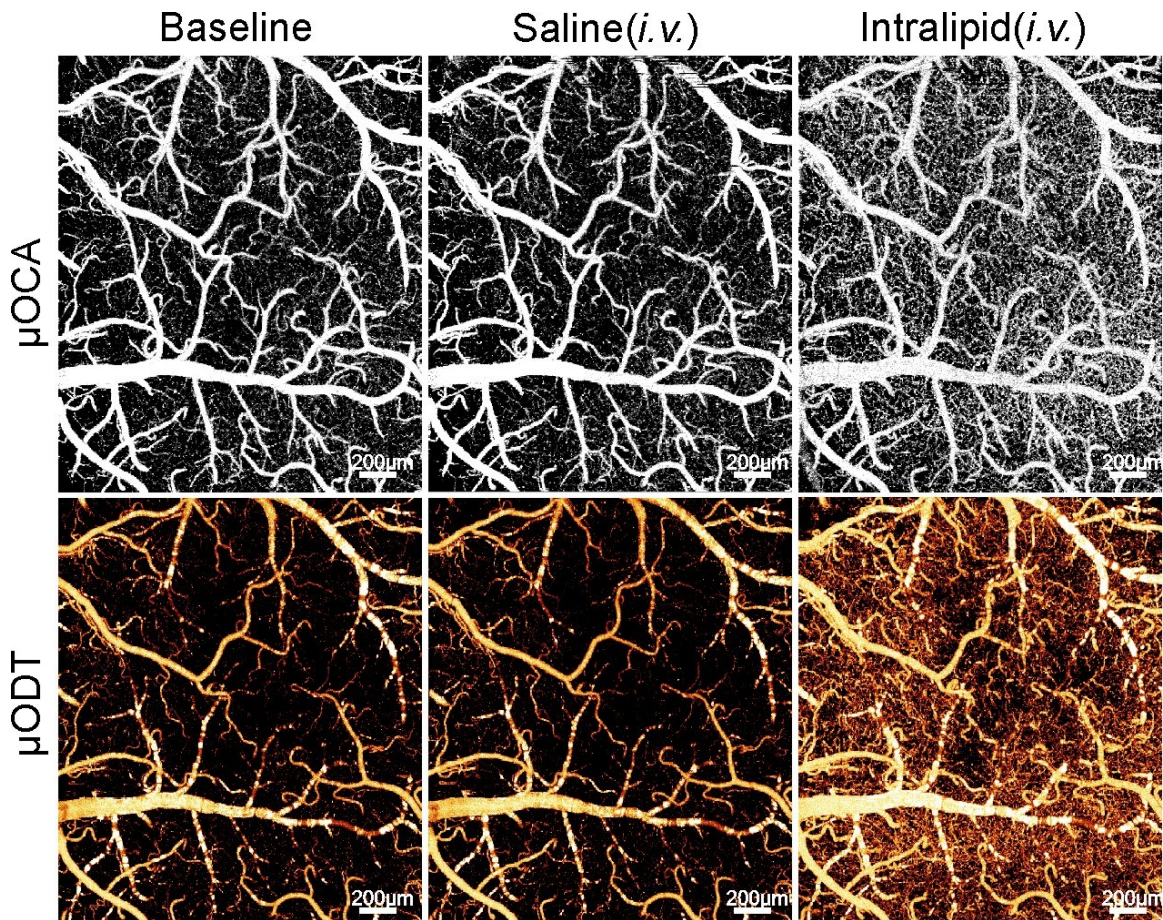


Fig. 11.3 Comparison of contrast enhancement by saline and the same amount of intralipid.

The bottom panel shows the corresponding Doppler flow images at baseline, after saline injection and after intralipid administration. Similar as angiographic images, the flow contrast didn't change after saline injection. However, after intralipid administration, the Doppler flow signals increased substantially. To quantify the accurate contrast enhancement by intralipid, statistical analysis was performed by randomly selecting vessels from the FOV, and the quantitative results are shown in Fig. 11. 4. At baseline, the average flow velocity was $90.7 \pm 30.9 \mu\text{m/s}$. After saline injection, the average flow velocity was $92.3 \pm 33.9 \mu\text{m/s}$, which remains similar as the baseline flow

velocity. However, after same amount intralipid injection, the average blood flow velocity increased to $299.5 \pm 36.7 \mu\text{m/s}$, which is about three times as the baseline flow velocity. Student's t-test reveals that this increase is statistically significant ($p < 0.001$), and confirms the contrast enhancement in Fig. 11. 3.

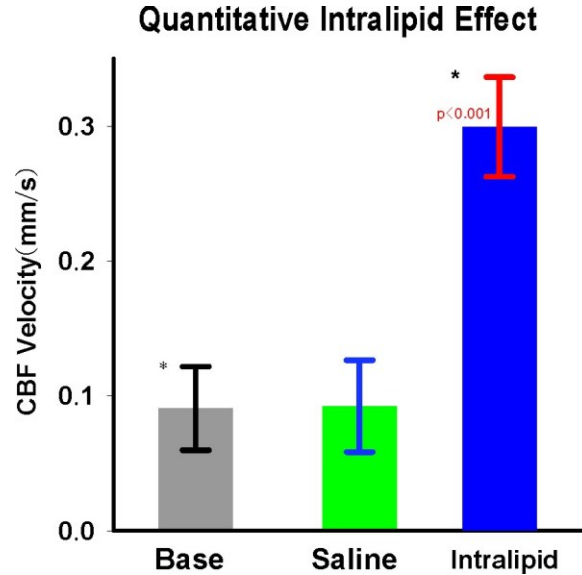


Fig. 11.4 Quantitative intralipid effect on CBF velocity and statistical analysis

11.3.3 Cocaine Self-Administration Rat

Fig. 11.5 shows the results of CBF responses to cocaine challenge of control, short access (SA) and long access (LA) rats. Fig. 11.5 a) shows the dynamic response from a control rat. The response profile can be divided into three phases. Phase I, the CBF velocity decreased immediately after cocaine administration, and the amplitude was about 20% less than the baseline. Phase II, CBF velocity quickly recovered to the baseline level within 5 minutes. Phase III, CBF overshoot to about 40% higher than the baseline and lasted until 30 minutes after cocaine administration. Unlike control rat, the

cocaine treated LA rat exhibited quite different response pattern, which is shown in Fig. 11.5 c). Phase I, the CBF velocity also decreased quickly, however, to a lower level which is about 60% of the baseline flow velocity. Unlike Phase II in the control rat, the CBF velocity remained a lower level (e.g., 60% of baseline) for ~20 minutes. Then, during Phase III, the CBF gradually recovered and increased to a level about 15% higher than baseline. Fig. 11.5 b) shows the response pattern of a SA rat, which appears to be a transition pattern from control rat to LA rat. During phase I, the CBF velocity decreased to a level of ~80% of baseline, which is very similar as a control rat. Phase II, the CBF recovered quickly to the baseline level. Phase III, the CBF velocity remained at a level close to baseline for more than 30 minutes, and no overshoot was observed.

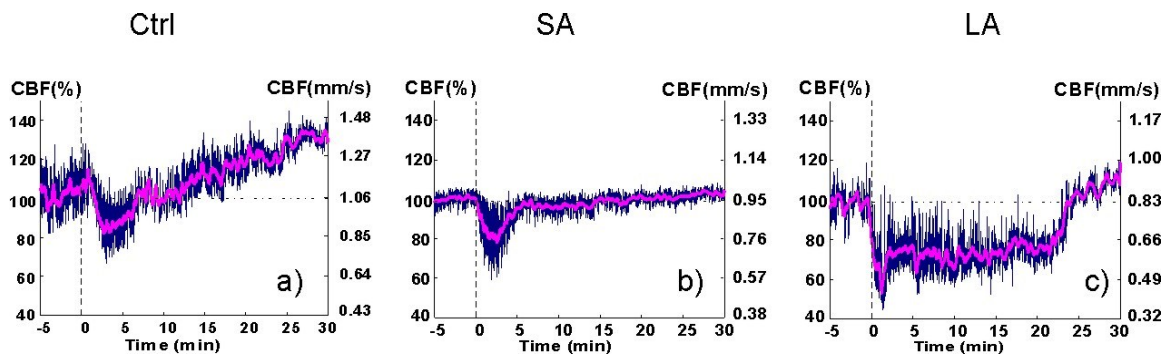


Fig. 11.5 CBF responses to cocaine challenge of control , short access (SA) and long access (LA) rats.

11.3.4 Congenital Learned Helplessness (cLH) Rat

Fig. 11. 6 shows the results of CBF responses to i.v. cocaine challenge of SD saline treated rat, SD cocaine treated rat, cLH saline treated rat, cLH cocaine treated rat at somatosensory cortex and cLH cocaine treated rat at frontal cortex. cLH is a rodent

depression model developed by scientists at Brookhaven National Lab. In this study, SD rats were chosen as the control group for cLH model, and saline treatment was performed as the control for cocaine effect investigation. As shown in Fig. 11.6, the blue curve represents the CBF response to i.v. cocaine challenge of SD rats with saline treatment. The CBF velocity decreased immediately after the cocaine injection, then quickly recovered to the baseline level within five minutes, and eventually overshoot, which is similar as the CBF response of control rat in Fig. 11.5. The red curve shows the CBF response of SD rats with cocaine treatment. After cocaine injection, the CBF velocity decreased quickly. However, different from the saline treated rat, the CBF velocity never came back and remained lower than the baseline level until 30 minutes after cocaine injection. The black curve shows the CBF response of cLH rat with saline treatment. Compared with the SD saline treated rat, the amplitude of CBF response is slightly lower and delayed. The pink curve shows the result of cLH rat with cocaine treatment. Within 10 minutes after cocaine injection, the CBF response is similar as the red curve (SD rat with cocaine treatment). However, 15 minutes after cocaine injection, the CBF of cLH rat gradually recovered to the baseline level. The green curve shows the result of frontal CBF response of cLH rat with cocaine treatment, which shows different pattern as the CBF response in the somatosensory area.

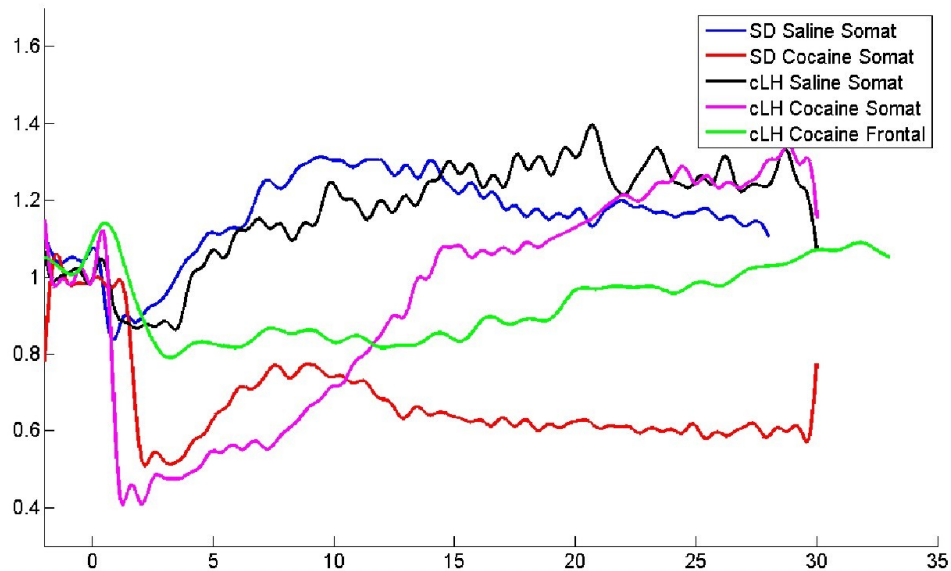


Fig. 11.6 CBF responses to cocaine challenge of SD saline treated rat, SD cocaine treated rat, cLH saline treated rat, cLH cocaine treated rat at somatosensory and cLH cocaine treated rat at frontal cortex.

11.3.5 Vascular Density of Cocaine Treatment Mice

Studies have shown that Dopamine receptors are linked to the genes which are responsible for controlling the vascular growth. In order to investigate the vascular density difference between control mouse and chronic cocaine treated mouse, OCA and ODT scans were performed on the mouse brain, and the typical results are shown in Fig. 11.7. The upper panel shows the OCA results of control mouse (left) and cocaine treated mouse (right). Since OCA image represents the vasculature information. A direct visualization reveals that the vascular density of cocaine treated mouse brain is higher than that of the control one. The bottom panel shows the corresponding ODT results, in

which the blood flow velocity was color coded with the same color bar. Since flow velocity in capillary fluctuates substantially, if we compare the flow velocities within the large branch vessels, on average, the CBF velocity of control mouse is higher than that of the cocaine treated mouse. However, these observations are all qualitative.

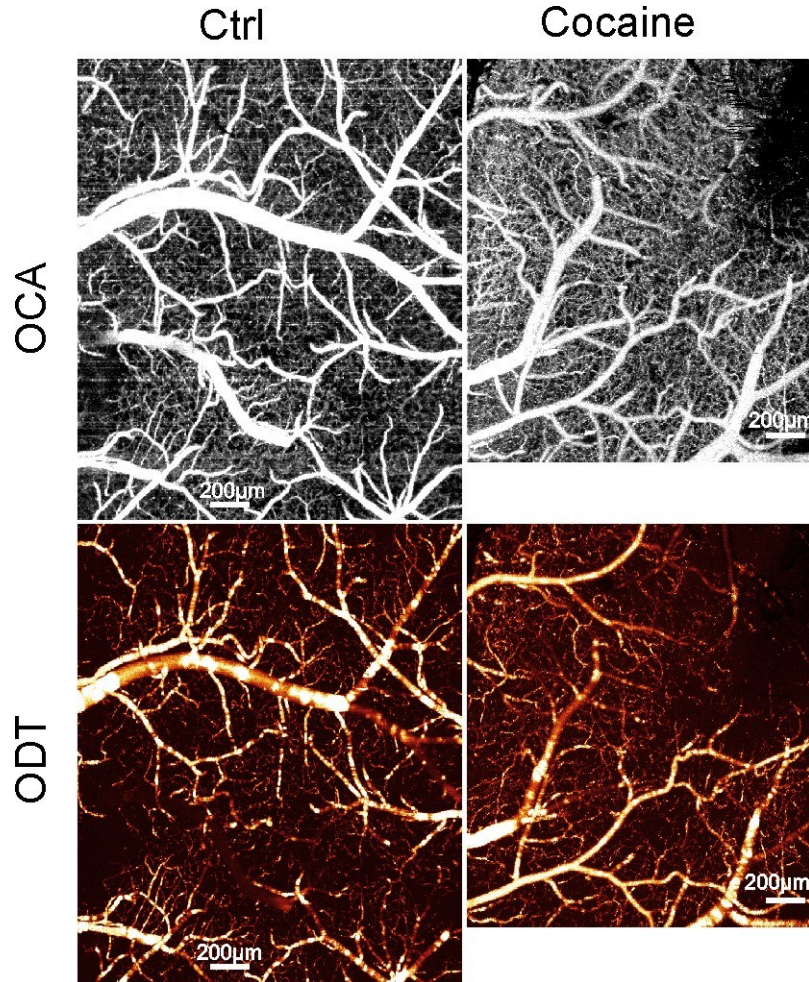


Fig. 11.7 Typical OCA (top panel) and ODT (bottom panel) images of control mouse (left panel) and chronic cocaine treated mouse (right mouse).

Fig. 11.8 shows the results of quantitative evaluation of vascular density of control and chronic cocaine treated rat. The image processing procedures can be

described as below. The OCA image was first converted to gray scale image, and then image registration was performed to align the central vein parallel with the short edge of the image. A ROI was then selected to extract the vessel areas which are at the same location relative to the whole brain. Once the ROI images were extracted, image segmentation was performed based on threshold to identify the vascular areas. In the end, the ratio of the vascular area compared with the whole ROI was calculated as the vascular density parameter. In this group of images, the vascular density of the cocaine naïve rat is 53%, while the vascular density of the cocaine treated rat is 60%, which is about 13% higher.

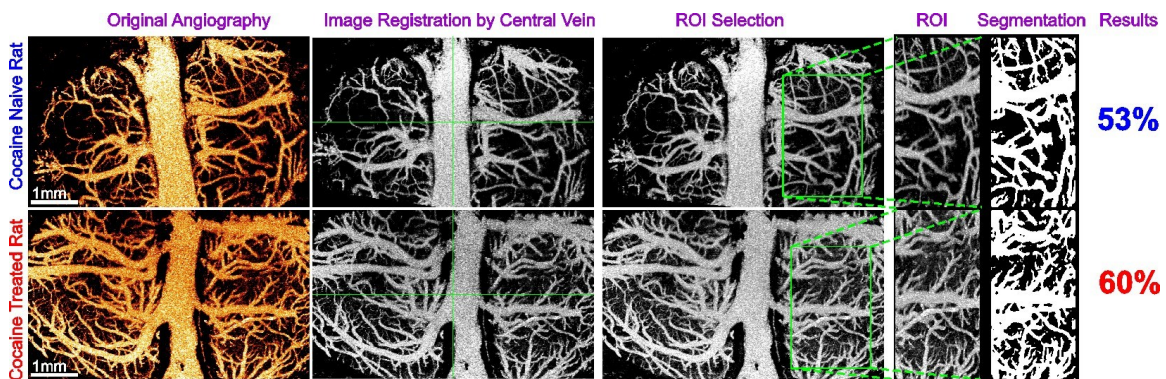


Fig. 11.8 Quantitative evaluation of vascular density difference between control rat and chronic cocaine treated rat.

11.4 Discussions

Investigations into the rewarding system of the brain play a crucial role in understanding the mechanisms of various neurological and psychiatric diseases. With the high spatial and temporal resolutions, optical Doppler tomography (ODT) provides an excellent platform for preclinical studies and potential clinical applications in the future.

Recently, in our group, we have developed an ultrahigh resolution optical Doppler tomography system to enable quantitative cerebral blood flow imaging in vivo at capillary level. The performance of the system was validated with an acute cocaine challenge model. In this chapter, an enhanced ODT system with improved scanning protocol and high performance contrast agent was presented, and the chronic cocaine effect was studied and compared with the control group.

A unique feature of the chronic cocaine treated rat is the long lasting CBF decrease after cocaine challenge. For instance, in the cocaine self-administration group, for the LA rats, after cocaine challenge, the CBF decrease lasted more than 20 minutes. While for the control rats, this is usually less than 5 minutes. This feature is likely due to the lack of elasticity of the blood vessels, which was induced by the long time high dose cocaine stimulation. The same effect was also observed in another group of chronic cocaine study by using a cLH rat model.

Another chronic cocaine effect discovered in this study is that the vascular density is correlated with the cocaine administration. Fig. 11.7 and Fig. 11.8 showed the qualitative and quantitative results of the vascular densities of control and cocaine treated groups. After chronic cocaine treatment, the vascular density increased. Together with the phenomenon observed in Fig. 11.5 and Fig. 11.6, this increase of the vasculature could likely be a way to compensate the decrease of the CBF velocity. The lower panel of Fig. 11.7 shows the quantitative CBF velocity maps of a typical control and a chronic cocaine treated mice, which also confirms similar result.

During the cocaine study, when we analyzed the CBF response data, we observed a low frequency fluctuation¹¹⁹ of the CBF at $\sim 0.12\text{Hz}$. Fig. 11.9 shows the results of an artery and a vein. Fig. 11.9 a) shows the 3D ODT map, and Fig. 11.9 b) shows the corresponding vein-artery separation results. One vein and one artery were selected, and their M-mode CBF profiles were shown in Fig. 11.9 c). Even with pure visual examination, this slow fluctuation of the CBF can be well observed. A short time Fourier transform analysis was performed and the result was shown at the bottom of Fig. 11.9 c). The peak frequency was clearly identified to be $\sim 0.12\text{ Hz}$ and did not change over a long period of time. The underlying mechanism of this low frequency fluctuation is still under investigation. However, this slow fluctuation of CBF was also documented by fMRI researcher before, and likely could reflect some of the functional activities of the brain.

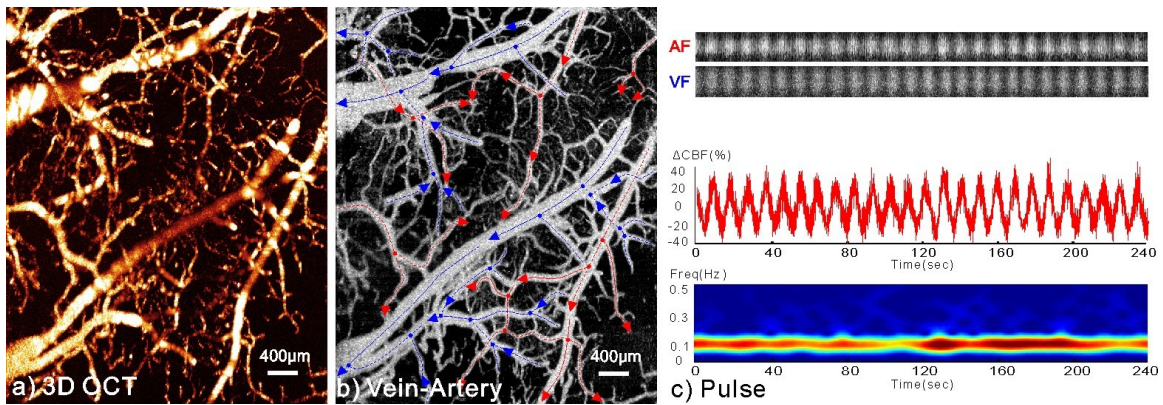


Fig. 11.9 Low frequency fluctuation of the CBF in veins and arteries.

11.4 Conclusions

In conclusion, we have improved the performance of ODT system with optimized system design, newly developed scanning protocol and high performance contrast agent.

With the enhanced performance, the chronic cocaine effect on CBF response was investigated with cocaine self-administration rat model, cLH rat model and chronic cocaine treated mouse model. It was found that the CBF decrease after cocaine challenge is lasting longer for the chronic cocaine treated animals than the control group. Also, the vascular density in the cocaine treated group was higher than that of the control group. In the future, further statistical analyses will need to be performed.

Chapter 12 Conclusions and Future Work

Optical coherence tomography (OCT) is a noninvasive imaging technique with high resolution (e.g., 1~10 μm) at intermediate depth. Since it was first introduced in the 1990s, OCT has evolved several generations from time-domain, spectral-domain to swept-source. At the same time, the performance, such as resolution, imaging speed, sensitivity roll-off, has been improved dramatically, which further enhances the clinical adoption of OCT. The first commercial OCT system was delivered by Carl Zeiss in 1996. Since then, OCT market has expanded quickly. However, due to the physical limitation of the light, intermediate penetration depth inside biological tissue has been a barrier to limit OCT clinical adoption mainly in the ophthalmology.

Endoscopic imaging via fiber-optic technique provides OCT the capability to image the internal organ directly *in vivo*. In this dissertation, cystoscopic OCT (COCT) technique was designed, developed and validated based on a bladder cancer model. In Chapter 3, a MEMS mirror based front-view rigid OCT endoscope was designed, optimized and developed. The unique touch-and-see feature enables user friendly OCT examinations. With more than 220 clinical cases performed in the operating room, MEMS mirror based COCT was demonstrated to provide a sensitivity of 92.4% and specificity of 85.2% for clinical bladder cancer diagnosis. To further enable early stage

bladder cancer diagnosis in the outpatient, in Chapter 4, we described a newly designed hybrid flexible cystoscopic OCT (FCOCT) probe for side-view imaging. The miniature size (i.e., 2mm) enables smooth integration of the probe into the commercial cystoscope used in the outpatient examination. Since the probe is flexible, for those lesions located close to the bladder neck, full access can be achieved through articulating the tip of the cystoscope, which was impossible for the MEMS mirror based rigid one. Moreover, with a field of view of larger than 8mm, FCOCT enables tumor boundary delineation and guided tumor resection.

Traditional OCT imaging diagnoses were based on descriptive and qualitative features, which is subjective and labor intensive. In the second part of my dissertation, quantitative diagnosis through computer aided image analysis was proposed, developed and performed based on a transgenic bladder carcinoma in situ model. Chapter 5 describes a newly developed 3D OCT based CAD algorithm to enhance the diagnosis of bladder carcinoma in situ (CIS) by evaluating the increased urothelial heterogeneity induced by carcinogenesis. This new technique promises to be an effective diagnostic method of bladder CIS with an estimated 95.7% sensitivity and 92.3% specificity. In order to translate our newly developed algorithm into clinical practice, in Chapter 6, we designed a comparative study to examine the advantages and potential limitations of current noninvasive bladder cancer diagnostic methods including white light cystoscopy (WLC), narrow band imaging (NBI), fluorescence cystoscopy (FC) and 3D OCT. The results of this study demonstrated the potential of NBI-guided cystoscopic OCT to effectively enhance the efficacy and efficiency of current cystoscopic procedure in the

diagnosis of CIS. Not only for cancer diagnosis, high resolution 3D OCT inspired another novel clinical application, which is to diagnose human fetal membrane diseases by detecting the subsurface cysts. In Chapter 7, we reported to our knowledge the first human fetal membrane study by using high resolution 3D OCT. 3D image segmentation was performed and the quantitative feature data were extracted. The results showed that the high resolution and 3D imaging capability of OCT enabled delineation of morphological details of human fetal membrane and early detection of microscopic chronic pseudocysts.

Functional imaging has always been a hot topic in the medical imaging field. Doppler OCT has been developed to probe blood flow information. However, due to limited resolution and sensitivity, only large branch vessels can be detected by conventional Doppler OCT. In the third part of my dissertation, an ultrahigh resolution optical Doppler tomography (ODT) system was developed and characterized. In Chapter 8, we first described the design and development of the ultrahigh resolution ODT system and the corresponding image processing algorithms. The superior resolution and sensitivity enabled quantitative imaging of blood flow at capillary level. This newly developed tool was then demonstrated to be a unique approach in the investigation of acute cocaine challenge in the rodent brain, and cocaine elicited micro-ischemia was observed 45 minutes after the cocaine administration. With this ultrahigh resolution, in Chapter 9, we proposed a new approach named particle counting μ ODT (pc- μ ODT) to accurately measure the instantaneous red blood cell velocity in vivo without contrast dye administration. Despite the high sensitivity, Doppler based flow imaging techniques have

been shown to provide lower vascular turnouts than angiographic approaches. In Chapter 10, we investigated the contrast differences between ODT and OCA, and found that the high contrast of OCA was partially due to the enhancement from the Brownian motion of the red and white blood cells. With this in depth understanding of Doppler technique, in Chapter 11, we improved the performance of the ODT system through optimized optical design, newly developed contrast agent and scanning protocol, and preliminary investigation into the chronic cocaine effect on the rodent brain was performed.

To further optimize the performance of quantitative structural and functional imaging *in vivo*, future developments include:

1. Design and development of a miniature 3D imaging COCT probe. As we demonstrated in Chapter 5, due to one more dimensional correlation, 3D imaging provides more information and better contrast than 2D imaging. For clinical diagnosis, large field of view also helps reduce sampling errors and shorten the examination time. Currently, the COCT probes developed are mainly 2D imaging ones. For instance, the FCOCT described in Chapter 4 achieved linear scanning based on push-pull mechanism. With the implementation of fiber rotary joint, fast circular scans can be combined with the current linear scan to enable 3D imaging. However, bladder cavity is filled with urine and only the bladder wall is the imaging target, synchronization between image acquisition and fiber rotation is critical.
2. Quantitative diagnosis of human bladder cancer *in vivo*. Current OCT diagnosis of human bladder cancer is based on descriptive and qualitative features, which is

labor intensive. In Chapter 5-6, we have demonstrated the efficacy and efficiency of quantitative image analysis for bladder cancer diagnosis through computer aided detection based on a rodent model. The diagnostic criterion is based on the increased heterogeneity of the urothelium induced by the non-uniform growth and distribution of cancer cells. The threshold used for the quantitative diagnosis was derived from a training data set prior to the study. It is promising that we can transfer the same technique to the clinical human bladder cancer diagnosis. However, unlike the transgenic rodent model, human cancer cases are more complicated and the symptoms are more diverse. Therefore, the threshold we used for the rodent model has to be updated based on the training data set of human bladder images. With the development of 3D COCT probe, quantitative and robust diagnosis of human bladder cancer at real time *in vivo* will be desired.

3. Long term, highly sensitive and automatic measurement of RBC velocity. In Chapter 9, for the first time, we showed that pc- μ ODT technique can be used to measure the RBC velocity based on transient phase information without contrast dye. Since the phase transient of moving RBC is very fast, high sampling rate is required. With limited cameras on the market, in our system, the maximum speed of the camera was limited to 27 kHz. Therefore, the frame rate was only around 1 kHz. Recently, a higher speed camera with 140 kHz from Basler was released. Combined with a resonant galvo scanner, the frame rate can be increased to \sim 5 kHz, and the measurement sensitivity will be

improved substantially. Also, with high sampling rate, large data set will be generated continuously. With current computer technology, fast data transfer between camera and computer memory can be achieved to enable continuous data buffer into memory, and therefore, long term monitor can be realized. More importantly, automatic RBC recognition, peak detection and other image and signal processing techniques can be combined to enable fully automatic RBC velocity measurement and analysis.

4. Endoscopic OCT & μ ODT for deep brain structural & functional imaging. Because of high resolution and high sensitivity, μ ODT has been demonstrated to be a valuable tool for brain functional imaging. In the first part of my dissertation, we have shown that endoscopic OCT can overcome the penetration barrier of the light to enable internal organ imaging. Specifically, for brain tissue, needle like GRIN relay lens can be employed as a miniature endoscope for deep brain structural and functional imaging. Since broadband light source is applied in OCT/ μ ODT, aberrations (e.g., spherical, chromatic) and dispersion has to be minimized or compensated.
5. Multimodality brain functional imaging with μ ODT, MPM and NIRS. For brain functional imaging, the utility of μ ODT, MPM and NIRS have been verified through various studies. However, different imaging modalities have different advantages and limitations. For instance, μ ODT enables label free high resolution blood flow imaging at large field of view, while only vascular information can be obtained. With the sub-micro resolution, MPM can be used

for single capillary as well as fluorescence imaging, the penetration depth is low and field of view is small. NIRS is a unique tool for high resolution large field of view hemoglobin concentration measurement to probe the metabolic level. By combining these three imaging modalities, high resolution, large field of view vascular, neuronal and metabolic information of the brain can be obtained simultaneously to accurately represent the brain functional activity.

6. Automatic full field vein and artery separation. For the first time, we showed that ODT technique can be used for vein and artery separation by combining Doppler effect with vascular 3D information. The 3D Doppler information can be obtained automatically from the 3D ODT data set. However, for automatic vein and artery separation, the vascular 3D layout information is still missing. Therefore, it is desired to develop a 3D image processing algorithm to retrieve the vascular 3D layout information. With both the Doppler signals and the 3D vascular data, automatic full field vein and artery separation can be achieved.

References

1. Weissleder, R. & Pittet, M.J. Imaging in the era of molecular oncology. *Nature* **452**, 580-589 (2008).
2. Vakoc, B.J. et al. Three-dimensional microscopy of the tumor microenvironment in vivo using optical frequency domain imaging. *Nature medicine* **15**, 1219-1223 (2009).
3. Huang, D. et al. Optical coherence tomography. *Science* **254**, 1178 (1991).
4. De Boer, J.F. et al. Improved signal-to-noise ratio in spectral-domain compared with time-domain optical coherence tomography. *Optics Letters* **28**, 2067-2069 (2003).
5. Choma, M.A., Sarunic, M.V., Yang, C. & Izatt, J.A. Sensitivity advantage of swept source and Fourier domain optical coherence tomography. *Optics Express* **11**, 2183-2189 (2003).
6. Leitgeb, R., Hitzenberger, C. & Fercher, A.F. Performance of fourier domain vs. time domain optical coherence tomography. *Opt. Express* **11**, 889-894 (2003).
7. Ren, H. et al. Diagnosis of bladder cancer with microelectromechanical systems-based cystoscopic optical coherence tomography. *Urology* **74**, 1351-1357 (2009).
8. De Boer, J.F., Milner, T.E., van Gemert, M.J.C. & Nelson, J.S. Two-dimensional birefringence imaging in biological tissue by polarization-sensitive optical coherence tomography. *Optics Letters* **22**, 934-936 (1997).
9. Wang, R.K. et al. Three dimensional optical angiography. *Optics Express* **15**, 4083-4097 (2007).
10. Chen, Z. et al. Noninvasive imaging of in vivo blood flow velocity using optical Doppler tomography. *Optics Letters* **22**, 1119-1121 (1997).
11. Izatt, J.A., Kulkarni, M.D., Yazdanfar, S., Barton, J.K. & Welch, A.J. In vivo bidirectional color Doppler flow imaging of picoliter blood volumes using optical coherence tomography. *Optics Letters* **22**, 1439-1441 (1997).
12. Yuan, Z., Luo, Z., Ren, H., Du, C. & Pan, Y. A digital frequency ramping method for enhancing doppler flow imaging in Fourier-domain optical coherence tomography. *Optics Express* **17**, 3951-3963 (2009).
13. Drexler, W. et al. Ultrahigh-resolution ophthalmic optical coherence tomography. *Nature medicine* **7**, 502-507 (2001).
14. Jang, I.K. et al. In vivo characterization of coronary atherosclerotic plaque by use of optical coherence tomography. *Circulation* **111**, 1551 (2005).

15. Baumgartner, A. et al. Polarization–Sensitive Optical Coherence Tomography of Dental Structures. *Caries Research* **34**, 59-69 (2000).
16. Yuan, Z. et al. Noninvasive and high-resolution optical monitoring of healing of diabetic dermal excisional wounds implanted with biodegradable in situ gelable hydrogels. *Tissue Engineering Part C: Methods* **16**, 237-247 (2009).
17. Ren, H., Yuan, Z., Waltzer, W., Shroyer, K. & Pan, Y. Enhancing Detection of Bladder Carcinoma In Situ by 3-Dimensional Optical Coherence Tomography. *The Journal of urology* **184**, 1499-1506 (2010).
18. Tearney, G. et al. Scanning single-mode fiber optic catheter-endoscope for optical coherence tomography. *Optics Letters* **21**, 543-545 (1996).
19. Bouma, B. & Tearney, G. Power-efficient nonreciprocal interferometer and linear-scanning fiber-optic catheter for optical coherence tomography. *Optics Letters* **24**, 531-533 (1999).
20. Boppart, S. et al. Forward-imaging instruments for optical coherence tomography. *Optics Letters* **22**, 1618-1620 (1997).
21. Liu, X., Cobb, M.J., Chen, Y., Kimmey, M.B. & Li, X. Rapid-scanning forward-imaging miniature endoscope for real-time optical coherence tomography. *Optics Letters* **29**, 1763-1765 (2004).
22. Chen, Z., Milner, T.E., Dave, D. & Nelson, J.S. Optical Doppler tomographic imaging of fluid flow velocity in highly scattering media. *Optics Letters* **22**, 64-66 (1997).
23. Zhao, Y. et al. Phase-resolved optical coherence tomography and optical Doppler tomography for imaging blood flow in human skin with fast scanning speed and high velocity sensitivity. *Optics letters* **25**, 114-116 (2000).
24. Bachmann, A.H., Villiger, M.L., Blatter, C., Lasser, T. & Leitgeb, R.A. Resonant Doppler flow imaging and optical vivisection of retinal blood vessels. *Optics Express* **15**, 408-422 (2007).
25. Szkulmowski, M., Szkulmowska, A., Bajraszewski, T., Kowalczyk, A. & Wojtkowski, M. Flow velocity estimation using joint Spectral and Time domain Optical Coherence Tomography. *Optics Express* **16**, 6008-6025 (2008).
26. Tao, Y.K., Davis, A.M. & Izatt, J.A. Single-pass volumetric bidirectional blood flow imaging spectral domain optical coherence tomography using a modified Hilbert transform. *Optics Express* **16**, 12350-12361 (2008).
27. Wang, R.K. & Hurst, S. Mapping of cerebro-vascular blood perfusion in mice with skin and skull intact by Optical Micro-AngioGraphy at 1.3 m wavelength. *Optics Express* **15**, 11402-11412 (2007).
28. Yu, L. & Chen, Z. Doppler variance imaging for three-dimensional retina and choroid angiography. *Journal of biomedical optics* **15**, 016029 (2010).
29. Xie, T., Xie, H., Fedder, G. & Pan, Y. Endoscopic optical coherence tomography with new MEMS mirror. *Electronics Letters* **39**, 1535-1536 (2003).
30. http://seer.cancer.gov/csr/1975_2005/results_single/sect_01_table.01.pdf.
31. Messing, E.M. & Catalona, W. Urothelial tumors of the urinary tract. *Campbell's Urology, ed 7*, 2327-2410.

32. Leyh, H. et al. Comparison of the BTA stat Test with Voided Urine Cytology and Bladder Wash Cytology in the Diagnosis and Monitoring of Bladder Cancer. *European urology* **35**, 52-56 (2000).
33. Sarosdy, M.F. et al. Clinical evaluation of a multi-target fluorescent in situ hybridization assay for detection of bladder cancer. *The Journal of urology* **168**, 1950-1954 (2002).
34. Cajulis, R.S., Haines III, G.K., Frias Hidvegi, D., McVary, K. & Bacus, J.W. Cytology, flow cytometry, image analysis, and interphase cytogenetics by fluorescence in situ hybridization in the diagnosis of transitional cell carcinoma in bladder washes: a comparative study. *Diagnostic cytopathology* **13**, 214-223 (1995).
35. Kriegmair, M. et al. Detection of early bladder cancer by 5-aminolevulinic acid induced porphyrin fluorescence. *The Journal of urology* **155**, 105-110 (1996).
36. Lerner, S.P., Goh, A.C., Tresser, N.J. & Shen, S.S. Optical coherence tomography as an adjunct to white light cystoscopy for intravesical real-time imaging and staging of bladder cancer. *Urology* **72**, 133-137 (2008).
37. Wang, Z., Durand, D., Schoenberg, M. & Pan, Y. Fluorescence guided optical coherence tomography for the diagnosis of early bladder cancer in a rat model. *The Journal of urology* **174**, 2376-2381 (2005).
38. Zagaynova, E.V. et al. In vivo optical coherence tomography feasibility for bladder disease. *The Journal of urology* **167**, 1492-1496 (2002).
39. Pan, Y. et al. Detection of tumorigenesis in rat bladders with optical coherence tomography. *Medical physics* **28**, 2432 (2001).
40. Tearney, G. et al. Optical biopsy in human urologic tissue using optical coherence tomography. *The Journal of urology* **157**, 1915-1919 (1997).
41. Wang, Z. et al. In vivo bladder imaging with microelectromechanical-systems-based endoscopic spectral domain optical coherence tomography. *Journal of biomedical optics* **12**, 034009 (2007).
42. Wojtkowski, M., Kowalczyk, A., Leitgeb, R. & Fercher, A. Full range complex spectral optical coherence tomography technique in eye imaging. *Optics Letters* **27**, 1415-1417 (2002).
43. Pan, Y., Xie, H. & Fedder, G.K. Endoscopic optical coherence tomography based on a microelectromechanical mirror. *Optics Letters* **26**, 1966-1968 (2001).
44. Pan, Y.T., Wu, Z.L., Yuan, Z.J., Wang, Z.G. & Du, C.W. Subcellular imaging of epithelium with time-lapse optical coherence tomography. *Journal of biomedical optics* **12**, 050504 (2007).
45. Yuan, Z. et al. High-resolution imaging diagnosis and staging of bladder cancer: comparison between optical coherence tomography and high-frequency ultrasound. *Journal of biomedical optics* **13**, 054007 (2008).
46. Galsky, M.D., Sonpavde, G. & Hutson, T. Current Management of Bladder Cancer. *US Oncol Dis*, 62-66 (2006).
47. Zaak, D. et al. Role of 5-aminolevulinic acid in the detection of urothelial premalignant lesions. *Cancer* **95**, 1234-1238 (2002).

48. Risse, T. Hough transform for line recognition: complexity of evidence accumulation and cluster detection. *Computer Vision, Graphics, and Image Processing* **46**, 327-345 (1989).
49. Amling, C.L. Diagnosis and management of superficial bladder cancer. *Curr Probl Cancer* **25**, 219-278 (2001).
50. May, M. et al. Comparative diagnostic value of urine cytology, UBC-ELISA, and fluorescence in situ hybridization for detection of transitional cell carcinoma of urinary bladder in routine clinical practice. *Urology* **70**, 449-453 (2007).
51. Sarosdy, M.F. et al. Clinical evaluation of a multi-target fluorescent in situ hybridization assay for detection of bladder cancer. *J Urol* **168**, 1950-1954 (2002).
52. Cauberg, E.C. et al. A new generation of optical diagnostics for bladder cancer: technology, diagnostic accuracy, and future applications. *Eur Urol* **56**, 287-296 (2009).
53. Bryan, R.T., Billingham, L.J. & Wallace, D.M. Narrow-band imaging flexible cystoscopy in the detection of recurrent urothelial cancer of the bladder. *BJU Int* **101**, 702-705; discussion 705-706 (2008).
54. Fradet, Y. et al. A comparison of hexaminolevulinat fluorescence cystoscopy and white light cystoscopy for the detection of carcinoma in situ in patients with bladder cancer: a phase III, multicenter study. *J Urol* **178**, 68-73; discussion 73 (2007).
55. Yuan, Z., Chen, B., Ren, H. & Pan, Y. On the possibility of time-lapse ultrahigh-resolution optical coherence tomography for bladder cancer grading. *J Biomed Opt* **14**, 050502 (2009).
56. Qi, X., Sivak, M.V., Isenberg, G., Willis, J.E. & Rollins, A.M. Computer-aided diagnosis of dysplasia in Barrett's esophagus using endoscopic optical coherence tomography. *Journal of Biomedical Optics* **11**, - (2006).
57. Lingley-Papadopoulos, C.A., Loew, M.H., Manyak, M.J. & Zara, J.M. Computer recognition of cancer in the urinary bladder using optical coherence tomography and texture analysis. *Journal of Biomedical Optics* **13**, - (2008).
58. Gossage, K.W., Tkaczyk, T.S., Rodriguez, J.J. & Barton, J.K. Texture, analysis of optical coherence tomography images: feasibility for tissue classification. *Journal of Biomedical Optics* **8**, 570-575 (2003).
59. Wu, X.R. & Sun, T.T.
60. Sylvester, R.J. et al. High-grade Ta urothelial carcinoma and carcinoma in situ of the bladder. *Urology* **66**, 90-107 (2005).
61. Witjes, J. Bladder Carcinoma in Situ in 2003: State of the Art* 1. *European urology* **45**, 142-146 (2004).
62. van Der Meijden, A.P.M. et al. EAU guidelines on the diagnosis and treatment of urothelial carcinoma in situ. *European urology* **48**, 363-371 (2005).
63. Schmidbauer, J. et al. Improved detection of urothelial carcinoma in situ with hexaminolevulinat fluorescence cystoscopy. *The Journal of urology* **171**, 135-138 (2004).

64. Gifford, R. et al. Report of the national high blood pressure education program working group on high blood pressure in pregnancy. *Am J Obstet Gynecol* **183**, 1-22 (2000).
65. Sibai, B., Dekker, G. & Kupferminc, M. Pre-eclampsia. *The Lancet* **365**, 785-799 (2005).
66. Weinstein, L. Syndrome of hemolysis, elevated liver enzymes, and low platelet count: a severe consequence of hypertension in pregnancy. *Obstetrical & Gynecological Survey* **37**, 461 (1982).
67. Sibai, B. Diagnosis and management of gestational hypertension and preeclampsia. *Obstetrics & Gynecology* **102**, 181 (2003).
68. Ness, R. & Roberts, J. Heterogeneous causes constituting the single syndrome of preeclampsia: a hypothesis and its implications. *American journal of obstetrics and gynecology* **175**, 1365-1370 (1996).
69. Stanek, J. & Weng, E. Microscopic chorionic pseudocysts in placental membranes: a histologic lesion of in utero hypoxia. *Pediatric and Developmental Pathology* **10**, 192-198 (2007).
70. Stanek, J. Diagnosing placental membrane hypoxic lesions increases the sensitivity of placental examination. *Archives of pathology & laboratory medicine* **134**, 989-995 (2010).
71. Pitris, C. et al. (Optical Society of America, 2000).
72. Adler, D. et al. Three-dimensional endomicroscopy of the human colon using optical coherence tomography. *Optics Express* **17**, 784-796 (2009).
73. Volkow, N.D., Mullani, N., Gould, K.L., Adler, S. & Krajewski, K. Cerebral blood flow in chronic cocaine users: a study with positron emission tomography. *The British Journal of Psychiatry* **152**, 641 (1988).
74. Howington, J.U., Kutz, S.C., Wilding, G.E. & Awasthi, D. Cocaine use as a predictor of outcome in aneurysmal subarachnoid hemorrhage. *Journal of neurosurgery* **99**, 271-275 (2003).
75. Pozzi, M., Roccatagliata, D. & Sterzi, R. Drug abuse and intracranial hemorrhage. *Neurological Sciences* **29**, 269-270 (2008).
76. Bartzokis, G. et al. Magnetic resonance imaging evidence of "silent" cerebrovascular toxicity in cocaine dependence. *Biological psychiatry* **45**, 1203-1211 (1999).
77. Toossi, S., Hess, C.P., Hills, N.K. & Josephson, S.A. Neurovascular Complications of Cocaine Use at a Tertiary Stroke Center. *Journal of Stroke and Cerebrovascular Diseases* **19**, 273-278 (2010).
78. Nanda, A., Vannemreddy, P., Willis, B. & Kelley, R. Stroke in the young: relationship of active cocaine use with stroke mechanism and outcome. *Brain Edema XIII*, 91-96 (2006).
79. Westover, A.N., McBride, S. & Haley, R.W. Stroke in young adults who abuse amphetamines or cocaine: a population-based study of hospitalized patients. *Archives of general psychiatry* **64**, 495-502 (2007).
80. Drew, P.J. et al. Chronic optical access through a polished and reinforced thinned skull. *Nature Methods* **7**, 981-984 (2010).

81. Brown, E.B. et al. In vivo measurement of gene expression, angiogenesis and physiological function in tumors using multiphoton laser scanning microscopy. *Nature medicine* **7**, 864-868 (2001).
82. Chaigneau, E., Oheim, M., Audinat, E. & Charpak, S. Two-photon imaging of capillary blood flow in olfactory bulb glomeruli. *Proceedings of the National Academy of Sciences of the United States of America* **100**, 13081 (2003).
83. Srinivasan, V.J. et al. Rapid volumetric angiography of cortical microvasculature with optical coherence tomography. *Optics letters* **35**, 43-45 (2010).
84. An, L., Qin, J. & Wang, R.K. Ultrahigh sensitive optical microangiography for in vivo imaging of microcirculations within human skin tissue beds. *Optics Express* **18**, 8220-8228 (2010).
85. Fujimoto, J.G. Optical coherence tomography for ultrahigh resolution in vivo imaging. *Nature biotechnology* **21**, 1361-1367 (2003).
86. Vakoc, B., Yun, S., de Boer, J., Tearney, G. & Bouma, B. Phase-resolved optical frequency domain imaging. *Optics Express* **13**, 5483-5493 (2005).
87. Yazdanfar, S., Yang, C., Sarunic, M. & Izatt, J. Frequency estimation precision in Doppler optical coherence tomography using the Cramer-Rao lower bound. *Optics Express* **13**, 410-416 (2005).
88. Liu, G. et al. Imaging vibrating vocal folds with a high speed 1050 nm swept source OCT and ODT. *Optics Express* **19**, 11880-11889 (2011).
89. Yuan, Z., Luo, Z., Volkow, N., Pan, Y. & Du, C. Imaging separation of neuronal from vascular effects of cocaine on rat cortical brain in vivo. *NeuroImage* (2010).
90. Ma, Z. et al. Measurement of absolute blood flow velocity in outflow tract of HH18 chicken embryo based on 4D reconstruction using spectral domain optical coherence tomography. *Biomedical optics express* **1**, 798-811 (2010).
91. Srinivasan, V.J. et al. Quantitative cerebral blood flow with optical coherence tomography. *Optics Express* **18**, 2477-2494 (2010).
92. Lewis, J. Fast normalized cross-correlation. *Vision Interface* **10**, 120-123 (1995).
93. Mehta, S.V., Gluncic, V., Iqbal, S.M., Frank, J. & Ansari, S.A. Role of Perfusion Imaging in Differentiating Multifocal Vasospasm-related Ischemia versus Thromboembolic Stroke in a Setting of Cocaine Abuse. *Journal of Stroke and Cerebrovascular Diseases* (2011).
94. Hatsukami, D.K., Thompson, T.N., Pentel, P.R., Flygare, B.K. & Carroll, M.E. Self-administration of smoked cocaine. *Experimental and Clinical Psychopharmacology* **2**, 115 (1994).
95. Luo, Z., Wang, Z., Yuan, Z., Du, C. & Pan, Y. Optical coherence Doppler tomography quantifies laser speckle contrast imaging for blood flow imaging in the rat cerebral cortex. *Opt. Lett.* **33**, 1156-1158 (2008).
96. Luo, Z., Yuan, Z., Tully, M., Pan, Y. & Du, C. Quantification of cocaine-induced cortical blood flow changes using laser speckle contrast imaging and Doppler optical coherence tomography. *Applied optics* **48**, D247-D255 (2009).
97. Krimer, L.S., Muly, E.C., Williams, G.V. & Goldman-Rakic, P.S. Dopaminergic regulation of cerebral cortical microcirculation. *Nature Neuroscience* **1**, 286-289 (1998).

98. He, G.Q., Zhang, A., Altura, B.T. & Altura, B.M. Cocaine-induced cerebrovasospasm and its possible mechanism of action. *Journal of Pharmacology and Experimental Therapeutics* **268**, 1532 (1994).
99. Ohtsuki, S., Yamaguchi, H., Kang, Y.S., Hori, S. & Terasaki, T. Reduction of L-Type Amino Acid Transporter 1 mRNA Expression in Brain Capillaries in a Mouse Model of Parkinson's Disease. *Biological & pharmaceutical bulletin* **33**, 1250-1252 (2010).
100. Albuquerque, M.L.C. & Dean Kurth, C. Cocaine constricts immature cerebral arterioles by a local anesthetic mechanism. *European journal of pharmacology* **249**, 215-220 (1993).
101. Du, C. et al. Differential effects of anesthetics on cocaine's pharmacokinetic and pharmacodynamic effects in brain. *European Journal of Neuroscience* **30**, 1565-1575 (2009).
102. Mandeville, J.B. et al. fMRI of Cocaine Self-Administration in Macaques Reveals Functional Inhibition of Basal Ganglia. *Neuropsychopharmacology* (2011).
103. Hollander, J.E. Cocaine intoxication and hypertension. *Annals of emergency medicine* **51**, 18 (2008).
104. Logothetis, N.K., Pauls, J., Augath, M., Trinath, T. & Oeltermann, A. Neurophysiological investigation of the basis of the fMRI signal. *Nature* **412**, 150-157 (2001).
105. Kleinfeld, D., Mitra, P.P., Helmchen, F. & Denk, W. Fluctuations and stimulus-induced changes in blood flow observed in individual capillaries in layers 2 through 4 of rat neocortex. *Proceedings of the National Academy of Sciences* **95**, 15741 (1998).
106. Yao, J., Maslov, K.I., Zhang, Y., Xia, Y. & Wang, L.V. Label-free oxygen-metabolic photoacoustic microscopy in vivo. *Journal of Biomedical Optics* **16**, 076003 (2011).
107. Jia, Y., An, L. & Wang, R.K. Label-free and highly sensitive optical imaging of detailed microcirculation within meninges and cortex in mice with the cranium left intact. *Journal of Biomedical Optics* **15**, 030510 (2010).
108. Vakoc, B.J. et al. Three-dimensional microscopy of the tumor microenvironment in vivo using optical frequency domain imaging. *Nature medicine* **15**, 1219-1223 (2009).
109. Ren, H. et al. Cocaine-induced cortical microischemia in the rodent brain: clinical implications. *Molecular Psychiatry* (2011).
110. Hutchinson, E.B., Stefanovic, B., Koretsky, A.P. & Silva, A.C. Spatial flow-volume dissociation of the cerebral microcirculatory response to mild hypercapnia. *Neuroimage* **32**, 520-530 (2006).
111. Wang, R.K. et al. Three dimensional optical angiography. *Opt. Express* **15**, 4083-4097 (2007).
112. Mariampillai, A. et al. Speckle variance detection of microvasculature using swept-source optical coherence tomography. *Optics letters* **33**, 1530-1532 (2008).

113. Makita, S., Jaillon, F., Yamanari, M., Miura, M. & Yasuno, Y. Comprehensive in vivo micro-vascular imaging of the human eye by dual-beam-scan Doppler optical coherence angiography. *Optics Express* **19**, 1271-1283 (2011).
114. Zotter, S. et al. Visualization of microvasculature by dual-beam phase-resolved Doppler optical coherence tomography. *Optics Express* **19**, 1217-1227 (2011).
115. Koob, G.F. & Le Moal, M. Drug addiction, dysregulation of reward, and allostasis. *Neuropsychopharmacology* **24**, 97-129 (2001).
116. Di Chiara, G. & Bassareo, V. Reward system and addiction: what dopamine does and doesn't do. *Current opinion in pharmacology* **7**, 69-76 (2007).
117. Gawin, F.H. Cocaine addiction: psychology and neurophysiology. *Science* **251**, 1580-1586 (1991).
118. Bartzokis, G. et al. Magnetic resonance imaging evidence of “silent” cerebrovascular toxicity in cocaine dependence. *Biological psychiatry* **45**, 1203-1211 (1999).
119. Diehl, R.R., Diehl, B., Sitzer, M. & Hennerici, M. Spontaneous oscillations in cerebral blood flow velocity in normal humans and in patients with carotid artery disease. *Neuroscience letters* **127**, 5-8 (1991).